SYNTHESIS AND CHARACTERIZATIONS OF NOVEL SOLID POLYMER ELECTROLYTES WITH CARBON NANOTUBE AS A FILLER

SURIANI IBRAHIM

DISSERTATION SUBMITTED IN FULFILMENT OF THE REQUIREMENTS FOR THE DEGREE OF MASTER OF ENGINEERING SCIENCE

FACULTY OF ENGINEERING
UNIVERSITY OF MALAYA
KUALA LUMPUR

2011

ABSTRACT

Nanocomposite solid polymer electrolyte based on poly (ethylene oxide) (PEO) as a host matrix, doped with lithium hexaflurophosphate (LiPF$_6$) salt, plasticized with ethylene carbonate (EC) and dispersed with amorphous carbon nanotubes (αCNTs) as nanocomposite filler were prepared by solution-casting technique. The polymer electrolytes were characterized by Impedance Spectroscopy (IS) to obtain the composition of additives which gives the highest conductivity value for each system. At room temperature, the highest conductivity was found to be 1.30×10^{-3} Scm^{-1} with a composition of PEO - 20wt% LiPF$_6$ -   15wt%EC and αCNTs - 5wt%. The ionic conductivities of the nanocomposite polymer electrolytes increased with temperature and obeyed the Vogel-Tamman-Fulcher (VTF) law. The crystallinity, chemical reaction, thermal behaviour, morphologies and optical properties of the nanocomposite polymer electrolytes were examined by using FTIR, XRD, DSC, TGA, UV Vis and PL Spectrophotometer. FTIR indicates the existence of interactions among PEO, LiPF$_6$, EC and αCNTs. XRD and DSC studies indicate that the increased conductivity was due to the increase in amorphous content. This enhanced the segmental flexibility of polymeric chains and the disordered structure of the electrolytes. TGA studies indicate that the stability of nanocomposite polymer electrolytes was decreased when 5wt% of αCNTs filler was added into plasticized polymer electrolytes. The SEM micrographs showed surface changes when LiPF$_6$, EC and αCNTs were added into the polymer systems. The optical band gaps for PEO - 20wt% LiPF$_6$ - 15wt% EC - 5wt% αCNTs was 4.60 eV. A neural network model was developed which could predict the Nyquist plot of nanocomposite polymer electrolyte system (PEO - LiPF$_6$ - EC - CNT). The Bayesian neural network was found to be successful in predicting the experimental results, which climates the time-consuming studies.

ABSTRAK

Elektrolit polimer pejal komposit berasaskan polietilena oksida (PEO) sebagai matriks, lithium hexaflurofosfat (LiPF$_6$) sebagai garam, etilena karbonat (EC) sebagai bahan pemplastik dan tiub nanokarbon amorfous (αCNTs) sebagai bahan pengisi komposit nano disediakan dengan menggunakan teknik tuangan larutan. Sifat elektrolit polimer tersebut dicirikan dengan menggunakan spektrometer berimpedans (IS) untuk mendapatkan komposisi aditif yang mempunyai kekonduksian tertinggi bagi setiap sistem. Pada suhu bilik, kekonduksian tertinggi diperolehi ialah 1.30×10^{-3} Scm^{-1} dengan komposisi PEO - 20wt% LiPF$_6$ - 15wt% EC - 5wt% αCNTs. Kekonduksian bagi semua elektrolit polimer komposit nano menunjukkan peningkatan dengan suhu dan mematuhi sifat Vogel-Tamman-Fulcher (VTF). Sifat hablur, tindak balas kimia, haba, morfologi dan optik untuk semua elektrolit polimer komposit nano telah dianalisis dengan menggunakan FTIR, XRD, DSC, TGA, Spektrofotometer UV- Vis dan PL. FTIR menunjukkan kewujudan tindak balas di antara PEO, LiPF$_6$, EC dan αCNTs. Kajian XRD dan DSC menandakan bahawa peningkatan kekonduksian adalah disebabkan oleh peningkatan kandungan amorfous. Oleh yang demikian, ia meninggikan kelenturan rantai polimer dan struktur tak teratur elektrolit. Kajian TGA menunjukkan keseimbangan terma elektrolit polimer komposit nano menurun apabila 5wt% αCNTs bahan pengisi ditambah pada elekrolit polimer berplastik. Kajian imej SEM menunjukkan perubahan pada permukaan apabila LiPF$_6$, EC dan αCNTs ditambah pada sistem polimer. Tenaga jurang jalur optik bagi PEO - 20wt% LiPF$_6$ - 15wt% EC - 5wt%. αCNTs ialah 4.60 eV. Sebuah model rangkaian neural telah dibangunkan untuk membuat jangkaan menggunakan plot 'Nyquist' untuk elekrolit polimer komposit nano sistem (PEO-LiPF$_6$-EC-αCNTs). Jaringan 'Bayesian neural' didapati berjaya dalam menjangka hasil eksperimen kajian ini.

ACKNOWLEDGEMENTS

Lastly, may this modest contribution to science be one of use to all to understand the universe and ultimately brings us closer to our Creator Himself. "We can only do the BEST of our Capability, PERFECTION is only for ALLAH THE ALMIGHTY". *Amin YaRabbal*

TABLE OF CONTENTS

Results and Discussion

References

Appendices

LIST OF PAPERS PUBLISHED FROM THIS WORK

Accepted Papers

1. ***Suriani Ibrahim***, Mariah Mohd Yassin, Roslina Ahmad, Mohd Rafie Johan, Effect of various $LiPF_6$ salt concentrations on the PEO based solid polymer electrolytes. Ionics. 17 (2011) 399.

2. Mohd Rafie Johan, ***Suriani Ibrahim,*** Neural networks for Nyquist plots prediction in a nanocomposite polymer electrolyte (PEO - $LiPF_6$ – EC - CNT). Ionics, , DOI 10.1007/s511981-011-0549-2.

3. ***Suriani Ibrahim***, Siti Mariah Mohd Yasin, Ng Meng Nee, Roslina Ahmad, Mohd Rafie Johan. Conductivity and Infrared Studies on PEO-$LiPF_6$-EC with Carbon Nanotube as Filler. *Paper presented at International Conference On Nanotechnology (ICONT 2009).* Pg 106-111.

LIST OF FIGURES

LIST OF TABLES

LIST OF SYMBOLS

n_i	density of carriers
q_i	charges of carriers
u_i	mobility of carriers in the polymer electrolytes
σ	ionic conductivity
GPa	Giga Pascal
l	electrolyte thickness between both electrodes
A	surface area of the electrolyte
R	total bulk electrolyte resistance
Z	Impedance
Θ	Bragg angle
V	*Volume*
Q	volume of the specimen
N	number of crystallites
η	number of point reflections
β	half-width of the broadened line
λ	wavelength
δ	disorientation angle
E	Young's modulus
μ	Poisson's ratio

A	weighted mean atomic weight
r	distance
v	frequency
k	wave vector of elastic
N	number of atoms
C_p	heat capacity
T_c	polymer's crystallization temperature
T_m	melting point
ε	the wavelength-dependent molar absorptivity coefficient
b	path length
c	velocity of light in a vacuum
Å	Angstrom
mμ	millimicron
R	reflection
n_f	refractive index
h	Planck's constant
ν	frequency
E	electronic energy
K	Kelvin
ε_r	Dielectric Constant
ε_i	Dielectric Loss

M_r	Real Electrical Modulus
M_i	Imaginary Electrical Modulus
$tan\ \delta$	Loss tangent
σ_w	regularisation constants
L	size of the committee
E_g	band gap
n	refractive index
R_b	bulk resistance

LIST OF ABBREVIATIONS

PEO	poly (ethylene oxide)
$LiPF_6$	lithium hexaflurophosphate
EC	ethylene carbonate
αCNTs	amorphous carbon nanotubes
IS	Impedance Spectroscopy
VTF	Vogel-Tamman-Fulcher
FTIR	Fourier Transform Infrared
XRD	X-Ray Diffraction
DSC	Differential Scanning Calorimetry
TGA	Thermogravimetric analysis
UV-vis	UV – Visible Spectrophotometer
PL	Photoluminescence Spectrophotometer
FESEM	Field Emission – Scanning Electron Microscope
GHG	green house gases
CNTs	carbon nanotubes
IR	Infrared
nm	nanometres
PPO	polypropylene oxide

NaI	Sodium iodide
NaSCN	Sodium thiocyanate
KSCN	Potassium thiocyanate
LiClO$_4$	lithium perchlorate
T$_g$	glass transition temperature
SPEs	Solid polymer electrolytes
S/cm	Siemens per centimetre
LiAsF$_3$	lithium hexafluoroarsenate
LiBF$_4$	Lithium tetrafluoroborate
LiCF$_3$SO$_3$ (LiTf)	lithium trifluoromethanesulfonate
LiN(CF$_3$SO$_2$)$_2$	Lithium trifluoromethane sulfonimide
LiTfsi	Lithium bisperfluoroethanesulfonimide
eV	electron Volt
V	Volt
AC	Alternating Current
PMMA	Poly(methyl methacrylate)
PTMG	poly(tetramethyene glycol)
ZnCl$_2$	Zinc chloride
Co(II)Cl$_2$	cobalt(II)chloride
Mg$_2^+$	Magnesium

Hg_2^+	Mercury
Li^+,	Lithium
Na^+,	Natrium
Ca^{2+}	Calcium
$NaBF_4$	Sodium tetrafluoroborate
$NaBH_4$	Sodium borohydride
LiSCN	lithium thiocyanate
$NaClO_4$	Sodium Perchlorate
$Zn(ClO_4)_2$	Zinc Perchlorate Hexahydrate
$ZnCl_2$	zinc chloride
ClO_4	perchlorate
$LiCF_3SO_3$	lithium triflate
LiCl	lithium chloride
LiBr	lithium bromide
PAN	polyacrylonitrile
PVP	poly(vinyl pyrrolidinone)
PVC	poly(vinyl chloride)
TiO_2	Titanium dioxide
$NaCH_3SO_3$	Sodium Formaldehydesulfoxylate
NaSCN	Sodium thiocyanate
NaI	Sodium iodide

NMR	nuclear magnetic resonance
CsSCN	cesium thiocyanate
WLF	Williams, Landel and Ferry equation
DC	Direct current
Hz	Hertz
Ω	Ohm
Z	Impedance
Z	atomic number
TEM	transmission electron microscope
HCl	Hydrochloric acid
A	absorbance
wt%	weight percentage
SEM	Scanning Electron Microscope
PVdF	Polyvinylidene fluoride
HFP	hexafluoropropylene
X_c	degree of crystallinity
ΔH_m	enthalpy change
LiF	Lithium fluoride
HF	Hydrogen fluoride
AE	absorption edge

CHAPTER ONE

Introduction

1.1   Background

In a time when oil prices are high and attention is being paid to the effects of human activities on our environment, a revision of our energy technologies is needed. In 1998, global leaders created a protocol to reduce significantly the amount of greenhouse gases (GHG) emitted in their countries (Winter and Brood, 2004). The use of alternative energy sources and the implementation of new technologies which reduces the amount of GHG emissions while improving the efficiency of fuel consumption is a key for the success of such initiatives.

Companies such as General Motors, Honda and Toyota had already introduced technologies in lithium ion batteries which store energy produced by the engines and the energy is utilized later to power the drive train of electric motors (Fu *et al*., 2005; Huggin *et al*., 2002; Robertson *et al*., 1997). The goal was to develop batteries which would supply the amount of energy required for the operation of devices for a longer period of time. The medium which allows ion transport from one electrode to another is called an electrolyte. Regardless of the processes which take place at the electrodes, improving the ion movement through the electrolyte is a key for the advancement of battery and fuel cell technologies, and has received significant

attention. One of the materials which is heavily used for the development of electrolytes is polymer.

The birth of synthetic polymer chemistry occurred about 175 years ago (Flory, 1953). Over the next fifty years then, vast numbers of other synthetic polymers were developed and commercialized in response to the growing need for new materials such as in automotive and aerospace industries (Fried, 2003). Some of the new materials include polyethylene, polypropylene, polystyrene and polycarbonate (Fried, 2003). In the late 20th century, the field of polymer chemistry began, which distracted attention from exploiting previously commercialized polymers and efforts were concentrated on developing new polymers for high-performance applications. Next generation batteries, fuel cells, visual displays, drug delivery platforms and fire retardants are only a few of the applications where new polymeric materials are currently being researched and developed. Over several decades lithium polymer batteries have been developed to substitute lithium ion batteries using liquid electrolytes (Gray, 1997; Abraham, 1993; Fauteux *et al*., 1993, Baril *et al*., 1997; Buriez *et al*., 2000; Kerr *et al*., 2000).

Since the 1970s, it is known that the addition of salts to polymers enable the polymers to conduct lithium ions. Thus, the material can serve as an electrolyte in lithium batteries. Lithium polymer batteries, when given full measure to the capacity for miniaturization of a fully solid state battery, can have the highest specific energy and specific power of any rechargeable technology. The advantages of lithium polymer batteries are easy battery assembly and a high energy density of lithium metal. This is because the former reduces the cost of battery production and the latter increases the energy of the battery per volume (Gray, 1997). Lithium polymer batteries typically consist of a lithium anode, a polymer electrolyte separator and a porous

composite cathode. The porous cathode is made of a polymer-electrolyte binder which also plays the role of electrolyte, electroactive particles which undergo charge and discharge and conducting carbon particles.

The cathode capacity is determined by the active particles, which are usually transition metal oxides capable of intercalating the lithium ions. During charging, lithium ions are de-intercalated from the active particles in a cathode, transported across the polymer electrolyte separator and electro-deposited on the lithium electrode. The transport mainly occurs through migration and diffusion of lithium ions. Convection and electro-osmosis can be neglected in polymer electrolytes. The concept of incorporating inorganic salts into a polymeric matrix for energy stroge applications began in the 1970s (Robertson, 1997). The first suggestion for the use of a poly(ethyleneoxide) PEO, based electrolyte came in 1978 (Robertson, 1997). PEO based complexes are the first solvent-free polymer electrolytes reported and have received a great deal of attention ever since their introduction. These solid electrolytes are of growing importance in solid-state electrochemistry in view of their applications and the most important being high-energy-density batteries. The motivation for developing solid polymer electrolytes came about from the desire of applying lithium metal, the highest of energy density metal as the anode of batteries in the most efficient and safe manner.

Currently, carbon nanotubes (CNTs) attract much attention as a new class of advanced ''filler'' materials due to their interesting properties and their possible applications in nanoelectronics and nanocomposites (Baughman *et al*., 2002; Kilbride *et al*., 2002; Poncharal, 1999). The CNTs/Nafion composites have been used in actuators, microscopic pumps, sensors

and electrocatalysts (Cooper *et al*., 2002; Ruan *et al*., 2003). Furthermore, Lahiff *et al.* (2006) have reported using such composites as an electrolyte, without obtaining any significant improvement in performance despite the higher mechanical stability.

Nanocomposite polymer electrolytes have been known for better thermal, mechanical and ionic conductivity compared to conventional composite polymer electrolytes due to stronger interactions between polymer and nano-filler phases (Garg *et al*., 1998; Kumar *et al*., 2002; Wall *et al*., 2006). CNTs-polymer composite materials have been used as an electrolyte in lithium-ion batteries and polymer electrolyte membrane fuel cells (Kis *et al*., 2004; Cooper *et al*., 2002; Frankland *et al*., 2002). It is known that the introduction of CNTs in polymers improves the stability and conductivity properties. The highly flexible nature of CNTs may improve interaction and cross-linking with polymer molecules, which may significantly enhance the morphological and electrical properties of composite electrolytes. In order to appreciate the importance of this technology, it is important to realize some of the efforts made in the progress of batteries and the aspiration that had led to the development of solid polymer electrolytes.

The successful employment of polymer electrolytes in engineering applications relies on the ability of the polymer electrolytes to meet design and service requirements. Their ability to do so depends on the physical properties of the polymer electrolytes. These properties can be precisely obtained with the appropriate measurements. They can also be estimated using models and correlations. However, many of these models are inaccurate, because they are not either based on thorough consideration of all relevant physical processes or the mathematical expression is inadequate. Recently, researchers have focused a great deal of attention on the

solution of non-linear problems in materials science (Bhadeshia, 1999; Bhadeshia *et al.*, 2009) to develop better expressions for physical material properties. In this study, Bayesian neural-networks (MacKay, 1992; MacKay, 1992; MacKay, 1995) were employed to predict the ionic conductivity of nanocomposite polymer electrolyte systems (PEO - LiPF$_6$ - EC - CNT).

1.2   Significance of Research Problems

The main objective for synthesizing polymer electrolytes is to produce the highest ionic conductivity. The high molecular weight poly(ethylene oxide) (PEO)-based composite polymer electrolytes are emerging as the best candidates to be used as polymer matrix because of their salvation power, complexion ability and ion transport mechanism directly connected with the alkaline salt (Li$^+$) (Pitawala *et al.*, 2007). However, the ionic conductivity of PEO–lithium salts (LiX) electrolytes at ambient temperature (10^{-7}–10^{-6} Scm^{-1}) is not sufficiently high for most practical applications. Enhancement of ionic in these polymer electrolytes has been achieved mainly by two techniques. The first technique involves the addition of low molecular weight plasticizers such as ethylene carbonate (EC), propylene carbonate (PC), dimethyl carbonate (DMC), and polyethylene glycol (PEG) into the conventional PEO–LiX systems. The plasticization is the conventional way to reduce crystallinity and increase the amorphous phase content of composite polymer electrolytes. However, the addition of plasticizer into polymer electrolytes reduces the mechanical properties of polymer electrolytes. To overcome this problem a filler is introduced into the polymer electrolytes. The improvement in mechanical properties has been explained on the premise that the filler particles act as a supporting matrix for the conductive polymer electrolytes so as to retain an overall solid structure even at higher temperatures (Raghavana *et al.*, 2008).

To the best of the author's knowledge, there are no studies reported regarding the use of amorphous carbon nanotubes (αCNTs) as a filler in polymer electrolytes. This dissertation reports the electrical, chemical, thermal and optical properties of novel nanocomposite polymer electrolytes. The electrical conductivity value is obtained to be 10^{-3} Scm^{-1} upon adding 5wt% αCNTs into the plasticized polymer electrolytes. FTIR studies show there are interactions between the polymer system with salt, plasticizer and filler. The thermal properties of novel nanocomposites increase when filler was added into plasticized polymer electrolytes.

1.3   Research Objectives

In line with the research problem discussed in the previous section, the objectives of this research are listed below:

1) To synthesize novel nanocomposite polymers electrolytes using solution-casting technique.

2) To characterize nanocomposite polymer electrolytes using analytical techniques such as IS, SEM, FTIR, DSC, TGA, XRD, UV-Vis and PL.

3) To develop a neural network model for nanocomposite polymer electrolytes.

1.4   Scope of Thesis

Chapter One is the introduction of the thesis. In this chapter, research background and research objectives are presented briefly.

Chapter Two presents a literature review of the synthesis techniques, material used and characterization techniques available to study the properties of nanocomposite polymer electrolytes.

Chapter Three describes the synthesis method to produce the optimized conditions of nanocomposite polymer electrolytes. The solution-casting technique is used to synthesize the nanocomposite polymer electrolytes. Finally, structural characterizations using Impedance Spectroscopy (IS), X-ray Diffraction (XRD), Fourier Transform Infrared (FTIR), Field Emission – Scanning Electron Microscope (FESEM), Differential Scanning Calorimetry (DSC), Thermogravimetric analysis (TGA), UV – Visible Spectrophotometer (UV-Vis) and Photoluminescence Spectrophotometer (PL) are presented.

Chapter Four presents the results on structure and morphology of the polymer electrolytes. The experimental results obtained from XRD and FESEM are discussed. The influence of key parameters on the structural changes and morphology is also presented.

Chapter Five presents the results of thermal and infrared of polymer electrolytes. The experimental results obtained from DSC, TGA and FTIR are discussed. The influence of key parameters on the thermal stability and polymer electrolyte complexation is also presented.

Chapter Six presents the results of conductivity and dielectric behaviour of polymer electrolytes. The experimental results obtained from IS are discussed. The influence of key parameters on conductivity is also presented.

Chapter Seven presents the results of the optical properties of nanocomposite polymer electrolytes. Optical properties like direct and indirect band gaps were investigated for pure and doped polymer films in the wavelength with a range of 200 – 400 nm. It was found that the energy gaps and band edge values shifted to lower energies upon doping. The reflectance and transmittance of the films are measured at room temperatures (298 K).

Chapter Eight presents the theoretical results using neural network for polymer electrolytes. A model was developed, which could predict the Nyquist plots for nanocomposite polymer electrolyte systems (PEO - $LiPF_6$ – EC - αCNTs).

Chapter Nine presents the conclusion and recommendations for future work.

CHAPTER TWO

Literature Review

2.1   Background

Polymers have been utilized by humans for as long as humans have been on earth. However, it was not until recently that humans learned how to make their own polymers. The birth of synthetic polymer chemistry occurred about 175 years ago. In 1839, Charles Goodyear in the United States and Thomas Hancock in Britain concurrently developed the vulcanization process which enhanced the properties of natural rubber via treatment with sulphur at elevated temperatures (Flory, 1953). Nitrocellulose, the first man-made thermoplastic, was developed in 1847, when Christian Schönbein treated cellulose with nitric acid (Flory, 1953). Then in 1907 the first synthetic polymer was invented by Leo Baekeland (Flory, 1953). This synthetic polymer, called Bakelite was a phenol-formaldehyde resin known for its high heat resistance. However, at this time, the modern definition polymer was not generally accepted in the scientific community.

The prevailing theory described the distinctive properties associated with polymeric materials as intermolecular interactions between many small molecules (Flory, 1953). It was not until early 20th century that this theory was challenged. In 1920, Herman Staudinger (1953 Chemistry Nobel Laureate) proposed that the unique characteristics of polymeric materials were not a result of interactions between many small molecules, but were long chain-like molecules

containing covalent chemical bonds (Staudinger 1920; Duclriux, 1923). Over the next decade Staudinger's "macromolecular theory" gained acceptance and was followed by a number of experiments performed by Wallace Carothers (Flory, 1953). In these experiments Carothers utilized well-characterized small molecules, monomers, to prepare high polymers, which provided support of the macromolecular theory.

Carothers invented the first synthetic rubber, a polyester which goes by the tradename Neoprener, and later went on and developed the first silk replacement, nylon or poly(hexamethylene adipamide), which also became the first synthetic polymer to be commercialized (Carothers, 1931; Mark, 1940). Over the next fifty years, vast numbers of other synthetic polymers were developed and commercialized in response to the growing need for new materials in the automotive and aerospace industries. Some of these new materials include polymers like polyethylene, polypropylene, polystyrene and polycarbonate (Fried, 2003). Then in the late 20th century, the field of polymer chemistry began to take its attention off of exploiting previously commercialized polymers and refocused its efforts on developing new polymers for high-performance applications. Next generation batteries, fuel cells, visual displays, drug delivery platforms and fire retardants are only a few of the applications where new polymeric materials are currently being researched and developed.

2.2 Polymeric Materials

Polymeric materials are something that humans could not live without. They are utilized in the simplest devices such as dental floss and tooth brushes, to the most complex devices NASA space shuttles. In addition to synthetically derived polymers, there are many naturally occurring polymers such as proteins, cellulose, silk and rubber which are utilized in everyday lives. The term "polymer" comes from the Greek word *poly*, which means "many", and *meres*, which means "parts". A polymer is a long-chain molecule which contains a large number of repeating units or monomers of identical structure. Most polymers are linear but there are many other types of architectures in which they exist. In combination with the polymer's architecture, the chemical structure of the monomer directly influences the physical properties of the polymer. This allows the physical properties of polymers to be tuned for specific applications.

2.3 Electrolytes

Electrolytes provide a medium for ions to diffuse between cathode and anode of the electrochemical cell. The flow rate of ions through the electrolytes, known as ionic conductivity, σ, limits the amount of current generated by a cell. The conductivity (σ) is a function of temperature and pressure as well as the density of carriers (n_i), their charge (q_i) and their mobility in the electrolyte (u_i), as shown in Equation (2.1).

$$\sigma(T.P) = \sum_j q_j n_j u_j \qquad (2.1)$$

While the number of carriers is important for electron conductivity, in the case of ionic conductors, the mobility of the ions is extremely important (Kohjiya *et al*., 2005). Electrolytes must have high enough ionic conductivity to satisfy the current requirements for the cell ($> 10^{-3}$ Scm^{-1} from -40 to 90ºC); they must be electrochemically stable within the redox potentials used during the operation of the cell (up to 5 V vs. lithium); they should be thermally stable at least up to 70ºC and they should be compatible with other components in the cell (Blonsky *et al*., 1984; Reddy and Hossain, 2002). Lithium ion batteries have used four different types of electrolyte systems: liquid electrolytes, gel electrolytes, polymer electrolytes and ceramic electrolytes.

.**Polymer Electrolytes for Lithium**

Polymer electrolytes are one of the most important components in all-solid state electrochemical devices, including rechargeable batteries and supercapacitors. Polymer electrolytes have two important functions in supercapacitors and batteries: (1) they carry cations (mostly lithium ions), and (2) they serve as an electrode spacer or a separator (Blonsky *et al*., 1984). The potential advantages of using ionic conducting polymers as solid electrolytes in batteries were first discussed by Armand *et al*. (1979). They reported that PEO complexes consisting of alkali-metal salts in acetonitrile solution have high ionic conductivity and may be fit for solid electrolytes in high energy batteries. In all solid polymeric electrolytes, high ionic conductivity requires an acceleration of ionic dissociation in the polymer. A low glass transition temperature (T_g) is beneficial for easy transport of ionic species.

There is recent interest in lithium-anode batteries for applications such as electric vehicles due to its theoretically high energy and power densities (Blonsky *et al*., 1984; Reddy and Hossain, 2002). Liquid electrolytes used in current rechargeable lithium-ion batteries are not suitable for lithium-anode batteries due to the instability of the lithium/electrolyte interface. A solid polymer electrolyte is a desirable alternative since it is solvent-free, stable against lithium metals, and able to form thin, flexible membranes. A promising polymer electrolyte for rechargeable lithium metal batteries is polyethylene oxide (PEO), which readily dissolves lithium salts of the form LiX such as $Li[N(SO_2CF_3)_2]$ (LiTFSI), $LiCF_3SO_3$ (lithium triflate), or $LiClO_4^-$ (lithium perchlorate). In this case, the ether oxygen on the PEO chain complexes with the Li^+ in LiX salts while the X^- is freely floating nearby to maintain electroneutrality. The effect of salts on the conductivity and structure of PEO-based polymer electrolytes will be discussed in this dissertation. Table 2.1 shows properties of several polymers and their conductivity values.

Table 2.1 Properties of selected polymers and polymer electrolytes (Omolola, 2002)

Polymer	Repeat Unit	T_g, °C	T_m, °C	Polymer electrolyte	Conductivity S/cm, 25°C
Poly(ethylene oxide)	$-CH_2CH_2O-$	-60	65	$(PEO)_8-LiClO_4$	-10^{-8}
Polyoxymethylene	$-CH_2O-$	-82	181	-	-
Poly(oxymethylene-oligo-oxyethylene)	$-(CH_2O)-$ (CH_2CH_2O-)	-66	13	$(PPO)_{25}-LiCF_3SO_3$	3×10^{-5}
Poly(propylene oxide)	$-(CH_3)CH_2CH_2O-$	-60	amorphous	$(PPO)_8-LiClO_4$	$\sim 10^{-8}$
MEEP		-83	amorphous	$(MEEP)_4-LiBF_4$	2×10^{-5}
Poly(dimethyl siloxane)	$-(-CH_3)_2-SiO-$	-127	-40	-	-

2.3.2 Gel Electrolytes

The first generation of Sony's lithium ion batteries used electrolyte solutions of lithium hexafluorophosphate in organic solvents such as ethylene carbonate (Winter and Brodd, 2004). However, the use of these solutions has given rise to a major problem: electrolyte leakage. This has pushed scientists to find ways to immobilize the electrolyte inside the battery to reduce leakage. Gelled polymer electrolytes have been used in Sony's second generation of lithium ion batteries. Gel electrolytes are made by impregnation of organic liquid electrolytes and lithium salts into a host polymer matrix (Nanno *et al*., 2005). Electrolyte solutions normally consist of a solvent mixture such as ethylene carbonate and propylene carbonate, whereas the polymer matrix consists of materials such as poly(acrylonitrile), poly(vinylidene fluoride), or block copolymers of poly(vinylidene fluoride) and poly(hexafluoropropylene) (Winter and Brodd, 2004; Nanno *et al*., 2005). The ionic conductivity of these systems depends on the weight ratio of host polymer / organic liquid electrolyte. Increasing the amount of liquid electrolyte on the formulation increases the ionic conductivity, but it also raises safety problems. In 1983, Tsuchida and his co-workers found that the physically cross-linked gelled PVDF had a conductivity of 1×10^{-3} Scm^{-1} at 25°C (Winter and Brodd, 2004). Generally, a polymeric gel is defined as a system which consists of a polymer network swollen with solvent (Nanno *et al*., 2005). Owing to their unique hybrid network structures, gels always simultaneously possess both the cohesive properties of solids and the diffusive transport properties of liquids. Some polymer gel electrolytes have high ionic conductivity of 10^{-3} Scm^{-1} at room temperature. However, their soft morphology, poor mechanical properties, and considerable viscosity may lead to internal short-circuits, give rise to

safety concerns, and make polymer gel electrolytes unsuitable for high-speed manufacturing processes (Nanno *et al*., 2005) .

2.3.3 Liquid Electrolytes

Organic carbonates have been used widely in the battery industry because they offer excellent stability, good safety properties and compatibility with electrode materials (Ehrlich, 2002). Conventional organic liquid electrolytes show lithium ion conductivity of 10^{-2} Scm^{-1} at room temperature, which is between one and two orders of magnitude lower than that of aqueous electrolytes (Reddy and Hossain, 2002; Ehrlich, 2002; Nanno *et al*., 2005). Ethylene carbonate, propylene carbonate, dimethyl carbonate, diethyl carbonate and ethylmethyl carbonate are some of the most common solvents used for lithium ion rechargeable batteries. Such solvents exhibit dielectric constants which range from 3 to 90, and solvate lithium salts at high concentrations (Ehrlich, 2002). However, it is typical to find electrolyte formulations which use a mixture of two to four different solvents to enhance cell performance (Ehrlich, 2002). Lithium hexafluorophosphate ($LiPF_6$) is currently the most common lithium salt used in lithium-ion batteries (Ehrlich, 2002). $LiPF_6$ solutions provide high ionic conductivity, $>10^{-3}$ Scm^{-1}, high lithium ion transference numbers (~ 0.35), and acceptable safety properties (Ehrlich, 2002). Other lithium salts have been used in industry, such as $LiClO_4$, $LiAsF_3$, $LiBF_4$. Organic lithium salts such as $LiCF_3SO_3$ (LiTf) and $LiN(CF_3SO_2)_2$ (LiTfsi) have also attracted a fair amount of attention from the battery industry (Ehrlich, 2002).

2.4   Solid Polymer Electrolytes (SPE)

A polymer electrolytes consisting of an inorganic salt dissolved in a polymer host was first described in the early 1970s (Kohjiya *et al.*, 2005). The concept was quickly adopted by the electrochemical community, which recognized the potential of using a flexible, plastic, ion-transporting medium in lithium ion cells for energy storage applications. Solid polymer electrolytes (SPEs) represent "non-liquid" battery systems that do not leak and become explosive, along with the flexibility of designing thin and light weight batteries in a variety of configurations. The conventional liquid electrolyte battery systems require heavy metal casing for their volatile electrolytes, whereby a polymer electrolyte battery needs merely foil coverage. Unfortunately, most of the PEO-based SPE's ionic conductivity are at least 10^2 to 10^3 times lower than that of liquid electrolytes.

Polyethers, polyimides or polythiols are among the more suitable polymer types. The most common polymer used in polymer electrolytes has so far been poly(ethylene oxide) (PEO), which has good solvating properties, as well as adequate thermal and chemical stability. High molecular weight polyethylene oxide (PEO)(MW = 5,000k) and lithium salts such as $LiClO_4$ and $LiN\ (CF_3SO_2)_2$ were among the first materials incorporated into solid polymer electrolytes (Reddy and Hossain, 2002). These systems have good mechanical properties but low conductivities (10^{-8} Scm^{-1} at 20^oC). A significant improvement in conductivities (10^{-5} Scm^{-1}) has been achieved with the combination of modified comb-shaped PEO structures with lithium salts, but these types of solid polymer electrolytes have poor mechanical properties and their

conductivity is still two orders of magnitude lower than that of most organic liquid electrolytes (Reddy and Hossain, 2002).

2.4.1 Structure and Morphology of Polymer Electrolytes

Poly(phenylene oxide) PPO is an amorphous polymer because of the bulky CH_3 side group which prevents the polymer from crystallizing. PEO has an identical backbone structure as PPO. PEO, however, lacks the CH_3 side group and is able to crystallize. When salts are dissolved in a polymer, small locally ordered structures can be identified in the polymer electrolyte. Since polymers are long linear molecules, polymers such as PEO are not able to crystallize completely. Instead, polymers crystallize in layers (Reddy and Hossain, 2002). A schematic of this situation is shown in Figure 2.1. Regions of amorphous polymer lie between the crystalline layers. It has been shown that ion conduction takes place primarily in these amorphous regions (Kohjiya *et al.*, 2005). The ion transport in the crystalline regions is negligible. Ideally, these crystalline layers would not be present since they restrict the number of pathways in which ion can travel. Amorphous and semi-crystalline polymers can be distinguished by their macroscopic properties. Amorphous polymers are usually clear and flexible whereas semi-crystalline polymers are usually more rigid and opaque. The DSC of semi-crystalline polymers shows peaks corresponding to melting transitions whereas no peaks are seen in amorphous polymers. PEO melts at around 60°C (Kohjiya *et al.*, 2005), and melting leads to a dramatic change in conductivity. The crystalline structure of PEO is shown in Figure 2.2 (Kohjiya *et al.*, 2005).
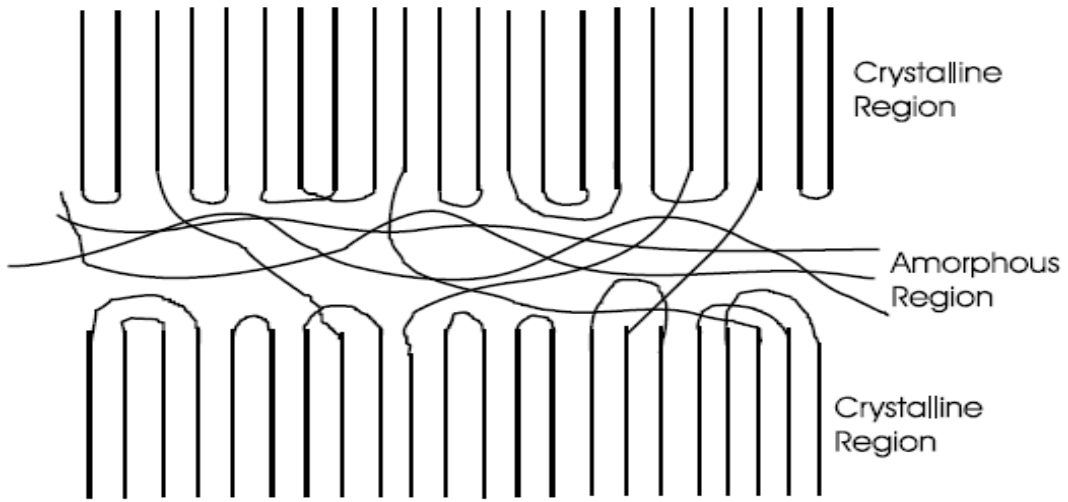
Figure 2.1 Schematic polymers as spherulites. The spherulites are made up of alternating layers of crystalline and amorphous regions (Kohjiya *et al.*, 2005).
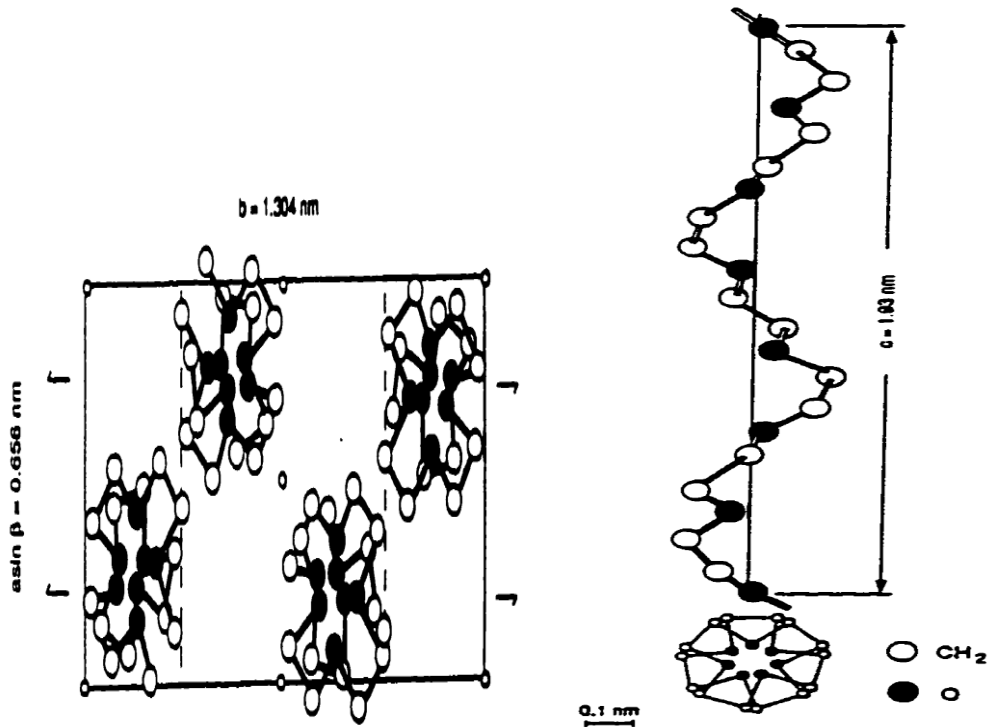
Figure 2.2 Structure of crystalline PEO (Kohjiya *et al.*, 2005)

2.4.2   Ion Mobility in the Amorphous Phase

Lithium ions move through amorphous domains by making and breaking complexes with ether oxygen atoms and the mobility of Li^+ is facilitated by the segmental relaxation of the polymer. Since ion and polymer mobility are coupled, efforts to improve conductivity have mainly focused on increasing polymer mobility in the amorphous phase. The segmental motion of PEO decreases for all SPEs with the addition of lithium salt. The extent of the decrease depends on lithium concentration, anion identity and temperature. It is reasonable to expect the dynamics of the polymer to decrease with the addition of $LiClO_4$, since multiple ether oxygen atoms coordinate with Li^+, thereby restricting the mobility of PEO (Kohjiya *et al.*, 2005). In SPEs composed of PEO/LiTFSI and PEO/LiBETI, not only were PEO segmental dynamics slowed with the addition of lithium, but a second process appeared on the timescale of the measurement (Kohjiya *et al.*, 2005). The origin of the extra process is attributed to the formation and disruption of "crosslinks" between Li^+ and ether oxygen atoms.

2.4.3   Ion Transport in Polymers

In 1973, Wright and co-workers reported the complexation of alkali metal ions by poly(ethylene oxide) (Kohjiya *et al.*, 2005). This is an important discovery that led to the development of new polymer/salt complexes known as solid polymer electrolytes. Berthier and co-workers demonstrated that in these semi-crystalline systems, the amorphous phase was responsible for ion transport (Kohjiya *et al.*, 2005). Angell and co-workers (1994) studying the conductivity of these electrolytes, observed curved Arrhenius plots of conductivity versus temperature and

suggested a similarity in behaviour with the viscosity and conductivity of supercooled molten salts (Kohjiya *et al.*, 2005).

2.4.4   Ionic Conductivity

A theoretical development in an area of polymer electrolytes has grown rapidly after Wright (1975) published the research on solid polymer electrolytes. The conductivity and conduction mechanism of solid electrolytes as a function of temperature and stoichiometry of salts is approached in thermodynamics and microscopic aspects. Conductivity, σ, of the polymer complex is closely dependent on the type of salts incorporated with polymers, i.e., the number of carrier ions, valence of the carrier ions the elementary electric charge and ionic mobility.

2.4.5   Temperature Effect

One of the most important parameters in characterizing ionic-conducting polymers is the temperature dependence of its ionic conductivity (Wright, 1975; Armand, 1987; Shriver *et al*., 1985). The first basic behaviour of temperature dependence on conductivity is normally described by the Arrhenius relationship. The Arrhenius law describes the behaviour as changing from high activation energy at low temperature to low activation energy at high temperature for PEO-NaCH$_3$SO$_3$, PEO-NaSCN, PEO-NaI, PEO-LiCF$_3$SO$_3$ (Wright, 1975; Armand, 1987; Shriver *et al*., 1985; Gauthier *et al*., 1988). The temperature dependency in PEO:LiCF$_3$SO$_3$ 8:1 complex agrees well with the Arrhenius law as the transition from high activation energy (2.0

eV) to low activation energy (0.6 eV) at below and above $55^{\circ}C$, respectively (Gauthier *et al.*, 1988). A similar trend was also observed for $PEO_{10}NaI$ electrolytes (Shriver *et al.*, 1985).

2.4.6 Ion Conduction Mechanism

Ionic-conductive polymers bear their own ion-generating groups chemically or physically bound to the polymer chain. The presence of a counter-ion maintains the electro neutrality of salt and also improves their conductivity. Binks and Sharples (1968) investigated ionic conductivity of melt-compressed polyethylene oxide, polytetramethylene oxide and polytrimethylene oxide with various types of electrodes including brass and silver. First, they studied that the possibility of ionic transport resulting from the presence of impurities had been eliminated and proposed that an inherent ionic process is operative involving the generation of protons and then subsequent transport by a handling-on process. In their research, polyethylene oxide itself generated a proton with transport by handling-on mechanism involving molecular rotation.

Figure 2.3 shows that the protons are removed from the polyethylene oxide chains by oxidation of the sample and transported via oxygen atoms by local segmental motions.

$$(2.21)$$
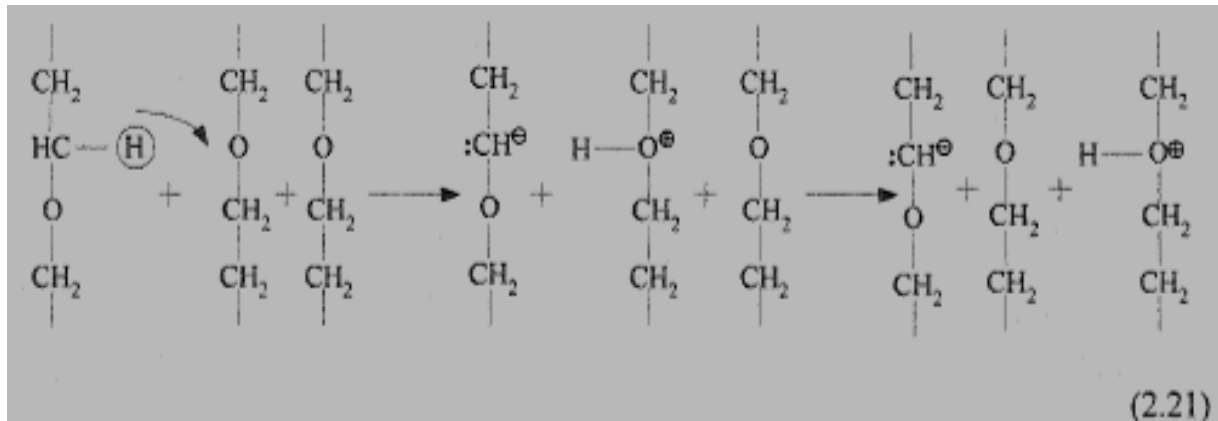
Figure 2.3 Schematic of protons removed from the PEO chain (Armand *et al.*, 1979).

From these two mechanisms, hydrogen ions arrive at the cathode and the polymer is progressively depleted of hydrogen as replenishment at the anode. The discharge of the negative species at the anode leaves radicals, which could decay either by mutual interaction or by reaction with the small amount of oxygen in the system or they could persist to recombine with the hydrogen transported back through the system on subsequent short-circuiting. However, PEO itself distributes very low conductivity less than 10^{-10} Scm^{-1} which belongs to the non-conductor category whereas the conductivity of PEO with added salt showed seven times higher than that of pure polymer at room temperature.

Armand *et al*. (1978) described ion conductivity using the hopping mechanism, which is assisted by polymer chain motion only or the contribution of ionic cluster in the conventional solid-state ionic conductors in the late 1970s. He suggested that the cation migrates in a helical tunnel in crystalline polymer-salt complexes and the cation moves from one site to the other by a free volume mechanism in amorphous materials (Armand *et al*., 1978). After the existence of the amorphous phase and their role in conductivity of these electrolytes came to be known, the hopping model was not suitable to explain the conduction of polymer complexes (Armand *et al*., 1979).

The conductivity of a material is its ability to allow the passage of electrons (electronic conductivity) or ions ionic conductivity). The specific conductivity of a material between two electrodes can be defined as (Patrick *et al*., 1986):

$$\sigma = \frac{l}{RA} \qquad (2.2)$$

where

l = electrolyte thickness between both electrodes

A = surface area of the electrolyte

R = total bulk electrolyte resistance

This resistance is determined using AC impedance measurements in which a sinusoidal voltage is applied across blocking electrodes (no significant electrode reactions) and the response current is measured. By knowing the applied voltage and measured current, the bulk resistance of the electrolyte can be determined using complex algebra and a complex-plane (Nyquist) plot of the impedance data. The SI unit for conductivity is Sm^{-1} ($\Omega^{-1}m^{-1}$). Maximum conductivity depends on the optimization of both the number of charge carriers and the mobility of those carriers. The addition of salt to a polymer matrix increases the number of charge carriers, leading to increased conductivity. However, this also leads to an increase in viscosity through the growing number of transient crosslinks. The increased viscosity decreases the mobility of the ions within the matrix. At a sufficiently high salt concentration, the ion mobility decreases to the extent that the conductivity no longer increases but begins to decline. To fully characterize the electrochemical properties of polymer electrolytes, several experiments have to be carried out. These include ionic conductivity measurements using AC impedance spectroscopy, electrochemical stability using cyclic voltammetry, cycling, and capacity-fade experiments. Further experiments to determine the cationic diffusion coefficient and transference number of ionic species also need to be carried out (Patrick *et al*., 1986).

2.4.7   Vogel Equation and Polymer Electrolytes

A number of similarities exist between the frequency-dependent conductivity of polymer electrolytes and disordered solids such as ionic glasses. These similarites are surprising since the ionic transport mechanism in polymer electrolytes is thought to be quite different than that in glasses. One reason is that the two mechanisms are thought to be so different such that the temperature-dependent conductivity in polymer electrolytes usually follows the Vogel equation whereas the conductivity in glasses is usually described by the Arrhenius equation (Patrick *et al.*, 1986). In particular, it is shown that under certain circumstances the Vogel equation fails to provide an adequate description of polymer electrolyte conductivity. Finally, conductivity of ionic glasses and ionic crystals are also shown to exhibit Vogel-like behaviour. This again demonstrates that ionic conduction in polymer electrolytes might not be so different from other ion conductors (Patrick *et al.*, 1986).

2.4.7.1 Free Volume Theories

The free volume approaches are attractive because of their intuitive plausibility. For a particle to move from one point to another, there must be some unoccupied volume large enough to accommodate the particle in the direction of particle movement. This unoccupied volume is part of the free volume of a system of particles. If the total volume of a system of particles is divided into two parts, the one part is occupied by the particles themselves. For example, the system of particles is a system of hard spheres. The volume occupied by the particles is $V_{particles} = NV_0$ where N is the number of particles and v_0 is the volume of one of the hard spheres. The free

volume is the total volume minus the volume of the particles, $V_{free} = V_{total} - V_{particles}$. Dividing by the total number of particles, N, gives $v_f = v_t - v_0$ where v_f is the free volume per particle and v_t is the total volume per particle. The free volume per particle, v_f , is the average free volume per particle. The free volume associated with an individual particle differs from particle to particle. In order for a particle to make a permanent displacement, there must be enough free volume associated with the particle for it to both move to a new location and for a different particle to move into its previous location.

A free volume mechanism is probably the dominant picture of transport among polymer electrolyte researchers. In the free volume picture, the ions in the polymer electrolyte need a certain amount of free volume in order to move. The constant redistribution of the free volume is due to the movement of the polymer. As the polymer structure evolves in time, ions are able to diffuse through the polymer. The two standard arguements leading to the Vogel equation have been presented in the previous section. As mentioned in the introduction, the Vogel equation has been successfully applied to a wide range of temperatures. Equation (2.3) represents the Vogel equation:

$$\sigma = AT^{-1/2} \exp[-B/(T - T_0)] \qquad (2.3)$$

where σ is the conductivity; B is a activation energy; T is the temperature and T_0 is the ideal glass transition temperature. A is proportional to the concentration of free ions, and $AT^{-1/2}$ is sometimes expressed as σ_0. T_0 is usually 30-50°C lower than the experimentally determined T_g. As the salt concentration increases, A should increase and the conductivity should also increase. However,

as the salt concentration increases, the number of free coordinating sites decrease and thus the activation energy required increases, which lowers the conductivity. Additionally, as the salt concentration increases, the rigidity of the side chains increases, which increases the T_g of the polymer, which also lowers the conductivity (Patrick *et al.*, 1986).

2.5   Role of Polymer Chemical Structure

A polymer which has a strong coordinating group dissolves salts easily. Some representatives of polymers are listed below:

1. Poly(ethylene oxide) (PEO) $(CH_2\text{-}CH_2\text{-}O)_n$

2. Poly(ethylene oxide) (PEO) $(CH_2\text{-}CH_2\text{-}O)_n$ (chemical (trifunctional urethane) and radiation crosslinked)

3. Poly(ethylene glycol, siloxane), (chemical (trifunctional urethane) linked)

$((CH_3\text{-}(OC_2H_4)m\text{-}O\text{-}C_3H_6SiCH_3O)n(Si(CH_3)_2O)_2)$

4. Poly(propylene oxide) (PPO) $(CH_2\text{-}CH(CH_3)\text{-}O)_n$

5. Poly(ethylene succinate) (PES) $(\text{-}C_2H_4\text{-}O\text{-}CO\text{-}C_2H_4\text{-}CO\text{-}O)_n$

6. Poly(aziridine) and Poly(N-methyl aziridine) $(CH_2\text{-}CH_2\text{-}NH)n, CH_2\text{-}CH_2\text{-}NCH_3\text{-})_n$

7. Poly(methylene sulfide) $((CH_2)p\text{-}S)n$ (p=2,5)

8. Poly(*bis*-methoxy-ethoxy-ethoxy) phosphazene $((CH_3O\text{-}C_2H_4\text{-}OC_2H_4O)_2PN)_n$

9. Poly(ethylene adipate) $(C_2H_4\text{-}O\text{-}CO\text{-}C_2H_4\text{-})_n$

10. Poly(oligo oxyethylene)methacrylate $((CH_2-(CH)-CO-(OC_2-H_4))pOCH_3)_n$

11. Poly(propiolactone) $(O-CH_2CH_2-CO-)_n$

12. Poly(dioxolane-co-trioxymethylene) $(CH_2O)n(CH_2CH_2-O)_p$

The ethylene oxide unit shows better complexing ability than propylene oxide, as the steric hindrance introduced by the methyl groups in propylene oxide reduces the stability of the complex. Table 2.2 compares the complexing ability of polyethylene oxide (PEO) and polypropylene oxide (PPO) with various alkali metal salts. Solid polymer electrolytes based on high molecular weight PEO contain crystalline PEO and/or high melting polymer-salt complex. The conductivity data for these SPEs vary considerably due to the complex phase behaviour of PEO-salt mixture. The high degree of crystallinity (~ 85%) in PEO has a detrimental effect on ionic conductivity (σ <10^{-8} Scm^{-1}) below the crystalline melting point (~65ºC). The conductivity can reach 10^{-5} Scm^{-1} at around 100ºC but the mechanical properties are poor due to the melting of crystalline phase. Thus, several studies have focused on synthesizing polymers which are amorphous at lower temperature. Atactic PPO appears to an amorphous host polymer, and the random arrangement of the methyl groups along the chain prevent crystallization. However, above 60- 65ºC, the conductivity of PPO-salt systems is lower than analogous PEO-salt complexes, and the steric hindrance of the methyl groups limits the segmental motion required to promote conductivity in addition to the decrease in stability of the polymer-salt complex. In contrast, PEO chains are capable of adopting a helical conformation with an oxygen-lined cavity that has ideal distances for oxygen cation interactions (Patrick *et al*., 1986).

Table 2.2 Complex formation ability of polyethylene oxide and poly(propylene oxide) with various alkali metal salts (Fenton et al., 1973).

	Li^+	Na^+	K^+	Rb^+	Cs^+	NH_4^+
F^-	− / −	− / −	− / −	− / −	− / −	− / −
Cl^-	+ / −	− / −	− / −	− / −	− / −	− / −
Br^-	+ / −	+ / −	− / −	− / −	− / −	− / −
I^-	+ / +	+ / −	+ / −	+ / −	+ / −	+ / −
SCN^-	+ / +	+ / +	+ / −	+ / −	+ / −	+ / −
ClO_4^-	+ / +	+ / +	+ / −	+ / −	+ / −	+ / −
$CF_3SO_3^-$	+ / +	+ / +	+ / −	+ / −	+ / −	+ / −
AsF_6^-	+ / +	+ / +	+ / −	+ / −	+ / −	+ / −
BF_4^-	+ / +	+ / +	+ / −	+ / −	+ / −	+ / −

+ complex formed
− no solubility

(Each cell: PEO (upper) / PPO (lower))

2.6 Poly(ethylene oxide) (PEO)

A vast number of studies on polymer electrolytes have focused on poly(ethylene oxide), (PEO), which polymer-salt systems constitute the first examples of "dry solid" polymer electrolytes

(Petersen *et al.*, 1992). The pioneer work of Wright on PEO complexes with sodium and potassium thiocyanate and sodium iodate brought attention to these materials and their potential use in batteries but it would not be until 1978 when these materials were used as separators in lithium batteries (Petersen *et al.*, 1992; Fenton *et al.*, 1973; Wright *et al.*, 1975; Kohjiya *et al.*, 2005). PEO has been considered a very good matrix for lithium ion conduction due to its low glass transition temperature, T_g and its ability to form complexes with alkali cations (Reddy and Hossain, 2002).

High molecular weight of PEO is highly crystalline and studies have shown conductivity values of the order of 10^{-8} Scm^{-1} at ambient temperature (Reddy and Hossain, 2002). This limits its applications to batteries which can operate at temperatures ranging between 60 and 100ºC, where the ionic conductivity of the system can reach values of 10^{-4} Scm^{-1} (Petersen *et al.*, 1997; Reddy and Hossain, 2002; Frech *et al.*, 2005; Lundberg *et al.*, 1966). Wright et al. (1973) reported the existence and conductivity of polyethylene oxide (PEO) containing NaI, NaSCN or KSCN. The PEO electrolytes are compatible with most electrode materials. PEO has a number of advantages for being a host polymer since it can solvate a wide range of metal salts and it has oxygen atoms with sufficient electron donor power to form coordinate bonds with cations. It provides a stable formation of multiple intrapolymer bonds with each cation due to a proper distance between coordinating sites. Due to its crystalline nature, PEO electrolytes has relatively low ionic conductivity ($<10^{-8}$ Scm^{-1}) at room temperature and thus its application as a polymer electrolyte in lithium batteries has a restricted use at higher temperatures ($>80^{\circ}$C only).

The choice of alkali metal salt as well as polymer matrix has been an important parameter on the final conductivity. Salts with large anions are easily polarisable and usually have weak Lewis bases and a reduced tendency for ion-pairing. Combining polymeric materials with salts

lead to higher conductivity complexes. Lithium is the most frequently used metal salt in polymer electrolyte research along with alkali metals such as copper, sodium, magnesium, potassium and mixed salts system, Martins and Sequeira (1990) reported that there was a relationship between maximum conductivities and anionic radii, while ionic conductivity was directly proportional to a rise in the cationic mobility at a fixed molar ratio of PEO to salt. Patrick *et al*. (1987) reported that electrolytes of perchlorates were generally better conductors than thiocyanates with alkali metals. There has been significant research done suggesting the kinetic mechanism of ionic transfer and the correlation of the salt radius to ionic conductivity in polymer electrolytes. However there is still controversy explaining the ion transfer and the effect of ion size on ionic conductivity.

2.6.1 PEO-based Polymer Electrolytes

Considerable research has been devoted to the development of polymer electrolytes for rechargeable battery systems. The objective is to identify solid polymer electrolytes with sufficiently high ionic conductivity which allows the operation of solid-state lithium batteries at ambient temperature with rates and recharge cycles similar to those of counter parts with liquid electrolytes. In addition to high ionic conductivity, other important criteria relating to the chemical, electrochemical and mechanical properties of the polymer electrolytes need to be satisfied for room-temperature lithium battery applications. The electrolyte must be electrochemically stable in the voltage range of 0 to about 4.5 V to be compatible with lithium and cathode materials such as vanadium oxide and manganese oxide (Patrick *et al*. 1987). The material must also be chemically compatible with lithium, possess low reactivity and have good

thermal stability to avoid severe safety problems described earlier. Additionally, the power must be dimensionally stable to allow processing as freestanding, thin films and to suppress the growth of dendrites.

To expect high ionic conductivity and dimensional stability in liquid and solid polymer electrolytes, this requires the co-existence of amorphous phase and preferable to conduct ions, as evident in the increase in ionic conductivity to values of 10^{-5} Scm^{-1} or higher. Several factors have been shown to affect the conductivity results. One of these factors is the sample history on the conductivity data obtained from PEO-lithium complexes. Volel and Armand (2004) indicated that conductivity, diffusion coefficient, and transference numbers, which were important properties of polymer electrolytes, are affected by the sample preparation history used in making the electrolyte complex. They observed different transport properties and morphologies for PEO-salt complexes made with acetonitrile (a good solvent for PEO) and complexes made with methyl formate (a bad solvent for PEO).

The most widely studied polymer electrolytes is polyethylene (oxide) (PEO) prepared with several lithium salts. The formation of a complex between PEO and lithium ion is dictated by the competition between the solvation energy of the polymer and the lattice energy of the lithium salt. Complexes form when the solvation energy involved in the formation of the coordination bond exceeds the lattice energy of the salt. Polyethylene oxide, a crystalline material at room temperature, forms complexes with lithium salts and exhibits ionic conductivity on the order of 10^{-4} Scm^{-1} at room temperature (Volel and Armand, 2004). However, above the melting point of PEO at 65°C, the PEO-salt complex is amorphous and is able to conduct ions better, as evident in the increase in ionic conductivity to values of 10^{-5} Scm^{-1} or higher (Volel and Armand, 2004).

To increase conductivity, the crystalline nature of a polymer must be suppressed by manipulating its structure. The crystallinity results from the regular packing of polymer chains. An amorphous polymer system can be designed by ensuring that the monomer has features which suppresses the regular packing. Techniques used in the design of amorphous polymer electrolytes include the formation of networks, branching and addition of inorganic backbone in comb-shaped polymers. The excellent salvating power of polyethylene oxide for lithium ions is due to the favorable spatial spacing of the oxygen donor atom in the polymer chain backbone. It can be observed that polyethylene oxide, which has a melting point of 65°C and a glass-transition temperature, T_g of -60°C, easily forms complexes with a variety of alkali and transition metal salts. The use of low-molecular-weight or short-chain-length polymers can result in reduced crystallinity in polymer systems. However, these groups of compounds are usually high-viscosity liquids and do not form solid polymer electrolyte, leading to a host of other problems. To eliminate the crystallinity in long polyethylene oxide chains and maintaining the rigidity, comb-branched structures have been synthesized with short-chain ethylene oxide pendant groups on the backbones. A series of methacrylate-based polymers have been synthesized by Xia *et al*. (1984) and Bannister *et al*. (1984) to study the effect of PEO side-chain length on crystallinity and polymer glass-transition temperatures. Their results showed that longer side chains provided higher flexibility and greater ionic mobility. However, there is a critical effective chain length since further increase of the ethylene oxide chain length leads to decreased conductivity due to the introduction of crystallinity in the polymer chain.

Another common technique used to increase conductivity while suppressing crystallinity is the combination of the structural flexibility of polysiloxanes with the high solvating capability

of the ethylene oxide unit in polymers with inorganic backbone such as poly(dimethyl siloxane-co-ethylene oxide) (Xia *et al*., 1984). The drawback of these systems is the susceptibility of the Si-O-C bonds to hydrolysis and structural degradation. A method of overcoming this problem is the synthesis of copolymers with the more stable Si-C bond, achieved by grafting PEO to the polysiloxane backbone. Kohjiya *et al*. (1990) prepared $LiClO_4$ complexes with such PEO-grafted polysiloxane. These PEO polymers had low molecular weights of 300 to 550 g/mol and low glass-transition temperatures between -54 and -77°C. The polymer systems showed room-temperature conductivities up to 10^{-5} Scm^{-1}. Synthesized comb-branched polymers with a phosphazene backbone have also shown room-temperature conductivity of about 10^{-5} Scm^{-1}.

Cross-linking to form polymer networks can also eliminate chain regularity and its crystalline effects. Several researchers have employed this approach in preparing highly conductive and mechanically stable polymer electrolytes (Lestel *et al*., 1990; Lenest *et al*., 1988; Cheradame and Niddammercier, 1988). They synthesized a series of electrolytes by cross-linking low molecular-weight PEO ranging between 600 to 2000 g/mol and forming $LiClO_4$ electrolytes with these network polymers with conductivities around 10^{-5} Scm^{-1} at room temperature. The low molecular weights of the PEO apparently provide chain flexibility while cross-linking ensures adequate mechanical strength. Most polymer electrolytes, however, are soft and have poor dimensional stability at room temperature. Cross-linking using either radiation or chemical methods has been used as a means of improving mechanical strength, but the resulting polymer is typically sticky, glue-like and rubbery. These cannot be used as separators in solid-state batteries as they have the tendency to flow under the slightest compression. Another method is by blending different polymers with various properties to achieve an electrolyte with combined

effects. Work has been done in this area by Wieczorck *et al*. (1991) and their results showed higher mechanical strength and conductivity in polymer electrolytes blends of PEO and poly(methyl methacrylate), with the PMMA serving as an interpenetrating network that enhances the mechanical strength of the electrolyte matrix.

2.6.2 Methods for Improving PEO-based Electrolytes

A significant improvement of ionic conductivity of polymer electrolytes can be achieved by choosing an anion to reduce the fraction of the crystalline phase in electrolytes, which would disturb regular alignment of polymer chains during crystallization and act as a plasticizer in the polymer matrix. A widely known example is the trifluoromethanesulfone (TFS-) anion, which can form special PEChLiTFS crystalline structures at high concentrations or become dissociated at low salt concentrations (Lestel *et al*., 1990; Lenest *et al*., 1988). An additional advantage of the TFS anion is its low lattice energy, which improves solubility and allows for achieving high values of ionic conductivity and minimizing ion-ion interactions (Cheradame and Niddammercier, 1988). The glass transition temperature T_g of electrolytes with LiTFS salts are usually lower than that of electrolytes with other types of salts, for example, e.g. Lil or LJAIO$_2$ (Cheradame and Niddammercier, 1988). However, those plasticizing properties of LiTFS are limited to electrolytes with low amounts of salt content. The addition of ceramic fillers into electrolytes is an effective strategy to further improve conductivity and mechanical properties of PEO electrolytes. Researchers have hypothesized that the interaction between surface groups on the polymer chains and charge carriers can improve the ionic conductivity. Thus, the electrolyte crystallinity can be decreased by introducing ceramic fillers (Wetton *et al*., 1976). However,

sedimentation of the ceramic fillers, leading to inhomogeneity of the electrolyte and nucleation of crystalline phase on the filler grains, has to be avoided.

Wang *et al*. (1998) reported that silane modified SiC could further improve the compatibility of SiC with the PEO/LiC matrix and effectively reduce the crystallinity of PEO/LiClCVSiCh composite electrolytes. XRD results show that the crystallinity of PEO decreases with an increase in the content of SiO_2. Thus, the conductivity of the PEO based electrolytes is gradually enhanced (Wetton *et al*., 1976). Wetton *et al*. (1976) also found that the addition of SiO_2 could improve the ion conductivity of a PEO/LiC/SiO_2 electrolytes from 10^{-6} to 10^{-4} Scm^{-1} at room temperature (Wetton *et al*., 1976). Due to its particular structure, ordered-mesoporous silica could provide a great deal of "inner surface", which facilitates the entrapment of liquid electrolytes into the mesoporous (MacCallum and Vincent 1987). The conductivity increase upon adding SiO_2 is usually attributed to inert fillers, which could enhance the formation of an amorphous phase in semi-crystalline electrolytes (MacCallum and Vincent, 1987). Since the ionic conduction takes place primarily through the amorphous phase of the polymer, high crystallinity leads to low conductivity. However, some research shows that T_m increases when the SiO_2 particles are added. This means that the volume fraction of crystalline phase increases. The results oppose former suggestions (MacCallum and Vincent, 1987).

However, the results are in accordance with recent assertions by Choi *et al*. (1998), who reported that the formation of the crystalline phase is possible if the filler particle acts as a nucleation center of the crystalline polymer phase. Comparing the reported results can be ambiguous since the conductivity is sensitive to many factors such as the salt species and its

concentration, particle size, temperature, thermal history, and preparative methods. Incorporating suitable plasticizer into the polymer electrolyte is one of the most successful approaches in increasing the amorphous nature (i.e., reduction of polymer crystallinity) and hence ionic conductivity. The essence of plasticization is to enhance the conductivity of solid polymer electrolytes using low molecular weight and high dielectric constant additives, such as propylene carbonate (PC), ethylene carbonate (EC), polyethylene glycol (PEG). These additives increase the amorphous content of the polymer matrix and tend to dissociate ion-pairs into free cations and anions, thereby leading to an overall enhancement in conductivity. Introducing side-chain structures provides another effective method for improving the ion conduction by preventing regular alignment of the polymeric chains into lamellae during crystallization (Preechain and Schulta, 1996). The approaches above rely on the preparation of polymer blends and composites.

These additives inhibit the crystallization of PEO-based electrolytes and often increase the polyether chain flexibility, causing an increase in ambient and subambient temperature conductivity. A stretching process is used to stiffen the polymer chains and cause the alignment of PEO helices in the force direction. Consequently, very few helices remain oriented in the perpendicular direction. This process forms additional thermally stable phases (Preechain and Schulta, 1996). One of the explanations for the conductivity increase is the creation of ion migration channels within the helical chains. Despite the conventional wisdom that ion transport in polymer electrolytes is mediated primarily by polymer segmental motion, Gooding *et. al* (2004) have measured semicrystalline PEO complexes with LiI, which suggests that transport occurs preferentially along the PEO helical axis, at least in the crystalline phase. The principal basis for this claim is an observed enhancement by a factor of 5-20 in electrical conductivity in

stretched polymer electrolyte films. Stretching results in partial alignment of the PEO helices and also induces small but observable changes in the Li+ solvation sheath. These results are correlated with the ionic conductivity enhancement in the stretched polymer (Preechain and Schulta, 1996).

2.7   Salts

Lundberg and co-workers studied the interactions of inorganic metal salt such as potassium iodide with polyethylene oxide (PEO) in 1966 (Gray; 1997). They reported that the association was due to an ion-dipole interaction and the anion was tentatively postulated as the species directly associating with the polymer. Those interactions showed that the incorporation of 10-30% of salt in the bulk polymer reduces crystallinity while retaining compatibility. However they did not measure the ionic conductivity of PEO-salt complex. Gray suggested that polymer electrolytes required strong coordination with cations to form electrolyte complex (Wetton *et al*., 1976). For example, polyethylene $(CH_2CH_2)_n$ has no electron donor to coordinate with cations and thus does not dissolve salt easily whereas polyethers, polyesters, polyamines and polythiols make electrolytes easier than PE.

PEO can solvate most metal cations, including alkali metals, alkaline earth metals, transition metals, lanthanides and rare earth metals (Wetton *et al*., 1976). Armand (1973) observed that the different physical behaviours of polymer electrolytes are responsible for the salt concentrations as the number of oxygen atoms in the chain per M^+ cation (O/M ratio). Papke (1981) applied the hard/soft acid base principle to classify the interaction strength between polymer and salt in solution. Hard acids refer to small cations with no valence electrons which can be easily polarized such as alkaline earth ions, Mg_2^+, whereas soft acids is that larger cations with several valence electrons which are removed easily, such as, Hg_2^-. Hard bases is that non-polarizable ligands of high electronegativity like oxygen in ether while soft ones is more polarisable groups like this group in thioether. The strongest interactions occur by matching

between hard acids with hard bases of soft acids with soft bases. Armand (1963) suggested that the strongest solvation in PLO can occur when PEO is associated with a hard cation like Li^+, Na^+, Mg^+ and Ca^{2+}.

Later, Patrick $et\ al.$ (1986) presented conductivity for $NaBF_4$ and $NaBH_4$ with PEO since the Na^+ salt complexes are highly crystalline and typically exhibit ionic conductivities of about 10^{-7} Scm^{-1} at room temperature, increasing to about 10^{-7} Scm^{-1} at 120^oC. Extensive contact ion pairing occurred in the $NaBH_4$ complex, but not in the $NaBF_4$ complex. They explained that the conductivity of the 4:5:1 $PEO:NaBF_4$ was about 1.2 x 10^{-7} Scm^{-1} while the same ratio of $PEO:NaBH_4$ has conductivity lower by 10^2 range due to trapping of the mobile sodium cations by the anion. MacCallum and Vincent (1987) measured the conductivity of a number of PEO electrolytes containing Mg, Ca, Sr and Zn perchlorates, and Mg and Ca thiocyanates. The PEO/alkaline earth complexes were more amorphous then PEO/alkali metal complexes and their T_g are much higher than the value for pure PEO. They presented that electrolytes containing perchlorates generally displayed higher conductivity than that of thiocyanates. The values of conductivity in decreasing order at 20^oC with 12:1 ratios of PEO: salt is $Mg^{2+}>Za^{2+}>Ca^{2+}>Sr^{2+}$ which corresponds to increasing order of ionic radius.

Parker (1962) explained that hydrogen bonding is crucial for specific anion solvation in addition to being responsible for long-range solvent structural effects. In less polar solvents such as tetrahydrofuran, acetonitrile or polymer solvent, charge dispersion is a main factor for the stability of anion solvation. Even for small anions, conductance experiments showed that anion mobility was a simple inverse function of crystal radius (Preechain and Schulta, 1996). Due to

the factor that large anions with delocalized charge requires little salvation, the most proper anions for polyether type polymer electrolytes formation would be arranged in the following order

$$F^-<<Cl^-<Br^-<I^-SCN^-<ClO_4^-CF_3SO_3-<BF_4-AsF_6^-$$

Martins and Sequeira (1990) compared mixed salt of PEO-LiSCN-NaClO$_4$ systems, PEO-KSCN-KI and single salt PEO-KSCN systems. Mixed salt (LiSCN-NaClO$_4$) systems increased the conductivity compared to that of PEO-LiSCN. It is suggested that molecular disorder occurs in the PEO-salt phase, configurational entropy and/or degree of salt dissociation. Mixed anions (KSCN-KI) increased conductivity in systems having high proportions of SCN-ions. The PEO-KSCN material of a molar ratio ethylene oxide unit to cation (O/K=) of 16/1 has low conductivity and its crystal structure is similar to that of pure PEO but with a lower crystallinity and melting point. The 8:1 EO:salt system showed a high conductivity and exhibits an almost completely amorphous phase and higher conductivity than either of the single-salt systems. Yang *et al* (1986) reviewed the effect of the anion, cation, casting solvent and stoichiometry on a series of polymeric electrolytes, formed by polyethylene oxide and salts of divalent metals. The compositions of PEO: LiClO$_4$ for maximum conductivity is 8:1 if the number of cation carriers is the relevant factor and 16:1 if the number of carriers is more significant. It is observed for both hydrated and dehydrated salt that isotherms of log (σ) against stoichiometry number, *n*.

2.7.1   Lithium Salts

Several factors affect the choice of a "best" lithium salt for a battery system. Relevant performance factors include conductivity, thermal stability, electrochemical stability at the anode and the cathode solubility, and cycling efficiency in rechargeable systems. Lithium salts with large anions are the most suitable for forming polymer electrolytes because of substantial delocalization of the negative charge. Additionally, large anions reduce ion-ion interactions as their size makes them less mobile and less likely to coordinate with the cation during ionic transport. Lithium salts with large anions such as lithium perchlorate ($LiCLO_4$), lithium triflate ($LiCF_3SO_3$), and lithium bis(trifluoromethanesulfonyl)imide ($LiN(CF_3SO_2)_2$) typically have lower lattice energies, defined as the ease with which ions dissociate. These salts provide more significant conductivity than small anion salts such as lithium chloride (LiCl) and lithium bromide (LiBr).

2.7.2 Lithium Hexaflurophosphate ($LiPF_6$)

Lithium hexafluorophosphate ($LiPF_6$) has a combination of well-balanced properties such as high-ionic conductivity, good dissociation, and good ion mobility. However, a major disadvantage is the sensitivity of $LiPF_6$ to residual water in the electrolyte. The $LiPF_6$ reacts with water and forms HF, which has a detrimental effect on cell performance because HF reacts with the graphite anode and forms a surface film consisting of LiF (Sloop, 2001). The LiF film increases the impedance of the electrolyte/electrode interface due to its poor ionic conductivity. Another disadvantage of the $LiPF_6$ is its thermal instability (Krause *et al*., 1997; Nagayama *et al*., 2001; Smagin *et al*., 1997; Zhang *et al*., 2001) which is believed to be the main cause for the poor performance of lithium-ion batteries at elevated temperature (Sloop *et al*., 2001; Sloop *et*

al., 2003; Ravdel *et al*., 2003; Campion *et al*., 2004; Tasaki *et al*., 1983). Another disadvantage is that $LiPF_6$ cannot be used in gel electrolytes based on fumed silica (FS) because $LiPF_6$ reacts with Si-OH to form HF which will react with silicon to form SiF_4.

2.7.3   Salt Solvation in Polymer Matrix

Salt dissolution in polymer matrix is accomplished through the solvation of cations or anions or both. Anion solvation generally occurs through hydrogen bonding or interaction with Lewis acids (Ramesh *et al*., 2008). Cation solvation takes place through the unshared electron pairs on heteroatoms such as ether -O-, sulfide -S-, amine -N- , phosphorous -P-, carbonyl C=O and cyano C=N. Three factors play significant roles in controlling the salt/polymer interactions: (1) Electron pair donicity/donor number (measures the ability of the solvent to donate the electrons to solvate the cations, (2) Acceptor number (quantifies the anion solvation ability of the solvent), and (3) Entropy. In polymer electrolytes the entropy of dissolution is generally negative because the loss of entropy of the polymer chains, due to their co-ordination with the cations, outweighs the entropy gain resulting from the breakup of the crystal lattice of the salt and subsequent ionic disorder. The polymer-salt complex formation corresponds to the competition between the following enthalpy changes: lattice energy of the salt (positive) + cohesive energy of the polymer (positive) + solvation energy (negative) + cohesive energy of the complex (negative). The lattice energy of the salt and the solvation enthalpy are the two major enthalpy terms associated with the dissolution of salt in polymer. The salts with smaller ionic radii and higher ionic charges have higher lattice energies. The solvation enthalpy depends on the strength of the co-ordinate bond formed between the cations and the groups on the polymer chains since anion solvation rarely occurs in polymer matrix. The solubility is most commonly explained in terms of Lewis acid-base interactions. The strongest interactions take place between hard acid (small cations without valence electrons) and hard base (non-polarizable ligands of high electronegativity) or soft acid (large cations with valence electrons that can be easily polarized or removed) and soft base

(more polarizable groups). Thus the best electron donors for hard Lewis acids (e.g.,Li^+, Na^+, Mg^{2+}, Ca^{2+}) are in the following order (order of electronegativity): -O-> -NH->>-S-. This also explains the strong complexation abilities of polyethers with Li^+.

A number of studies have been conducted to investigate PEO used in polymer electrolytes. Ramesh et al. (2008) proved that in $PEO-LiCF_3SO_3$ system, PEO having 12wt% of $LiCF_3SO_3$ exhibit the highest conductivity with a value of 1.10 x 10^{-6} Scm^{-1}, whereas PEO with 5 wt% Li_2SO_4 possesses the lowest conductivity with a value of 7.27 x 10^{-10} Scm^{-1}. Paruthimal et al. (2006) investigated PEO complexed with KI salt and obtained a conductivity of about 6.23 x 10^{-5} Scm^{-1} at 303 K for a molar ratio of 12:1 (PEO:KI). Siva Kumar et al. (2006) studied PEO complexed with $NaClO_3$ and obtained a conductivity value of 3.36 x 10^{-7} Scm^{-1} at 303 K. In this research, the conductivity for pure PEO is found to be 5.28 x 10^{-10} Scm^{-1} at 303 K, and the value increases gradually to 6.76 x 10^{-5} Scm^{-1} when 20 wt% $LiPF_6$ was added into the PEO. Ibrahim et al. (2010) proved that in $PEO-LiPF_6$ system, PEO having 20wt% of $LiPF_6$ exhibit the highest conductivity with a value of 4.10 x $10^{-5}Scm^{-1}$.

2.7.4   Mechanism of Solvation of Salt in PEO

For most polymer/salt complexes, cations should bind to the polymer chain instead of other ions. Also, to freely move in the polymer matrix, anions should have minimal interactions with polymers and cations (Ravdel et al., 2003). A salt with a small univalent cation and a large anion is needed to satisfy all these requirements, e.g., weak anion-cation interaction and strong cation-polymer bonding. The solubility and ionization of a salt in the PEO is determined by cation-

polymer interactions, which can be predicted by the hard/soft acid base (HSAB) principle (Ravdel *et al*., 2003), The HSAB principle was formulated by Pearson (1963) as a means to explain and predict the solubility of complexes between Lewis acids and bases. A "hard" acid consists of smaller and non-polarizable cations such as alkali ions, whereas a "soft " acid has larger and easily distorted cations such as Hg^{2+}. A "hard" base has non polarizable ligands with high electronegativity such as ether oxygen, wheareas a "soft" base has ligands with more polarizable groups such as the thio group in thioether. The HSAB principle states that matching hard acids with hard bases or soft acids with soft bases yields the strongest interactions, or the strongest solvation. Therefore, for PEO polymers with hard bases, the best candidates for cations are non-polarizable small cations, e.g. Li^+ or Na^+. A large anion with delocalized charge is required to dissolve ions in less polar solvents, such as polyether. The following order predicts the most appropriate anions for polyether-based polymer electrolytes (Ravdel *et al*., 2003):

$$F"«Cr<r<A1O_2"<C1O_4"<~CF_3SO_3"<BF_4"~AsF_6"$$
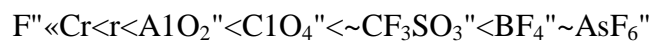
Large and polarizable monatomic anions are very easily dissolved in polyether-based polymer electrolytes.

2.8   Effect of Plasticizing Additives

Certain compounds, called plasticizers can be added to polymer electrolytes to improve the ionic conductivity. These are typically low molecular weight organic solvents that convert the semicrystalline polymer electrolyte into an amorphous material. These compounds lower the

viscosity of the electrolyte, which increase ionic mobility and consequently ionic conductivity. Polymer electrolytes which contain plasticizers such as ethylene carbonate (EC) and propylene carbonate (PC) are referred to as gel electrolytes. These compounds have a low vapour pressure to prevent solvent evaporation during preparation and stroge that may lead to compositional change of the electrolyte mixture. The solvents are chemically and electrochemically compatible with lithium to ensure efficient cycling of the rechargeable lithium batteries. Such solvents have a high dielectric constant which promotes greater dissociation of the lithium salt. For example, the dielectric constant of propylene carbonate and ethylene carbonate are 64.4 and 89.6, respectively compared to that of pure PEO, which is between 5 and 8. Several research groups have explored the use of plasticizers in improving the ionic conductivity of polymer electrolytes (Abraham, 1990).

The conductivity of (PEO)-LICF$_3$SO$_3$ was increased from ~10^{-7} to 10^{-4} Scm^{-1} at 40°C by the addition of 20 mol% poly(ethylene glycol) dimethyl ether, PEGDME (Nort, 1984). However, the increase in ionic conductivity does not correlate with the increased in strength, as the mechanical properties of these films were poor. Additionally, Abraham (1990) obtained conductivities as high as 10^{-3} Scm^{-1} at room temperature by plasticizing electrolytes of PEO and LiClO$_4$ with mixtures of ethylene carbonate and propylene carbonate. Poor dimensional stability of the resulting electrolyte films occurred in these compounds. Two methods frequently used to avoid this problem are cross-linking the polymer with PEO units before plasticization or using polymer electrolytes which have minimal solubility in the plasticizer. Extensive research by various groups leading to significantly battery development involve cross-linking polyethylene based polymer electrolytes either using chemical means, or photopolymerization and electron

beam radiation polymerization techniques (Abraham, 1990). Polymer systems, such as polyacrylonitrile (PAN), poly(vinyl pyrrolidinone) (PVP), and poly(vinyl chloride) (PVC) which do not contain the $-CH_2CH_2-O-$ backbone and are insoluble in these plasticizers have been also studied (Abraham, 1990). However, polyacrylonitrile (PAN) is the most extensively studied among these electrolytes and considerable amount of data on electrolyte properties and cell cycling are available for these PAN polymer systems (Baughman, 2002). Additionally, electrolytes having these plasticizing additivies are electrochemically unstable. This is because the organic solvents such as polypropylene carbonate and ethylene carbonate are particulary reactive at the interface. They degrade upon cycling making these systems unstable over time when used with lithium electrodes.

2.9   Carbon Nanotubes

Carbon is known to be the most versatile element that exists on the earth. It has many different properties which can be used in different ways depending on how the carbon atoms are arranged. For more than 6000 years carbon has been used for the reduction of metal oxides. Carbon in the form of graphite was discovered in 1779, and 10 years later in the form of a diamond. It was then determined that both of these forms belong to a family of chemical elements. It was not until about 200 years later that the next advancements in carbon took place. In 1985 Kroto, Smalley and Curl discovered fullerenes (Scharff, 1998). A few years later the carbon nanotube (CNT) was discovered by Sumio Iijima in fullerene soot (Biro *et al*., 2003; Burstein, 2003). It was a product of the carbon-arc discharge method, which is similar to the method used for fullerenes preparation. In this form, carbon is arranged in tubular formations on a nanoscopic level. To

observe such materials, high resolution transmission electron microscopy was used (Burstein, 2003; Dresselhaus *et al*., 1996). Carbon nanotubes are a completely new type of carbon fibre which comprises coaxial cylinders of graphite sheets, which range from 2 to 50 sheets (Yamabe, 1995). The first observations Sumio made (Burstein, 2003) were of multi-walled nanotubes, and it was not until two years later when single wall nanotubes were observed. Ijima and Ichihasi (1993) used carbon electrodes with a small amount of iron and filled the chamber around the carbon arc with methane and argon gas which yielded the single wall carbon nanotube. Single wall nanotubes are basically a single fullerene molecule that has been stretched out and therefore their lengths are million times their diameter (Alford *et al*., 2001). Around the same time, Bethune and colleagues also observed the single wall carbon nanotube (Dresselhaus *et al*., 1996). In 1996, Smalley synthesized bundles of single wall carbon nanotubes for the first time (Yamabe, 1995).

The name of carbon nanotube is derived from their size, which is only a few nanometers wide. By definition carbon nanotubes are cylindrical carbon molecules with properties which render them potentially useful in extremely small scale electronic and mechanical applications. These tubes consist of rolled up hexagons, 10,000 times thinner than human hair. Ideal nanotubes can be described as a seamless cylinder of rolled up hexagonal networks of carbon atoms, which is capped with half a fullerene molecule at the end (Biro *et al*., 2003). Their strength is one to two orders of magnitude with weight six times lighter than steels. Possible applications range from semiconductors, electronic memory, drive products, and medical delivery systems to uses in plastics such as automobile body panels, paint, tires and as flame retardants in polyethylene and polypropylene (Dunn *et al*., 2004). Nanotechnology has been

recently supported with Nanotechnology Research and Development Act allowing $3.7 billion over the next four years to be administered by the National Nanotechnology Initiative with plans to create a National Nanotechnology Program (NNP) (Laplaze *et al*., 2002) in the United States.

2.9.1 Addition Nanoparticle Fillers for Conductivity Enhancement

Since the initial studies by Capuano and co-workers (1991), many studies have been devoted demonstrating conductivity enhancements in SPEs by a wide range of nanoparticle fillers including TiO_2, SiO_2, Al_2O_3, ZnO, $BaTiO_3$,$PbTiO_3$ and $LiNbO_3$.. Despite much effort on this topic, the mechanism by which nanoparticles enhance the transport in filled systems remains unclear. Due to the burst development of nanomaterial fabrication, a large window of opportunities has opened for using nanoscale fillers in polymer composites. The increased surface area of nanoscale fillers offers several advantages over traditional micron-scale fillers. One of the most used nanoscale filler type is carbon nanotubes due to its easy fabrication, excellent mechanical properties and electrical conductivity.

2.9.1.1 Influence of Nanoparticles on Polymer Mobility

Since Li^+ transport and polymer segmental motion are coupled in amorphous SPEs, nanoparticles could increase charge-carrier mobility by increasing the segmental motion of the polymer. One way to evaluate polymer mobility is by measuring the glass transition temperature (T_g). Since T_g is a broad transition, a change in T_g of greater than five degrees is regarded as a significant change when nanoparticles are added. The T_g can increase, decrease, or remain unchanged with nanoparticle addition for a variety of PEO-based SPEs at similar salt and nanoparticle concentrations (Collins *et al*., 1997). These results appear independent of salt or nanoparticle identity and do not correlate with increasing or decreasing conductivity. In the case of PEO/$LiClO_4$/Al_2O_3, the T_g has been reported to decrease and remain unchanged with

nanoparticle addition. Therefore, if nanoparticles influence the polymer mobility, the effect cannot be evaluated by T_g measurements alone. One method to measure the molecular-level mobility of a polymer is with quasi-elastic neutron scattering (QENS). Unlike T_g, mobility is directly measured over timescales relevant to this problem (pico to nano-seconds). QENS has been used to measure the mobility of a nanoparticle-filled SPE based on the copolymer, PEG (trihydroxy poly(ethylene oxide-co-propylene oxide). The results showed that the addition of TiO_2 nanoparticles (21 nm diameter) slowed the mobility of the polymer (Collins *et al*., 1997). They estimated that a layer extending 5 nm from the particle surface was immobilized, whereas the dynamics of the polymer outside this region were unaffected. This observation leads to another possible mechanism for increasing conductivity: nanoparticles decrease polymer mobility by immobilizing ether oxygen atoms on the particle surface, thereby reducing the number of ether oxygens coordinated with lithium ions. For ether oxygen atoms to be attracted to the surface of the nanoparticle, the surface must have acidic sites (electron accepting). Several studies have focused on how the surface chemistry of nanoparticles influences the conductivity, and all studies indicate that nanoparticles with acidic surface chemistry increase the conductivity more than nanoparticles with basic or neutral surface chemistries (Collins *et al*., 1997).

The surface chemistry can notably affect conductivity even within different polymorphs of the same ceramic material. For example, it is known from molecular dynamics simulation that the surface of Al_2O_3 is terminated by aluminum atoms (acidic sites), whereas Al_2O_3 is terminated by aluminum and oxygen atoms (acidic and basic sites). One consideration regarding polymer mobility in nanoparticle-filled SPEs is the issue of confinement. Confinement can affect both the extent of crystallization and polymer mobility (Collins *et al*., 1997). A nanoparticle-filled SPE

could be viewed as a confined, capped system (substrate on both sides), provided the nanoparticles are well-dispersed. In fact, such a connection has been made between capped thin films and nanocomposites. However, confinement is only relevant in the case where nanoparticles are not aggregated, and the extent of aggregation is rarely reported for nanoparticle-filled SPEs.

However, this structure suggests another possible way that nanoparticles could increase lithium ion mobility: by creating percolating pathways for lithium ions to travel faster than they would through the bulk. To date, there is no evidence supporting the theory that the interface between the nanoparticle and the polymer/salt is superior for ion transport. Another example of how nanoparticles could influence polymer mobility and hence ion mobility is by altering the crystalline fraction in the SPE. Some crystalline complexes, such as pure PEO and the $(PEO)_6$:LiX complex at high molecular weight decrease conductivity, as observed by a steep drop in conductivity at temperatures below the melting point of these structures. Other crystalline structures increase conductivity, such as the low molecular weight $(PEO)_6$:LiX complex described above. It is possible that nanoparticles could prevent the formation of non-conductive structures, or promote the formation of highly conductive structures (Collins *et al*., 1997).

2.9.1.2 Influence of Nanoparticles on the Number of Charge Carriers

The second way in which ionic conductivity can increase at a fixed lithium concentration is an increase in the number of charge carriers, specifically cations. If the role of the nanoparticle is to promote cation/anion dissociation, this could happen if acidic sites on the nanoparticle surface

attract anions, freeing Li^+ cations to move through the SPE. The influence of nanoparticles on salt dissociation can be assessed by measuring the lithium transference number, T^+, which quantifies the fraction of lithium ions contributing to the conductivity. Croce and co-workers reported a 37% increase in the lithium-ion transference number for $PEO/LiCF_3SO_3$ when acidic Al_2O_3 nanoparticles were added (Collins *et al*., 1997). Only a slight increase (4%) was observed when nanoparticles with basic surface chemistry were added. These results suggest that the role of nanoparticle is to promote salt dissociation in SPEs.

2.9.1.3 Understanding the Mechanism for Conductivity Improvement

Several possible mechanisms reported in the literature are highlightedas to how nanoparticles could improve conductivity in SPEs. The absence of one unifying mechanism can partially be attributed to conflicting results that exist between different investigations of the same SPE system. The fact that results vary from study to study is not surprising, given the sensitivity of SPEs to sample preparation. PEO is hydrophilic and although water cannot be present in a lithium-ion battery, it can act as a plasticizer for the SPE and boost the conductivity. Furthermore, variables such as pH, nanoparticle size and concentration and annealing time are known to influence nanoparticle aggregation - a factor likely to affect conductivity (Collins *et al*., 1997). Thermal history is also critically important, since some crystalline phases can form within seconds, while others require days. Some crystalline phases require months to recrystallize depending on the water content. Moreover, some crystalline morphologies increase conductivity, while others block conducting pathways, making it important to characterize the crystalline morphology.

2.9.1.4 Effect of Filler Properties on Percolation Threshold

The properties of the fillers, which include type, size, shape, as well as orientation within the polymer matrix, play a significant role in determining the percolation threshold and the conductivity of the composite (Chambers *et al*., 1998). For example, carbon fibres and carbon black, the different shapes of carbon, have different inherent conductivities. In the region of higher filler loadings, the composite conductivity should level off to a value slightly lower than that of fillers. Different forms of carbon generally have different microstructures and therefore, will affect electrical conductivity in different ways. For spherical particles, smaller particles have been reported to lower the percolation threshold (Collins *et al*., 1997). For fillers with an aspect ratio (length/diameter) >1, carbon fibre for instance, a broader range of aspect ratios and larger aspect ratios have been shown to lower the percolation threshold (Collins *et al*., 1997). The surface properties of filler and polymer also have a significant effect on composite conductivity (Collins *et al*., 1997). Differences of surface energies between the filler and polymer indicate how well the polymer can wet the surface of the filler. The smaller of the differences between the two surface energy values, the better wetting of the filler by the polymer. Better wetting effect means that larger amounts of the polymer coat the filler surface and that the filler has better and uniform dispersion within the composite. However, this increases the composite percolation threshold because larger amounts of filler are required before the particles come in contact with one another. This can also result in increased composite electrical conductivity once the percolation threshold is reached (Collins *et al*., 1997). Manuel (2000) studied the electrical conductivity of carbon-filled polymers by the addition of three single fillers to nylon 6,6 and polycarbonate in increasing concentrations.

2.10 Dielectric Studies

Dielectric spectroscopy, also known as Electrochemical Impedance Spectroscopy (IS), measures the dielectric properties of a medium as a function of frequency. It is based on the interaction of an external field with the electric dipole moment of the sample, often expressed by permittivity. This technique measures the impedance of a system over a range of frequencies, and therefore the frequency response of the system, including the energy storage and dissipation properties, is revealed. The data obtained by IS is often expressed graphically in a Bode plot or a Nyquist plot. Impedance is the opposition to the flow of alternating current (AC) in a complex system. A passive complex electrical system comprises both energy dissipater (resistor) and energy storage (capacitor) elements. If the system is purely resistive, then the opposition to AC or direct current (DC) is simply resistance. Almost any physico-chemical system, such as electrochemical cells, mass-beam oscillators, and even biological tissue possesses energy storage and dissipation properties. IS is capable to examine such systems. This technique has grown tremendously in stature over the past few years and is now being widely employed in a wide variety of scientific fields such as fuel cell testing, biomolecular interaction, and microstructural characterization. IS often reveals information about the reaction mechanism of an electrochemical process: different reaction steps will dominate at certain frequencies, and the frequency response shown by IS can help identify the rate limiting step (Chambers *et al*., 1998) .

2.10.1 Dielectric Mechanisms

There are a various dielectric mechanisms related to the way a studied medium reacts to the applied field. Each dielectric mechanism is centered around its characteristic frequency, which is the reciprocal of the characteristic time of the process. In general, dielectric mechanisms can be divided into relaxation and resonance processes. The most common, starting from high frequencies, are:

(i)   Electronic Polarization

This resonant process occurs in a neutral atom when the electric field displaces the electron density relative to the nucleus it surrounds. This displacement occurs due to the equilibrium between restoration and electric forces. Electronic polarization may be understood by assuming an atom as a point nucleus surrounded by spherical electron cloud of uniform charge density.

(ii)   Atomic Polarization

Atomic polarization is observed when the electronic cloud is deformed under the force of the applied field, so that the negative and positive charge are formed. This is a resonant process.

(iii)   Dipole Relaxation

This originates from permanent and induced dipoles aligning to the electric field. Their orientation polarisation is disturbed by thermal noise (which mis-aligns the dipole vectors from the direction of the field) and the time needed for dipoles to relax is determined by the local viscosity. These two facts make dipole relaxation heavily dependent on temperature and chemical surrounding.

(iv)   Ionic Relaxation

Ionic relaxation comprises ionic conductivity, interfacial and space charge relaxation. Ionic conductivity predominates at low frequencies and introduces only losses to the system. Interfacial relaxation occurs when charge carriers are trapped at interfaces of heterogeneous systems. A related effect called Maxwell-Wagner-Sillars polarization, where charge carriers blocked at inner dielectric boundary layers (on the mesoscopic scale) or external electrodes (on a macroscopic scale) lead to a separation of charges. The charges may be separated by a considerable distance and therefore make contributions to the dielectric loss that are orders of magnitude larger than the response due to molecular fluctuations.

(v)   Dielectric Relaxation

Dielectric relaxation as a whole is the result of the movement of dipoles (dipole relaxation) and electric charges (ionic relaxation) due to an applied alternating field, and is usually observed in the frequency range 10^2-10^{10} Hz. Relaxation is relatively slow compared to resonant electronic transitions or molecular vibrations, which usually have frequencies above 10^{12} Hz (Chambers *et al*., 1998).

2.11   X-Ray Diffraction (XRD) Studies

There are several special considerations for using XRD to characterize thin film samples. Firstly, reflection geometry is used for these measurements as the substrates are generally too thick for transmission. Secondly, high angular resolution is required because the peaks from semiconductor materials are sharp due to very low defect densities in the material. Consequently, multiple bounce crystal monochromators are used to provide a highly collimated X-ray beam for these measurements. For example, in the Philips MRD used in the X-ray facility, a 4-crystal monochromator made from Ge is used to produce an incident beam with less than 5 arc seconds of angular divergence (Chambers *et al*., 1998).

2.11.1 Applications

X-ray powder diffraction is most widely used for the identification of unknown crystalline materials (e.g. minerals, inorganic compounds). Determination of unknown solids is critical to studies in geology, environmental science, material science, engineering and biology.

Other applications include:

a) Characterization of crystalline materials

b) Identification of fine-grained minerals such as clays and mixed layer clays that are difficult to determine optically

c) Determination of unit cell dimensions

d) Measurement of sample purity

e) With specialized techniques, XRD can be used to:

- determine crystal structures using Rietveld refinement

- determine of modal amounts of minerals (quantitative analysis)
- characterize thin films samples by:
    - determining lattice mismatch between film and substrate and to infer stress and strain
    - determining dislocation density and quality of the film by rocking curve measurements
    - measuring superlattices in multilayered epitaxial structures
    - determining the thickness, roughness and density of the film using glancing incidence X-ray reflectivity measurements
- make textural measurements, such as the orientation of grains, in a polycrystalline sample

2.12   Fourier Transform Infrared Spectroscopy (FTIR)

Fourier transform infrared spectroscopy (FTIR) is a powerful tool for identifying types of chemical bonds in a molecule by producing an infrared absorption spectrum as a molecular "fingerprint". The principle of this technique is that molecular bonds vibrate at various frequencies depending on the elements and the type of bonds. There are several specific frequencies at which any given bonds can vibrate. According to quantum mechanics, these frequencies correspond to the ground state (lowest frequency) and several excited states (higher frequencies). One way to cause the frequency of a molecular vibration to increase is to excite the bond by having it absorb light energy. Molecular bonds vibrate at various frequencies depending on the elements and the type of bonds. Since FTIR provides information about the chemical

bonding or molecular structure of materials without causing destruction, it could be used to identify unknown materials, detect the organic and some inorganic additives in the level of few percent, and characterize the chemical structure change and solvent residue. The FTIR peaks that appear in PEO based polymer electrolytes are listed in Table 2.3 (Wen *et al*., 1996; Zain and Arof, 1998; Rao, 1967). The appearance of the new peaks in FTIR spectrum indicates the formation of new chemical bond, whereas the small position shift of the certain peak reflects the chemical environment change. The weakening or broadening of a peak means the materials with this chemical bond are being consumed or undergoing degradation (Wen *et al*., 1996). In-situ FTIR is a really useful tool for monitoring the reaction process. Disappearance of reactant peaks may indicate that the reactant was fully consumed.

Bands in the hydroxyl region vary markedly with hydrogen bonding, allowing one to separate different contributions from 'free' (non-hydrogen-bonded) and associated (hydrogen bonded) hydroxyl forms. Assuming that only these two forms (free and associated) are distinguishable in IR spectra, a deconvolution treatment was employed, using Gaussians as primitive functions, according to the similar mathematical treatment employed to the (ClO_4^-) band by Wieczorek *et al*. (1996). The total areas were then normalized and the ratio of free and associated forms were taken from the relative areas associated to each form. Despite the control of the thickness of the samples, small differences do not influence the quantitative determinations, since the spectroscopic fractions are taken from relative areas of the same band. The humidity control was done by obtaining FTIR spectra of PEO samples prepared concomitantly and treated the same manner as the samples of the blends.

Infrared spectroscopy has been used to characterize the chain structure of polymers and has led the way in interpreting the reactions of multifunctional monomers including rearrangements and isomerizations. The wave length or the frequency of the bank represents the electronic structure of an atom in a compound. Therefore, the interactions among the atoms or ions in the electrolytes system will induce changes in the electronic levels of the atoms, resulting in the influence of the spectrum (Wen *et al.*, 1996).

Table 2.3 FTIR peaks that appear in PEO based polymer electrolytes (Wen *et al.*, 1996)

Peak Position	Peak assignment
650 to 600 cm^{-1}	Peak of t(ClO$_4^{-1}$) band
636 cm^{-1}	Cis C-H wagging mode
772 cm^{-1}	CF$_3$ stretching
787 – 790 cm^{-1}	The combination of C-S and S-N stretching
842 cm^{-1}	CH$_2$ wagging
918 cm^{-1}	Stretching of C---N of acetonitrile
959 cm^{-1}	Trans C-H wagging mode
962 cm^{-1}	The stretching of ether bond (C-O) of PEO
991 cm^{-1}	CH$_2$ twisting
1033 cm^{-1}	Symmetric SO$_3$ vibrations of LiCF$_3$SO$_3$
1040 cm^{-1}	Stretching of C----N of acetonitrile
1062 cm^{-1}	The C-O-C stretching vibrations
1100 cm^{-1}	The stretching of ether bond (C-O) of PEO
1107 cm^{-1}	The C-O-C stretching vibrations
1144 cm^{-1}	The C-O-C stretching vibrations
950 – 1250 cm^{-1}	The C-O-C stretching vibrations
1207 cm^{-1}	CF$_3$ stretching
1266 cm^{-1}	Asymmetric SO$_3$
1267 – 1164 cm^{-1}	-C-F and –CF$_2$- stretching
1282 cm^{-1}	CH$_2$ twisting vibration from PEO
1350 cm^{-1}	The CH$_2$ wagging mode
1355 cm^{-1}	Asymmetric SO$_2$ stretching mode
1408 cm^{-1}	-C-F stretching
1450 cm^{-1}	Asymmetric bending
1465 – 1485 cm^{-1}	CH$_2$ scissoring
1602 cm^{-1}	C-C bonds stretching vibration in aromatic ring, the C=C bonds of benzene rings
1630 cm^{-1}	The bending mode of water molecules

1688 cm^{-1}	-CH=CF-skeletal bending
1693 cm^{-1}	Overoxidation of the polymers in the mixed electrolytes, resulting in the formation of carboxyl groups on the polymer chain
1950 – 1970 cm^{-1}	Asymmetric stretching
2700 cm^{-1}	C-H stretching mode
2800 – 2935 cm^{-1}	C-H stretching mode
2982 cm^{-1}	C-H stretching mode
3000 cm^{-1}	C-H stretching mode
3300 – 3500 cm^{-1}	N-H stretch
3200 – 3600 cm^{-1}	OH stretch from alcohol or phenol

Even though the salts are dissolved by the polymer, this does not mean that cations and anions are well separated from each other. There is ample evidence that the ions interact with each other. These interactions lead to the formation of ion pairs and ion aggregates. The most direct evidence for ion-ion interactions is probably from vibrational spectroscopy. It is necessary to use an anion that has a set of vibrational modes, in orders to use vibrational spectroscopy. These vibrational modes will be sensitive to the association of the anion with the cation. A vibrational peak associated with the free anion will be in a slightly different location than a peak associated with an anion that is paired with a cation. The reason the peaks shift is that the electron distribution around the anion is perturbed when the cation is paired with the anion. In speaking of ionic species it would be a mistake to think of the species as static entities. The vibrational spectrum of the anion is a time average spectrum over a relatively long period. During that time the ionic species are not static but are changing from free to pair, pair to free, aggregate to pair, etc. The simultaneous presence of free ions, pairs, and aggregates has important consequences for polymer electrolyte conductivity. Since pairs are charge neutral, an applied electric field will not cause translational motion of a pair (Dissanayake *et al*., 2003).

In order to investigate the effect of filler particles on ion–polymer and ion–ion (i.e. cation/anion) interactions in the polymer complexes and composites under study, the FTIR spectroscopic studies have been carried out. The fraction of "free" anions and "ion pairs" has been calculated as the ratio of the area corresponding to the peaks attributed to free anions and the ion pairs to the total area of the band corresponding to the envelop of ν_4 (PF_6^-) mode (Dissanayake *et al*., 2003). These fractions of free anions and the ion pairs have been found to be influenced substantially due to the dispersion of the filler particles in the polymer–salt complex matrices (Dissanayake *et al*., 2003). The spectral region 1000–1200 cm^{-1} corresponding to the C–O–C stretching mode has also been found to be affected with the dispersion of the filler particles. This spectral region consists of basically contributions from unresolved symmetric and antisymmetric C–O–C vibrations. Changes in the position, intensity and shape of the bands arising from these modes are associated with polymer–ion interactions (Wendsjo *et al*., 1992; Papke *et al*., 1981; Shriver *et al*., 1981). It has been observed that a significant variation in the peak position of the band due to the ν(C–O–C) mode as a function of filler concentration takes place for both the systems. Initially, a shift in the wave number has been observed. It is widely described in literature that the changes in the position of the C–O–C stretching mode are connected with the polymer–ion (cation) interactions (Wieczorek *et al*., 1998; Wiezorek *et al*., 1996; Wendsjo *et al*., 1992; Papke *et al*., 1981).

2.13 Scanning Electron Microscope (SEM)

In a typical SEM, an electron beam is thermionically emitted from an electron gun fitted with a tungsten filament cathode as shown in Figure 2.4. Tungsten is normally used in thermionic

electron guns because it has the highest melting point and lowest vapour pressure of all metals, thereby allowing it to be heated for electron emission, and because of its low cost.
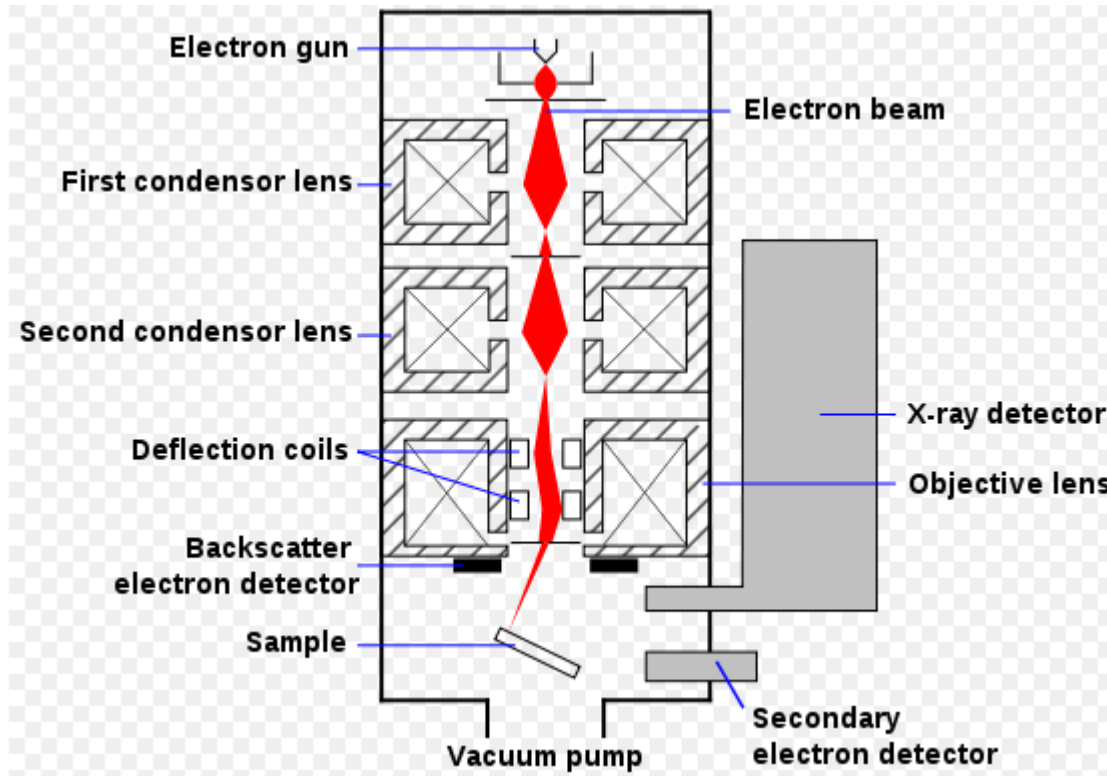
Figure 2.4 Schematic diagram of an SEM (Dissanayake *et al*., 2003).

Other types of electron emitters include lanthanum hexaboride (LaB_6) cathodes, which can be used in a standard tungsten filament SEM if the vacuum system is upgraded and field emission guns (FEG), which may be of the cold-cathode type using tungsten single crystal emitters or the thermally-assisted Schottky type, using emitters of zirconium oxide. The electron beam, which typically has an energy ranging from 0.5 to 40 keV, is focused by one or two condenser lenses to a spot about 0.4 to 5 nm in diameter. The beam passes through pairs of scanning coils or pairs of deflector plates in the electron column, typically in the final lens, which deflect the beam in the x and y axes so that it scans in a raster fashion over a rectangular area of the sample surface.

When the primary electron beam interacts with the sample, the electrons lose energy by repeated random scattering and absorption within a teardrop-shaped volume of the specimen known as the interaction volume, which extends from less than 100 nm to around 5 μm into the surface. The size of the interaction volume depends on the electron's landing energy, the atomic number of the specimen and the specimen's density. The energy exchange between the electron beam and the sample results in the reflection of high-energy electrons by elastic scattering, emission of secondary electrons by inelastic scattering and the emission of electromagnetic radiation, each of which can be detected by specialized detectors. The beam current absorbed by the specimen can also be detected and used to create images of the distribution of specimen current. Electronic amplifiers of various types are used to amplify the signals which are displayed as variations in brightness on a cathode ray tube. The image may be captured by photography from a high resolution cathode ray tube, but in modern machines is digitally captured and displayed on a computer monitor and saved to a computer's hard disc (Dissanayake *et al*., 2003).

2.14   Differential scanning calorimetry (DSC)

Differential scanning calorimetry (DSC) is a thermoanalytical technique in which the difference in the amount of heat required to increase the temperature of a sample and reference are measured as a function of temperature. The DSC is mainly applied to study phase transitions, such as melting, glass transitions, or exothermic decompositions. These transitions involve energy changes or heat capacity changes that can be detected by DSC with great sensitivity. The result of a DSC experiment is a curve of heat flux versus temperature or versus time as shown in Figure 2.5. The exothermic reaction of the sample appears as a positive peak in Figure 2.5. Glass

transitions (T_g) may occur as the temperature of an amorphous solid is increased. These transitions appear as a step in the baseline of the recorded DSC signal. This is due to the sample undergoing a change in heat capacity (Ferry, 1996). As the temperature increases, an amorphous solid will become less viscous. At one point the molecules may obtain sufficient freedom of motion to spontaneously arrange themselves into a crystalline form. This is known as the crystallization temperature (T_c). This transition from amorphous solid to crystalline solid is an exothermic process, and results in a peak in the DSC signal. As the temperature increases, the sample eventually reaches its melting temperature (T_m). The melting process results in an endothermic peak in the DSC curve. The ability to determine transition temperatures and enthalpies makes DSC a valuable tool in producing phase diagrams for various chemical systems.
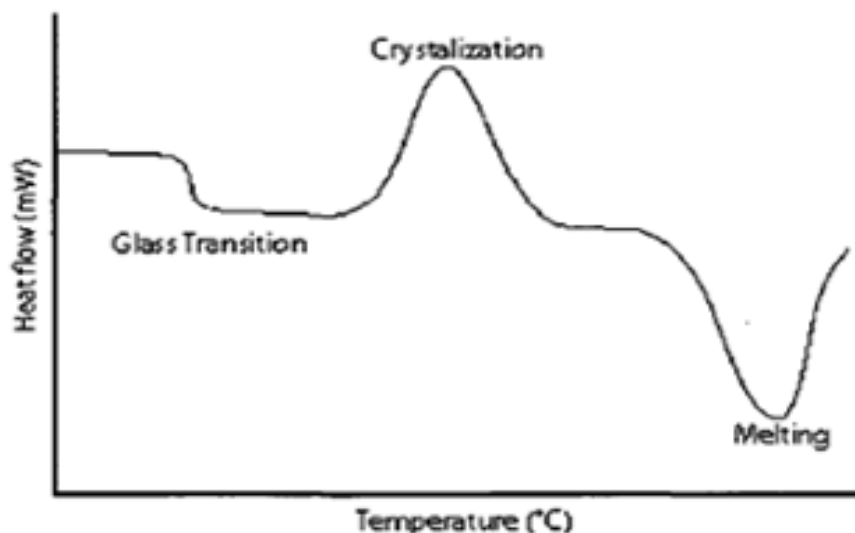
Figure 2.5 Schematic of DSC curve demonstrating the appearance of several common features (Dissanayake *et al.*, 2003).

The degree of crystallinity is the single most important characteristic of a polymer in that it determines mechanical properties, such as yield stress, elastic modulus and impact resistance (Kong and Hay, 2002). The degree of crystallinity of a polymer is temperature-dependent (Kong and Hay, 2002) and in comparing its effect on material properties, it is vital to carry out these measurements at the same temperature, invariably at ambient temperature and not at the melting point. The usual procedure in measuring the degree of crystallinity by DSC involves drawing a linear arbitrary baseline from the first onset of melting to the last trace of crystallinity and determines the enthalpy of fusion from the area under this endotherm. The degree of crystallinity is then defined as:

$$X_c = \Delta H_f / \Delta H_f^o (T_m^o)$$ (2.4)

where X_c is the weight fraction extent of crystallinity, ΔH_f is the entalphy of fusion measured at the melting point, T_m and $\Delta H_{f^o} (T_m)$ is the entalphy of fusion of the totally crystalline polymer measured at the equilibrium melting point, T_{m^o}. The degree of crystallinity is then defined as (Kong and Hay, 2002):

$$X_c = (\Delta H_f - \Delta H_{c)}) / \Delta H_f^o$$ (2.5)

Where ΔH_f is the enthalpy of fusion, ΔH_c the entalphy of crystallisation and ΔH_{f^o} the heat of fusion of the completely T_{m^o}.

2.15   Thermogravimetric Analysis (TGA)

Polymers represent another large area in which thermal analysis finds strong applications. Thermoplastic polymers are commonly found in everyday packaging and household items, but for the analysis of the raw materials, effects of the many additives used (including stabilisers and colours) and fine-tuning of the moulding or extrusion processing used can be achieved using DSC. An example is oxidation induction time (OIT) by DSC which can determine the amount of oxidation stabiliser present in a thermoplastic (usually a polyolefin) polymer material. Compositional analysis is often made using TGA, which can separate fillers, polymer resin and other additives. TGA can also give an indication of thermal stability and the effects of additives such as flame retardants (Dissanayake *et al.*, 2003).

2.16   UV-Vis Studies

Theory

Ultraviolet and visible (UV-Vis) absorption spectroscopy is the measurement of light absorption by a sample. This absorption or attenuation can occur when light passes through a translucent liquid sample, or when light is reflected from a sample surface. The difference in the incident light and the transmitted light is used to determine the actual absorbance. When an atom or molecule absorbs energy, electrons are promoted from their ground state to an excited state. Molecules can only absorb radiant energy in definite units, or quanta, which correspond to the energy difference between the ground and excited states. The energy, *E,* carried by any one quantum is proportional to its frequency of oscillation:

$$E = h\nu = \frac{hc}{\lambda} \hspace{4cm} (2.6)$$

where v is the frequency, λ the related wavelength and h is the Planck's constant (6.624 x 10^{-27} ergs/seconds). In addition to electronic excitation, the atoms within a molecule can rotate and vibrate with respect to each other. These vibrations and rotations also have discrete energy levels, which can be considered as being packed on top of each electronic level. Absorption of ultraviolet and visible radiation in organic molecules is restricted to certain functional groups (chromophores) that contain valence electrons of low excitation energy. The spectrum of a molecule containing these chromophores is complex as the superposition of atomic rotational and vibrational transitions on the electronic transitions gives a combination of overlapping lines. This appears as a continuous absorption band.

Figure 2.6 shows the various kinds of electronic excitation which may occur in organic molecules, as shown on the left. Of the six transitions outlined, only the two lowest energy ones (left-most, colored blue) are achieved by the energies available in the 200 to 800 nm spectrum.
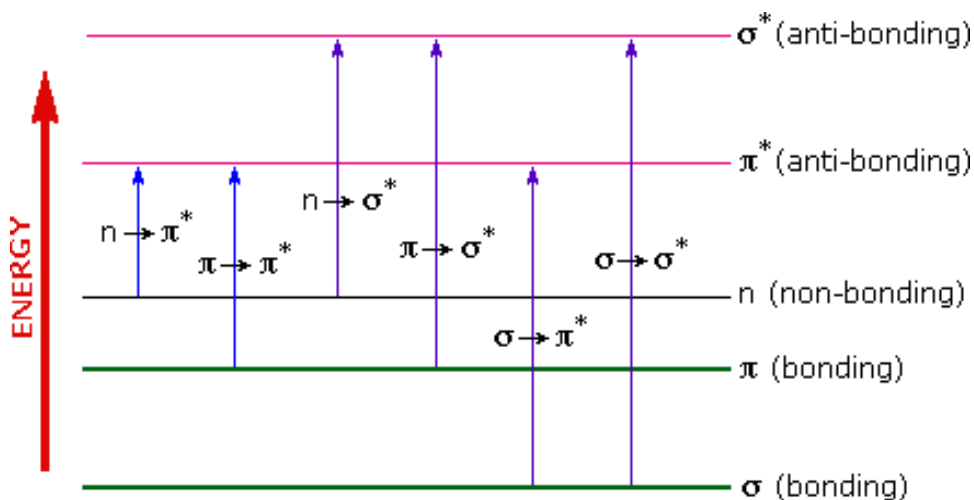
Figure 2.6 Electronic excitation of electrons between molecular orbitals (wikipedia)

The energies noted above are sufficient to promote or excite a molecular electron to a higher energy orbital. Consequently, absorption spectroscopy carried out in this region is sometimes called "electronic spectroscopy".

$\sigma \rightarrow \sigma^*$ Transitions

An electron in a bonding σ orbital is excited to the corresponding antibonding orbital. The energy required is large. For example, methane (which has only C-H bonds, and can only undergo $\sigma \rightarrow \sigma^*$ transitions) shows an absorbance maximum at 125 nm. Absorption maxima due to $\sigma \rightarrow \sigma^*$ transitions are not seen in typical UV-Vis spectra (200 - 700 nm).

$n \rightarrow \sigma^*$ Transitions

Saturated compounds containing atoms with lone pairs (non-bonding electrons) are capable of $n \rightarrow \sigma^*$ transitions. These transitions usually need less energy than $\sigma \rightarrow \sigma^*$ transitions. They can be initiated by light whose wavelength is in the range of 150 - 250 nm. The number of organic functional groups with $n \rightarrow \sigma^*$ peaks in the UV region is small.

$n \rightarrow \sigma^*$ and $\pi \rightarrow \pi^*$ Transitions

Most absorption spectroscopy of organic compounds is based on transitions of n or π electrons to the π^* excited state. This is because the absorption peaks for these transitions fall in an experimentally convenient region of the spectrum (200 - 700 nm). These transitions need an unsaturated group in the molecule to provide the π electrons.

The solvent in which the absorbing species is dissolved also has an effect on the spectrum of the species. Peaks resulting from $n \rightarrow \pi^*$ transitions are shifted to shorter wavelengths (*blue shift*) with increasing solvent polarity. This arises from increased solvation of the lone pair, which

lowers the energy of the *n* orbital. Often (although *not* always), the reverse (i.e. *red shift*) is seen for $\pi \rightarrow \pi^*$ transitions. This is caused by attractive polarisation forces between the solvent and the absorber, which lower the energy levels of both the excited and unexcited states. This effect is greater for the excited state, and therefore the energy difference between the excited and unexcited states is slightly reduced, resulting in a small red shift. This effect also influences *n* $\rightarrow \pi^*$ transitions but is overshadowed by the blue shift resulting from solvation of lone pairs (wikipedia).

The type of monomer bonding are shown below:

i) σ (bonding) molecular as in

$$
\begin{array}{c|c|}
 & | & | \\
-\!\!-\!\!C\!\!-\!\!-\!\!C\!\!-\!\!- \\
 & | & | \\
\end{array}
$$
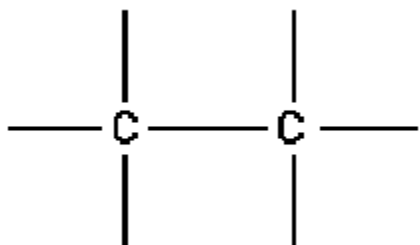
ii) π (bonding) molecular orbital as in

$$
\begin{array}{l}
\diagup C = C \diagdown \qquad \diagup C = O \qquad \begin{array}{c} -N{=}N- \\ -C{\equiv}C- \end{array}
\end{array}
$$
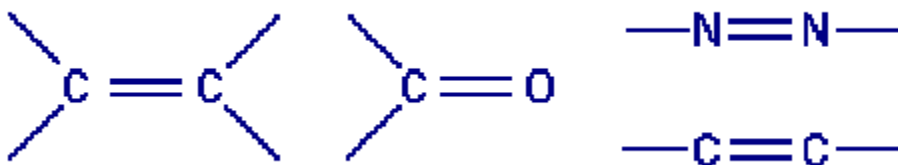
iii) n (non-bonding) atomic orbital as in

$$
\begin{array}{ccc}
| & | & | \\
-\!\!C\!\!-\!\!Br & -\!\!C\!\!-\!\!OH & -\!\!C{=}NH \\
| & | & |
\end{array}
$$
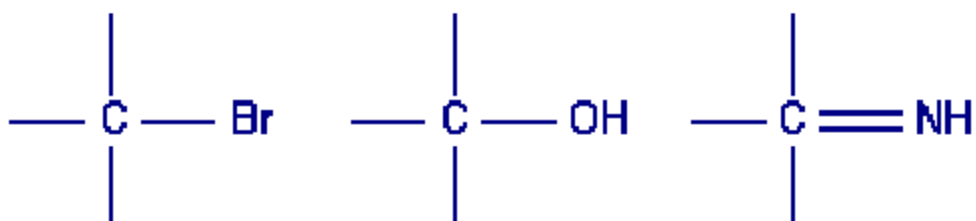
Table 2.4 Examples of transitions and resulting λ_{max} (wikipedia)

Molecule	Transition	λ_{max} (nm)
Ethane	$\sigma \rightarrow \sigma^*$	135
Methanol	$\sigma \rightarrow \sigma^*$	150
	$\eta \rightarrow \sigma^*$	183
Ethylene	$\pi \rightarrow \pi^*$	175
Benzene	$\pi \rightarrow \pi^*$	254
Acetone	$\eta \rightarrow \pi^*$	290

It will be seen presently that the wavelength of maximum absorption and the intensity of absorption are determined by molecular structure. Transitions to π* antibonding orbitals which occur in the ultraviolet region for a particular molecule may well take place in the visible region if the molecular structure is modified. Many inorganic compounds in solution also show absorption in the visible region. These include salts of elements with incomplete inner electron shells (mainly transition metals) whose ions are complexed by hydration e.g. $[Cu(H_2O_4)]^{2+}$. Such absorptions arise from a charge transfer process, where electrons are moved from one part of the system to another by the energy provided by the visible light.

2.16.1 Calculation of the Optical Properties of Thin Films

Transmission and reflection spectra provide important information regarding the refractive indices of the film and the substrate which can be used to calculate the film thickness. For the simple case of high absorption and no interference,

$$R = \left(\frac{n_f - 1}{n_f + 1}\right)^2 \qquad (2.7)$$

$$n_f = \frac{1 + R + \sqrt{R}}{1 - R} \qquad (2.8)$$

where R is the reflection and n_f is the refractive index of the film.

When interference cannot be neglected, the calculation of refractive index is more complicated but is nevertheless possible. If the refractive index is already known and interference is present, the film thickness may be estimated by the wavelengths at which the peaks of the fringes occur for constructive and destructive interference.

2.17   Photoluminescene (PL) Studies

Photoluminescence (abbreviated as PL) is a process in which a substance absorbs photons (electromagnetic radiation) and then re-radiates photons. Quantum mechanically, this can be described as an excitation to a higher energy state and then a return to a lower energy state accompanied by the emission of a photon. This is one of many forms of luminescence (light emission) and is distinguished by photoexcitation (excitation by photons), hence the prefix *photo-*. The period between absorption and emission is typically extremely short, in the order of 10 nanoseconds. Under special circumstances, however, this period can be extended into minutes or hours. Ultimately, available energy states and allowed transitions between states (and therefore wavelengths of light preferentially absorbed and emitted) are determined by the rules of quantum mechanics. A basic understanding of the principles involved can be gained by studying the electron configurations and molecular orbitals of simple atoms and molecules. More complicated molecules and advanced subtleties are treated in the field of computational chemistry.

The simplest photoluminescent processes are resonant radiations, in which a photon of a particular wavelength is absorbed and an equivalent photon is immediately emitted. This process involves no significant internal energy transitions of the chemical substrate between absorption and emission and is extremely fast, of the order of 10 nanoseconds. More interesting processes occur when the chemical substrate undergoes internal energy transitions before re-emitting the energy from the absorption event. The most familiar of such effect is fluorescence, which is also typically a fast process, but in which some of the original energy is dissipated so that the emitted

light photons are of lower energy than those absorbed. The generated photon in this case is said to be red shifted, referring to the loss of energy in the Jablonski diagram shown in Figure 2.7.

A Jablonski diagram, named after the Polish physicist Aleksander Jabłoński, is a diagram which illustrates the electronic states of a molecule and the transitions between them. The states are arranged vertically by energy and grouped horizontally by spin multiplicity. Non-radiative transitions are indicated by squiggly arrows and radiative transitions by straight arrows. The vibrational ground states of each electronic state are indicated with thick lines, the higher vibrational states with thinner lines. Radiative transitions involve the absorption, if the transition occurs to a higher energy level, or the emission, in the reverse case, of a photon. Nonradiative transitions arise through several different mechanisms, all differently labeled in the diagram. Relaxation of the excited state to its lowest vibrational level is labelled v_r in the diagram. This process involves the dissipation of energy from the molecule to its surroundings, and thus it cannot occur for isolated molecules. A second type of non-radiative transition is internal conversion (IC), which occurs when a vibrational state of an electronically excited state can couple to a vibrational state of a lower electronic state. A third type is intersystem crossing (ISC); this is a transition to a state with a different spin multiplicity. In molecules with large spin-orbit coupling, intersystem crossing is much more important than in molecules which exhibit only small spin-orbit coupling. This type of non-radiative transition can give rise to phosphorescence (wikipedia).
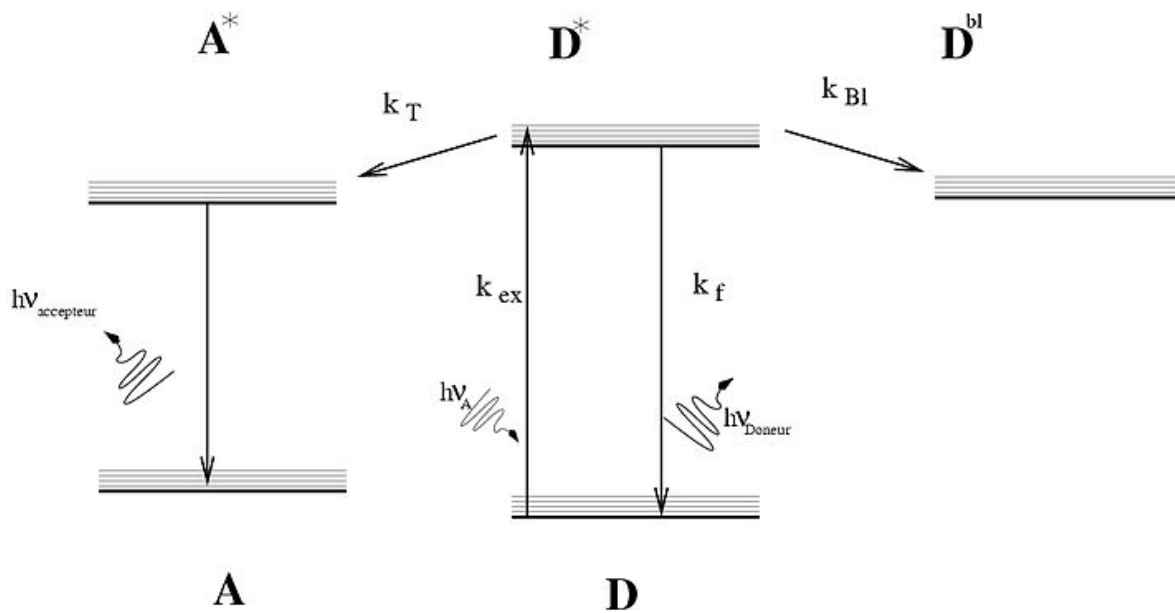
Figure 2.7 A Jablonski diagram representing Förster resonance energy transfer (FRET) (wikipedia)

Photoluminescence is an important technique for measuring the purity and crystalline quality of semiconductors such as GaAs and InP. Several variations of photoluminescence exist, including photoluminescence excitation (PLE).

CHAPTER THREE

MATERIALS AND METHODOLOGY

3.1   Materials

The materials used in this work were poly(ethylene oxide) (PEO) (M_W = 600,000, Acros), lithium hexafluorophosphate ($LiPF_6$) (Aldrich), ethylene carbonate (EC) (Alfa Aesar) and acetonitrile (Fisher). Amorphous carbon nanotubes (αCNTs) were prepared by chemical route at low temperature (Ng and Johan, 2010). Table 3.1 summarizes the materials used in the research.

Table 3.1 Raw materials for polymer electrolytes

Chemical Name	Chemical Structure	Molecular Weight	Supplier
Poly(ethylene oxide)	$-(CH_2-CH_2-O)_n-$	6×10^6	Acros
Lithium hexafluorophosphate	$LiPF_6$	NA	Aldrich
Acetonitrile	CH_3CN	NA	Fisher Scientific
Ethylene Carbonate	$C_3-H_4-O_3$	NA	Alfa Aesar
Carbon Nanotube	C_n	NA	-

3.2 Sample Preparation

Prior to use, PEO was dried at 50 $^{\circ}$C for 48 hours. Different weight percent of salt, plasticizer and filler were added into the PEO matrix. All components were added and dissolved in acetonnitrile using solution-casting technique, as shown in Figure 3.1. The weight percent of salt, plasticizer and filler in the PEO matrix corresponding to mole concentration were calculated by the formula below:

$$\text{PEO/Li}^+ \ (\text{wt\%}) = \frac{W_{Li}^+}{W_{PEO} + W_{Li}^+} \times 100\% \qquad (3.1)$$

$$\text{PEO/Li}^+\text{/EC} \ (\text{wt\%}) = \frac{W_{EC}}{W_{PEO} + W_{Li}^+ + W_{EC}} \times 100\% \qquad (3.2)$$

$$\text{PEO/Li}^+\text{/EC/}\alpha\text{CNT} \ (\text{wt\%}) = \frac{W_{PEO/Li^+/EC/\alpha CNT}}{W_{PEO} + W_{Li}^+ + W_{EC} + W_{\alpha CNT}} \times 100\% \qquad (3.3)$$

where,

W   -   weight

PEO   -   polyethylene oxide

Li$^+$ -   lithium hexafluro salt

EC   -   ethylene carbonate

α-CNT -   amorphous carbon nanotube

Figure 3.1 Solution-casting for thin films

The solutions were stirred for 24 hours at room temperature until homogeneous solutions were obtained. The solutions were cast onto glass Petri dishes and left to evaporate slowly to form films. Table 3.2 summarizes the various weight percent of polymer electrolyte samples. Each sample was tested twice to obtain a representative data set. All samples were prepared at room temperature and stored under dry conditions. The average thickness for film was found to be 0.76 ± 0.01 mm. Other samples were prepared for electrical, optical, chemical, morphology and thermal testing. The films were stored in desiccators until further use. Figure 3.2 shows the flowchart of sample preparation.

Table 3.2: Polymer electrolytes with various weight percent of $LiPF_6$, EC and αCNTs.

Sample	PEO (wt%)	$LiPF_6$ (wt%)	EC (wt%)	αCNTs (wt%)
1	95	5	0	0
2	90	10	0	0
3	85	15	0	0
4	80	20	0	0
5	75	20	5	0
6	70	20	10	0
7	65	20	15	0
8	64	20	15	1
9	60	20	15	5

```
                    PEO              +        Acetonitrile (50ml)
                   (wt%)

Stir for 24h

                          Pure polymer                  Material
                          electrolytes                  Characterizations
                                                        IS, FTIR, XRD, DSC,
                                                        TGA, UV, PL, SEM


                          acetonitrile +
                          LiPF₆ (5, 10, 15 & 20 wt%)

Stir for 24h

                          Salted polymer                Material
                          electrolytes                  Characterizations
                                                        IS, FTIR, XRD, DSC,
                                                        TGA, UV, PL, SEM


                          acetonitrile +
                          EC (5, 10, 15 & 20 wt%)

Stir for 24h

                          Plasticized polymer           Material
                          electrolytes                  Characterizations
                                                        IS, FTIR, XRD, DSC,
                                                        TGA, UV, PL, SEM


                          acetonitrile +
                          αCNTs (1 & 5 wt%)

Stir for 24h

       Neural             Nano-composite               Material
       Network            polymer electrolytes         Characterizations
                                                        IS, FTIR, XRD, DSC,
                                                        TGA, UV, PL, SEM
```

The labels on the boxes read:

- PEO (wt%) + Acetonitrile (50ml)
- Stir for 24h
- Pure polymer electrolytes
- Material Characterizations: IS, FTIR, XRD, DSC, TGA, UV, PL, SEM
- acetonitrile + $LiPF_6$ (5, 10, 15 & 20 wt%)
- Stir for 24h
- Salted polymer electrolytes
- Material Characterizations: IS, FTIR, XRD, DSC, TGA, UV, PL, SEM
- acetonitrile + EC (5, 10, 15 & 20 wt%)
- Stir for 24h
- Plasticized polymer electrolytes
- Material Characterizations: IS, FTIR, XRD, DSC, TGA, UV, PL, SEM
- acetonitrile + αCNTs (1 & 5 wt%)
- Stir for 24h
- Neural Network
- Nano-composite polymer electrolytes
- Material Characterizations: IS, FTIR, XRD, DSC, TGA, UV, PL, SEM

Figure 3.2: Flowchart of sample preparation for nanocomposite polymer electrolytes

3.3   Material Characterizations

3.3.1   X- Ray Diffraction (XRD)

Figure 3.3 shows the X-ray diffraction (XRD) machine, which is an important technique in the field of material characterization. By observing the characteristic patterns of the X-ray diffractogram, one can determine whether the material is crystalline or amorphous, (Moulder et al., 1992). The XRD technique was employed to examine the absence of pure salt or pure polymer and the existence of new peaks of the complexed material. Complexation is indicated by peak-shifting and changes in the relative intensities of the peaks of the salt or the polymer host.

Phase identification using X-ray diffraction relies mainly on the positions of the peaks in a diffraction profile and to some extent, on the relative intensities of these peaks. The shapes of the peaks however, contain additional and often valuable information. The shape, particularly the width of the peak is a measure of the amplitude of thermal oscillation of the atoms at their regular lattice sites. It can also be a measure of valency and impurity element concentration and plastic deformation for any factor which results in a distribution of d-spacings. Reduction in the crystallite size may also cause peak broadening. The Scherrer equation explains peak broadening in terms of incident beam divergence, which makes it possible to satisfy the Bragg condition for non-adjacent diffraction planes (Moulder et al., 1992). Once instrument effects have been excluded, the crystallite sizes is easily calculated as a function of peak width (specified as the full width at half maximum peak intensity (FWHM), peak position and wavelength.

The polymer electrolytes were adhered onto clean microscope slides and placed in the sample chamber around which a detector is moved. As the sample rotates, the angle (θ) between

the incident beam and normal to the film is changed. A convenient form of the geometrical relationship determining the angular distribution of the peak intensities in the diffraction pattern is represented by the Bragg's equation:

$$n\lambda = 2d \sin \theta \qquad\qquad (3.4)$$

where, d is the interplanar spacing between the crystal lattice planes responsible for a particular diffracted beam, θ refers to the Bragg angle which the incident beam makes with the lattice planes, n is an integer referring to the order of reflection, and λ represents the wavelength of light radiation.

X-rays are reflected to the detector when the Bragg condition shown in Figure 3.4 is fulfilled:

Figure 3.3: X-ray diffraction machine
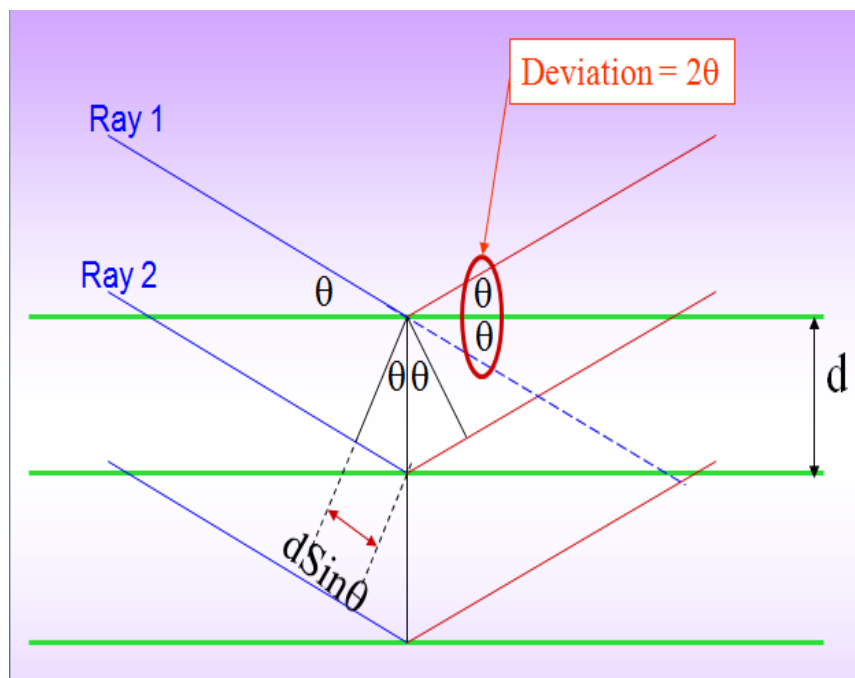
Figure 3.4: Schematic of Bragg's reflection from a crystal

The diffractometer assembly controls the alignment of the beam, as well as the position and orientation of both specimen and the X-ray detector. X-ray monochromatic radiations is generated by excitation of κ-radiations from a pure metal target and filtering the beam by interposing a foil, which strongly absorbs the β-component of the κ-radiation without any appreciable reduction in intensity of α-component. The use of a nickel filter ($E_{Ni-\kappa}$ = 0.1488 nm) with copper target ($E_{Cu-\kappa}$=0.138 nm), transmits the Cu-κ_α beam (0.154 nm), but blocks the Cu-κ_β component. In this study, the X-ray diffraction (XRD) patterns of the films were recorded at room temperature using Phillips X-pert MRD X-ray diffractometer with angle (2θ) range from 10 to 60.

3.3.2　　Fourier Transform Infrared Spectroscopy (FTIR)

Fourier Transform Infrared spectroscopy (FTIR) is the subset of spectroscopy which deals with the infrared region of the electromagnetic spectrum. It covers a range of techniques, the most common being a form of absorption spectroscopy. It can be used to identify the compound and sample composition.

The infrared portion of the electromagnetic spectrum is usually divided into three regions, namely, near-IR, mid-IR and far-IR. The far-IR, approximately $400 - 10$ cm^{-1} ($1000 – 30$ μm), lying adjacent to the microwave region has low energy and may be used for rotational spectroscopy. The mid-IR, approximately $4000 - 400$ cm^{-1} ($30 - 2.5$ μm) may be used to study the fundamental vibrations and associated rotational- vibrational structure. The near-IR, approximately $14000 - 4000$ cm^{-1} ($2.5 - 0.8$ μm) can excite overtone or harmonic vibrations. The names and classifications of these sub-regions are merely conventions. They are neither strict division nor based on exact molecular or electromagnetic properties.

Infrared spectroscopy exploits the fact that the molecules absorb specific frequencies which are characteristic of their structures. These absorption are resonant frequencies, i.e. the frequency of the absorbed radiation matches the frequency of the bond which vibrates. The energies are determined by the shape of the molecular potential energy surfaces, the asses of the atoms, and the associated vibronic coupling.

Figure 3.5: Spectrum FTIR Spectometer dual system

In particular, in the Born-Oppenheimer and harmonic approximations, i.e., when the Hamiltonian corresponding to the electronic ground state can be approximated by a harmonic oscillator in the neighborhood of the equilibrium molecular geometry, the resonant frequencies are determined by the normal modes corresponding to the molecular electronics ground state potential energy surface. Nevertheless, the resonant frequencies can be related to the strength of the bond, and the mass of the atoms at either ends of it. Thus, the frequency of the vibrations can be associated with a particular bond type.

FTIR spectroscopy does not require vacuum, since neither oxygen nor nitrogen absorbs infrared rays. FTIR analysis can be applied to minute quantities of materials, whether solid, liquid, or gaseous. When the library of FTIR spectral patterns does not provide an acceptable match, individual peaks in the FTIR plot may be used to yield partial information about the specimen.

In this work, the FTIR spectra of the samples were recorded using Perkin Elmer FL Winlab FTIR spectrometer, equipped with an air-cooled rare earth oxide filament source, CSI beam splitter and DTGS detector, as shown in Figure 3.5. The instrument was set for ten scans at 4 cm^{-1} resolution with cosine apodisation in the mid-IR region: 4,000 - 400 cm$^{-1.}$ No purging was carried out. The samples were placed into the sample holder made and contacted with a diamond stub.

3.3.3   Impedance Spectroscopy (IS)

Impedance Spectroscopy (IS) has long been employed for studying electrochemical systems (Lasin, 1999). Figure 3.6 shows the IS machine used in this work, HIOKI 3531 LCR Hi-Tester, with frequency range of 50 Hz to 5 MHz.

Figure 3.6 HIOKI HiTESTER machine

The results were analyzed using the HIOKI software to extract the impedance, which was then used to calculate the bulk conductivity of the electrolyte. This technique is used to determine the ionic conductivity of the electrolyte. It involves the application of voltage, particulary alternating voltage in the appropriate frequency range, to a cell containing the electrolyte and measuring the resulting current. The impedance of the electrolyte can then be calculated from this current value. Figure 3.7 shows an example of a cole-cole plot obtained in this work. The semicircles are clearly represented, providing information about bulk electrolyte behaviour. The curves to the right of the semicircle characterize the properties of the electrode.

Ideally, this line should be perpendicular to the x-axis, but the roughness of the stainless-steel electrode combines with imperfect contact between the electrolyte and the blocking electrodes. This accounts for the orientation of the spike. This is typical in real test cell measurements.
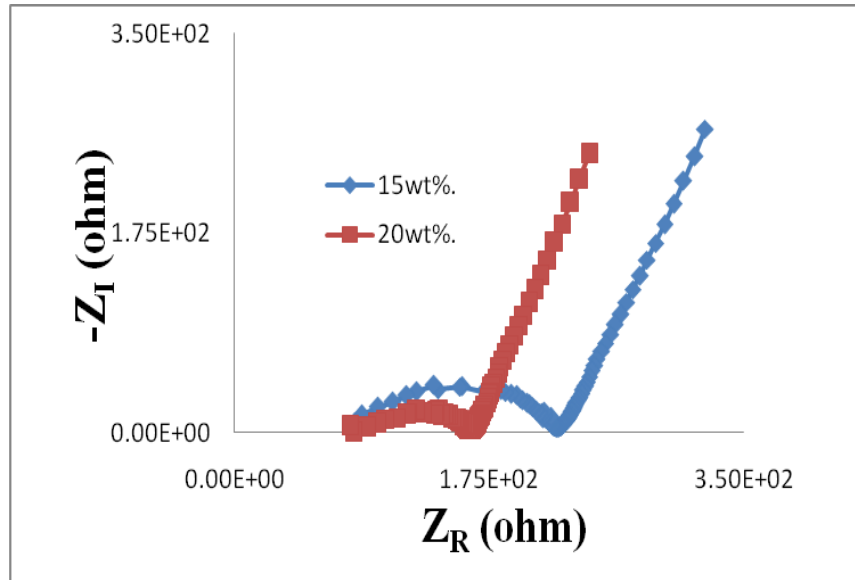
Figure 3.7: Cole – Cole plot for PEO-LiPF$_6$ (a) 15; (b) 20. (Ibrahim *et. al*, 2010)

A simple way to determine bulk resistance of the electrolyte is to apply a direct voltage across the electrolyte, measure the resulting current and then calculate the resistance using Ohm's law. Direct-current measurements are often not applied to ionic conductivity measurements of polymer electrolytes despite their straightforward and simple approach for several reasons. This method is undesirable because concentration changes occur in the electrolyte and an interfacial resistance occurs at the interface with the electrodes.

AC impedance spectroscopy involves the application of a sinusoidal voltage and the measurement of the sinusoidal current resulting from the perturbation. Since the applied voltage is indirect, the two parameters required to relate the applied potential and current flowing in the cell are the magnitude of the resistance and the phase difference between the voltage and the current, which are both functions of the applied frequency. The combination of these two parameters makes up the impedance of the cell, a vector quantity comprising both magnitude and phase, represented schematically in Figure 3.8.
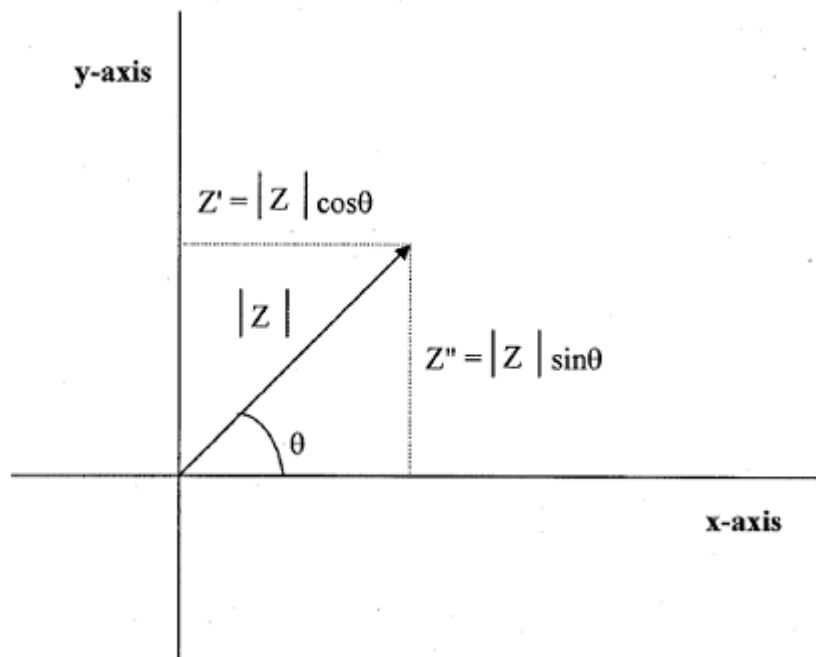
Figure 3.8: Schematic representation of the components of impedance, Z*(Bahri, 1980)

The equations defining these relationships are given as:

$$Z* = Z' - iZ''$$ (3.6)

$$Z* = |Z|\cos\theta - |Z|\sin\theta$$ (3.7)

where:

$Z*$ = complex impedance

Z' = real component of complex impedance

Z'' = imaginary component of complex impedance

$|Z|$ = magnitude of complex impedance

θ = phase angle

i = complex number operator = $\sqrt{-1}$

A typical AC impedance experiment plot, also called Nyquist plot or Cole-Cole plot, consists of a representation of the real impedance, Z' on the x-axis and the imaginary impedance, Z'' on the y-axis as a function of the applied frequency. To interpret accurately the data obtained from AC impedance spectroscopy, it is essential to develop an equivalent circuit which represents the various components of the electrochemical cell. The blocking electrodes are typically modelled as capacitors, whereas the electrolyte is a combination of both a resistor and a capacitor. Figure 3.9 is a schematic representation of the complex impedance plot representing this system.
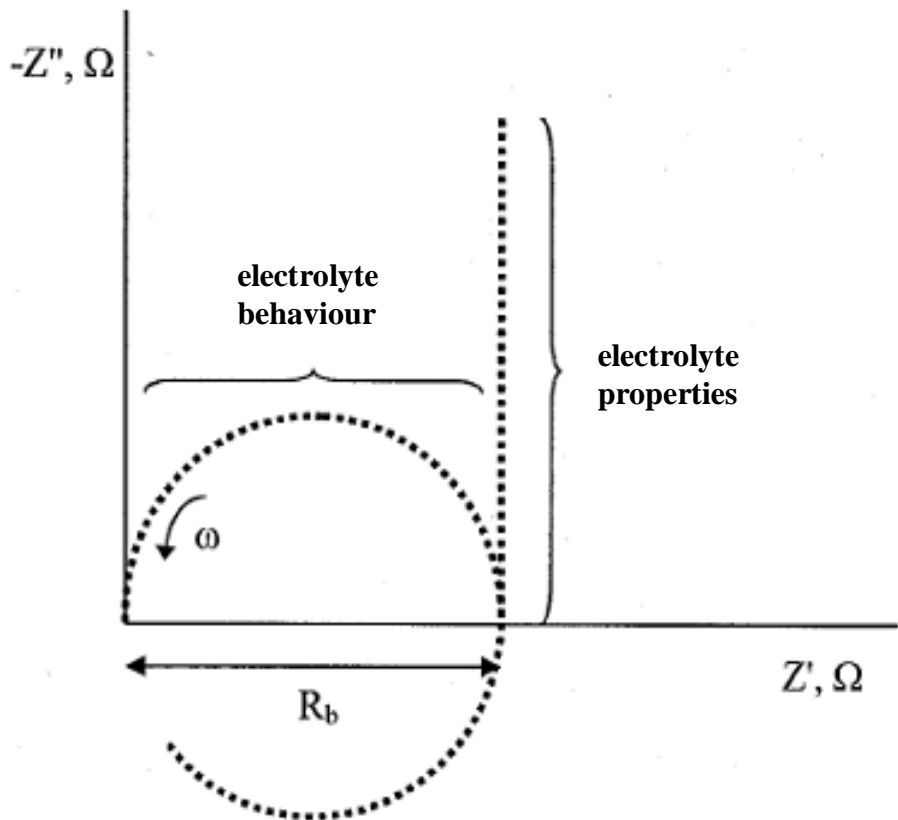
Figure 3.9: Schematic representation of an ideal Nyquist plot (Bahri, 1980)

The calculation resulting from this combination of components and consequently the shape of

the ensuing complex plot is given below.

For a resistor, voltage is in phase with current and $\theta = 0$, so

$$Z* = |Z| = R \qquad (3.8)$$

For a capacitor, voltage that behind current by 90V and $\theta = -\pi / 2$, so

$$Z* = |Z|\cos\left(-\frac{\pi}{2}\right) - i|Z|\sin\left(-\frac{\pi}{2}\right) \qquad (3.9)$$

$$Z* = -i|Z| = -\frac{i}{\omega C} \tag{3.10}$$

where:

R = resistance

C = capacitance

W = angular frequency

In an equivalent circuit, the electrolyte is represented as a parallel combination of the resistance and the capacitance and the total impedance is given as:

$$\frac{1}{Z^*_{electrolyte}} = \frac{1}{Z^*_{resistor}} + \frac{1}{Z^*_{capacitor}} \tag{3.11}$$

$$Z^*_{electrolyte} = \frac{R}{1 + i\omega CR} = \left(\frac{R}{1 + i\omega CR}\right)\left(\frac{1 - i\omega CR}{1 - i\omega CR}\right) \tag{3.12}$$

$$Z^*_{electrolyte} = \frac{R - i\omega CR^2}{1 + (\omega CR)^2} \tag{3.13}$$

Separating the real component from the imaginary component, gives :

$$Z^*_{electrolyte} = R\left[\frac{1}{1 + (\omega CR)^2}\right] - iR\left[\frac{\omega RC}{1 + (\omega RC)^2}\right] \tag{3.14}$$

This represents a semicircle in the complex impedance plane with the intercept of the semicircle with the x-axis representing R, the bulk resistance of the electrolyte. The equivalent circuit also indicates that the parallel resistor and capacitor of the electrolyte is in series with the

electrode capacitors. Factoring this into the electrolyte impedance is additive and gives an overall impedance of:

$$Z_{total}^* = R_{bulk}\left[\frac{1}{1+(\omega C_{bulk}R_{bulk})^2}\right] - i\left(R_{bulk}\left[\frac{\omega R_{bulk}C_{bulk}}{1+(\omega R_{bulk}C_{bulk})^2}\right] + \frac{1}{\omega C_{electrode}}\right) \quad (3.15)$$

Equation (3.15) is graphically represented by Figure 3.9, which shows the semi-circle and electrode spike. The high frequency section of the plot reveals information about the properties of the electrolyte whereas the low frequency region indicates behaviour at the electrode/electrolyte interface.

In the case of non-blocking electrolytes in which electrochemical reaction are occurring at the electrodes, several semi-circles may be observed indicating a variety of electrochemical processes occurring within the system. The semicircle obtained at high frequencies represents the migration of ions within the bulk electrolyte, the same circle observed with non-blocking electrodes. A second semicircle at intermediate frequencies can be associated with electrode reactions and charging and discharging at the electrode/electrolyte interface. Sometimes, a third semicircle may be observed at low frequencies, which corresponds to diffusion due to concentration gradients within the electrolyte. Transport numbers for the mobile ions could potentially be extracted from the theory predicting this diffusional impedance.

The equations described above represent an ideal electrolyte system in which the salt and polymer are homogeneously mixed, no phase disparities are present, and the ions are completely dissociated. This is not the case in real polymer electrolytes and is evident in the shape of the

complex impedance plot for a real polymer electrolyte/blocking electrode system. The semi-circles are typically broadened to account for the inhomogeneities in the polymer electrolyte and the uneven distribution of salt throughout the matrix. Also, a non-vertical electrode spike which is a result of the rough interface between the electrode and electrolyte, is observed at low frequencies.

Using Ohm's Law and replacing V by IR, where R is the buk sample DC resistance, the following relation is derived for σ:

$$\sigma = \tau / RA \hspace{4cm} (3.16)$$

where τ is thickness of the sample, R is bulk resistance, A is area of sample holder and σ is conductivity.

As A and τ can be measured by a micrometer, and R by impedance spectroscopy, the bulk sample conductivity can be determined. Typically conductivity values are expressed in units of siemen (Ohm $^{-1}$) per centimeter (Scm^{-1}).

3.3.4 Differential Scanning Calorimetry (DSC)

Differential scanning calorimetry (DSC) was used to determine the phase and temperature transitions in the polymer systems. Figure 3.10 shows the DSC used in this work, whereby DSC 820 was fitted with 56 thermocouples and the temperature range was between -100 to 200°C. The technique is based on heating a polymer sample and a reference pan and measuring the amount of heat needed to maintain both samples at a particular temperature. If a sample pan (containing the sample test material) and an empty reference pan both made of the same metallic material (usually aluminium) are heated at a known rate in a controlled environment, the temperature increase in the sample and reference pans should be equivalent, unless a heat related change takes place in the sample, allowing it either to evolve (cooling cycles) or absorb heat (heating cycle) at the phase transition point. The DSC machine used for these experiments controls the cell temperature by heating a silver block with a resistive wound heater and monitoring its temperature with a closely coupled control thermocouple. The samples were heated at 5°C/min with the temperature ranging from -100 to 200°C.

In this work, the transition and crystalline melting behaviour in PEO electrolytes were investigated using a diffrential scanning calorimeter with a heating rate of 5 °C/min. The samples were weighed about 5 to 8 mg and sealed in the aluminum hermetic pans and lids. The glass transiton temperature (T_g) was estimated at the onset point of an endothermic shift whereas the melting temperature was estimated from the extrapolated midpoint of melting endotherm peak.

The degree of relative crystallinity (X_c) was calculated using the following relationship

$$X_c = \frac{\Delta H_m^{\text{sample}} \times 100}{\Delta H_m^o} \qquad (3.17)$$

where pure PEO was taken as being 100% crystalline as a reference. Here $\Delta H_m^{\text{sample}}$ and ΔH_m^o represent the melting enthalpy of the sample and pure PEO, respectively.
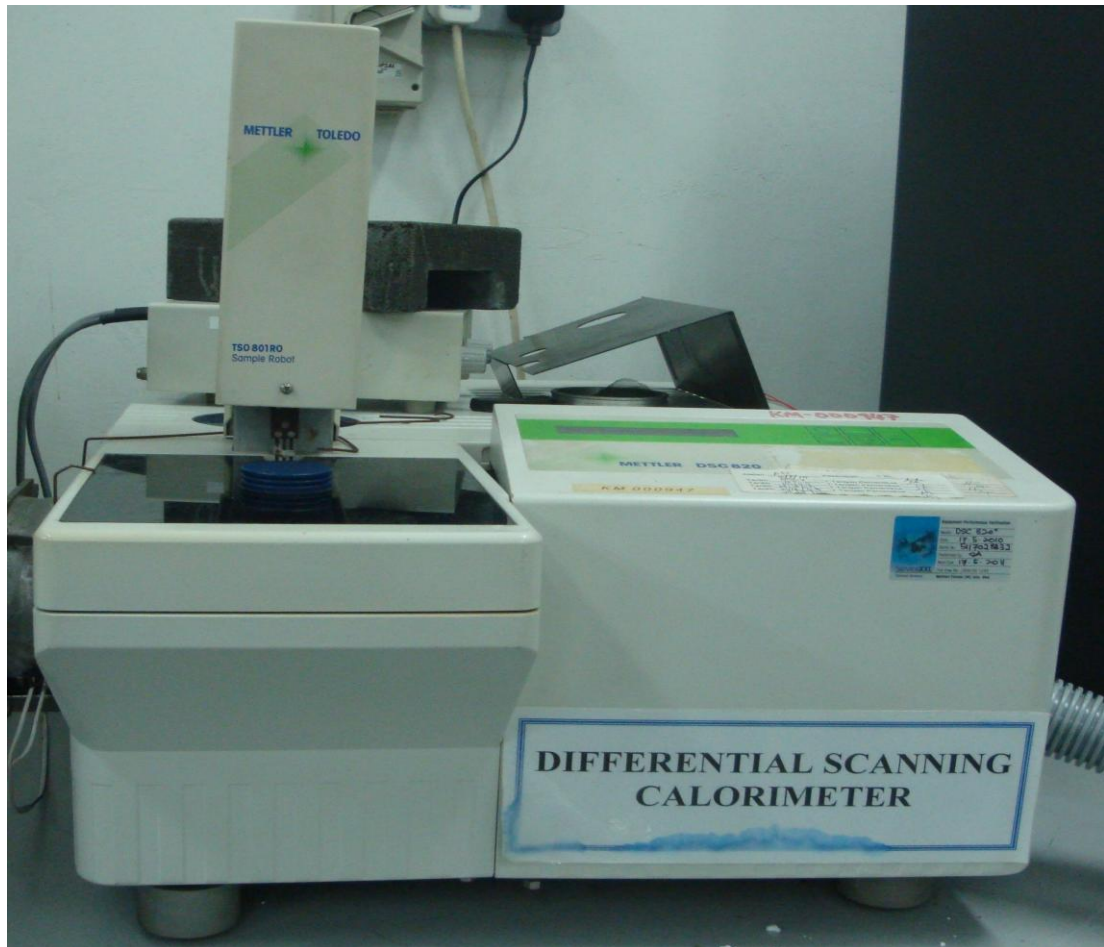
Figure 3.10: Differential scanning calorimetry (DSC)

3.3.5   Thermogravimetric Analysis (TGA)

Thermogravitmetric analysis analysis (TGA) is commonly used to determine the characteristics of materials such as degradation temperatures, absorbed moisture content of materials, the level of inorganic and organic components in materials, decomposition points of explosives and solvent residues. Figure 3.11 shows the TGA used in this work (TGA/SDTA 851 Mettler Toledo). This instrument is also often used to estimate the corrosion kinetics in high temperature oxidation. Analysis is carried out by raising the temperature of the sample gradually and plotting the weight (percentage) against temperature. The temperature in many testing methods routinely reaches 1000°C or greater. Once the data is generated, curve smoothing and other operations may be carried out such as to find the exact points of inflection.

A method known as hi-resolution TGA is often employed to obtain greater accuracy in areas where the derivative curve peaks. In this method, the temperature increase slows as weight loss increases. This method identified the exact temperature where a peak occurs more accurately. Several modern TGA devices can vent burnoff to an infrared spectrophotometer to analyze composition.

Figure 3.11: Transgravimetric analysis machine

3.3.6   Field Emission Scanning Electron Microscopy (FE-SEM)

Figure 3.12 shows the field emission electron microscopy used in this work (FE-SEM; JSM 5410LV, JEOL, Japan). The high beam energies have been used in order to achieve good resolution and small probe diameters when non-conductive materials have been coated, to avoid charging problems. For analytical applications and for high resolution imaging, the instrument should also provide excellent high-voltage performance.

Figure 3.12: FE-SEM machine

All samples must also be of an appropriate size to fit in the specimen chamber and are generally mounted rigidly on a specimen holder called a specimen stub. For conventional imaging in the SEM, specimens must be electrically conductive, at least at the surface, and electrically grounded to prevent the accumulation of electrostatic charge at the surface. Metal objects require little special preparation for SEM except for cleaning and mounting on a specimen stub. Non-conductive specimens tend to charge when scanned by the electron beam, and especially in secondary electron imaging mode, this causes scanning faults and other image artifacts. They are therefore usually coated with an ultrathin coating of electrically-conducting material, commonly

gold, deposited on the sample either by low vacuum sputter coating or by high vacuum evaporation. Conductive materials in current use for specimen coating include gold, gold/palladium alloy, platinum , osmium, iridium, tungsten, chromium and graphite. Coating prevents the accumulation of static electric charge on the specimen during electron irradiation.

There are two reasons for coating, even when there is enough specimen conductivity to prevent charging, which to increase signal and surface resolution, especially with samples of low atomic number (X). The improvement in resolution arises because backscattering and secondary electron emission near the surface are enhanced and thus an image of the surface is formed.

3.3.7   Ultra-Violet Visible (UV-Vis) Spectroscopy

A UV-Visble spectrophotometer was employed to measure the amount of light which a sample absorbs. The instrument operates by passing a beam of light through the sample, and measuring the intensity of light reaching a detector. The beam of light consists of a stream of photons. When a photon encounters an analyte molecule (the analyte is the molecule being studied), there is a chance that the analyte will absorb the photon. This absorption reduces the number of photons in the beam of light, thereby reducing the intensity of the light beam.

A diagram of the components of a typical spectrometer is shown in Figure 3.13. Particularly, the light source is set to emit 10 photons per second. The motion of the photons is monitored and the photons absorbed are observed as the beam of light passes through the cell

containing the sample solution. The intensity of the light reaching the detector is less than the intensity emitted by the light source. The extent to which a sample absorbs light depends strongly upon the wavelength of light. For this reason, spectrophotometry is performed using monochromatic light. Monochromatic light is light in which all photons have the same wavelength. In analyzing a new sample, a chemist first determines the sample's absorbance spectrum. The absorbance spectrum shows how the absorbance of light depends upon wavelength off-light. The spectrum itself is a plot of absorbance (A) versus wavelength (λ), and is characterized by the wavelength (l_{max}) at which the absorbance is the greatest.
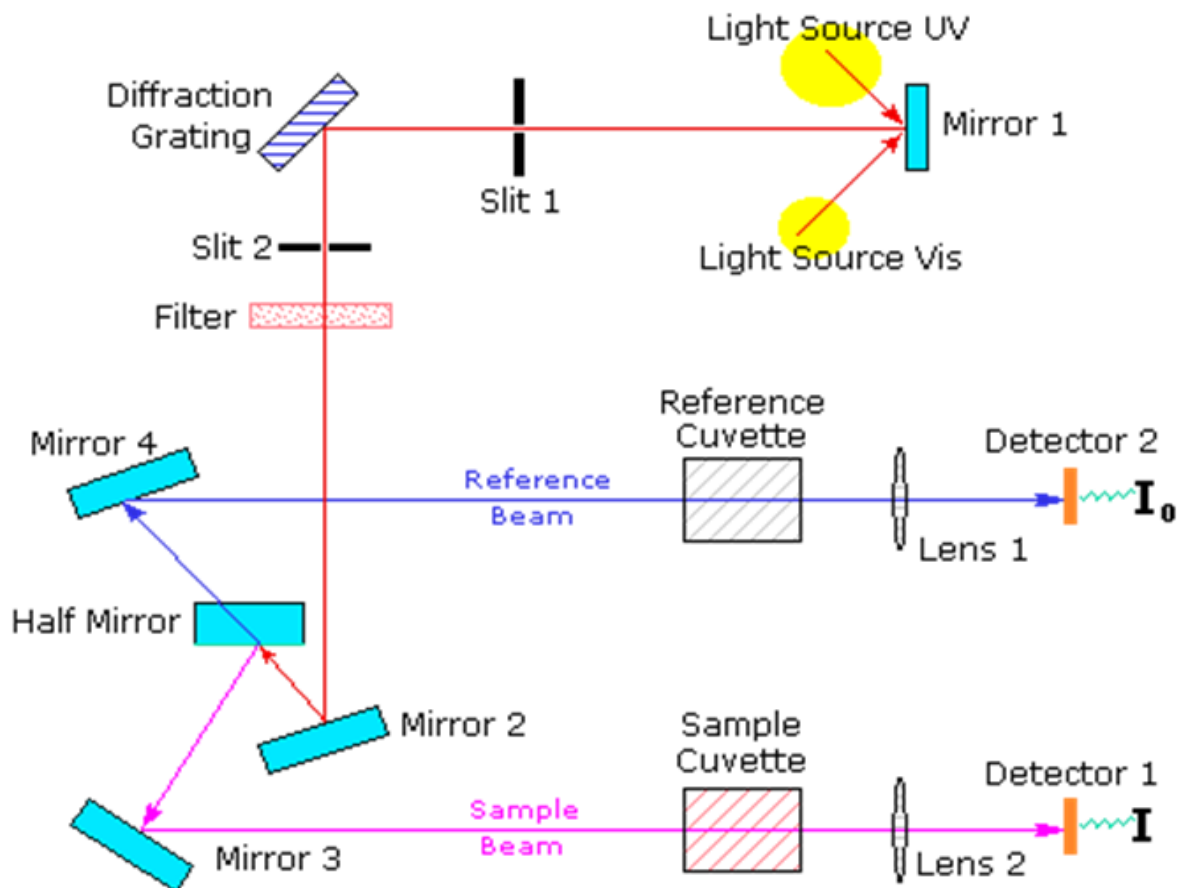
Figure 3.13: The components of a typical UV – Vis spectrophotometer

The absorption of light radiation in a sample obeys the Beer-Lambert relationship, which states that the concentration of a substance in a sample is directly proportional to the absorbance, A. From Figure 3.13, the incident radiation refers to I_o and the intensity of transmitted radiation refers to I,

$$A = \varepsilon bc \tag{3.18}$$

where ε is the molar absorptivity constant, b is the path length and c is the molar concentration of the absorbance. When monochromatic radiation passes through a homogeneous sample, the intensity of the emitted radiation depends upon the thickness, L and concentration, c. The ratio I_o/I, known as transmittance, is expressed as a percentage and is therefore referred to as % transmittance. The absorbance is related to percent transmittance, T by the expression:

$$A = long\left(I_o/I\right) = \log\left(100/T\right) = \varepsilon bc \tag{3.19}$$
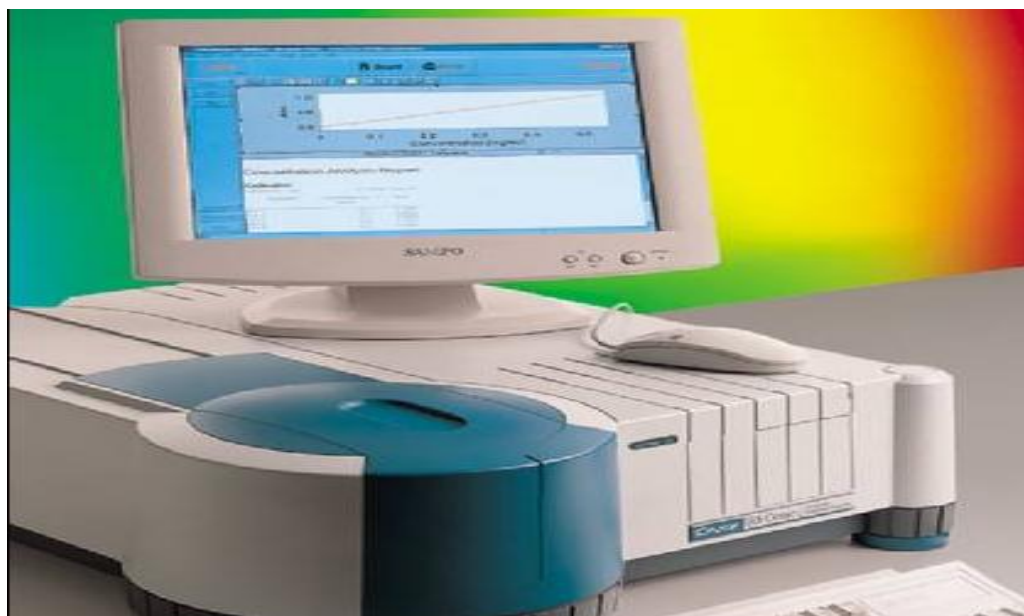
Figure 3.14: UV – Vis spectrophotometer

Figure 3.14 shows Cary 50 UV-Visible spectrophotometer used for optical characterization of polymer electrolytes. The wavenumber range for this equipment is 180-900 nm, and the wavenumbers considered in this research are within the range of 300 – 600 nm at a scan speed of 60 nm/min. Prior to using 'UV-Cary50' software, baseline correction of the spectrophotometer was carried out using acetonnitrile for polymer electrolyte solution. 1 mL of polymer electrolyte was diluted in 10 mL of acetonnitrile and rinsed in ultrasonic bath with re-distilled deionized water for 10 min. The absorption spectra were recorded at a rate of 60 nm min-1, with a spectral resolution of 2 nm at room temperature in a 1 cm optical path quartz cuvette.

3.3.8   Photoluminescence (PL) Spectroscopy

The Perkin Elmer LS 55 luminescence spectroscopy is a very versatile instrument which allows measurement of fluorescence, phosphorescence, and chemiluminescence or bioluminescence of liquid, solid, powder, or thin film samples. The instrument is simple to operate and is controlled by user-friendly software. The sample is illuminated in the wavelength range of 200 to 800 nm and the emission spectrum is recorded from 200 to 900 nm. Excitation and emission monochromators can be independently or synchronously scanned, whereas the Prescan mode is ideal for method development and locating of peak excitation and emission maxima.

The LS 55 Model Series shown in Figure 3.15 uses a pulsed Xenon lamp as the excitation source. Fluorescence data are collected at the instant of the flash whereas phosphorescence data are collected in the dark period between each flash. The use of the pulsed Xenon lamp obviates the need for a mechanical means of chopping the excitation and emission

beams. This leads to improved precision and speed of analysis. The instrument software includes application programs for observing short (millisecond) and long (seconds) phosphorescence decay curves in addition to spectra. Figure 3.16 shows the schematic diagram of the Photoluminescence Spectroscopy.
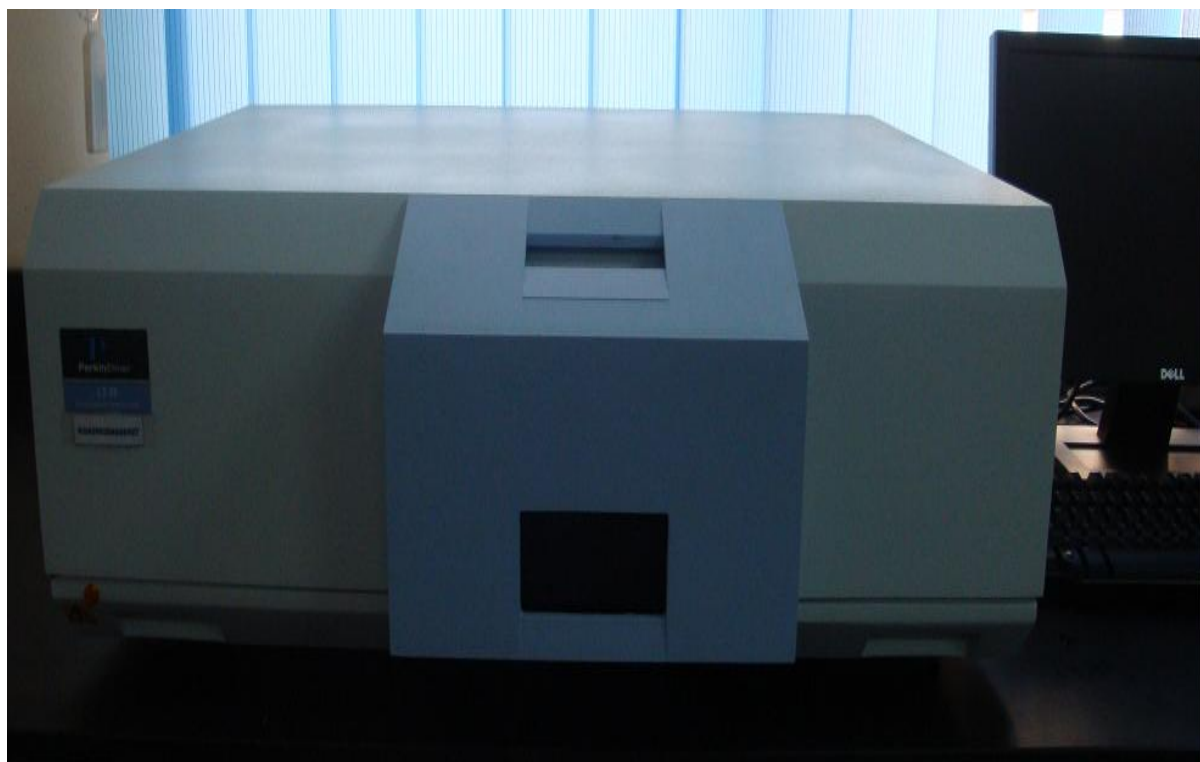
Figure 3.15: Photoluminescence spectrophotometer

The LS 55 includes a single cell sample holder which can accommodate 1 cm path length cells as well as semi-micro cuvettes. Semi-micro cuvettes are particularly useful for samples which are precious or where the volume is limited. The spectrometer only requires 0.3 mL of sample but offers a 5 mm path length. Most operators will use standard inexpensive plastic cuvettes. The schematic of the photoluminescence system is shown in Figure 3.16, and includes an automated

polarizer which consists of 2 filter wheels, whereby each wheel contains a horizontal and vertical polarizing element. Polarizer positions are software controlled and can be manually set or automatically controlled for polarization, anisotoropy or G-factor.
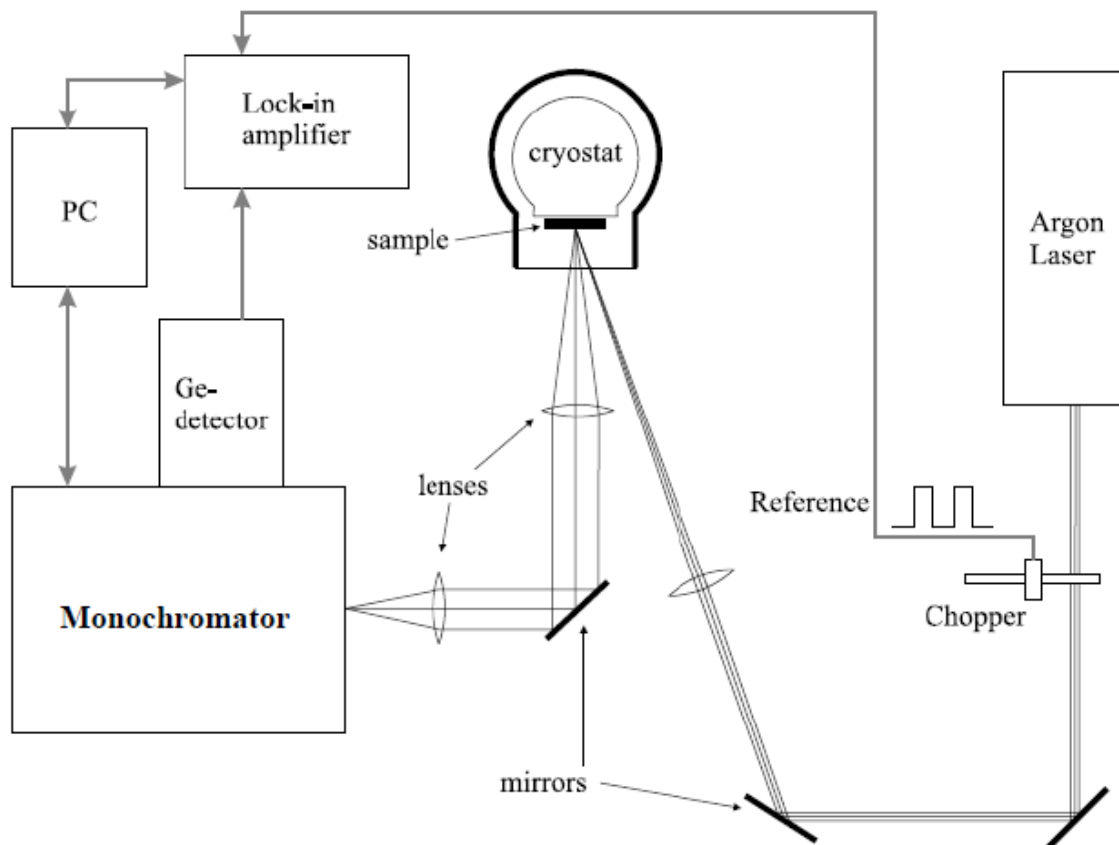
Figure 3.16: Schematic of the arrangement of component in photoluminescence (PL) spectrometer.

FL Winlab Perkin Elmer LS 55 was used to characterize the luminescence behaviour of polymer electrolytes. The available emission spectra range for this equipment is 200-900 nm; however, in this study, the samples were scanned within the wavelength range of 300-480 nm at a scan speed of 1200 nm min^{-1}. Configuration of the spectrometer was carried out by adjusting the pre-scan

button. The samples were placed into the cuvette and fixed into the holder. Scanning of excitation and emission was run and the numerical data were stored. The PL emission spectra for all samples were recorded and plotted.

3.3.9   Theoretical Studies of Nanocomposite Polymer Electrolytes

3.3.9.1 Bayesian Neural Networks

Neural networks are parallel-distributed information processing systems used for empirical regression and classification modelling. Their flexibility makes them useful for discovering more complex relationships in data than traditional linear statistical models. They consist of a number of highly interconnected processing elements organized into layers, the geometry and functionality of which have been likened to that of the human brain, as shown in Figure 3.17.
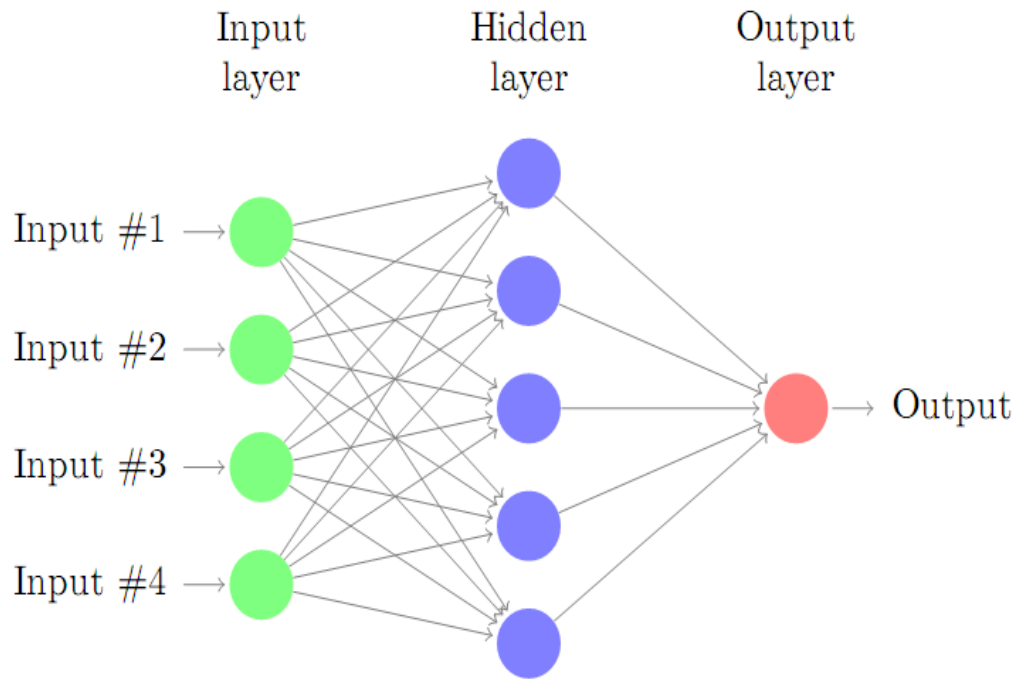
Figure 3.17 The structure of three-layered neural network used in the present study

A neural network is trained on a set of examples of input and output data. The outcome of this training is a set of coefficients (called weights) and a specification of the functions which in combination with the weights relate the input to the output. The training process involves a search for the optimum non-linear relationship between the inputs and the outputs. Once the network is trained, the estimation of the outputs for any given inputs is very rapid. Neural networks used have been developed in a statistical framework to automatically infer the appropriate model complexity (MacKay, 1992; MacKay, 1995). This helps avoid the problems of over-fitting the very flexible equations used in neural network models. The output variable is expressed as a linear summation of activation functions h_i with weights w_i and the bias θ:

$$y = \sum_i w_i h_i + \theta \qquad (3.20)$$

with the activation function for a neuron i in the hidden layer is given by:

$$h_i = \tanh\left(\sum_j w_{ij} x_j + \theta_i\right) \qquad (3.21)$$

with weights w_{ij} and biases θ_i. The weightings are simplified by normalising the data within the range ± 0.5 using the normalisation function

$$x_j = \frac{x - x_{min}}{x_{max} - x_{min}} - 0.5 \qquad (3.22)$$

where x is the value of the input and x_j is normalised value. In the Bayesian neural network (Bhadeshia, 1999; Bhadeshia, 2009; MacKay, 1992; MacKay, 1995), training is achieved by altering the parameters by back-propagation to optimise an objective function which combines an error term to assess how good the fitting is and regularisation term to penalise large weights,

$$M(w) = \beta \frac{1}{2} \sum_i \left(t^{(i)} - y^{(i)}\right)^2 + \alpha \left(\frac{1}{2} \sum_i w_i^2\right)$$

(3.33)

where β and α are complexity parameters which greatly influence the complexity of the model, $t^{(i)}$ and $y^{(i)}$ are the target and corresponding output values for one example input from the training data $x^{(i)}$. The Bayesian framework for neural network has two further advantages. Firstly, the significance of the input variables is quantified automatically. Consequently, the significance perceived by the model of each input variable can be compared against existing theory. Secondly, the network's predictions are accompanied by error bars which depend on the specific position in input space. These quantify the model's certainty about its predictions.

CHAPTER FOUR

Structural and Morphological Studies of Nanocomposite Solid Polymer Electrolytes

4.1 X-Ray Diffraction (XRD) Analysis of Polymer Electrolytes at various wt% of LiPF$_6$ Salt

Figure 4.1 shows the XRD patterns for polymer electrolytes at various wt% of LiPF$_6$. The crystalline nature for each sample was compared with respect to pure PEO. There are sharp and intense diffraction lines occured at angle of 20° and 24°, indicating the crystalline nature of pure PEO (Khiar and Arof, 2010). The intensities of PEO peaks at that angles are observed to decrease upon the addition of salt. However, it can be seen that the diffraction pattern resembles that of pure PEO. The sharpness of the diffraction lines remains unchanged, suggesting that a portion of the PEO remains salt-free and the other portion of the PEO containing salt transforms to an amorphous phase. This indicates that the crystalline phase of uncomplexed PEO exists in the solid electrolyte films. As the salt concentration increases, it can be observed that there are slight changes in the position of the peaks from $2\theta = 24°$ to 23.3° and $2\theta = 20°$ to 19.2°. In this regime, it can be noticed that the intensities of the diffraction peaks at angles of 23.3° and 19.2° decrease slightly. Therefore, the angles of 23.3° and 19.2° appear to be the preferred crystallographic direction whereby an interaction of PEO and salt takes place. The variation in peak intensity at different salt concentrations indicates the increase in the number of preferred oriental ions for each concentration (Ibrahim *et al*., 2010). This will increase the ionic conductivity in this regime. New peak at $2\theta = 29.4°$ begins to appear in the diffractogram for film with 20 wt% of LiPF$_6$, showing the formation of a new crystalline phase. The new peak suggests the formation of crystalline PEO-LiPF$_6$ complexes.
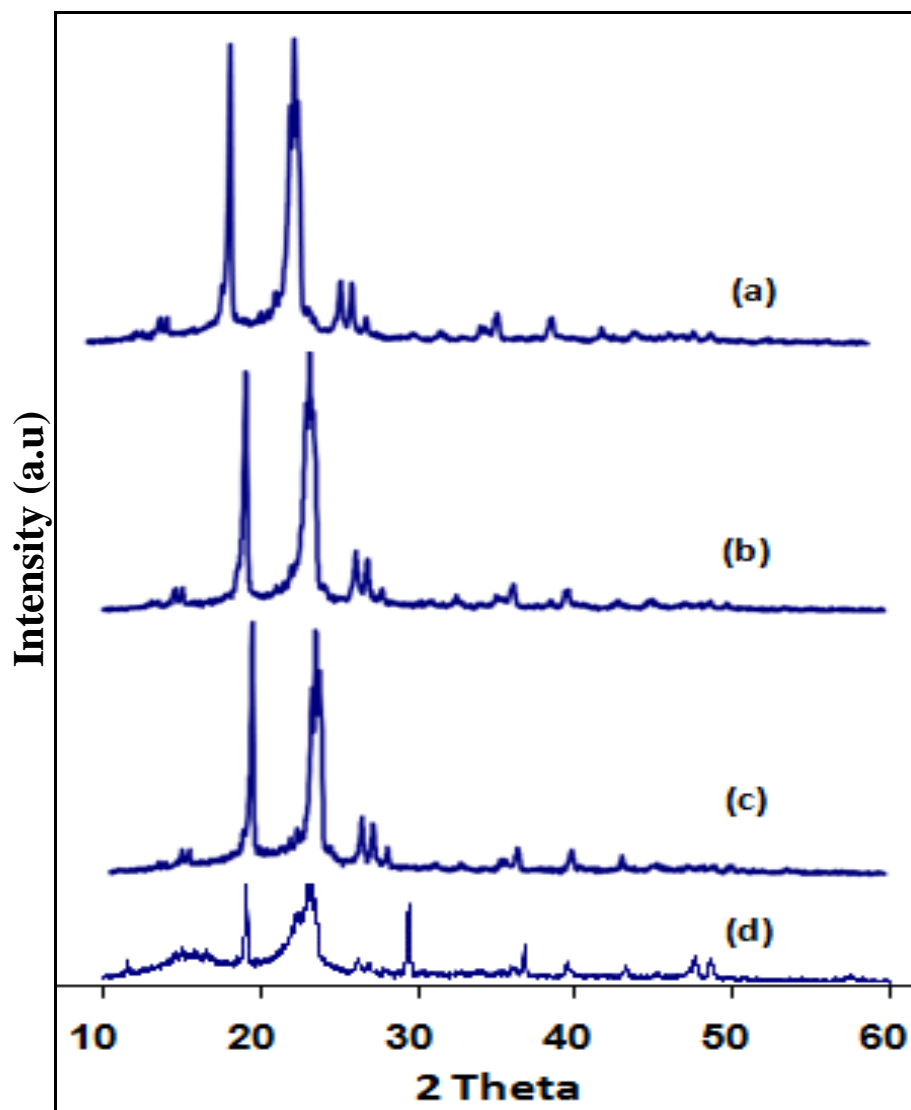
Figure 4.1: XRD patterns of polymer electrolyte at various wt% of $LiPF_6$ (a) 5; (b) 10; (c) 15; and (d) 20.

4.2 X-Ray Diffraction (XRD) Analysis of Salted Polymer Electrolytes at various wt% of EC Plasticizer

Figure 4.2 shows the XRD patterns for various concentrations of PEO-$LiPF_6$-EC complexes. Three significant peaks appeared at 2θ angle of 19.2°, 23°and 24° when 5wt% of EC was added. The peaks intensities are observed to decrease upon a continous addition of EC. In this concentration regime, it can be noticed that the intensities of the diffraction peaks at $2\theta = 19.2°$

and 23° are slightly decreased. Therefore, this angles appear to be the preferred crystallographic direction whereby an interaction of salted polymer and plasticizer takes place. However the peak at $2\theta = 27°$ reduces extremely at higher concentrations of EC. New peaks at $2\theta = 22°$ begin to appear in the diffractogram for films with 15 wt% of EC, showing the formation of a new crystalline phase. The new peaks suggest the formation of crystalline PEO-$LiPF_6$-EC complexes. The addition of EC initially leads to the formation of Li^+–EC complex, which will reduce the fraction of PEO–Li^+ complex and increase the flexibility of PEO chains. The increase in flexibility is reflected by a decrease in glass transition temperature T_g and reduced crystallinity of polymer electrolytes, as discussed in the following chapter. These observations appear to reveal that the polymer undergoes a significant structural reorganization due to the presence of the chosen salt and plasticizer.
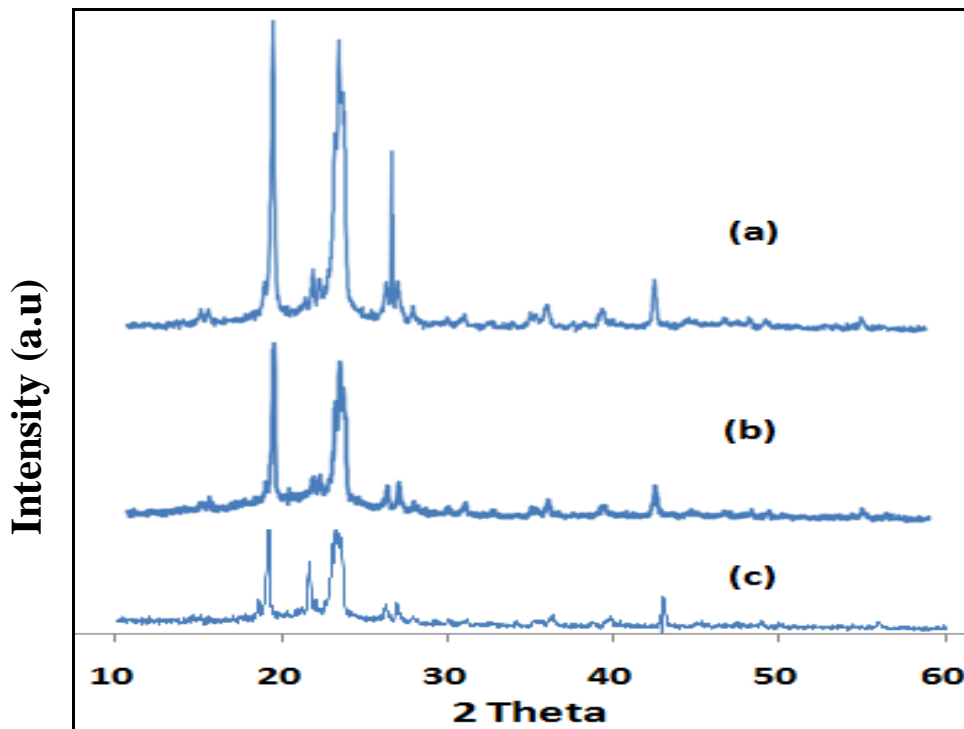
Figure 4.2: XRD patterns of salted polymer electrolytes at various wt% of EC (a) 5; (b) 10; and (c) 15.

4.3 X-Ray Diffraction (XRD) Analysis of Salted Plasticized Polymer Electrolytes at various wt% αCNTs filler

Figure 4.3 shows the XRD pattern for αCNTs, in which a very broad band is observed indicating the amorphous nature of αCNTs. Figure 4.4 shows the XRD patterns of polymer electrolytes with two different wt%., of αCNTs. Sharp and intense diffraction peaks appeared at 2θ of 19.3° and 23°, indicating the crystalline nature of complexes. The peak intensities decreased significantly with the addition of αCNTs filler. This may be due to the further increase of amorphous nature of nanocomposite polymer electrolytes. New peaks emerged at 2θ of 43° and 22°, showing the formation of a new crystalline phase (Ulanski *et al.*, 1998). The improvement in the mechanical properties has been explained on the premise that the filler particles act as a supporting matrix for the conductive polymer electrolytes to retain an overall solid structure even at higher temperatures (Raghavana *et al.*, 2008).
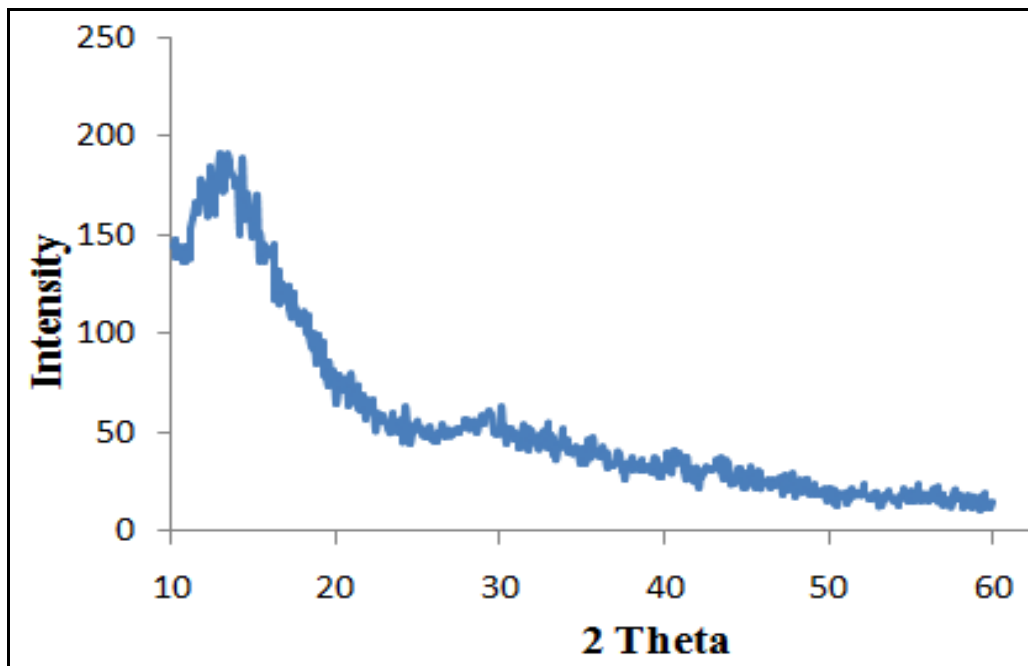
Figure 4.3: XRD pattern of αCNTs
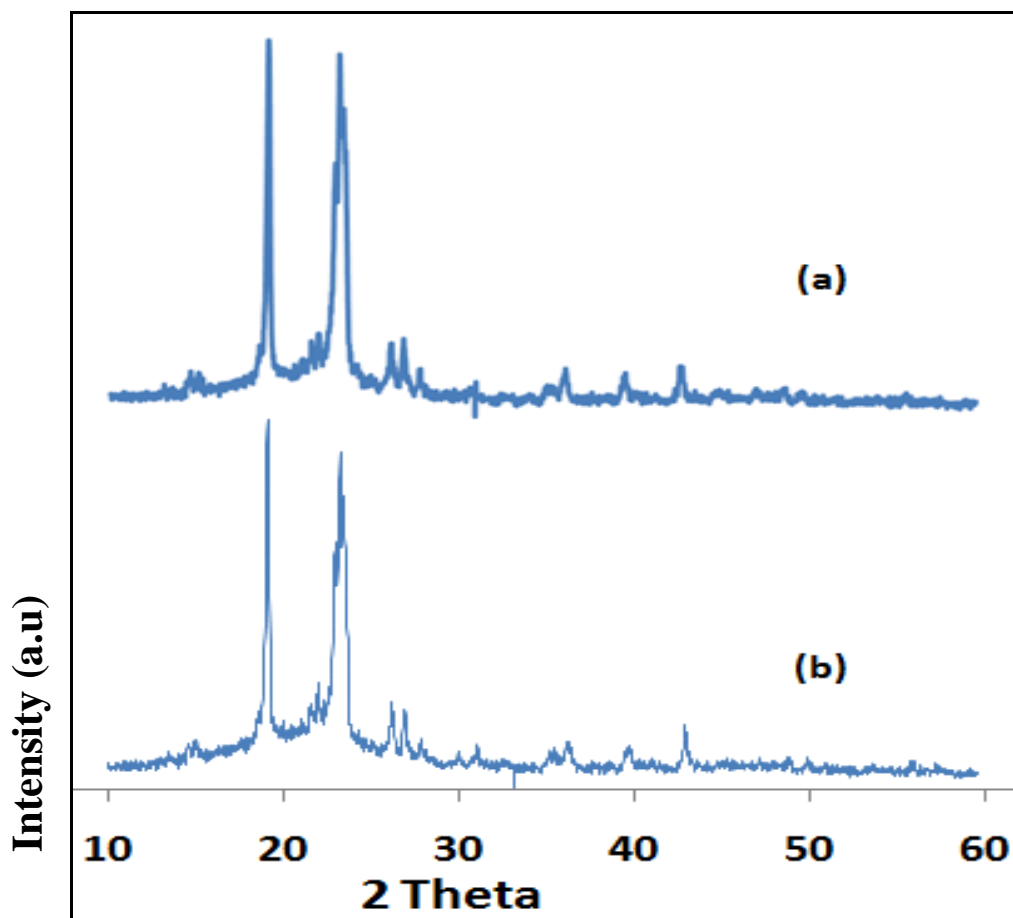
Figure 4.4: XRD patterns of salted plasticized polymer electrolytes at various wt% of αCNTs (a) 1 and (b) 5

4.4 X-Ray Diffraction (XRD) Analysis of Nanocomposite Polymer Electrolytes at optimum wt% of LiPF$_6$, EC and αCNTs

Figure 4.5 shows the XRD patterns of pure PEO and PEO doped with 20wt% of LiPF$_6$, 15wt% of EC and 5wt% of αCNTs. The optimum weight percent of LiPF$_6$, EC and αCNTs upon polymer electrolytes was defined by referring to their maximum ionic conductivity at room temperature, as discussed in Chapter Six. Sharp and intense diffraction peaks occurred at 2θ angles of 19.3° and 23°, indicating the crystalline nature of pure PEO, as shown in Figure 4.5(a)

(Ulanski *et al*, 1998). The intensities of the peak angles decreased significantly with the addition of salt, plasticizer and αCNTs. This may be due to the further increase of amorphous nature of polymer electrolytes. New peaks emerged at 2θ of 43° in the diffractogram for films $LiPF_6$ (20 wt%), showing the formation of a new crystalline phase (Ulanski *et al*, 1998). The ordering in PEO is disturbed in the presence of Li salt due to the coordination interactions between the Li^+ ion and ether O atoms (Onoda *et al*., 1989). As a result, a marked decrease in the crystallinity of polymer complex is observed compared to the pure PEO, as shown in Figure (4.5b). Further dilution of the crystalline phase can be noticed in Figure (4.5c) with the addition of the plasticizer, whereby broad and less intense peaks appeared. The small peaks at 2θ of 26° and 26.1^o slowly disappeared when plasticized polymer was added with αCNTs.
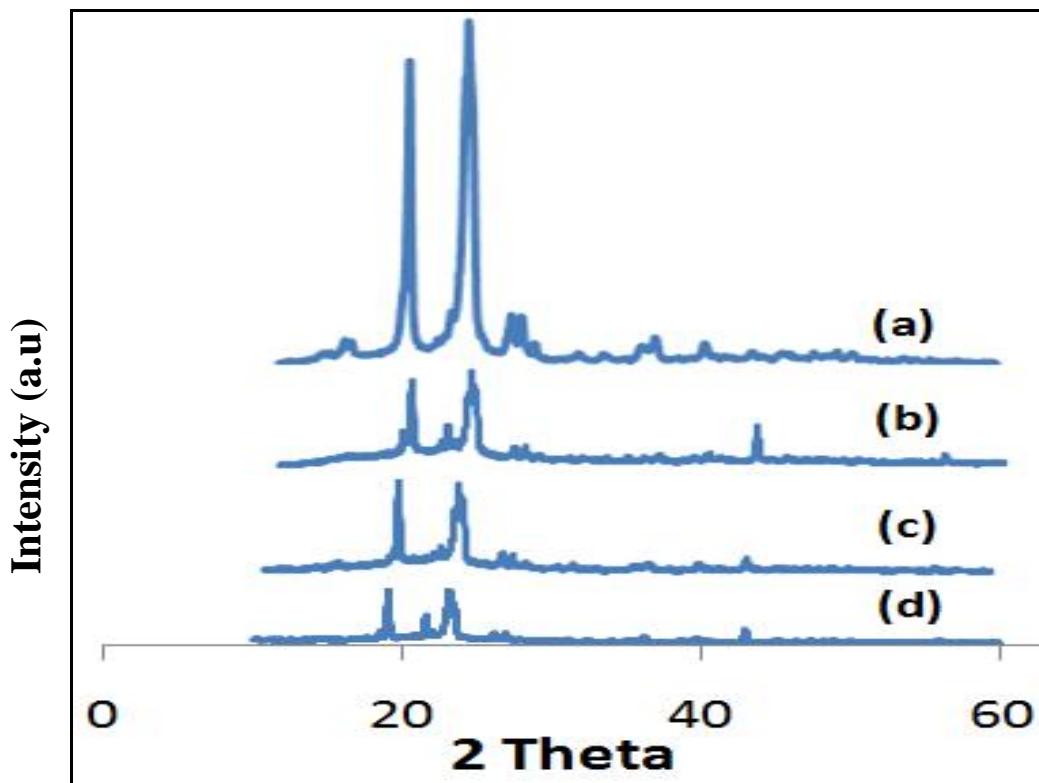
Figure 4.5: XRD patterns of (a) PEO (b) PEO-$LiPF_6$ (c) PEO-$LiPF_6$-EC (d) PEO-$LiPF_6$-EC-αCNTs.

4.5 Scanning Electron Microscopy (SEM) Analysis of Polymer Electrolytes at various wt% of LiPF$_6$ Salt

Figure 4.6 shows the morphology of polymer electrolytes at various salt concentrations. The pure PEO sample shows a spherical shape and uniformly distributed particles on the thin film surface, as shown in Figure 4.6(a) (Reddy and Peter, 2002). Two different phases were formed when LiPF$_6$ was added into the polymer matrix, namely, spheres and agglomerated particles, as shown in Figures 4.6(b-d). It can be noted that the distribution of LiPF$_6$ on thin film increases as their concentration increases. The thin film surface was dominated by LiPF$_6$ at higher concentration, as shown in Figure 4.6(e). Furthermore, the surfaces became rough, as shown in Figures 4.6(d-e). The increase in degree of roughness with increased LiPF$_6$ concentration indicates segregation of the dopant in the matrix (Reddy and Peter, 2002). This is due to the high salt categories having a salt content higher than 2-3 moles ($x \leq 20$), which are brittle with rough surfaces and are very hygroscopic (Joykumar and Bhat, 2003).
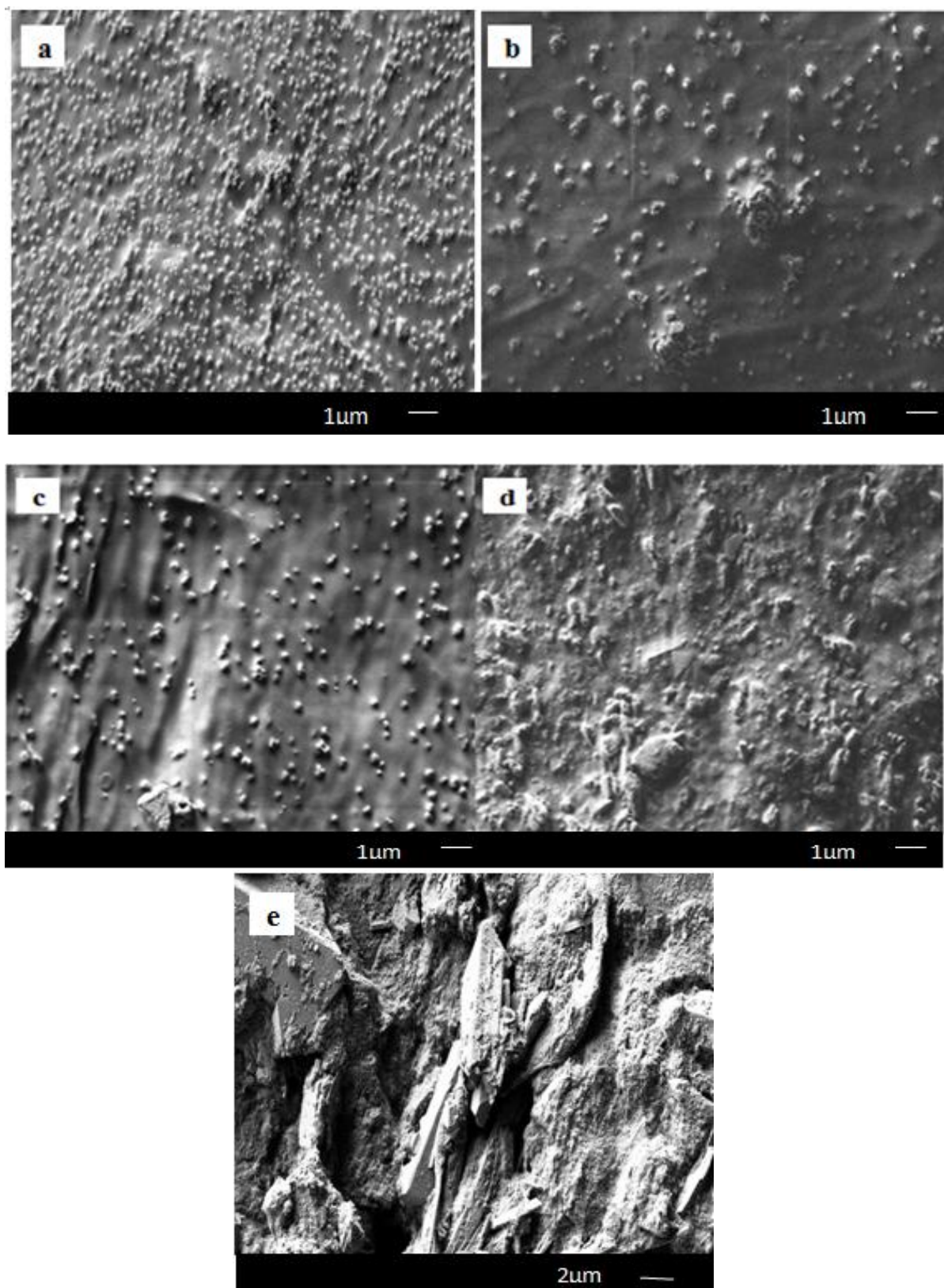
Figure 4.6: SEM micrographs of polymer electrolytes at various wt% of LiPF$_6$ (a) pure PEO (b) 5; (c) 10; (d) 15; and (e) 20 .

4.6 Scanning Electron Microscopy (SEM) Analysis of Salted Polymer Electrolytes at various wt% of EC Plasticizer

Figure 4.7 shows the micrographs of salted polymer electrolytes at various EC concentrations. After addition of EC, the morphology of complexes was changed severely. The wrinkled 'clothlike' morphology of a salted polymer with EC is observed. Several craters, which formed on the surface were due to rapid evaporation of acetonnitrile used during film preparation. Acetonnitrile evaporates slowly after casting and subsequent drying. Small pores were observed when 5wt% of EC was added into the salted polymer. The presence of small pores in the plasticizer polymer was caused by the fast evaporation of the solvent. When 10 wt% of EC was added, more larger pores appeared, indicating the uneven aggregation of $LiPF_6$ salt, PEO or even EC. It could be inferred that the 'pathway' could be formed much effectively only in the surface shown in Figure 4.7(c) so that larger free moving space for ions were available (Missan *et al*., 2006; Tran-Van *et al*, 2008; Godinez, 2008). Hence, this composite polymer electrolyte exhibits conductivity superior to others. At higher wt% of EC, phase separation takes place due to its segregation. A white fine powder is seen at 15wt% of EC. However, the plasticized films prepared by casting the acetonitrile solution containing the mixture of EC, $LiPF_6$ and PEO had an opaque appearance.
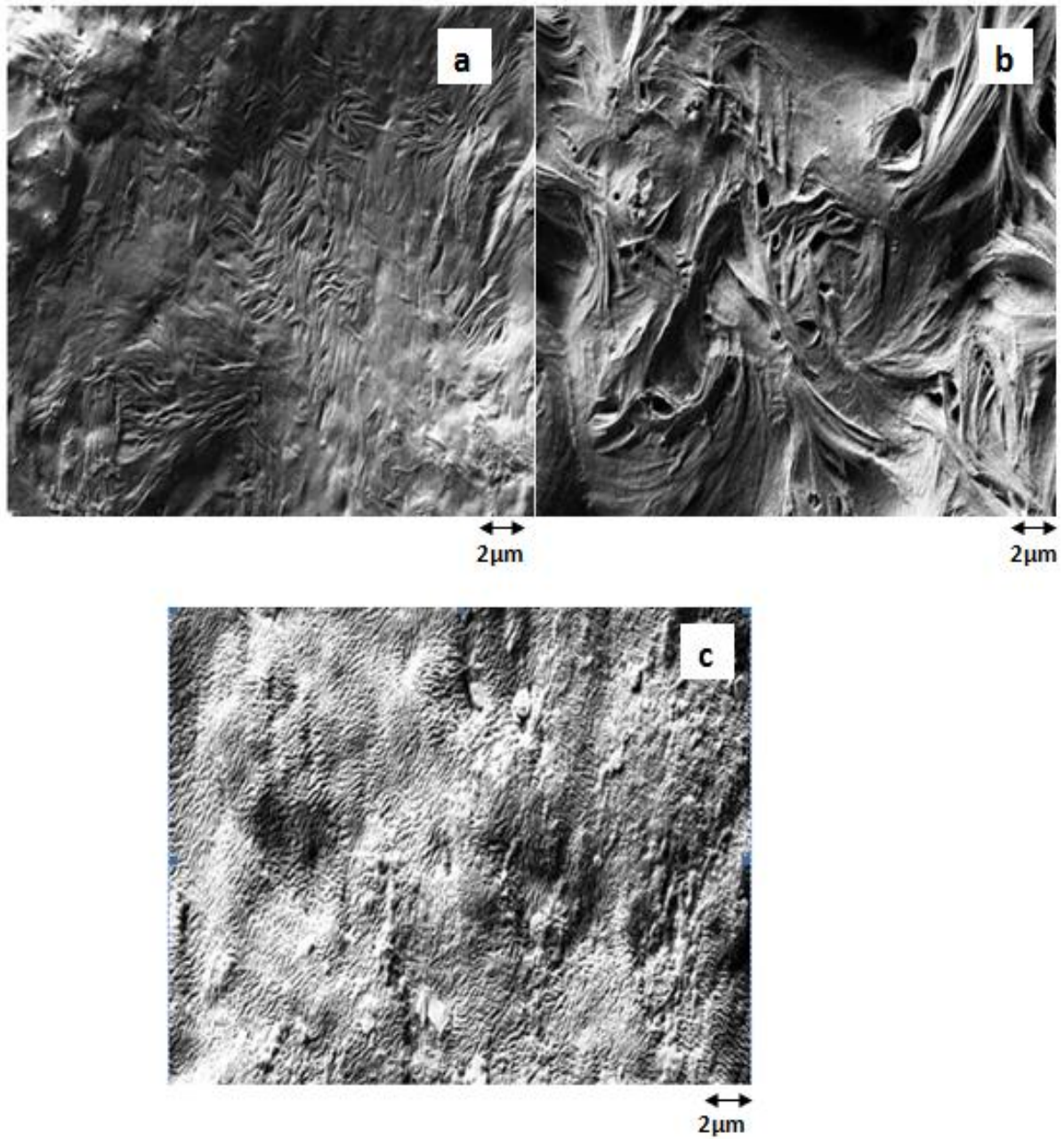
Figure 4.7: SEM micrographs of salted polymer electrolytes at various wt% of EC plasticizer (a) 5; (b) 10; and (c) 15.

4.7 Scanning Electron Microscopy (SEM) Analysis of Salted Plasticized Polymer Electrolytes at 5wt% of αCNTs Filler

Figure 4.8 represents the SEM micrograph of the amorphous carbon nanotubes (αCNTs). A mass of entangled αCNTs can be seen in this image, ranging in diameter from 70 to 100 nm, and about 6 μm in length. Figure 4.9 shows the SEM micrograph of salted plasticized polymer electrolytes with 5wt% of αCNTs. The surface became smooth (using casting technique) and it can be observed that the αCNTs is embedded within the nanocomposites polymer electrolyte as individual tubes.
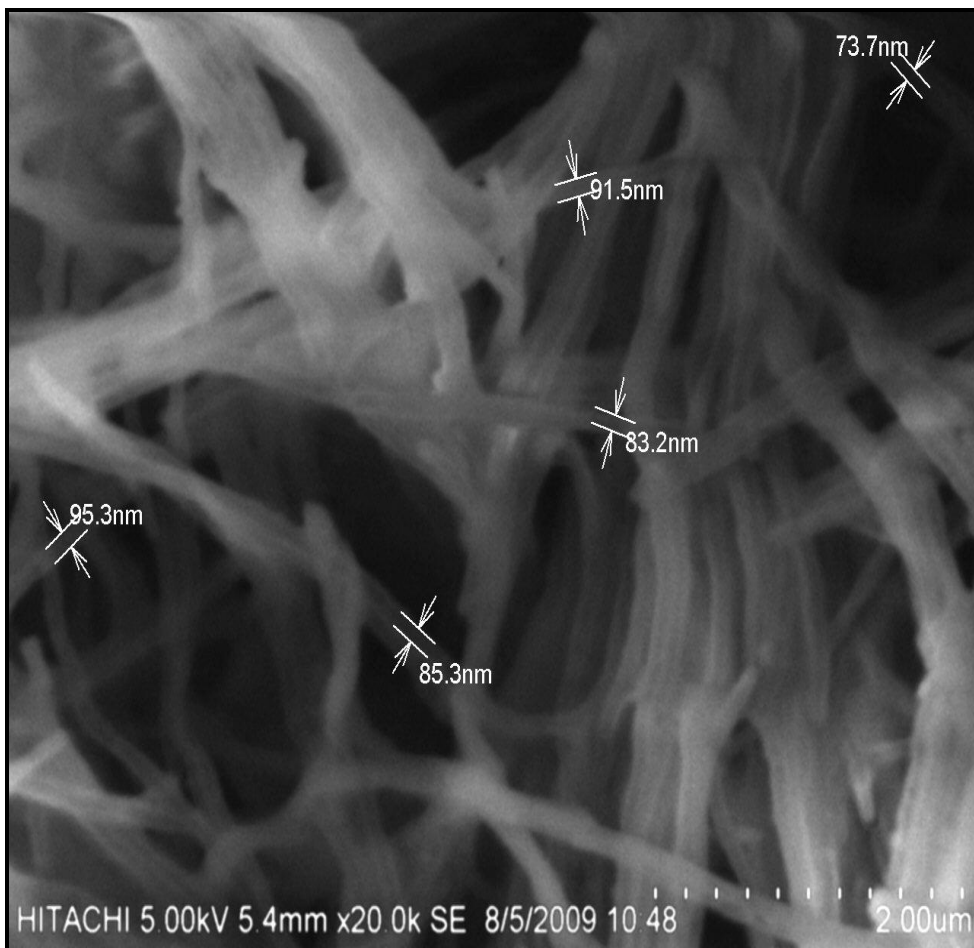
Figure 4.8 SEM micrograph of amorphous carbon nanotubes (αCNTs)
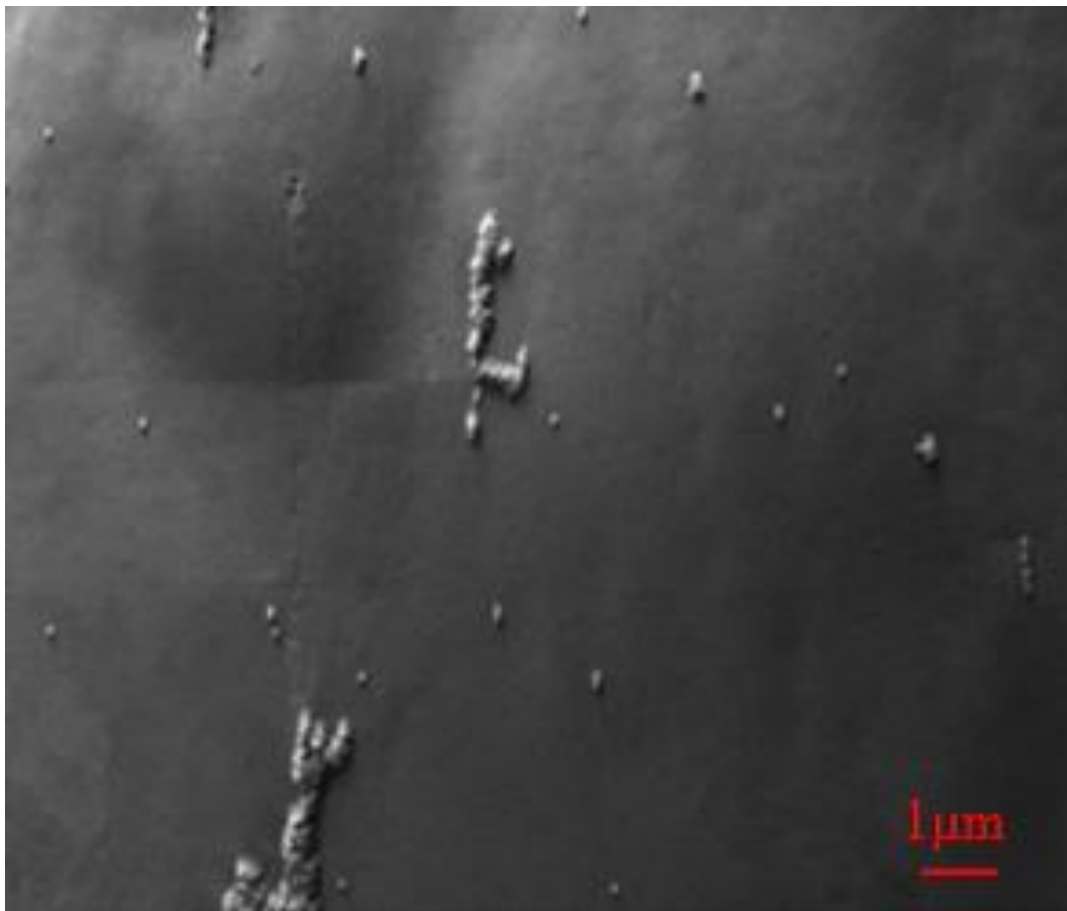
Figure 4.9 SEM image of nanocomposites polymer electrolytesfor 5wt% αCNTs.

4.8 Scanning Electron Microscopy (SEM) Analysis of Nanocomposite Polymer Electrolytes at optimum wt% of LiPF₆, EC and αCNTs

Figure 4.10 shows the SEM micrographs of nanocomposite polymer electrolytes. The image of pure PEO is shown in Figure 4.10(a), which demonstrates clear spherulite structure at room temperature (Reddy *et al*., 2002; Joykumar and Bhat, 2003). With the addition of LiPF₆ into the polymer matrix, Li salt is well dissociated and affects the weak complexation of PEO, which leads to the disruption of continuous crystalline, and results in smaller lamellae dimension, as

shown in Figure 4.10(b) (Reddy *et al*., 2002). The observed pores with optimum EC content is obtained for plasticized polymer electrolyte, as shown in Figure 4.10(c). The same phenomenan was observed by Song et al. (2003) for PVdF-HFP-EC films with high EC content. Upon addition of αCNTs, the surface became smooth (using casting technique). It can be observed that the αCNTs is embedded within the nanocomposite polymer electrolyte as individual tubes, as shown in Figure 4.10(d).
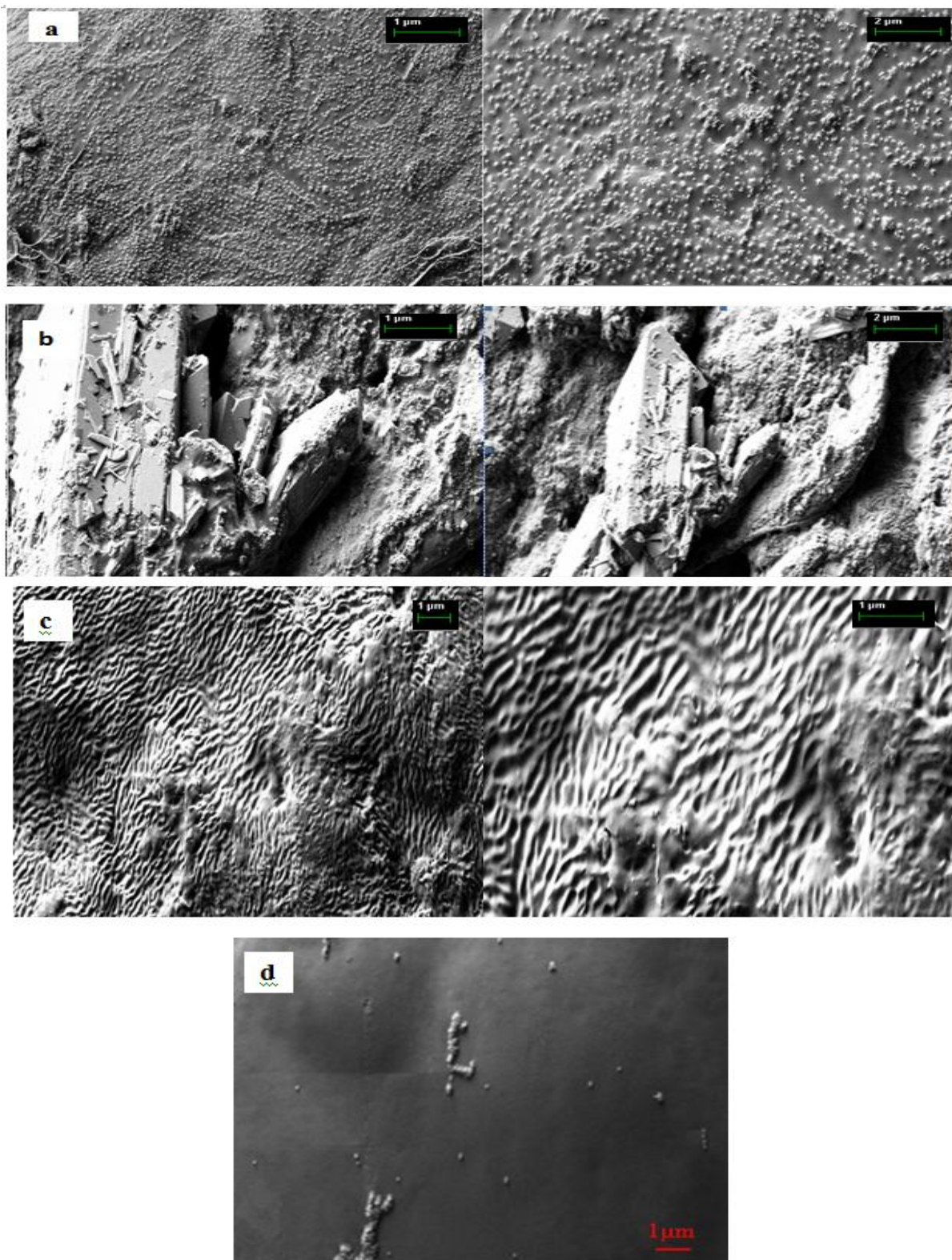
Figure 4.10 SEM micrographs of (a) PEO (b) PEO-20 wt% LiPF$_6$ (c) PEO-20 wt% LiPF$_6$- 15 wt% EC and (d) PEO-20 wt% LiPF$_6$-15 wt% EC-5 wt% αCNTs.

CHAPTER FIVE

Thermal and FTIR Studies of Nanocomposite Solid Polymer Electrolytes

5.1 Differential Scanning Calorimetry (DSC) Analysis of Polymer Electrolytes at various wt% of LiPF$_6$

Figure 5.1 shows the DSC curves of polymer electrolytes at various weight percent of LiPF$_6$. The sharp endothermic peak observed at 69°C corresponds to the crystalline melting temperature (T_m) of pure PEO (Figure 5.1(a)). The endothermic peak for pure PEO shows a the transition from 69 to 67°C upon the addition of 5wt% of salt. The T_m value continues to decrease as more wt% of salt is added. This observation shows the reduction in T_m value by the addition of salt. The endothermic curves also indicate a reduction in PEO crystallinity. The relative percentage of crystallinity X_c of PEO has been calculated using Equation (5.1).

$$X_c = \frac{\Delta H_m}{\Delta H_m^o} x100\% \tag{5.1}$$

where ΔH_m is the melting enthalpy estimated experimentally and ΔH_m^o used as referenced is the melting enthalpy for 100% crystalline PEO (213.7 Jg^{-1}) used as reference(Ali *et al.*, 2008). The calculated values of X_c are summarized in Table 5.1. The crystallinity degree of the electrolyte decreases with the wt% of the salt, which causes an increase in the amorphous phase. The polymeric chain in the amorphous phase is more flexible, which results in the enhancement of segmental motion of the polymer. The reduction of T_m and X_c suggests that the interaction

between the polymer host backbone and $LiPF_6$ affects the main chain dynamics of the polymer. This is due to the coordination bonds between ether units of PEO and Li^+ ions where Li^+ and PF_6^- ions interrupt the packing of PEO molecules and decrease the degree of crystallinity. This will promote the amorphous phase which is expected to favour ion transport, thus enhancing the electrolytes' conductivity. The glass transition temperature (T_g) involves the freezing of large-scale molecular motion without a change in structure at which a glassy phase of the sample becomes a rubbery amorphous phase on heating. T_g of a polymer concerns with the mobility of the polymer chain. Lower T_g usually leads to easier chain relaxation, In PEO-based polymeric electrolytes, lithium ion conduction is promoted by such segmental motion in the amorphous phase. This shows that T_g is lowered when $LiPF_6$ is added which suggests that the segmental mobility of PEO in this region increases upon the addition of $LiPF_6$. An electrolyte with low T_g always implies fast ion conduction.

Table 5.1 Thermal properties of salted polymer electrolytes

Sample	T_g (°C)	T_m (°C)	ΔH_m (Wg⁻¹)	X_c (%)
Pure PEO	-66	68.8	181.37	84.87
PEO-5wt% $LiPF_6$	-68	67.4	144.93	67.82
PEO-10wt% $LiPF_6$	-68	65.1	124.94	58.46
PEO-15wt% $LiPF_6$	-70	64.4	117.59	55.03
PEO-20wt% $LiPF_6$	-72	63.5	101.56	47.52
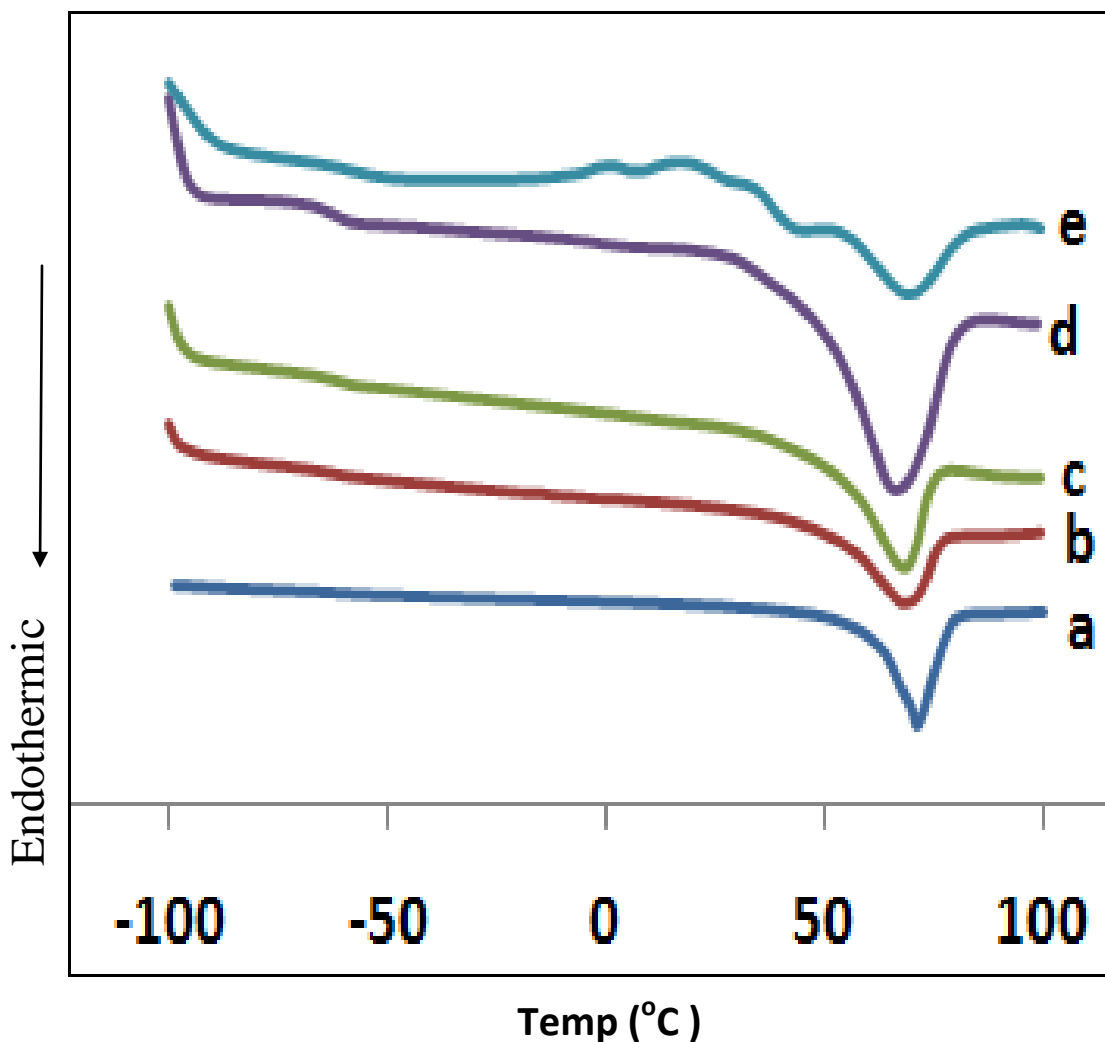
Figure 5.1 DSC curves of polymer electrolyte at various wt% of LiPF$_6$ (a) 0 ; (b) 5 ; (c) 10 ; (d) 15 ; (e) 20.

5.2 DSC Analysis of Salted Polymer Electrolytes at various wt% of EC Plasticizer

Figure 5.2 shows the DSC curves of PEO:LiPF$_6$ with various wt% of EC over the temperature range of -100 to 100 ^{o}C. In the case of PEO-LiPF$_6$-EC mixture, the sizes of crystallinity peaks are smaller and T_m and T_g are lower than pure PEO. As the ratio of EC increases in the mixture, the relative crystallinity, X_c, T_m and T_g tend to decrease. These results seem to be caused by the

addition of EC, which increases the interfacial area by phase separation, which results in the fall of crystallinity. The results obtained from the reheating cycle are summarized in Table 5.2. The presence of EC favours the entropy configuration of the polymer to provide more free volume, in which the ions move easily in the bulk through the plasticizer rich phase (Agnohotry *et al*., 1999).

It is evident from Table 5.2 that there is a marked decrease in T_g, T_m and X_c during heating as a result of EC addition. The high conductivity of the samples is due to the increase of amorphous phase in the polymer with the presence of the plasticizer. It can be inferred that the amorphous phase of the polymer electrolytes facilitates fast Li-ion motion in the polymer network, which further provides a larger free volume upon temperature increase (Yahya and Arof, 2002). Since lithium-ion conduction in PEO-based polymer electrolytes mainly takes place in the amorphous phase, low crystallinity should be favourable for ion conduction at low temperatures.
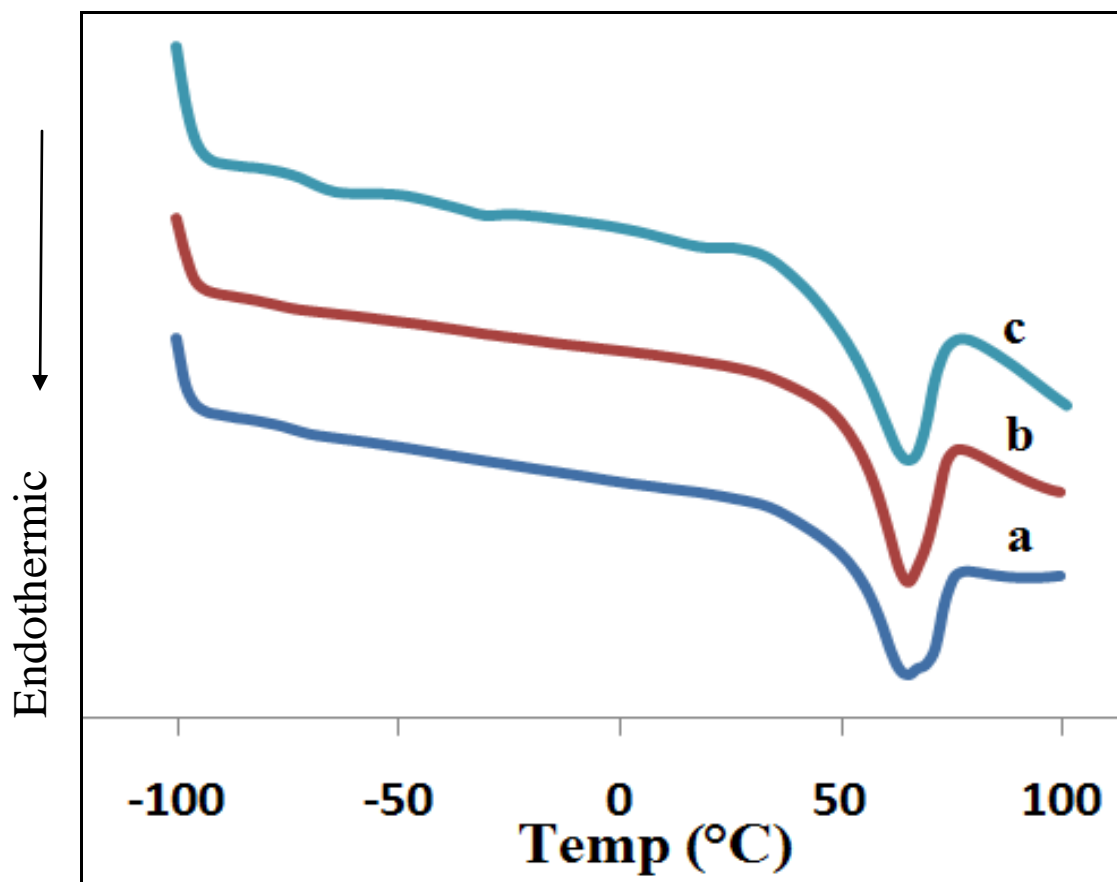
Figure 5.2 DSC curves of salted polymer electrolytes at various wt% of EC (a) 5 ; (b) 10 ; (c) 15.

Table 5.2 Thermal properties of plasticized polymer electrolytes

Sample	T_g (°C)	T_m (°C)	ΔH_m (Wg^{-1})	X_c (%)
PEO-20wt% LiPF$_6$-5wt% EC	-72	63.2	127.08	59.47
PEO-20wt% LiPF$_6$-10wt% EC	-74	63.1	109.55	51.27
PEO-20wt% LiPF$_6$-15wt% EC	-76	62.9	101.19	47.35

5.3 DSC Analysis of Salted Plasticized Polymer Electrolytes at various wt.% of αCNTs Filler

Figure 5.3 shows the DSC curves of PEO:LiPF$_6$:EC with various wt% of αCNTs over the temperature range of -100 to $100\ ^oC$. The results obtained are summarized in Table 5.3. The sharp endothermic peak corresponds to the crystalline melting temperature (T_m) and shows a slight transition from 62 to 61 °C upon the addition of 5wt% of αCNTs. The endothermic peak also indicates a reduction in PEO crystallinity. The relative percentage of crystallinity (X_c) for the electrolyte decreases with wt% of the αCNTs, which causes an increase in the amorphous phase. The polymeric chain in the amorphous phase is more flexible, which results in the enhancement of segmental motion of the polymer. The position of T_g for PEO-LiPF$_6$-EC filled with different wt% of αCNT is slightly shifted towards lower temperature. This suggests that the segmental mobility of PEO-LiPF$_6$-EC in this region increases upon the addition of αCNTs and that the segment becomes less rigid. The filler effect such as nanosized αCNTs, interacts with the PEO polymer matrix to suppress the crystallization of PEO, leading to an increase in ionic conductivity, especially at temperature lower than its melting point (Appeteechi *et al*., 2001). A similar behaviour was also observed in the PEO polymer electrolyte containing fillers such as SiO$_2$ and TiO$_2$ (Appeteechi *et al*., 2001; Shu *et al*., 2008). A contribution to the conductivity enhancement comes from the structural modifications associated with the polymer host caused by the filler especially at temperatures below T_g and T_m should possibly be due to this effect. The samples clearly point towards the existence of a second conductivity enhancement mechanism, other than that involving the polymer host directly (Appeteechi *et al*., 2001). This conductivity enhancement at temperatures above as well as below T_g and T_m, should therefore be caused by a different mechanism directly associated with the surface groups in the filler (Shu *et al*., 2008).
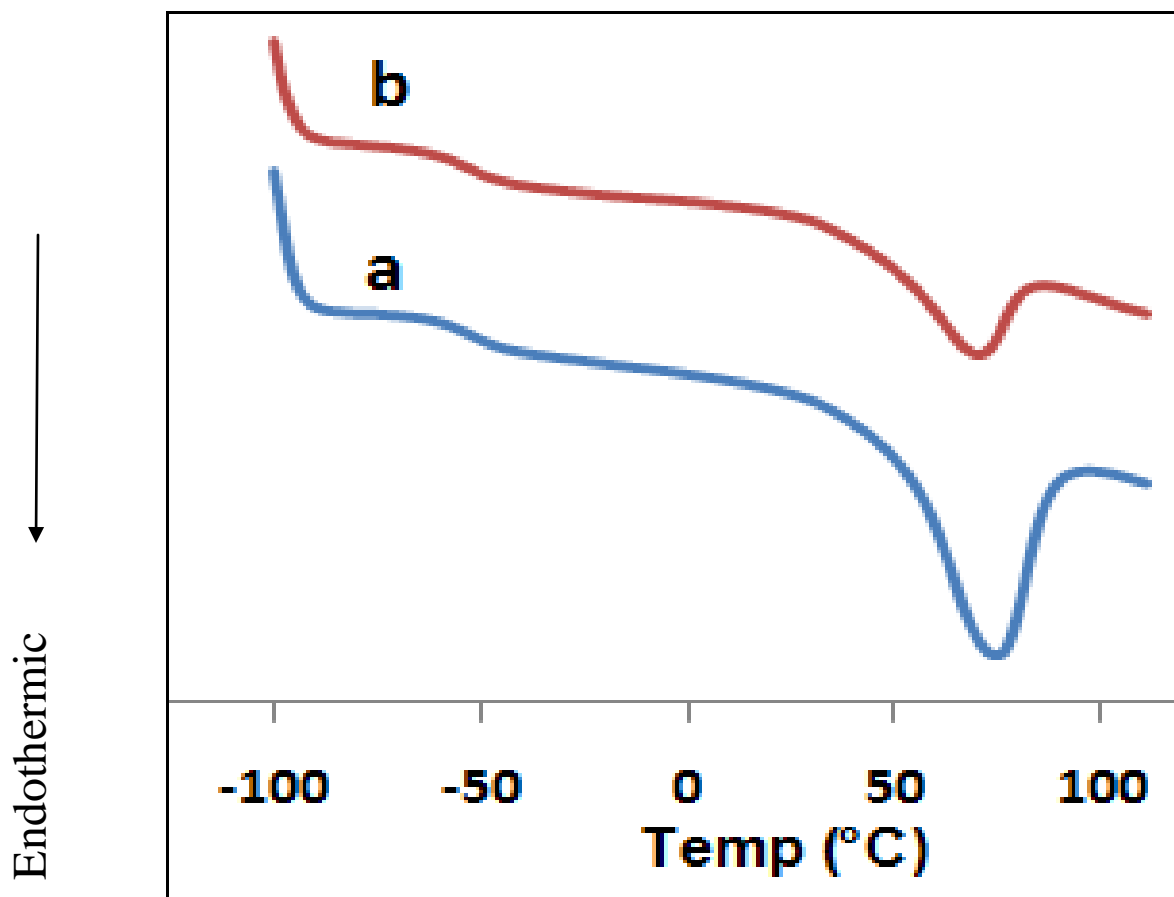
Figure 5.3 DSC curves of polymer electrolytes at various wt% of αCNTs (a) 1 and (b) 5.

Table 5.3 Thermal characteristics of nanocomposite polymer electrolytes

Sample	T_g (°C)	T_m (°C)	ΔH_m (Wg^{-1})	X_c (%)
PEO-20wt% LiPF$_6$-15wt% EC -1wt% αCNT	-78	62	98.75	46.21
PEO-20wt% LiPF$_6$-15wt% EC -5wt% αCNT	-80	61	57.95	27.12

5.4 DSC Analysis of Nanocomposite Polymer Electrolytes at optimum wt% of LiPF₆, EC and αCNTs

Figure 5.4 shows the DSC curves for various polymer electrolytes with optimum wt% of LiPF$_6$, EC and αCNTs over the temperature range of -100 to 100^oC. The results obtained are summarized in Table 5.4. All polymer electrolytes exhibit endothermic peaks between 50 and $70\ ^oC$, which suggest the presence of a crystallization phase, based on the melting point for PEO (60 – 75 ^oC). The curves show that the addition of salt, plasticizer and filler will influence the relative degree of crystallinity (X_c), the glass transition temperature (T_g) and melting temperature (T_m) of polymer electrolytes. A sharp endothermic peak is observed near 65 ^oC during the heating process for the melting of pure PEO, as shown in Figure 5.4(a). The addition of $LiPF_6$ salt causes a change in the shape of the endothermic peak, and the peak shifts towards lower temperature. This also indicates the complexation process between $LiPF_6$ and PEO. The T_g and T_m continues to decrease with the addition of plasticizer (EC). The addition of filler (αCNTs) causes peak broadening. The peak slightly shifted toward lower temperature. These observations clearly suggest that a major contribution of conductivity enhancement comes from structural modifications associated with the polymer host caused by the salt, plasticizer and filler (Taner *et al*., 2005). The reorganization of polymer chain may be hindered by the cross-linking centres formed by the interaction of Lewis acid groups of filler with the polar groups of polymer (Change *et al*., 2002). Consequently, the degree of crystallization of the polymer matrix decreases with the addition of filler (Change *et al*., 2002).

It is evident that there is a marked decrease in T_g, T_m and X_c during heating upon the addition of salt, plasticizer and filler. Therefore, a significant contribution to the observed conductivity enhancement in the salt, plasticized and filler-added electrolyte, PEO + 20 wt% LiPF$_6$+15 wt% EC+5 wt% αCNTs, having the lowest T_g and T_m values, evidently comes from the increased segmental flexibility and the increased amorphous nature of the host polymer caused by the salt, plasticizer and the filler (Taner *et al.*, 2005). Since lithium-ion conduction in PEO-based polymer electrolytes mainly takes place in amorphous phase, low crystallinity should be favourable for ion conduction at low temperatures.
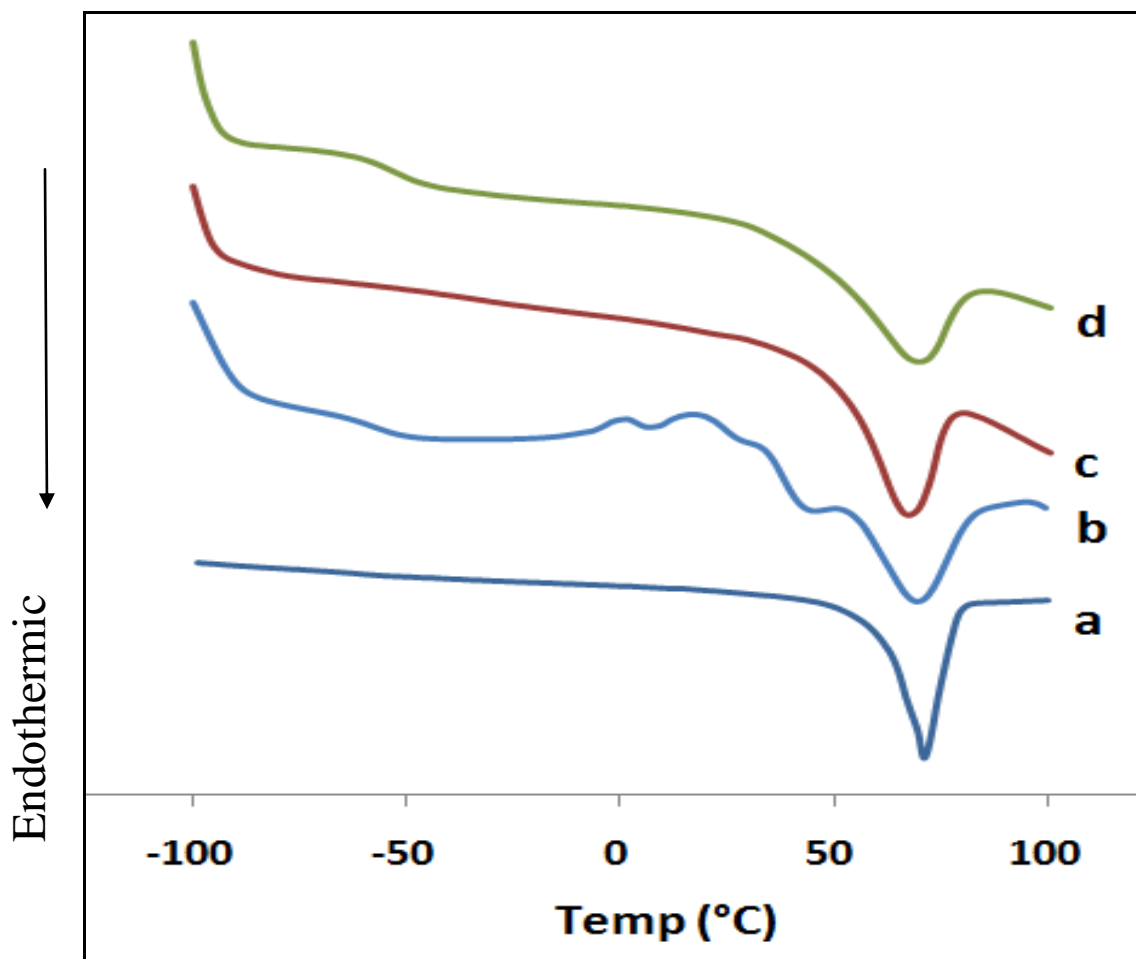

Figure 5.4 DSC curves of (a) PEO (b) PEO-20 wt% LiPF$_6$ (c) PEO-20 wt% LiPF$_6$-15 wt% EC (d) PEO-20 wt% LiPF$_6$-15 wt% EC-5 wt% αCNTs.

Table 5.4 Thermal characteristics of nanocomposite polymer electrolytes

Sample	T_g (°C)	T_m (°C)	ΔH_m (Wg^{-1})	X_c (%)
Pure PEO	-66	69	181.37	84.87
PEO-20wt% LiPF$_6$	-72	64	101.56	47.52
PEO-20wt% LiPF$_6$-15wt% EC	-76	63	101.19	47.35
PEO-20wt% LiPF$_6$-15wt% EC -5wt% αCNT	-80	61	57.95	27.12

5.5 Thermogravimetric (TGA) Analysis of Polymer Electrolytes of various wt% of LiPF$_6$ Salt

Figure 5.5 shows the TGA and DTG curves of the polymer electrolytes with various wt% of LiPF$_6$. The TGA and DTG curves of the PEO-salt films reveal two main weight loss regions, which appear as two peaks in the DTG curves. The first region at a temperature of 40-100°C is due to the evaporation of physically weak and chemically strong H$_2$O bonding. The second transition region of around 230-280°C is due to decomposition of PEO-salt membrane. It can be clearly seen that all samples exhibit minimal weight loss until the samples reached 200 °C, at which an endothermic peak appears. This indicates that the PEO-LiPF$_6$ is stable up to 200 °C before decomposition. At 200°C, the LiPF$_6$ starts to melt and the system is no longer stable. The results of weight-loss ratios for all samples accelerating between 200 and 400 °C are summarized in Table 5.5.
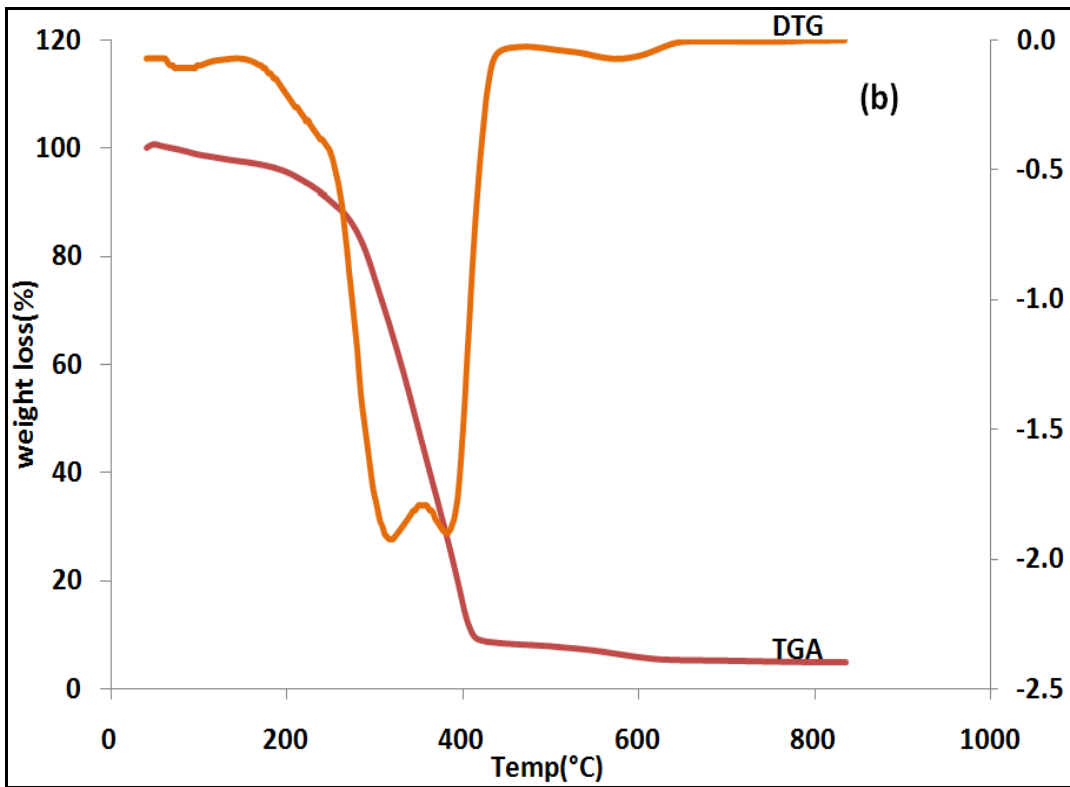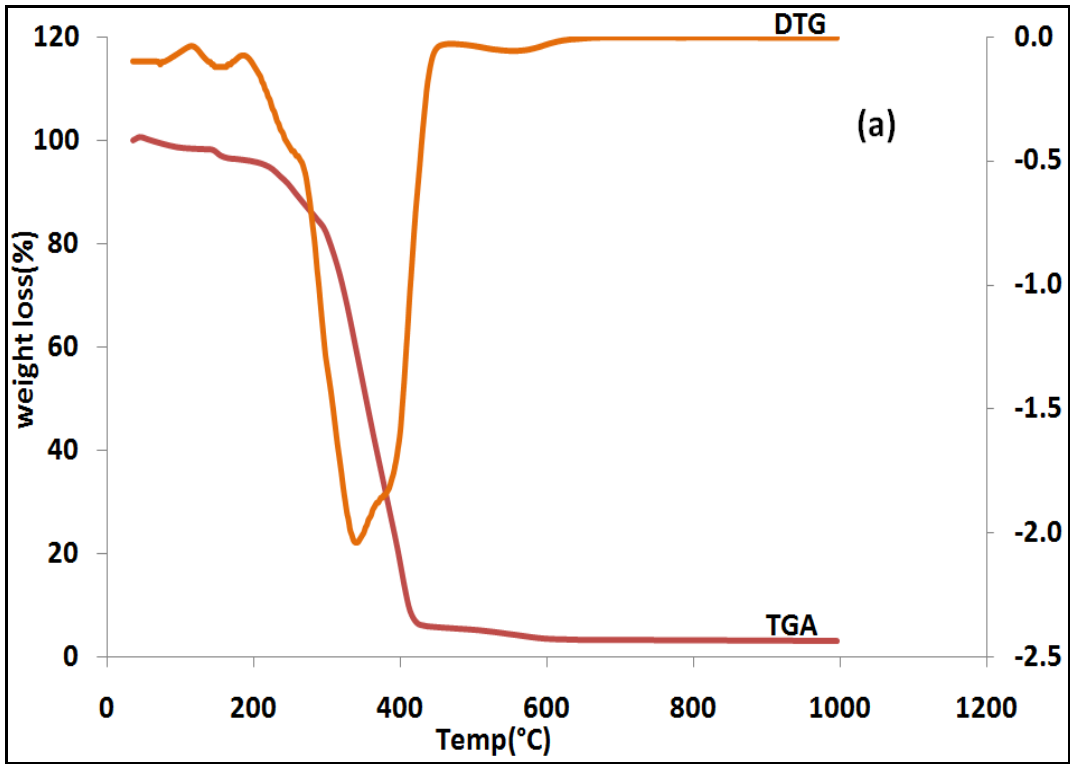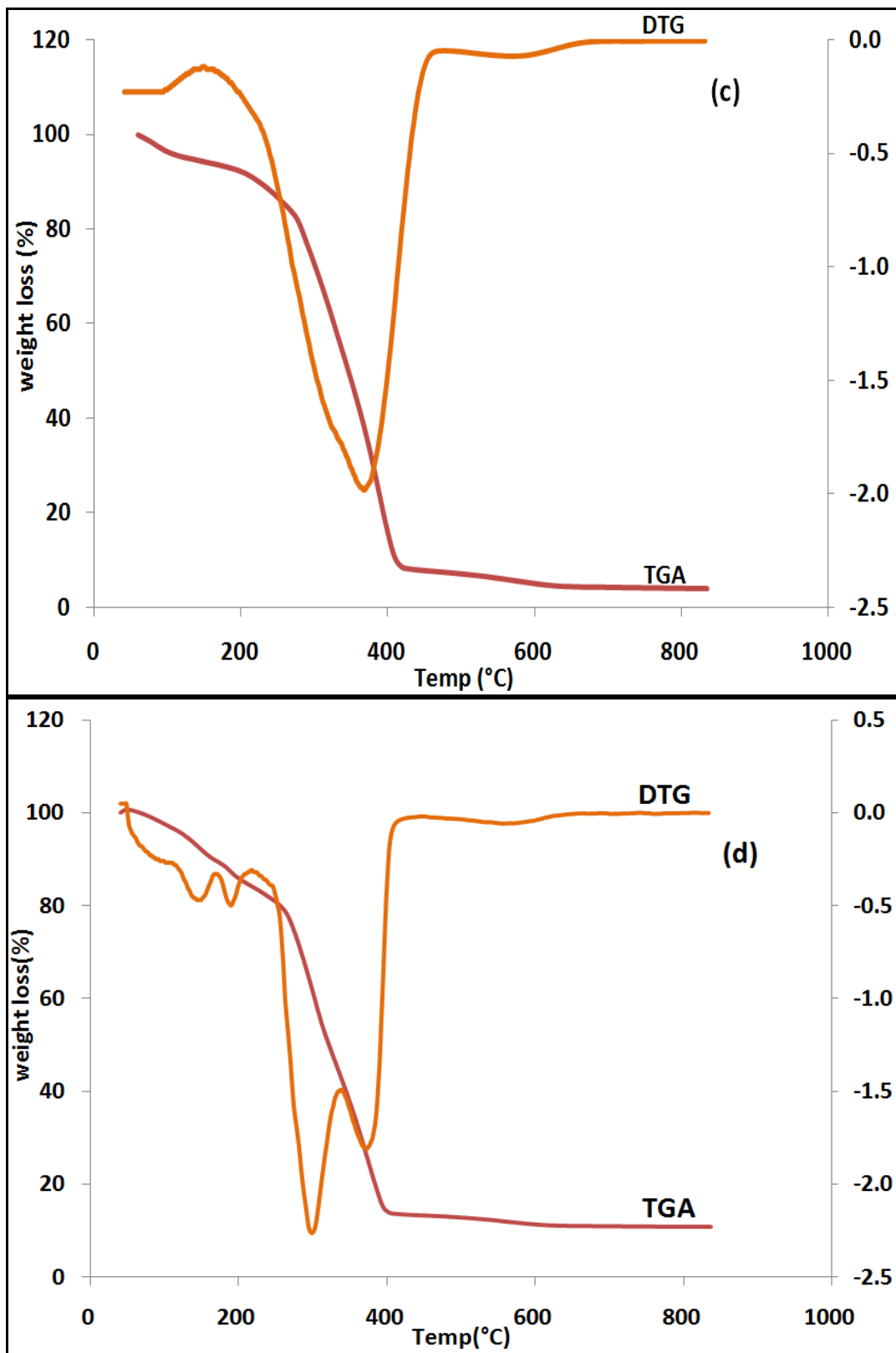
Figure 5.5 TG-DTG curves of polymer electrolytes at various wt% of LiPF$_6$ (a) 5; (b) 10; (c) 15; (d) 20.

Table 5.5 Initial and decomposition temperatures and percentage of total weight loss for various PEO-LiPF$_6$ samples

Sample	Initial Weight Loss Temperature (°C)	Weight Loss (%)	Decomposition Temperature (°C)	Weight Loss (%)	Total Weight Loss (%)
PEO+5wt% salt	48	8	230	88.45	96.45
PEO+10wt% salt	70	9	250	84.84	93.84
PEO+15wt% salt	80	8	230	87.00	95.00
PEO+20wt% salt	85	20	280	68.00	88.00

5.6 Thermogravimetric (TGA) Analysis of Salted Polymer Electrolytes at various wt% EC Plasticizer

Figure 5.6 shows the TGA and DTG curves of the polymer electrolytes with different wt% of EC. The DTG curves display two main inflection regions. The first region at lower temperatures (<100°C) originates from the loss of absorption water and solvent whereas the region at higher temperature (200°C) is associated with the decomposition of PEO. As seen from DTG curves, the maximum temperatures of weight loss (T_m) of polymer electrolytes are 355, 396 and 376°C, respectively. It can be clearly seen that all samples exhibit minimal weight loss until the samples reached 100 °C, at which an endothermic peak appears. The results of weight-loss ratios for all samples accelerating between 100 and 400 °C are summarized in Table 5.6. From the table, it can be stated that an increase in the amount of plasticized content in the samples promotes a slight increase in weight loss.
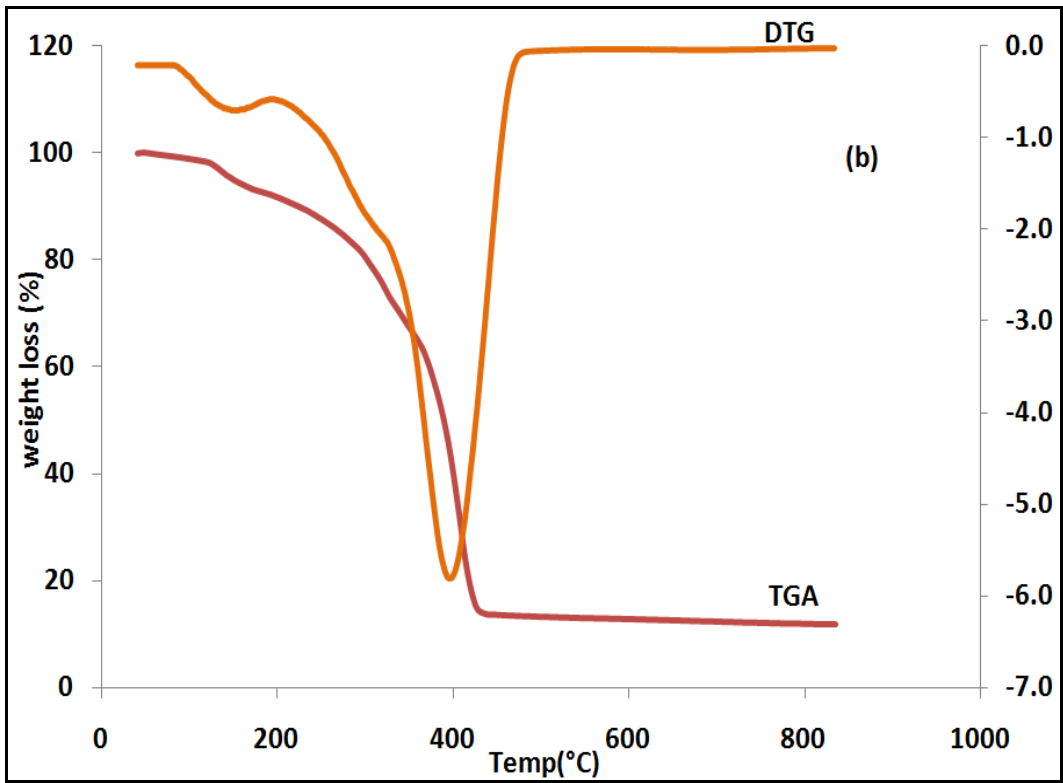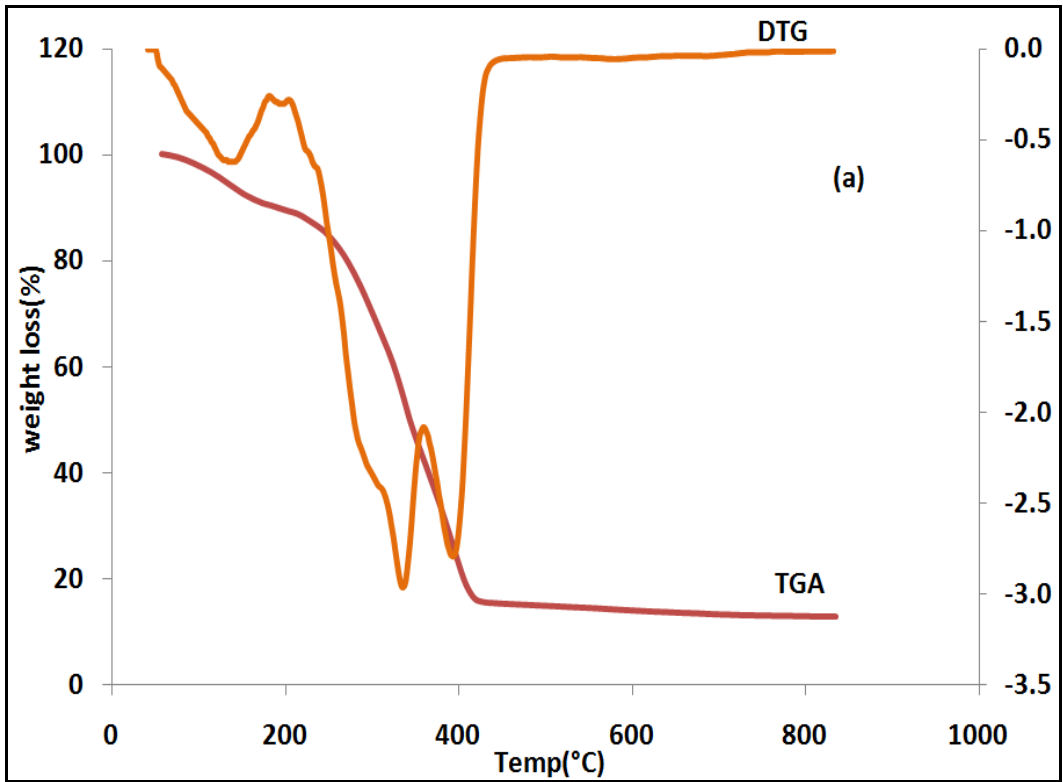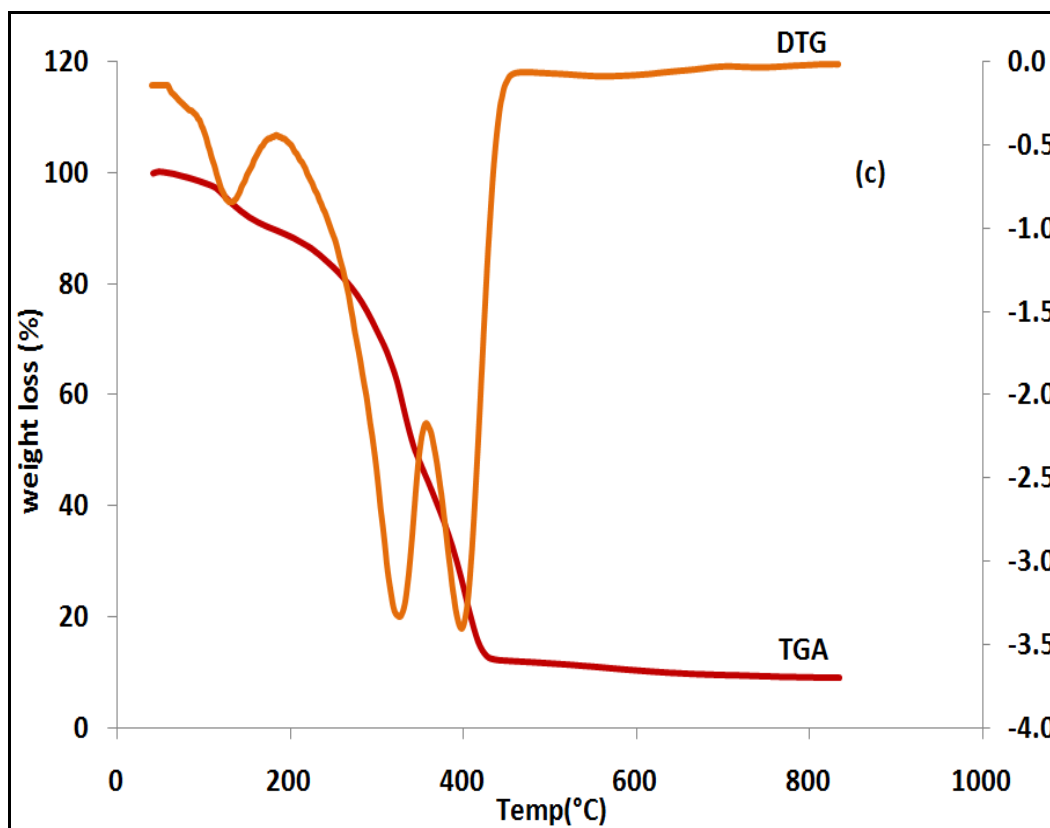
Figure 5.6 TG-DTG curves of salted polymer electrolytes at various wt% of EC (a) 5; (b) 10; (c) 15.

Table 5.6 Initial and decomposition temperatures and percentage of total weight loss for various PEO-LiPF$_6$-EC samples

Sample	Initial Weight Loss Temperature (°C)	Weight Loss (%)	Decomposition Temperature (°C)	Weight Loss (%)	Total Weight Loss (%)
PEO+20wt% salt+5w% EC	82	8	200	80.46	88.46
PEO+20wt% salt+10wt% EC	90	10	205	80.00	90.00
PEO+20wt% salt+15wt% EC	91	9	210	81.00	90.00

5.7 Thermogravimetric (TGA) Analysis of Salted Plasticized Polymer Electrolytes at various wt% of αCNTs Filler

Figure 5.7 shows the TGA and DTG curves of polymer electrolytes with different wt% of αCNTs. The results of weight-loss ratios for all samples accelerating between 100 and 400 °C are summarized in Table 5.7. It can be seen from Figure 5.7 that the percentage weight loss for 1wt.% αCNTs is 90% and increases to 93% when 5wt% αCNTs is added into the PEO system. As the doping of αCNT nanoparticle increases, the total weight loss ratio increases, which proves that αCNT nanoparticles reduce the thermal stability of nanocomposite polymer electrolytes. Nevertheless, after subtraction of the filler mass, the thermal degradation behaviour of polymer electrolytes is only slightly affected by the αCNT content.
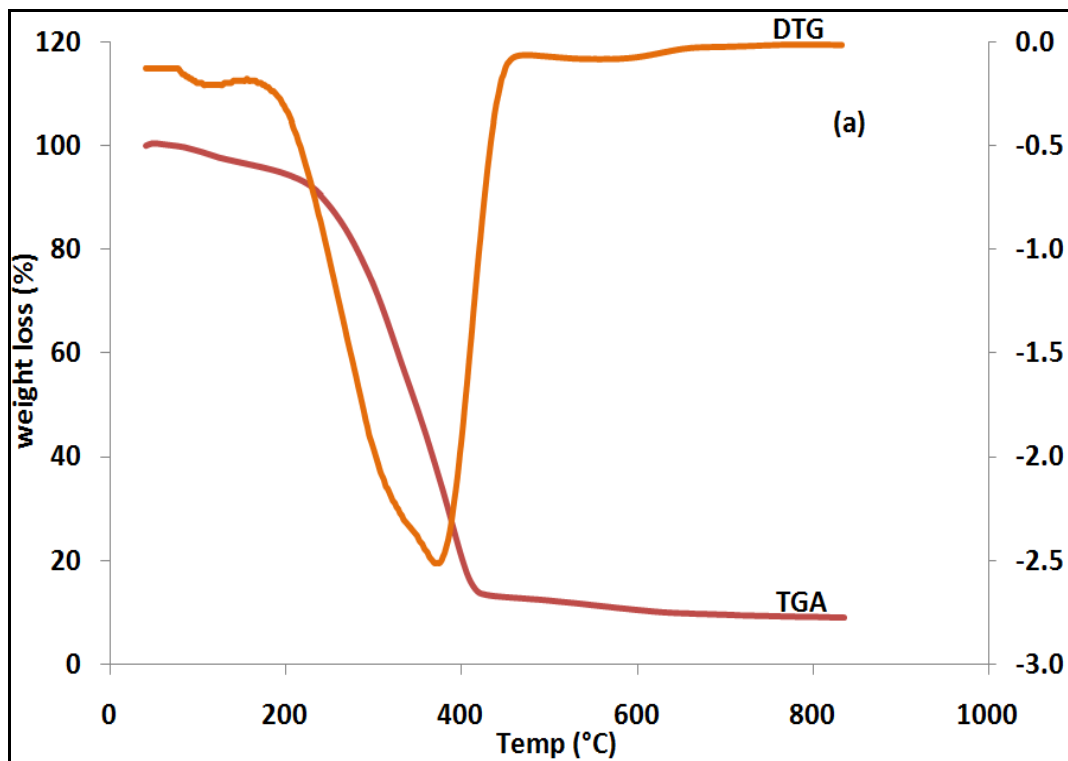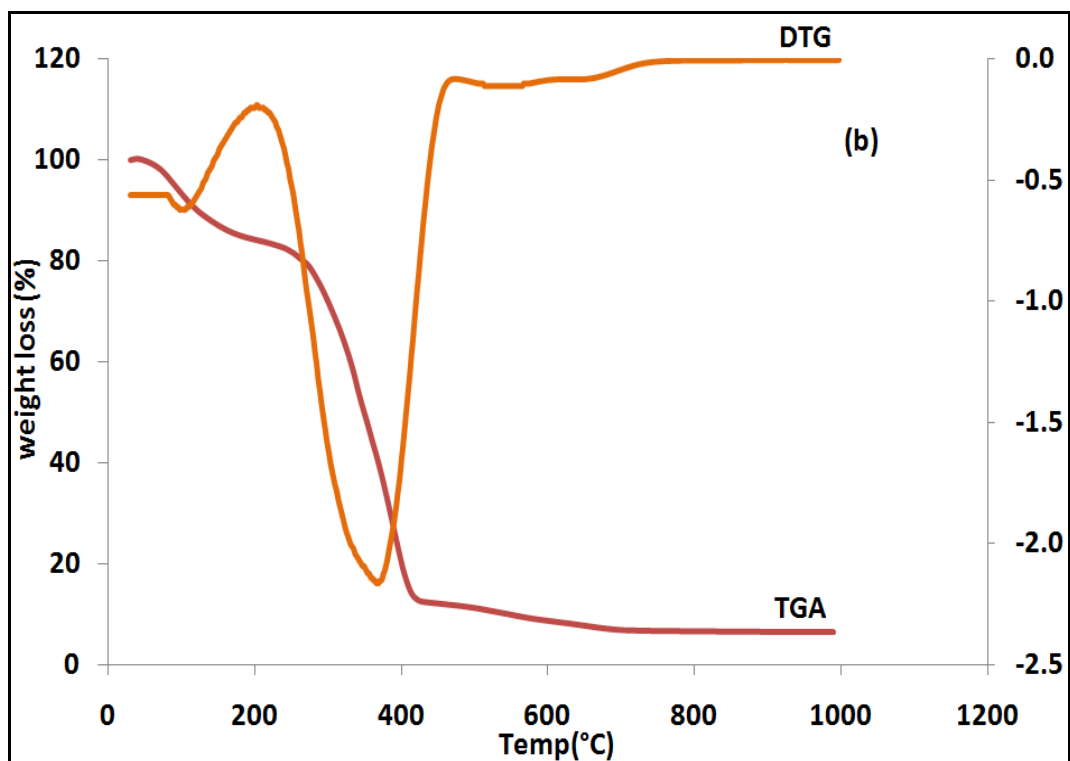
Figure 5.7 TG-DTG curves of polymer electrolytes at various wt% αCNTs (a) 1; (b) 5.

Table 5.7 Initial decomposition temperatures and percentage of total weight loss for various nanocomposite polymer electrolytes

Sample	Initial Weight Loss Temperature (°C)	Weight Loss (%)	Decomposition Temperature (°C)	Weight Loss (%)	Total Weight Loss (%)
PEO+20wt% salt+15wt% EC+1wt% CNT	97	5.2	198	84.88	90
PEO+20wt% salt+15wt% EC+5wt% CNT	198	17.0	210	76.00	93

5.8 Thermogravimetric (TGA) Analysis of Nanocomposite Polymer Electrolytes at optimum wt% of LiPF$_6$, EC and αCNTs

Figure 5.8 shows the TGA and DTG curves weight loss of composites polymer electrolytes. The sample shows the lost weight at around 25-100°C, which is complete at around 200-280°C. This decomposition temperature is considerably higher than those of the liquid electrolytes currently used in lithium batteries (Kuo *et al.*, 2002). The weight loss process of the solid polymer electrolytes is gradual rather abrupt, as in the case for liquid electrolytes. For this reason, solid polymer electrolytes are more thermally stable than liquid electrolytes for applications in lithium ion batteries. Table 5.8 summarizes the results for optimum concentrations of solid polymer electrolytes.
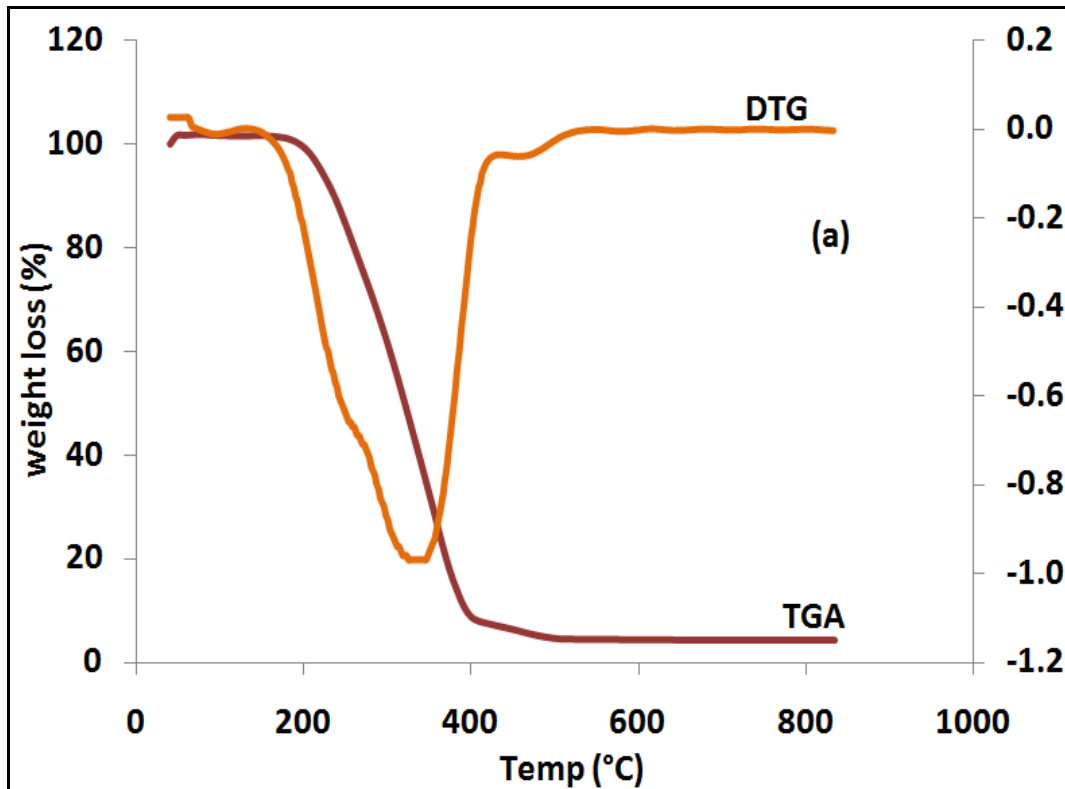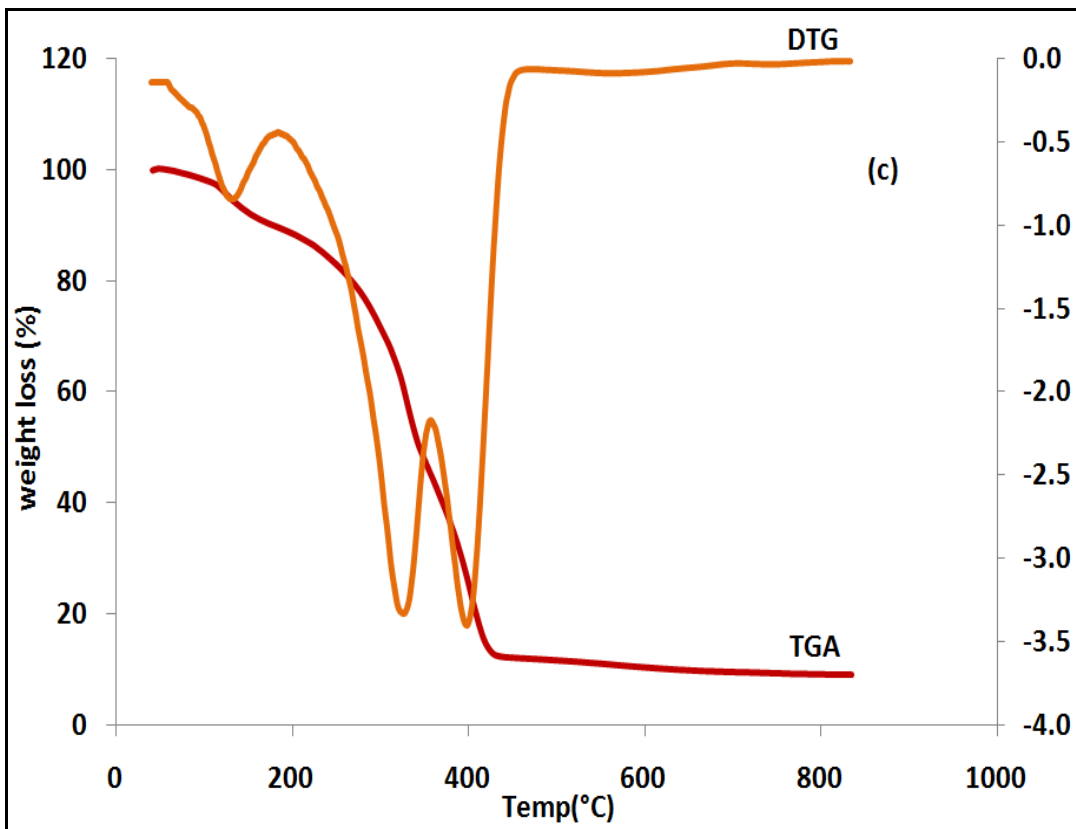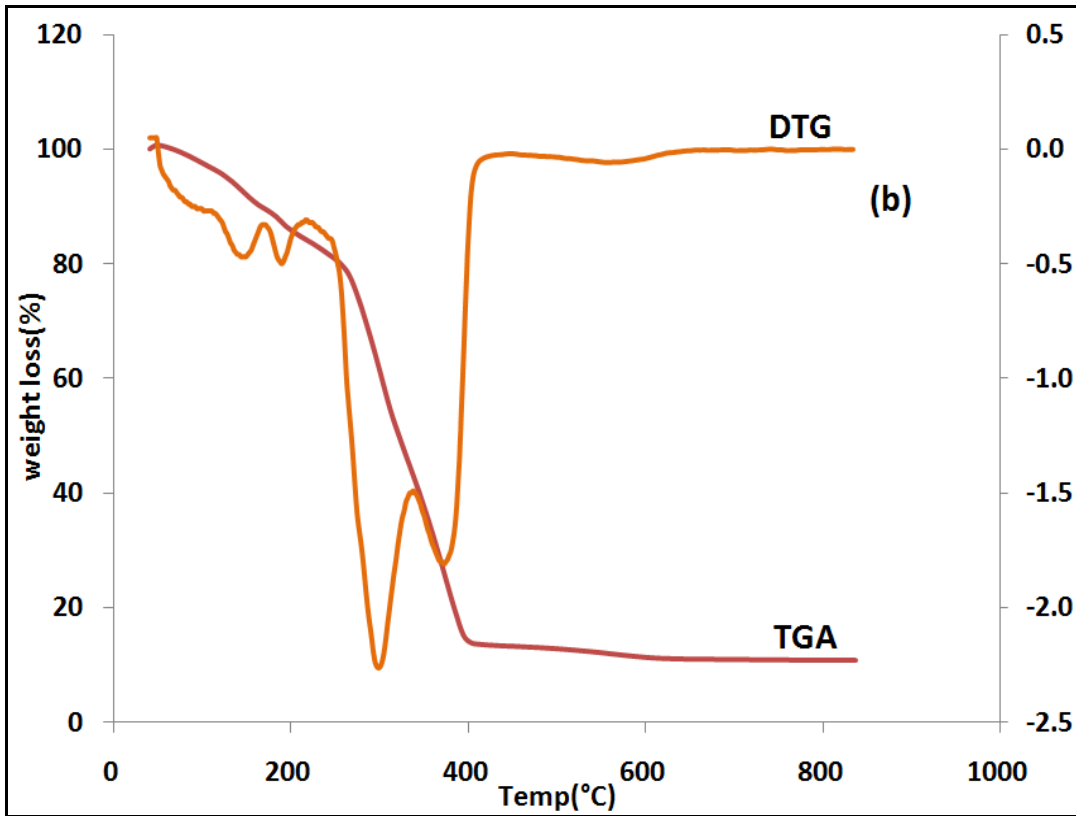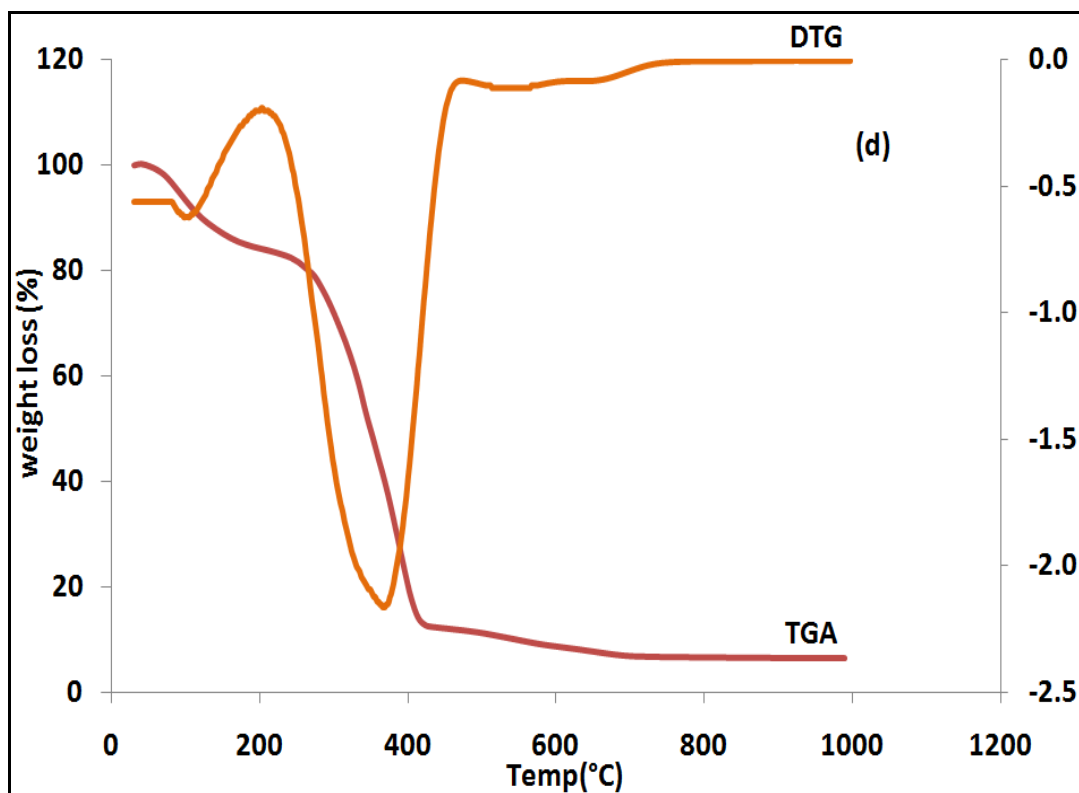
Figure 5.8 TG-DTG curves of nanocomposite polymer electrolytes (a) PEO; (b) PEO+LiPF$_6$; (c) PEO+LiPF$_6$+EC; (d) PEO+LiPF$_6$+EC+αCNTs

Table 5.8 First and second decomposition temperatures and percentage of total weight loss for various nanocomposites polymer electrolytes

Sample	Initial Weight Loss Temperature (°C)	Weight Loss (%)	Intermediate Weight Loss Temperature (°C)	Weight Loss (%)	Total Weight Loss (%)
PEO	75	0.22	200	88.74	88.96
PEO+20wt% salt	85	20	280	68.00	88.00
PEO+20wt% salt+15wt% EC	91	10	210	81.00	90.00
PEO+20wt% salt+ 15wt% EC+ 5wt% CNT	100	10.83	220	76.00	86.53

5.9 Fourier Transform Infrared (FTIR) Analysis of Polymer Electrolytes at various wt% of LiPF$_6$

Figure 5.9 depicts the IR transmittance spectra of the samples recorded at room temperature in the region of 4000 – 500 cm^{-1}. The spectra exhibit bands characteristic of stretching and bending vibrations of the films. FTIR transmittance bands' positions and assignments of the individual materials are listed in Table 5.9. It is observed that peaks occur between 4000 - 3100 cm^{-1} corresponding to the OH group. The peaks broaden with an increase in LiPF$_6$ salt concentration. This is due to the decomposition of LiPF$_6$ solid LiF and gases of OPF$_3$ and HF, which is represented by the following equation (Anantha and Hariharan, 2005):

$$LiPF_6 + H_2O \rightarrow LiF(s) + OPF_3(g) + HF(g)$$

(5.2)
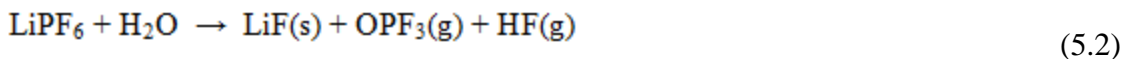
As the LiPF$_6$ salt concentration increases, the intensity of symmetric stretching vibration band of pure PEO is increased and shifts to 2869, 2873 and 2890 cm^{-1}, as shown in Figure 5.9(a), Figures 5.9(b-c) and Figure 5.9(d), respectively. This is due to the additional amount of Li$^+$ in the complexes. The anti-symmetric stretching vibration band at 1100 cm^{-1} of pure PEO is shifted to 1094 cm^{-1} (Figure 5.9(a)), 1090 cm^{-1} (Figures 5.9(b-c)) and 1110 cm^{-1} (Figure 5.9(d)) as LiPF$_6$ concentration increases. The peaks broaden with the exception of the spectrum for 20 wt% of LiPF$_6$. This may be due to the ion aggregates such as ion pairs and ion triplet formation, which causes constraints to ions and polymer segmental mobility. A similar reaction occurs to the twisting vibration bands at 842 and 963 cm^{-1} for pure PEO. When the weight percent of LiPF$_6$ is increased, the peaks are shifted to 839 and 944 cm^{-1} (Figure 5.9(a)) 945 and 837 cm^{-1} (Figure 5.9(b)) 945 and 835 cm^{-1} (Figure 5.9(c)), 963 and 844 cm^{-1} (Figure 5.9(d)). The peaks' intensities are increased with the exception for spectrum for 20 wt% of LiPF$_6$.
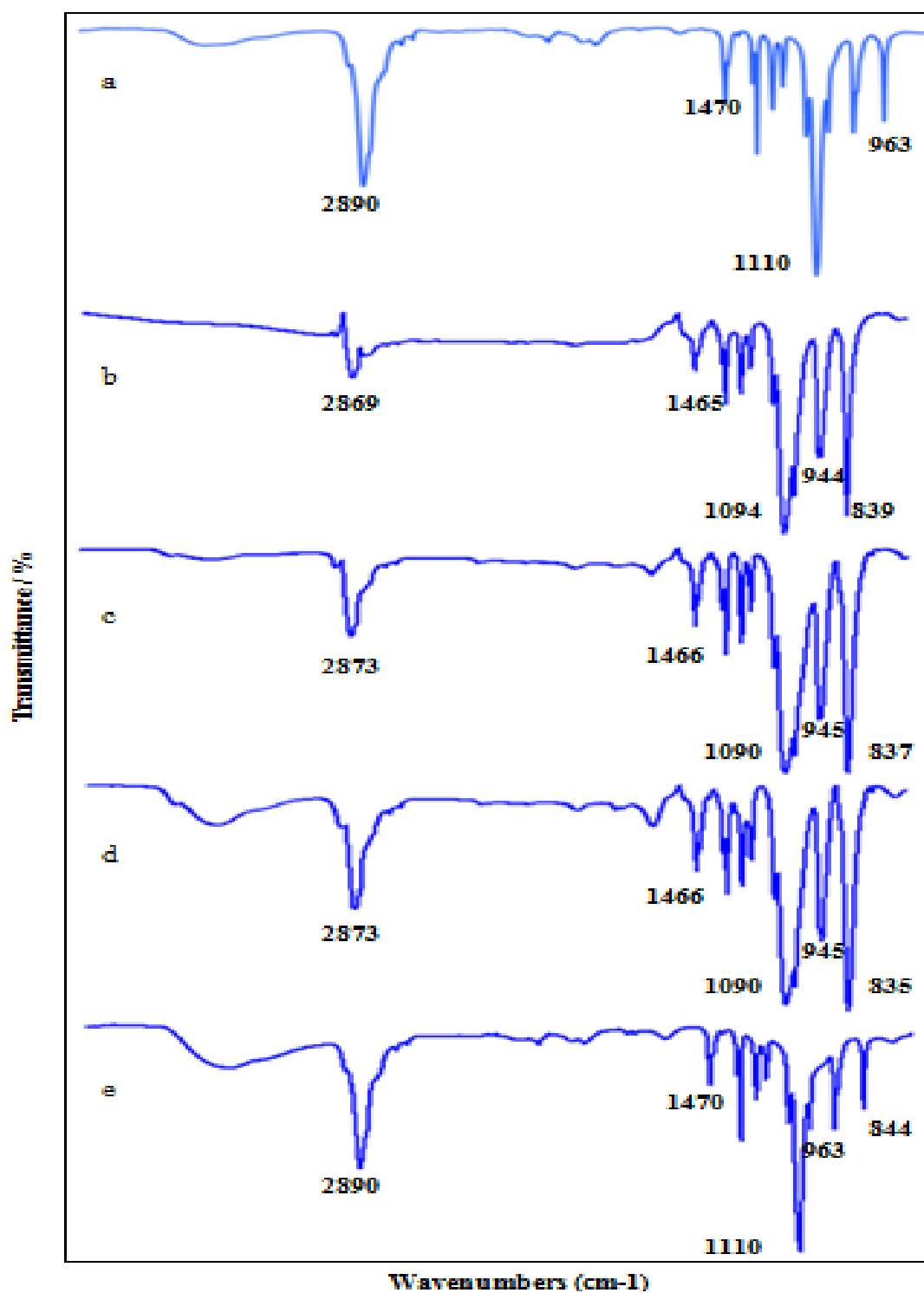
Figure 5.9 FTIR spectra of pure PEO and various wt% of LiPF$_6$ in the complexes (a) PEO; (b) 5;(c) 10; (d) 15; (e) 20.

5.10 Fourier Transform Infrared (FTIR) Analysis of Salted Polymer Electrolytes at various wt% of EC Plasticizer

Figure 5.10 depicts the IR transmittance spectra of the samples recorded at room temperature in the region of 4000 – 500 cm^{-1}. FTIR transmittance bands' positions and assignments of the individual materials are listed in Table 5.9. It is observed that peaks occur between 4000 - 3100 cm^{-1} corresponding to the OH group. The intensity of OH is invariant when various weight percent of EC are added into salted polymer. The peak at 2866 cm^{-1} represents CH stretching and shifts to 2868 cm^{-1} when the EC concentration increases from 5 to 10wt%. This peak shifts to 2862 cm^{-1} when 15wt% of EC is added into the salted polymer. The similar situation was observed at 1078 cm^{-1}. These peaks represent C-O-C stretching. When 10wt% EC is added into the salted polymer, the peak shifts to 1080 cm^{-1} and back to 1078 cm^{-1} when 15wt% EC is added into the salted polymer. The peak at 940 cm^{-1} represents CH$_2$ twisting and changes constantly when EC concentration varies from 5 to 15 wt%. The shifting of these bands indicates that there are possible interactions between the salted polymer and plasticizer. The peaks at 720 and 830 cm^{-1} remain unchanged.
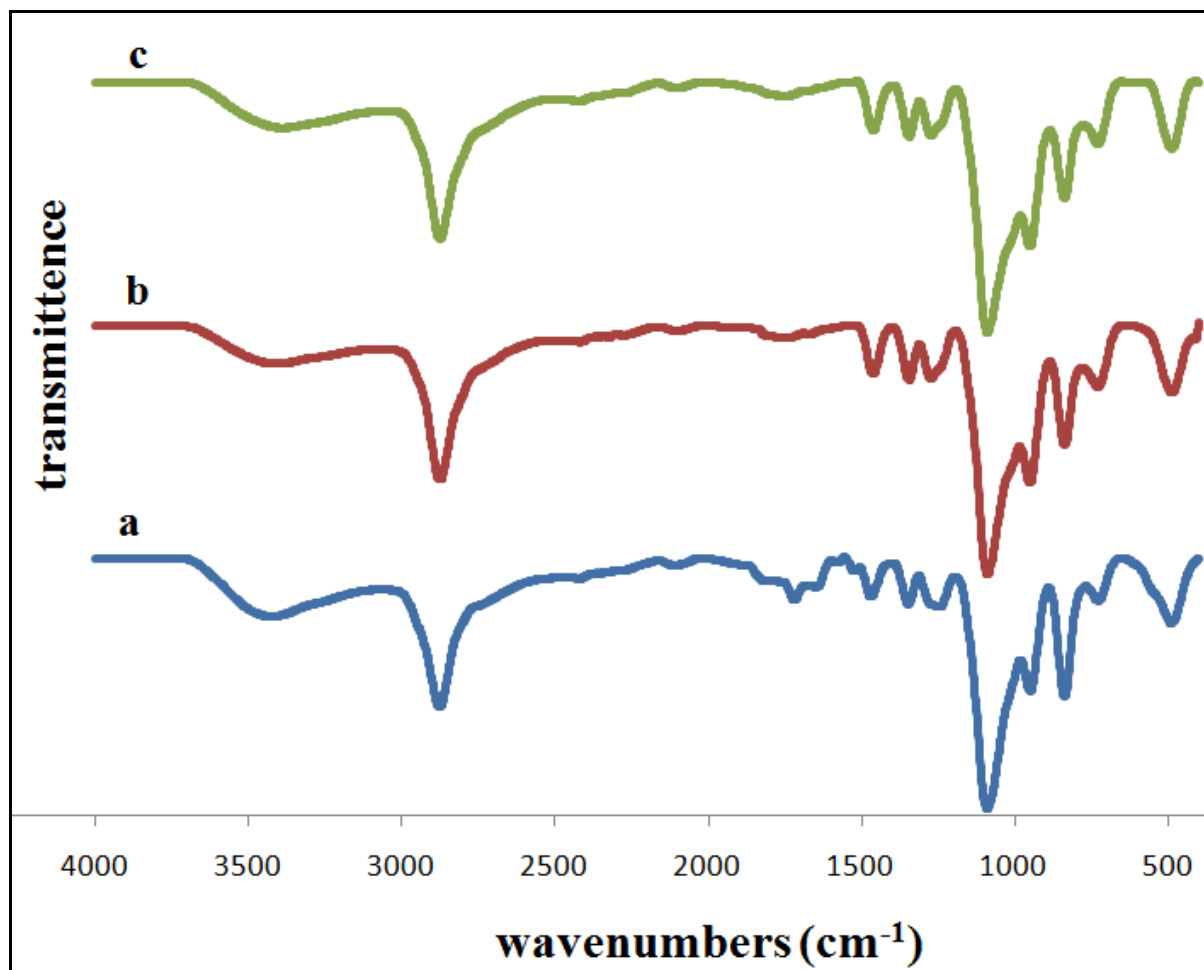
Figure 5.10 FTIR spectra of various wt% of EC in the complexes (a) 5; (b) 10; (c) 15.

5.11 Fourier Transform Infrared (FTIR) Analysis of Salted Plasticized Polymer Electrolytes at various wt% of αCNTs Filler

Figure 5.11 shows the FTIR spectra for αCNTs and the chemical bonding for αCNTs are summarized at Table 5.9. Figure 5.12 (a-b) shows the FTIR spectra of polymer electrolytes at 1 and 5 wt% αCNTs. The trend in Figures 5.12(a–b) indicates that the polymer–cation interaction are affected substantially upon the addition of filler. A shift in C–O–C stretching mode towards

the lower frequency side upon the addition of the filler particles results in the weakening of the C–O–C bonds thereby enhancing the flexibility of the polymeric chains. The hydroxyl group increases with increasing intensity of nanocomposite polymer electrolyte at 3500 cm^{-1}. The peaks at 2892, 1478 and 1342 cm^{-1} are assigned to CH$_2$ stretching, CH$_2$ scissoring and CH$_2$ wagging, respectively. The intensity remains unchanged when 1 and 5wt% αCNTs are added into the polymer complex. This proves that there are no interactions between the filler and PEO backbone for these peaks. The peaks shifts to lower wavenumbers from 1102 to 1100 cm^{-1} and 848 to 844 cm^{-1}, which are assigned to C-O-C stretching and CH$_2$ wagging. This strongly proves that there are chemical reactions between αCNTs and plasticized salted polymer. Table 5.9 shows a list of shifted wavenumbers for polymer complexation.
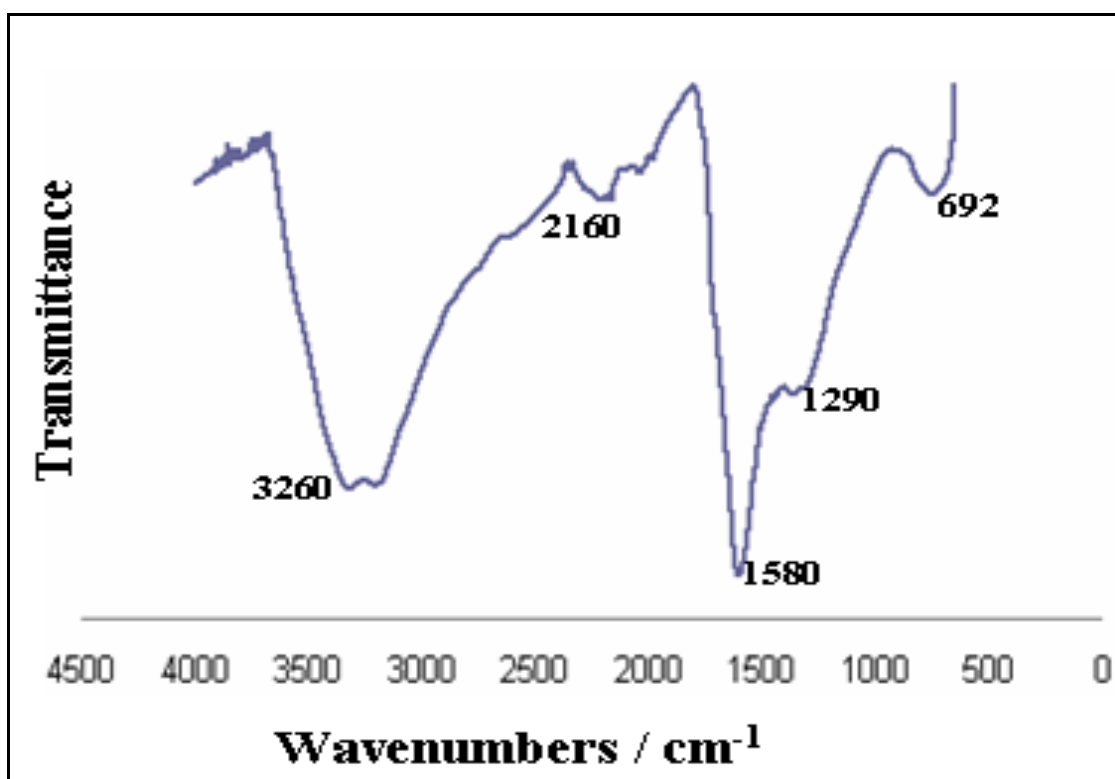
Figure 5.11 FTIR spectra of αCNTs.
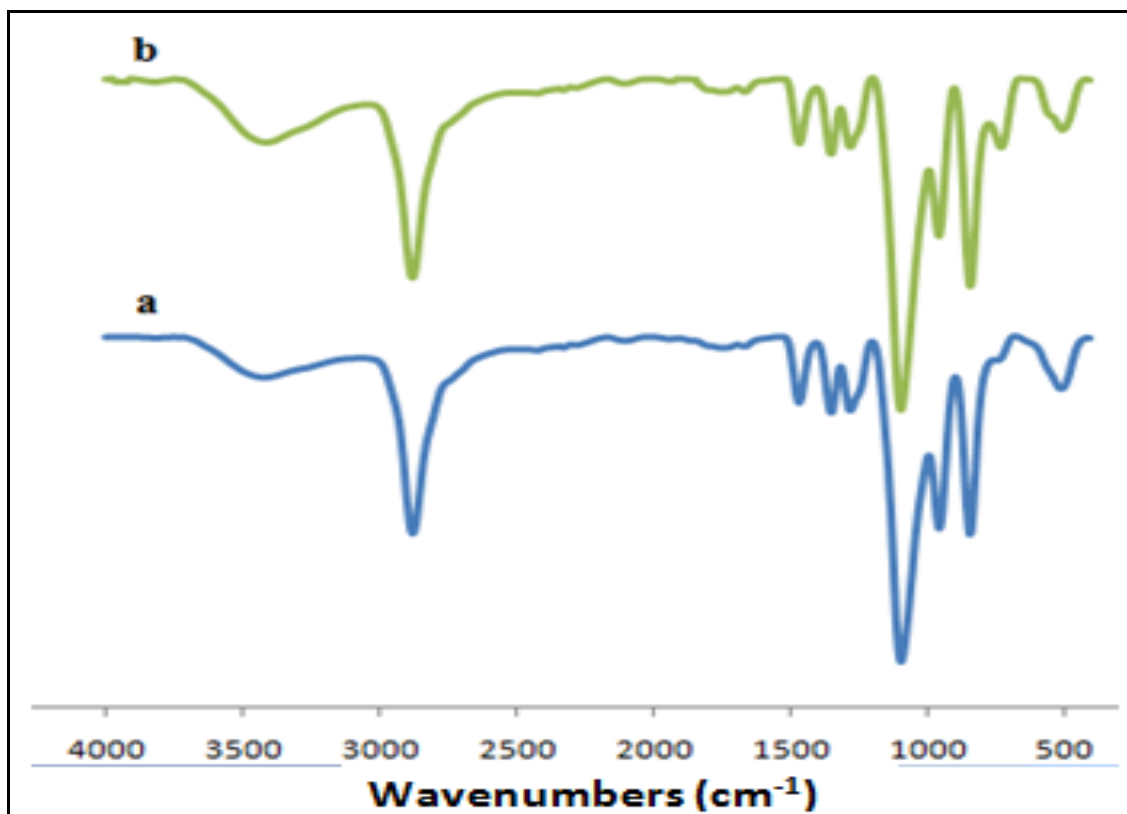
Figure 5.12 FTIR spectra of polymer electrolytes at various wt% of αCNTs (a) 1 (b) 5

5.12 Fourier Transform Infrared (FTIR) Analysis of Nanocomposite Polymer Electrolytes at optimum wt% of LiPF$_6$, EC and αCNTs

Figure 5.13 depicts the IR transmittance spectra of various electrolytes recorded at room temperature in the region of 4500 – 500 cm^{-1}. The spectra exhibit bands characteristic of stretching and bending vibrations of the films, which are listed in Table 5.9. The vibration modes and wavenumbers exhibited by PEO are CH$_2$ rocking modes observed at 842 and 963 cm^{-1}, respectively. The strongest interaction in PEO is the anti-symmetric bridge C-O-C stretching vibration at 1100 cm^{-1} (Zain and Arof, 1998), asymmetric CH$_2$ twisting at 1241 and 1280 cm^{-1}, and asymmetric CH$_2$ at 1455 cm^{-1}. Other absorption bands are observed for symmetric and

asymmetric C-H stretching vibrations at 2800 – 3000 cm^{-1} and 2700 – 3800 cm^{-1}, respectively (Subban and Arof, 2004). When LiPF$_6$ is added into the PEO system, CH and C-O-C stretching modes are shifted to 1101 cm^{-1}. When EC is added to PEO- LiPF$_6$ system, CH and C-O-C stretching modes are shifted to 2886 and 1100 cm^{-1}, respectively. A small shoulder appeares at 1800 and 700 cm^{-1} for the PEO-LiPF$_6$-EC system due to the reaction of EC with PEO. The peaks become more obvious when αCNTs was added into the PEO- LiPF$_6$-EC system, whereby the CH and C-O-C stretching modes are shifted to 2880 and 1100 cm^{-1}, respectively. The observation implies that interactions occur among the components.
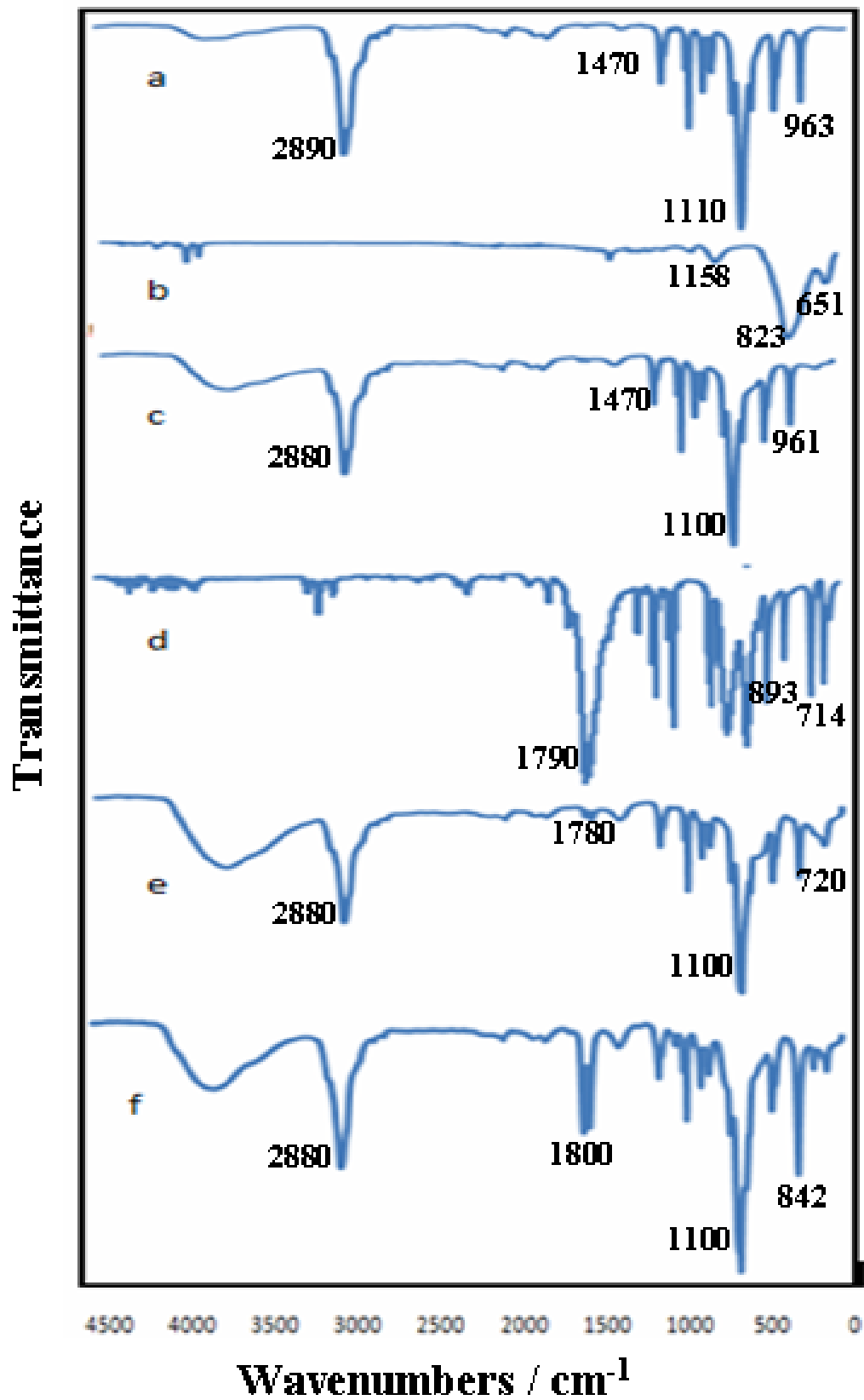
Figure 5.13 FTIR spectra of (a) PEO (b) LiPF$_6$; (c) PEO+LiPF$_6$; (d) EC; (e) PEO+LiPF$_6$+EC;
(f) PEO+LiPF$_6$+EC+αCNTs.

Table 5.9 FTIR transmittance bands' positions and their band assignments.

Method	Vibrational frequency (cm^{-1})	Band assignment
PEO	842, 963	CH$_2$ twisting nagging (Osman and Arof, 2003)
	1100	anti-symmetric bridge C-O-C stretching (Osman and Arof, 2003)
	1241, 1280	asymmetric CH$_2$ twisting (Osman and Arof 2003)
	1455	asymmetric CH$_2$ (Osman and Arof, 2003)
	2800-3000	symmetric C-H stretching (Osman and Arof, 2003)
	2700-2800	asymmetric C-H stretching (Osman and Arof, 2003)
LiPF$_6$	651	ν(PF$_6$-) (Jacek et al., 2005)
	837	ν(PF$_6$-) (Jacek et al., 2005)
	1164	ν(PF$_5$) (Jacek et al., 2005)
EC	718	C=O bending (Monalisa et al., 2008)
	893	ring breathing (Monalisa et al., 2008)
	1774	C=O stretching bands (Monalisa et al., 2008)
	1775	C=O stretching bands (Monalisa et al., 2008)
CNT	1635	H-bonded (C=O stretching) (Krawiec et al., 1995)
	1708	C=O stretching bands (Krawiec et al., 1995)
	3437	OH stretching (Krawiec et al., 1995)

CHAPTER SIX

Conductivity and Dielectric Studies of Nanocomposite Solid Polymer Electrolytes

6.1 Conductivity Analysis of Polymer Electrolytes at various wt.% of LiPF$_6$ Salt

Figure. 6.1 shows the complex impedance spectra for samples with 0, 5, 10, 15, 20 wt% of LiPF$_6$ at room temperature (25°C). A part of a semicircle can be observed for the salted free sample as shown in Figure 6.1(a). The semicircle can be represented by a parallel combination of a capacitor, which is due to the immobile polymer chain (Ramesh and Arof, 2001). As the salt concentration begins to increase, the semicircle in the plots is observed to lessen, and finally results in a low-frequency spike. This observation suggests that only the resistive component of the polymer electrolytes exists, which is due to the mobile ions inside the polymer matrix (Ramesh and Arof, 2001; Baskaran *et al*., 2004).

The bulk resistance R_b for all samples were calculated from the low frequency intercept of the semicircle or high-frequency intercept of the spike on the real axis. It is found that R_b decreases with an increase in salt concentration. This may be due to an increase in mobile charge carriers upon the addition of LiPF$_6$. The R_b values obtained are 5.36 x 10^6, 4.64 x 10^3, 5.19 x 10^2, 2.52 x 10^2 and 1.61 x 10^2 Scm^{-1} for 0, 5, 10, 15 and 20 wt% concentration of LiPF$_6$, respectively.
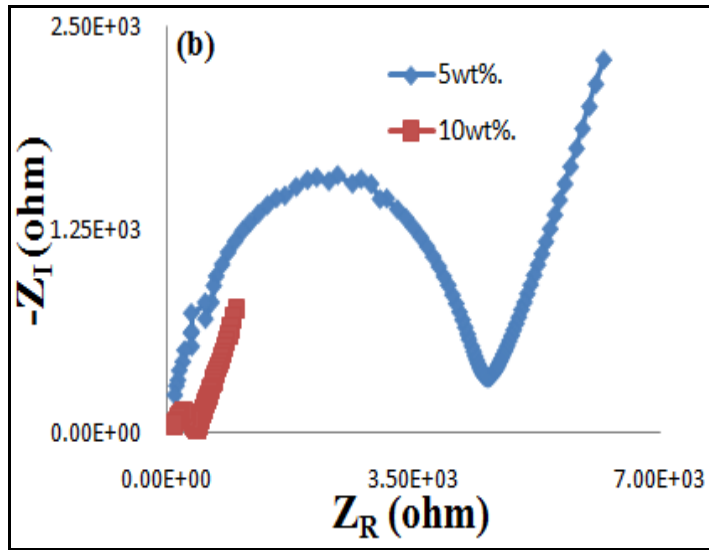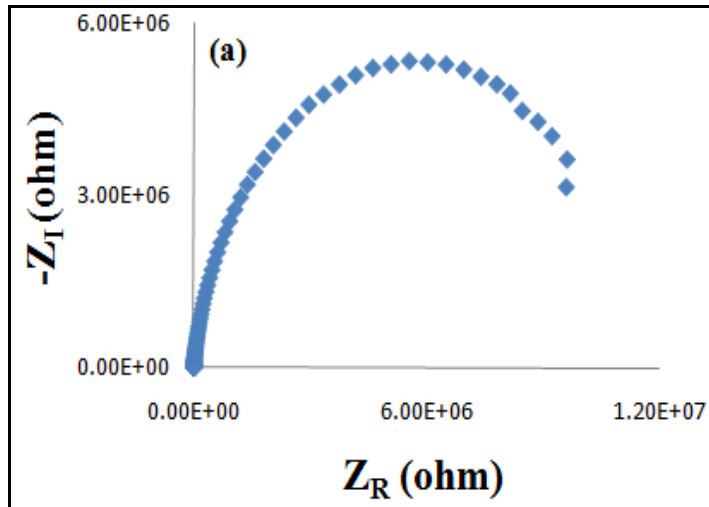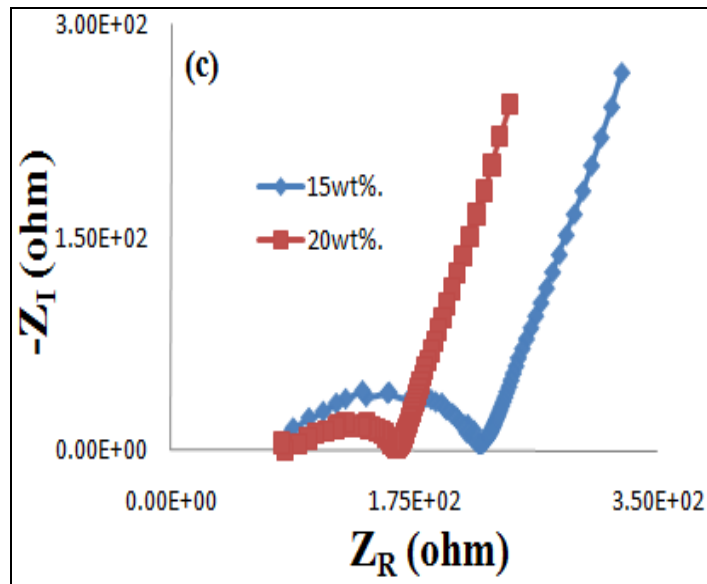
Figure 6.1 Complex impedance spectra of polymer electrolytes at various wt% of LiPF$_6$ (a) 0; (b) 5, 10; (c) 15, 20.
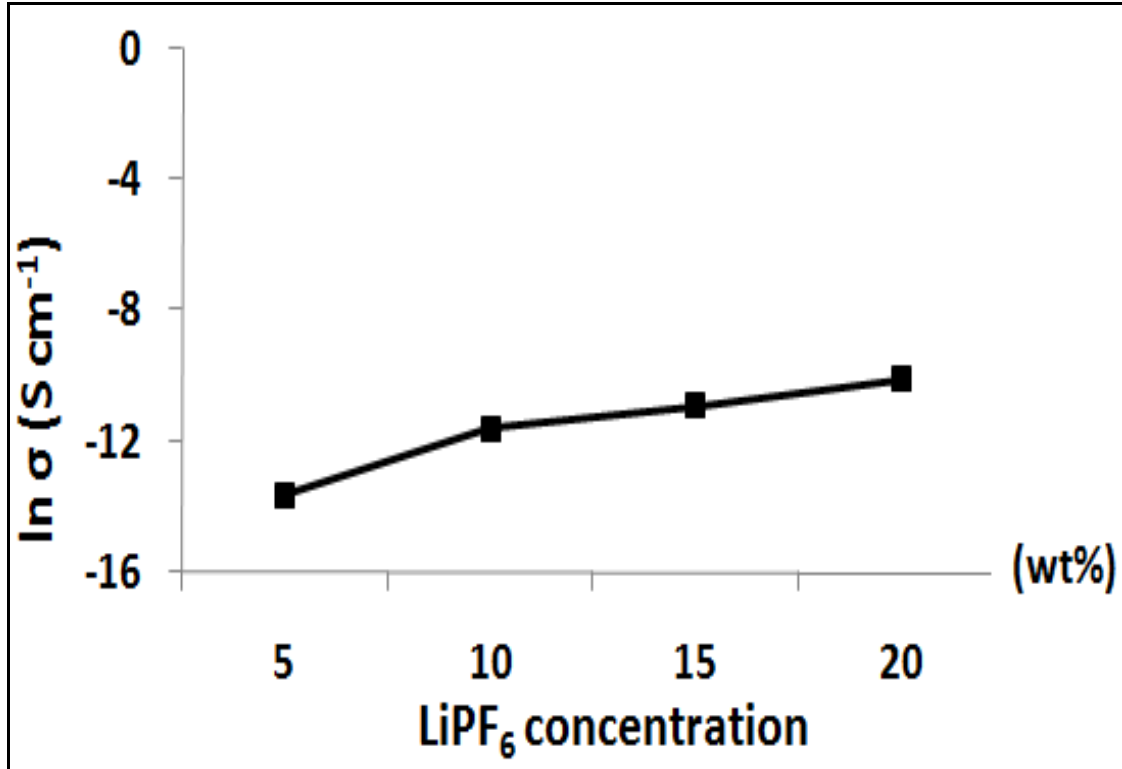
Figure 6.2 Variation of conductivity as a function of LiPF$_6$ content at room temperature

As the salt content increases, the conductivity increases due to the increased density of mobile ions and the polymer segment's motion is promoted (Rajendran *et al.*, 2007). The results agree well with the Rice and Roth's model below (Ramesh *et al.*, 2008; Khiar and Arof, 2010):

$$\sigma = \frac{2}{3}\left[\frac{(Ze)^2}{k_B Tm}\right]\eta E_A \tau \exp\left(-\frac{E_A}{k_B T}\right) \tag{6.1}$$

where σ, η, Z, e, E_A and m represents the conductivity, density, valency, and mass of the conducting ions, respectively. Furthermore, the parameters T, k_B, e and τ represent the absolute temperature, Boltzman constant, electronic charge and time travel of ions between sites, respectively. From Equation (6.1), it can be seen that the conductivity increases when the density of mobile ions increases.

The highest composition of salt obtained for the PEO-LiPF$_6$ films was 20 wt.% of LiPF$_6$. Beyond this composition, the films failed to form and remained in a gel-like state. This may be due to the presence of water molecules. It is known that LiPF$_6$ salt possesses a high capability to absorb water molecules at high temperature (approximately 40°C) (Teng et al., 2005). Thus, at higher compositions of LiPF$_6$ salt, more moisture are absorbed, which eventually increase the mobility of PEO-LiPF$_6$ system. Consequently, water molecules form hydrogen bonds with PEO and disrupt the linkage between PEO-LiPF$_6$ systems (Ramesh et al., 2008).

The initial increase in conductivity shown in Figure 6.2 is presumably due to an increase in the number of charge carriers in the matrix. Hence, the conductivity reaches the maximum value at 20 wt% of LiPF$_6$ complex. This shows a balance between the two opposing forces, which is an increase in number of charge-carrier ions and decrease in ionic mobility (Rajendran et al., 2007). The polar and flexibility of the PEO main chain dissociates LiPF$_6$ to generate carrier ions, and the migration of these ions through interchain and intrachain polymer segments in the amorphous region of the complex (Druger et al., 1983) is responsible for the increase in conductivity.

Figure 6.3 shows the complex impedance spectra of polymer electrolytes at the elevated temperature. The disappearance of a depressed semicircle at high frequency and temperature reveals the absence of capacitive nature and indicates solely diffusion process (Ratner and Nitzan, 1989). The intercept ion at the real axis gives the electrolytes' resistance and the values decrease with increasing temperature and ionic mobility. However, the charge concentrations do not necessarily increase with temperature for polymeric electrolytes (Khiar and Arof, 2010).
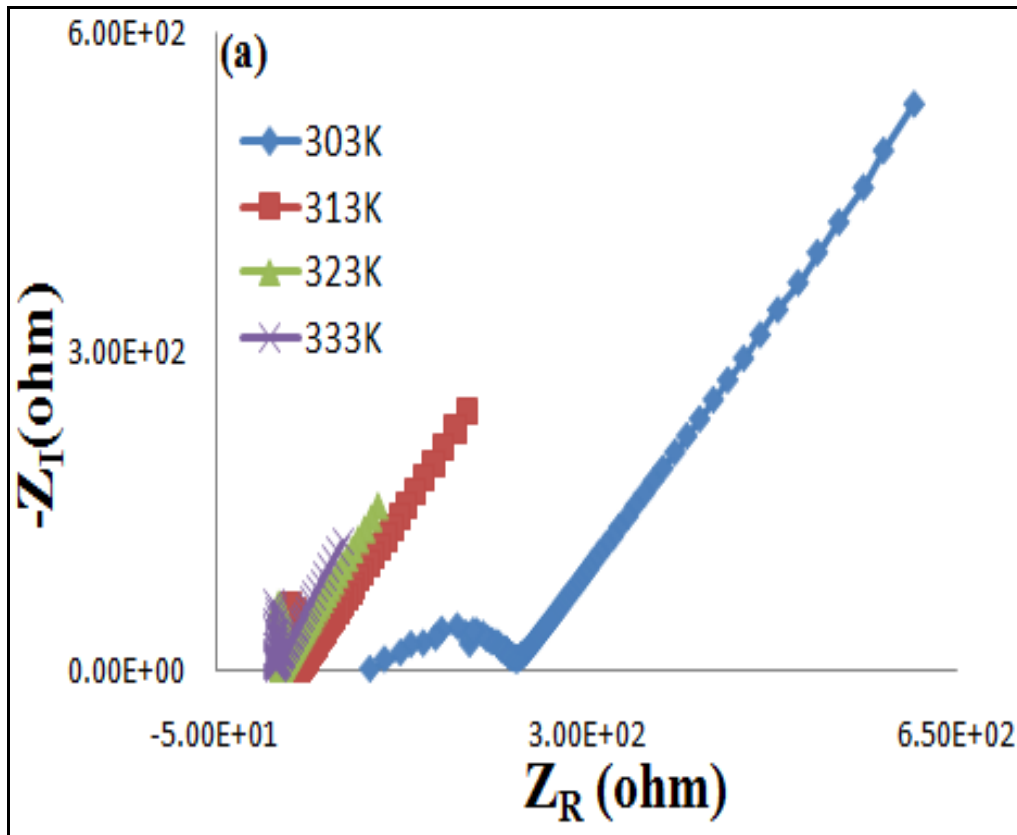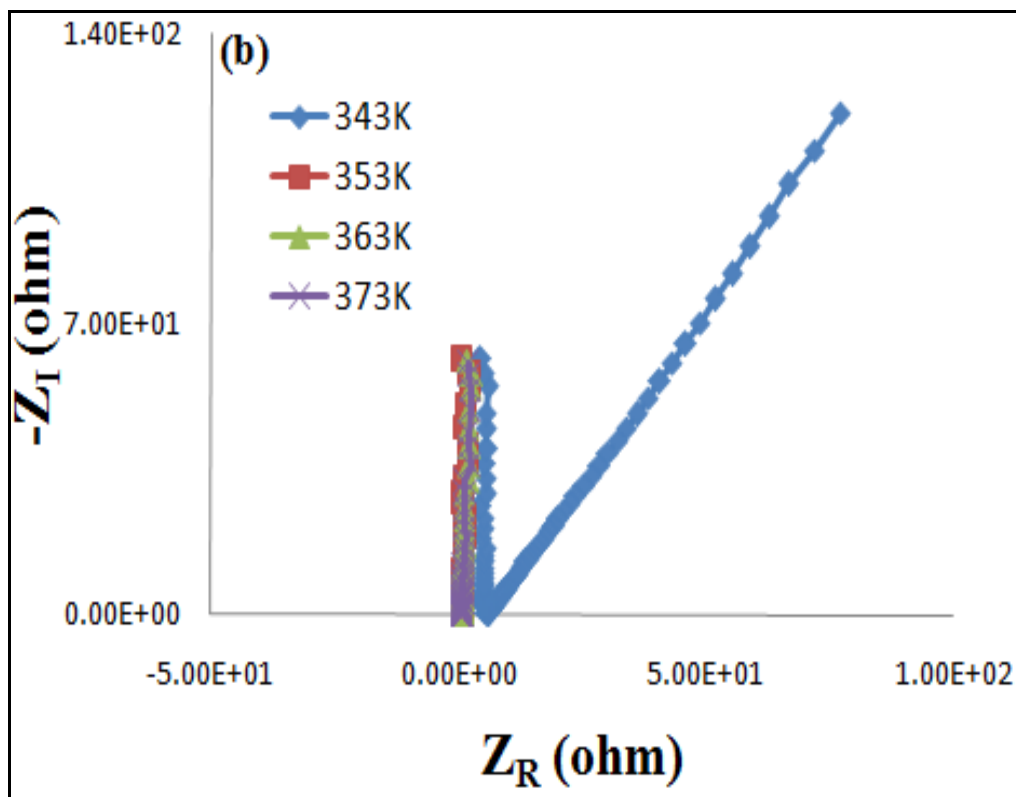
Figure 6.3 Complex impedance spectra of PEO-10wt% $LiPF_6$ at various temperature of (a) 303-313 K and (b) 343-373 K

Figure 6.4 shows the plot of conductivity dependence temperature at various weight percent of $LiPF_6$. The temperature dependence of the ionic conductivity is not linear and obeys the VTF (Vogel-Tamman-Fulcher) relationship. The conductivity of salted polymer electrolytes is found to increase with temperature, from 303 to 373K. At higher temperature, the thermal movement of polymer chain segments and the dissociation of salts were enhanced the ionic conductivity (Rajendran *et al*., 2007).
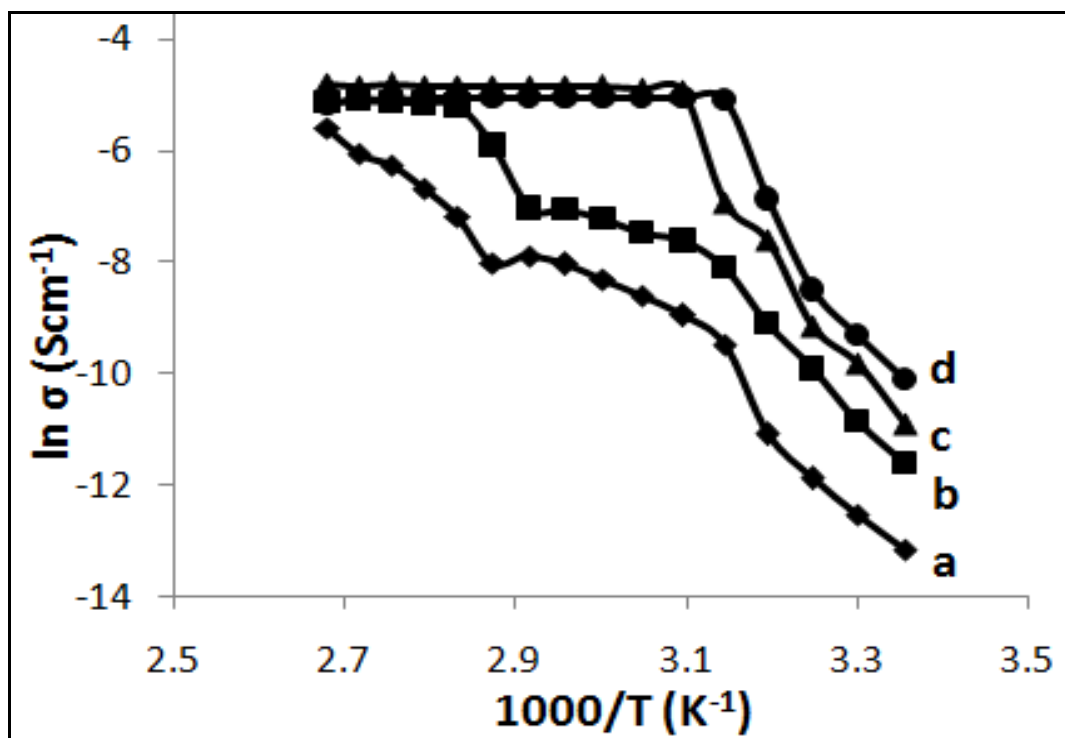
Figure 6.4. Conductivity dependence temperature of polymer electrolytes at various wt% of LiPF$_6$ (a) 5 ; (b) 10 ; (c) 15 ; (d) 20.

6.2 Conductivity Analysis of Salted Polymer Electrolytes at various wt% of EC Plasticizer

Figure 6.5 shows the variation of room temperature conductivity as a function of plasticizer concentration. The dependence of conductivity on EC concentration provides information on the specific interaction between the plasticizer, salt and polymer matrix. It is evident that the room temperature conductivity increases with different chemical compositions. The conductivity is increased by an order of magnitude with the addition of 10wt% of EC from 7.43 x 10^{-5} to 1.43 x 10^{-4} Scm^{-1}. The conductivity is slightly increased to 2.06 x 10^{-4} Scm^{-1} with the addition of

15wt% of EC. This reflects the effect of the physicochemical properties of the individual plasticizers such as the high dielectric constant of EC (ε_{25}=85.1), which contributes significantly towards improving the conductivity performance (Tobishima and Yamaji, 1984). The addition of plasticizer also reduces the ion pairing (Tobishima and Yamaji, 1984). The high dielectric constant of EC effectively reduces the inter-ion Coulomb interactions; hence, more Li^+ ion contribute to the conductivity of the complexes. Moreover, the addition of the plasticizer reduces the crystallinity of the complexes, which is confirmed from the XRD and DSC analyses, and this to obtain better ionic conductivity (Kelly *et al*., 1984; Gorecki *et al*., 1986; Macfarlane *et al*., 1995). The lower viscosity of EC (1.9 cP at 40°C) may also contribute to the enhancement in conductivity (Macfarlane *et al*., 1995) The anionic part of Li salt plays an important role in contributing towards the conductivity and stability of the resultant electrolyte (Limb *et al*., 2006). The plasticizer-rich phase will be less fragmented (or more interconnected), which makes ion transport much easier.
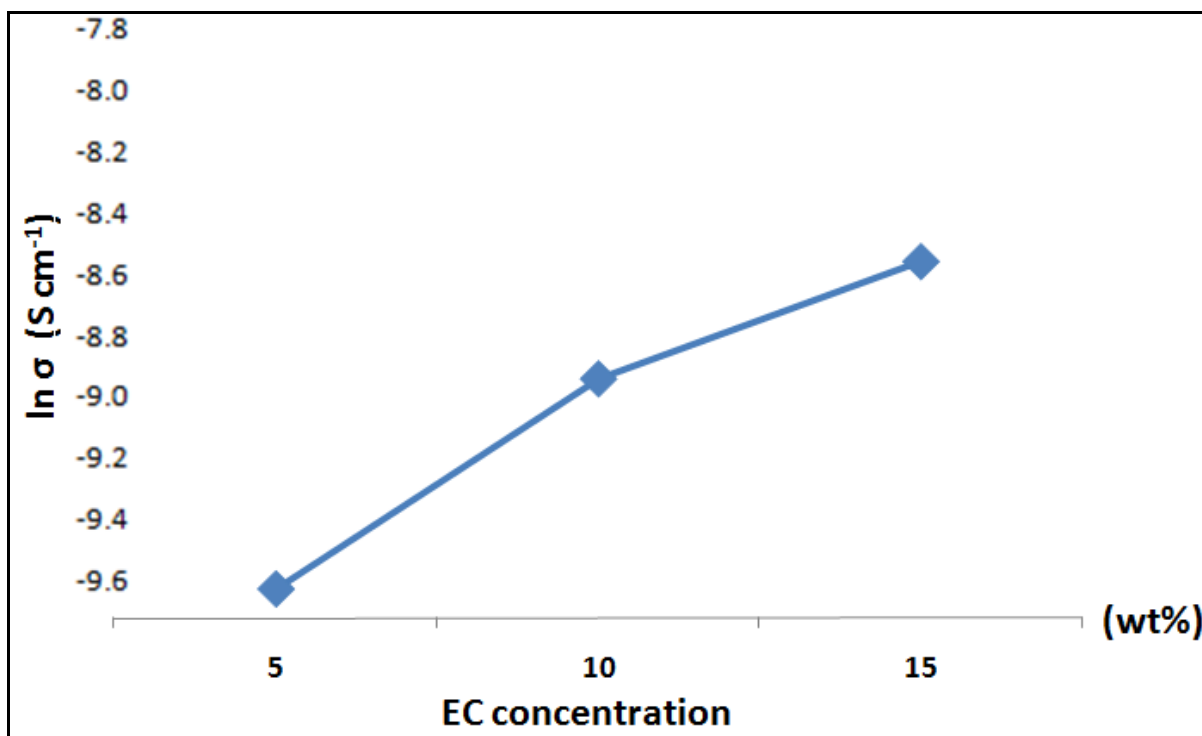
Figure 6.5 Variation of conductivity of salted polymer electrolytes as a function of various wt% of EC content at room temperature

Figure 6.6 shows the complex impedance spectra for various plasticized electrolytes at lower and higher temperatures. The semicircle represents the ionic resistance of the polymer electrolyte in the higher frequency range and an inclined line at lower ones. This shows a typical blocking electrode capacitive behaviour. The slopes of the inclined lines do not strongly depend on the components' molar ratio at higher temperatures. This indicates that the resistance on the inclined line is mainly against ion passage in the electrolyte/electrode interface. However, it is a different case for lower temperatures, in which the inclined lines are strongly dependent on the components' molar ratio. The semicircle shrinks and decays as a result of shifting to higher frequencies due to the decrease of the ionic resistance of the electrolyte at higher temperatures. However, at higher temperatures, the curve for 10wt% EC moves forward due to increased ion dissociation, resulting in the formation of more free ions. The curve for 15wt% EC is similar

with 5wt% EC due to the high concentration plasticizer which may eventually cause displacement of the host polymer and resulting in decreased conductivity. The arc's intercept on the real axis gives the value of the bulk resistance, which decreases with increasing temperature.
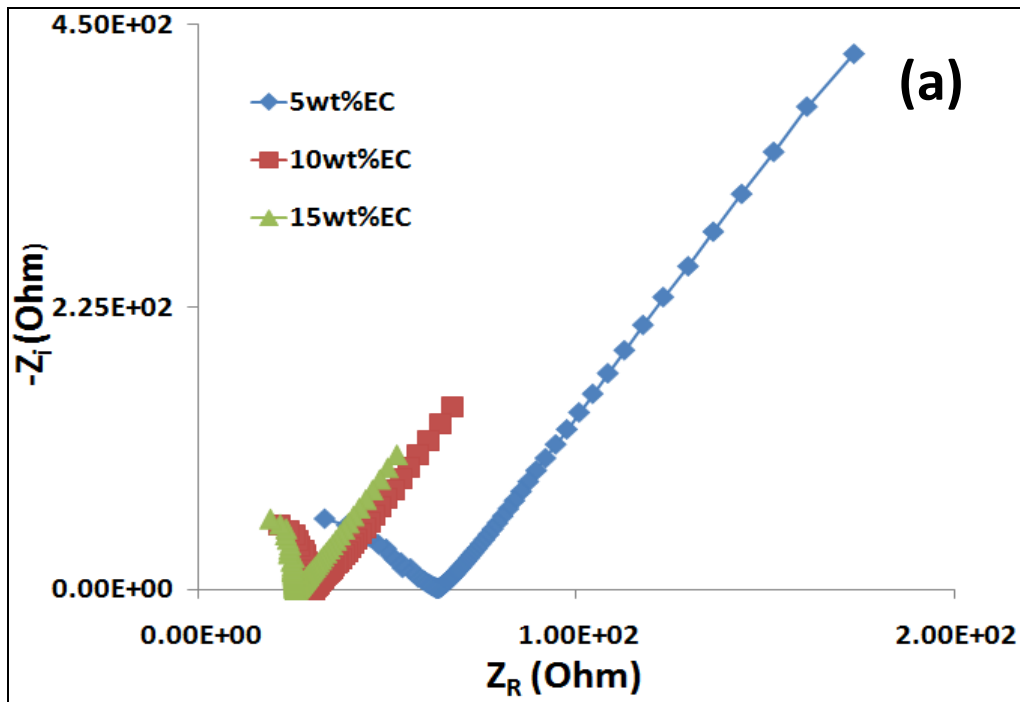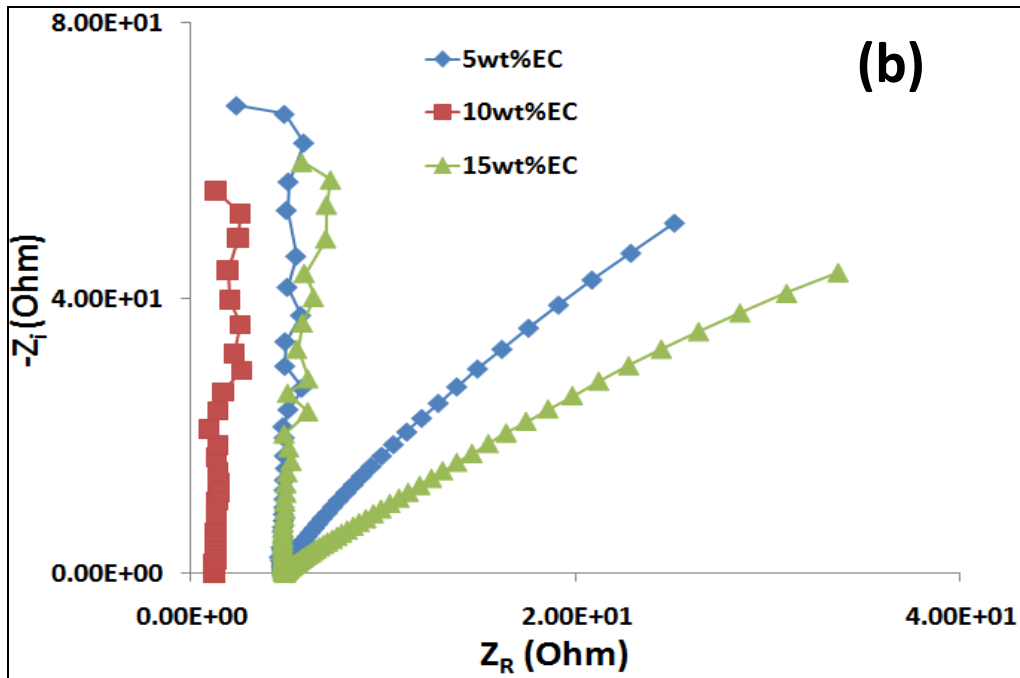
Figure 6.6 Complex impedance spectra of various plasticized polymer electrolytes at different temperature (a) 298 K and (b) 373 K

Figure 6.7 shows the plot of ionic conductivity temperature dependence at various wt% of EC. The temperature dependence of the ionic conductivity is not linear and obeys the VTF (Vogel-Tamman-Fulcher) relationship.
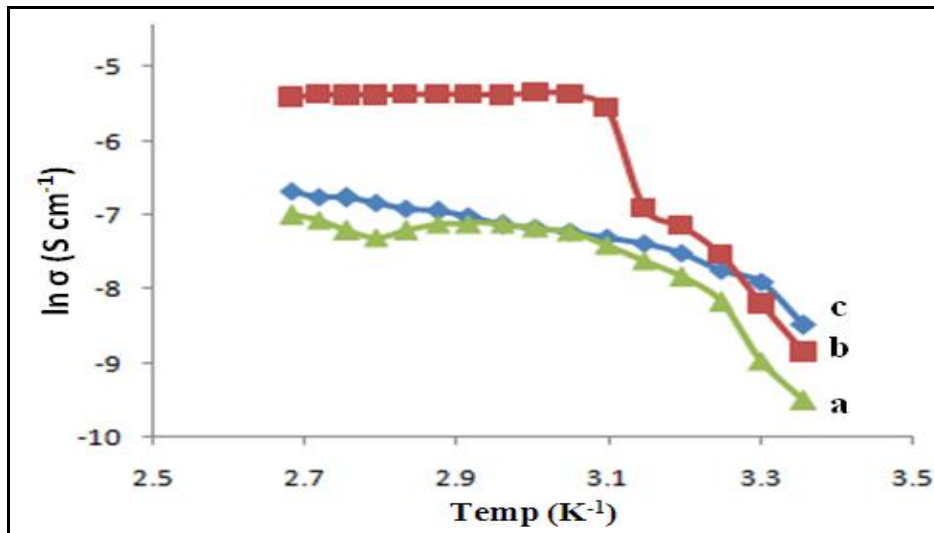
Figure 6.7 Conductivity dependence temperature of complexes at various wt% of EC (a) 5 ; (b) 10 ; (c) 15.

The conductivity increases with increasing temperature upon the addition of 5 and 10wt% of EC, as shown in Figure 6.7. It is evident that the ionic conductivity increases with an increase in plasticizer content and temperature. This can be explained in terms of two factors, first: an increase in the degree of interconnection between the plasticizer-rich phases due to an increase in the volume fraction of these phases; and second, increase in the free volume of the plasticizer rich phase due to an increase in the relative amount of the plasticizer compared with that of PEO. At higher concentrations of plasticizer, the transport of ions may be expected to take place along the plasticizer-rich phase.

Although the improvement in conductivity in certain electrolyte systems has been interpreted in terms of plasticization of the polymer structure (Cameron *et al.*, 1990) or an alteration in the ion transport mechanism (Croce *et al.*, 1993), other effects related to the viscosity of the ionic environment may also contribute. As the amount of plasticizer is increased, an optimum composition is reached whereby ion interactions between the solubilizing polymer and the plasticizer are such that ion mobility is maximized. A further increase in plasticizer content may eventually cause displacement of the host polymer by plasticizer molecules within the salt complexes and a decrease in ionic mobility.

6.3 Conductivity Analysis of Salted Plasticized Polymer Electrolytes at various wt% of αCNTs Filler

Figure 6.8 shows the complex impedance spectra for nanocomposite polymer electrolytes at various wt% of αCNTs at 298 and 373K. The plots show two well-defined regions namely, a high-frequency region depressed semi-circle which is due to the bulk effect of the electrolytes and a linear region in the low-frequency range, which is attributed to the effect of blocking electrodes. The low-frequency intercept on the Z_r axis gives the bulk electrical resistance (R_b) value. The bulk resistance decreases with increasing αCNTs concentration. The improved ionic conductivity is due to enhancement of the ionic mobility and number of carrier ions (Macdonald, 1987). The addition of αCNTs into the polymer matrix prevents local chain reorganization with freezing at ambient temperature and a high degree of disorder which in turn favours fast ionic transport. Lewis acid-base interaction centers with the electrolyte ionic species, which lowers ionic coupling process and increases conductivity (Anantram and Leonard, 2006) .
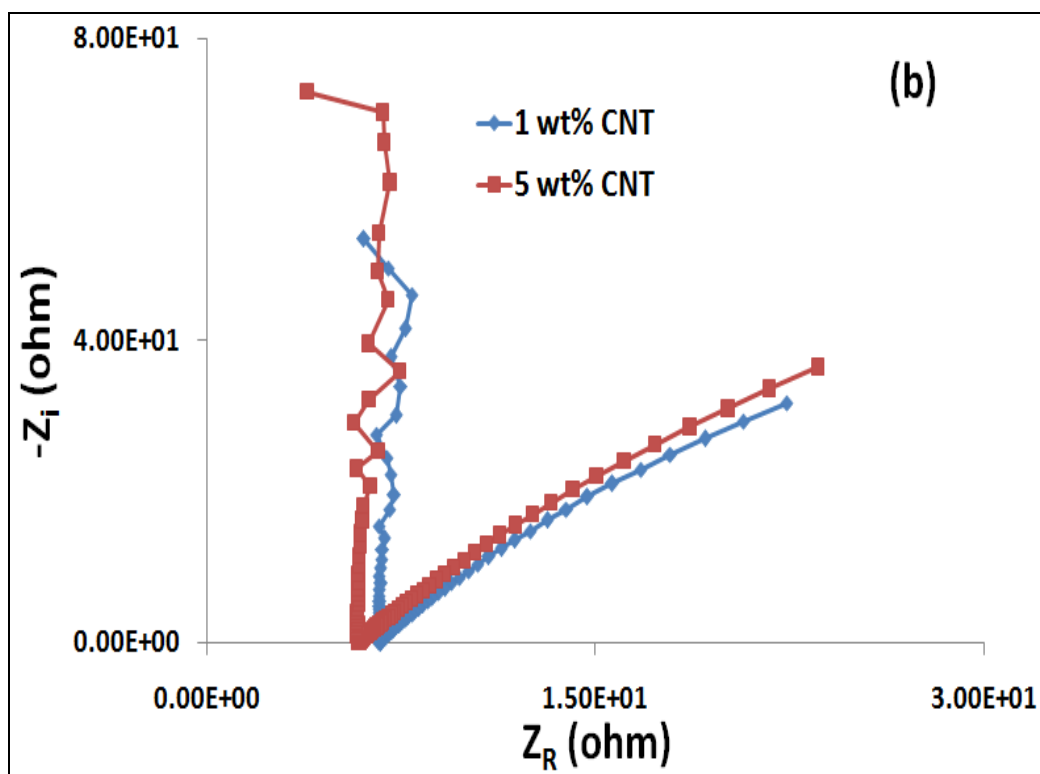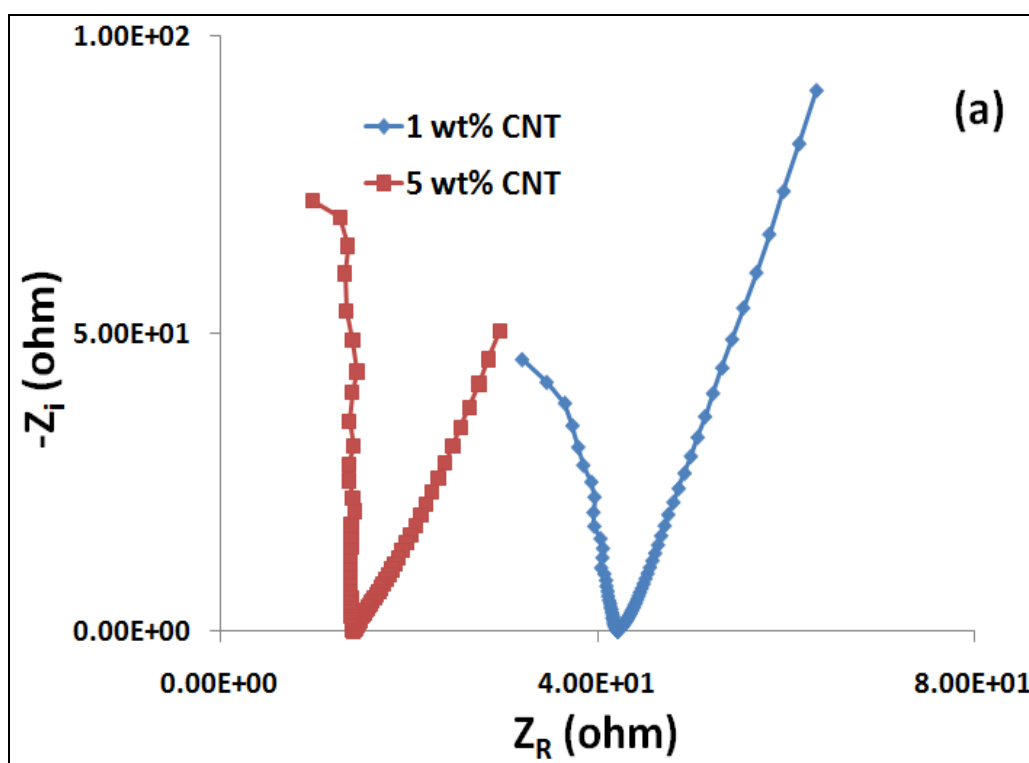
Figure 6.8 Complex impedance spectra for nanocomposite polymer electrolytes at different temperature (a) 298 K and (b) 373 K.

Figure 6.9 shows the temperature dependence of conductivity for polymer electrolytes between 298 to 373K. It is evident that the room temperature conductivity increases with different wt% of αCNTs. When the organic filler was added to the polymer electrolytes, new interfaces were connected with the filler surface such as the αCNTs/polymer spherulite interfaces, which provide more effective paths for the migration of the conductivity ions (Przluski *et al.*, 1995). Moreover, the nanosize αCNTs improve the conduction of the mobile ions due to their extremely high surface energy (Przluski *et al.*, 1995; Capuano *et al.*, 1991; Borghini *et al.*, 1995; Wen *et al.*, 2000; Kim *et al.*, 2000; Kumar *et al.*, 1999). This, prevents local PEO chain reorganization with the result of freezing at ambient temperature and a high degree of disorder, which in turn favours fast ionic transport. As the αCNTs concentration increases, the conductivity also increases due to more mobile ions which can be transported in nanocomposite polymer electrolytes. The conductivity values at room temperature for 1wt% of αCNTs is 2.2 x 10^{-4} Scm^{-1} and increases to 1.3 x 10^{-3} Scm^{-1} when 5wt% of αCNTs were added into polymer complexes. The conductivity value increases by an order of magnitude with the increase of αCNTs concentrations. However, there is a possibility of increased proton conductivity with increases αCNTs concentrations. It is well known that αCNTs are very good electronic conductors (Anantram and Leonard, 2006; Kilbride *et al.*, 2002), but the effect on proton conductivity is less studied. It is also suggested that structural modifications occuring at the αCNT surface due to the specific action of the polar surface groups of the organic filler act as Lewis acid-base interaction centers with the electrolyte ionic species (Anantram and Leonard, 2006). Thus, it is expected that lowering ionic coupling promotes salt dissociation via a sort of ion-filler complex formation.
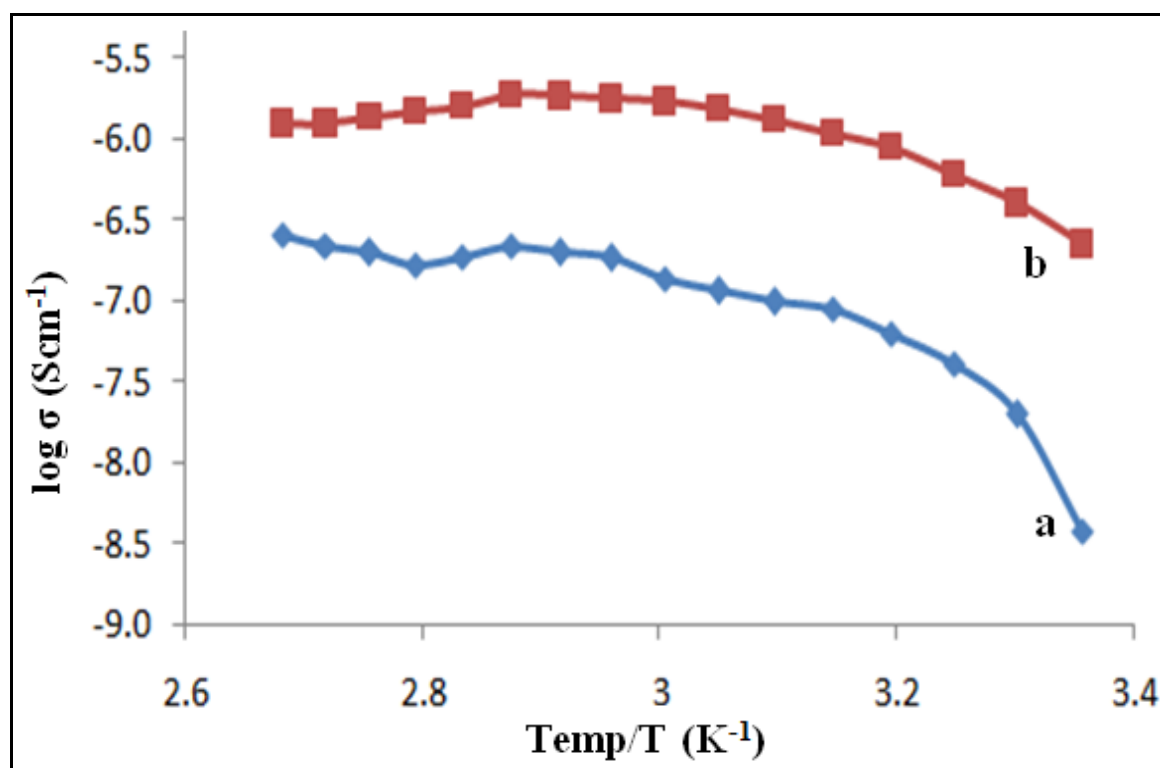
Figure 6.9 Temperature dependence conductivity for polymer electrolyte at different wt% of αCNTs of (a) 1 and (b) 5.

6.4 Conductivity Analysis of Nanocomposite Polymer Electrolytes at the optimum wt% of LiPF$_6$, EC and αCNTs

Figure 6.10 shows the complex impedance spectra for various electrolytes at lower and higher temperatures. The semicircle represents the ionic resistance of the polymer electrolyte in the higher frequency range and an inclined line at lower ones. This shows a typical blocking electrode capacitive behaviour. The slopes of the inclined lines do not strongly depend on the components' molar ratio at higher temperatures. This indicates that the resistance on the inclined line is mainly against ion passage in the electrolyte/electrode interface. However, it is a different case for lower temperatures, in which the inclined lines are strongly dependent on the

components' molar ratio. The semicircle shrinks and decays as a result of shifting to higher frequencies due to the decrease of ionic resistance of the electrolyte at higher temperatures. The arc's intercept on the real axis gives the value of the bulk resistance, which decreases with increasing temperature.
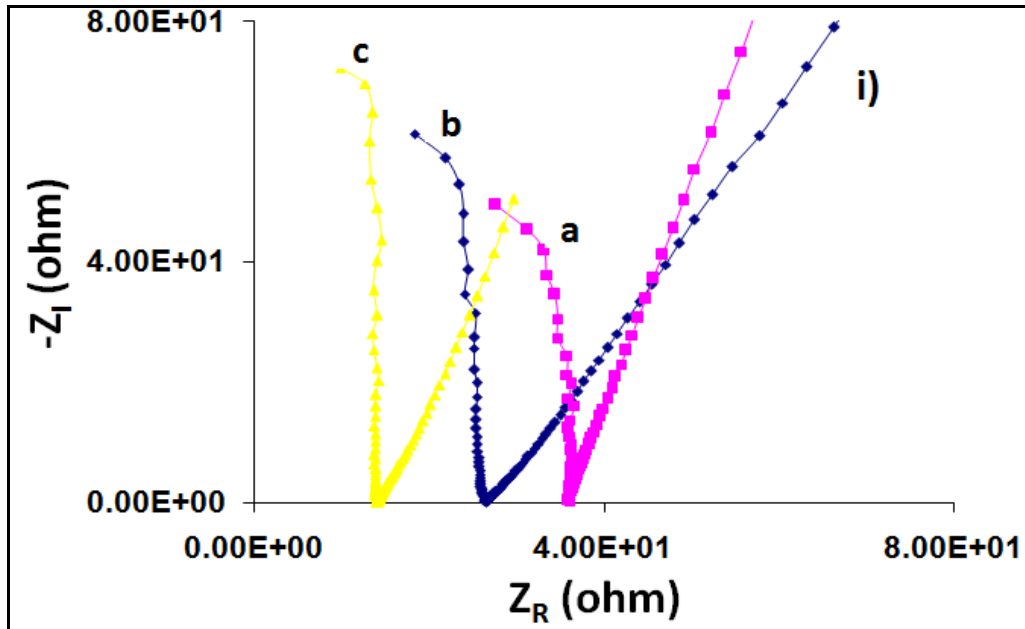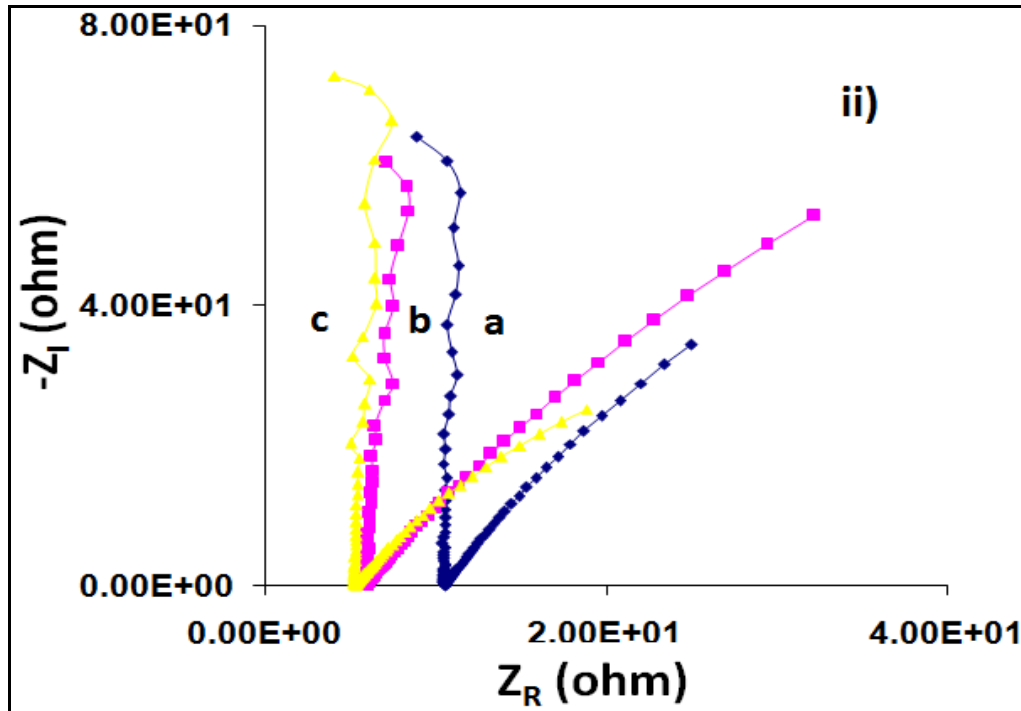
Figure 6.10 Complex impedance spectra of polymer electrolyte for (a) PEO- 20 wt % LiPF$_6$ (b) PEO -20 wt% LiPF$_6$ -15 wt% EC (c) PEO- 20 wt% LiPF$_6$ -15 wt% EC -5 wt% αCNTs at (i) 298K (ii) 373K.

Figure 6.11 shows the temperature dependence of conductivity for various electrolytes between 298 and 373K. It is evident that the room temperature conductivity increases with different chemical composition. The conductivity increases by 5 orders of magnitude with the addition of LiPF$_6$, 4 orders of magnitude with the addition of EC and 3 orders of magnitude with the addition of αCNTs. The sudden increase of conductivities is due to the role of lithium ions in the PEO, the increase in flexibility of the polymer chain due to the EC and high electrical conductivity properties of αCNTs on polymer electrolytes.

There is a sudden increase in conductivity for pure PEO electrolyte at 313 – 323K (Figure 6.11(a)). However, the ionic conductivity increases linearly beyond 323K. With the addition of LiPF$_6$, EC and αCNTs, the thermal effects are clearly observed in Figures 6.11 (b) – (d), which show a slight increase in conductivity in a wide temperature range. When EC was

added into the system, more salts are dissociated into ions, which have low viscosity and therefore increases ionic mobility. The addition of αCNTs increases the conductivity by inhibiting recrystallization of the PEO chains and providing Li^+ conducting pathway at the filler surface through Lewis Acid base interaction among different species in the electrolytes (Ulanski *et al.*, 1998). A transportation lithium ion within the polymer matrix requires low energy and hence increases the conductivity. This is possibly due to size of the filler and plasticizer molecule compared to the polymer molecule, which can penetrate easily into the polymer matrix (Pradhan *et al.*, 2005). The sample, which consists of $LiPF_6$, EC and αCNTs, shows lower activation energy at ambient temperature (298K ~ 373K). A transportation lithium ion within the polymer matrix requires low energy and hence increases the conductivity. This is possibly due to size of the filler and plasticizer molecule compared to the polymer molecule, which can penetrate easily into the polymer matrix (Pradhan *et al.*, 2005).
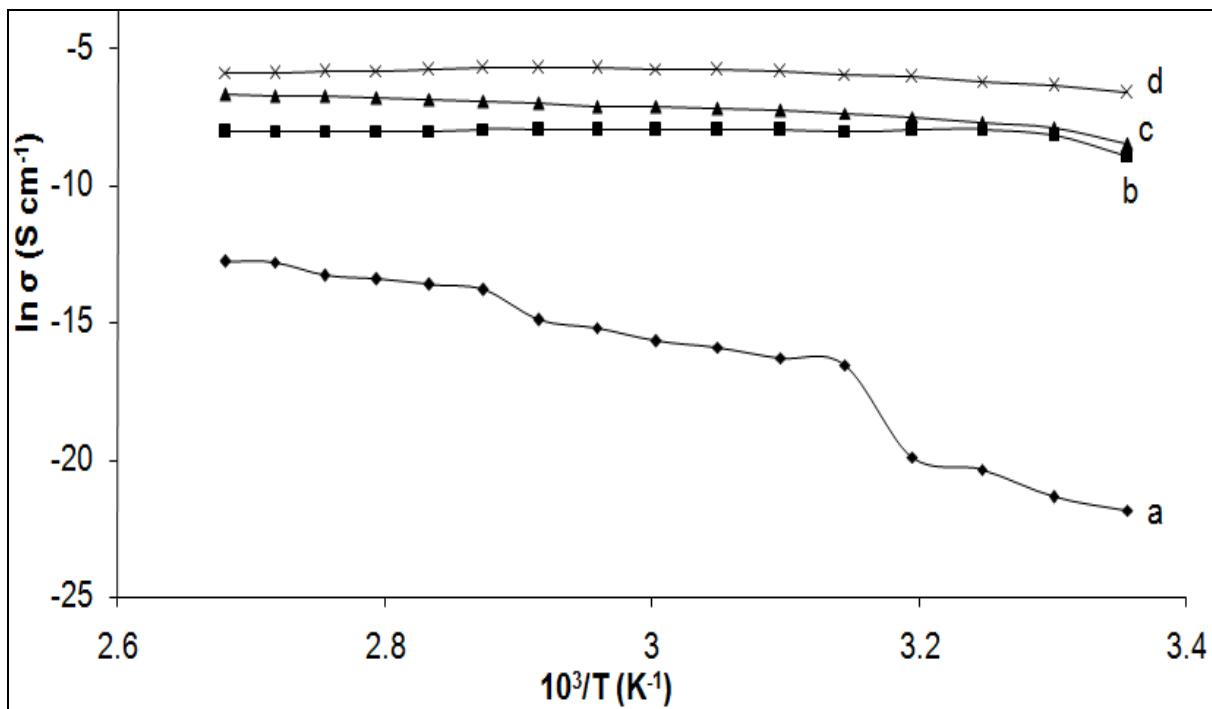
Figure 6.11 Conductivity dependence temperature of nanocomposite polymer electrolytes at optimum compositions (a) PEO; (b) PEO -20 wt% LiPF$_6$; (c) PEO -20 wt % LiPF$_6$ - 15 wt % EC (d) PEO -20 wt% LiPF$_6$ - 15 wt% EC -5 wt% αCNTs.

Table 6.1 The conductivity and activation energy values for the composite polymer electrolytes system

Polymer electrolytes	Conductivity at 298 K, σ (S cm^{-1})	Activation energy, E_A (eV)
PEO	3.25×10^{-10}	0.61
PEO + 20 wt .% LiPF$_6$	3.57×10^{-5}	0.19
PEO + 20 wt. % LiPF$_6$ + 15 wt. % EC	2.06×10^{-4}	0.14
PEO + 20 wt. % LiPF$_6$ + 15 wt. % EC + 5 wt. % CNT	1.30×10^{-3}	0.08

6.5   Dielectric Analysis of Nanocomposite Polymer Electrolytes at the optimum wt% of LiPF$_6$, EC and αCNTs

6.5.1   Dielectric Studies

Figures 6.12 and 6.13 show the frequency dependence of the dielectric constant and dielectric loss, ε_r and ε_i, at 298 and 373K for polymer nanocomposite electrolytes. Since appreciable relaxation peaks are not observed, the dielectric constants and losses, ε_r and ε_i, are used as to indicate that the increase in conductivity is mainly due to an increase in density of mobile ions (Majid and Arof, 2007). It is clearly observed that the values of ε_r and ε_i increase upon the addition of salt, plasticizer and filler into the polymer matrix. The dielectric constants decrease continuously with increasing frequency, and reaches a constant value at about 2.5 kHz. A rapid decrease in dielectric constant may be noticed above a frequency range of 4 kHz. This may be attributed to the tendency of dipoles in the macromolecules to orient themselves in the direction of the applied field within the low frequency range.

However, in the high frequency range, the dipoles are unable to orient themselves in the direction of the applied field. Hence, the values of the dielectric constant decreases (Reicha *et al*., 1991). The conductivity in polymer-salt is due to the migration of Li$^+$ (Stevens *et al*., 1997). The dielectric permittivity rises sharply towards low frequencies due to electrode polarization effects (Campbell *et al*., 2001; Mishra *et al*., 1998). Thus, the addition of carbon nanotubes is expected to increase the degree of salt dissociation and redissociation for the increase in number of mobile Li$^+$. The enhancement in conductivity is explained based on the assumption that the filler particles act as a supporting matrix. This, in turn, helps to retain an overall solid structure with unchanged volume for Li$^+$ transport at ambient and elevated temperatures (Park *et al*., 2004). The observed variations in ε_r versus frequency

for the two electrolytes could be attributed to the build-up of space charge regions at the electrode-electrolyte interface.

At low-frequency regions, the dielectric constants ε_r for both electrolytes are proportional to ω^{n-1}, indicating non-Debye dependence (Gondivaraj *et al.*, 1995). This implies that the conductivity exhibits relaxation, which is non-exponential in time (Balaya and Goyal, 2005). This dispersion reflects the existence of space charge polarization where there is time for the charges to build up at the interface before the applied field changes direction, giving a large value of ε_r (Majid and Arof, 2007). On the other hand, there is no time for charge build-up at the interface with increasing frequencies due to the increasing rate of electric field reversal. The polarization due to charge accumulation decreases, which leads to the decrease in value of ε_r (Molak *et al.*, 2005; Shafee, 1996).
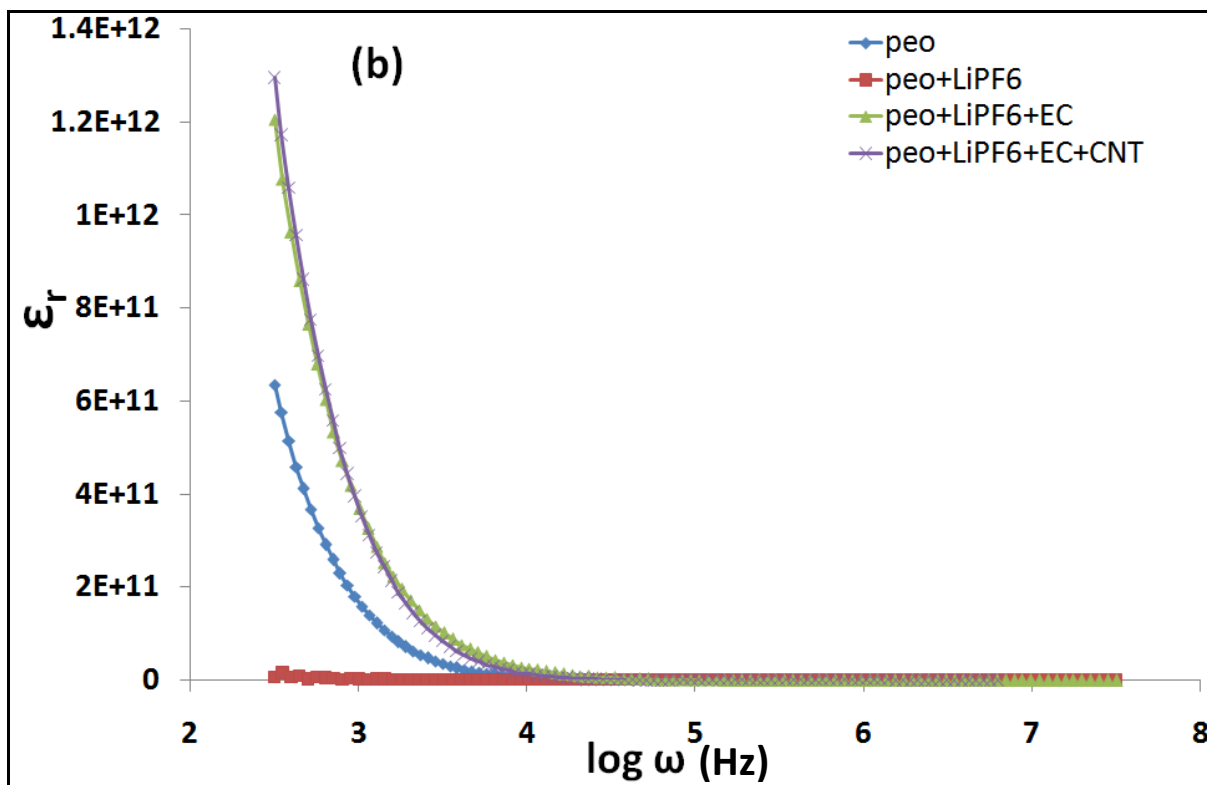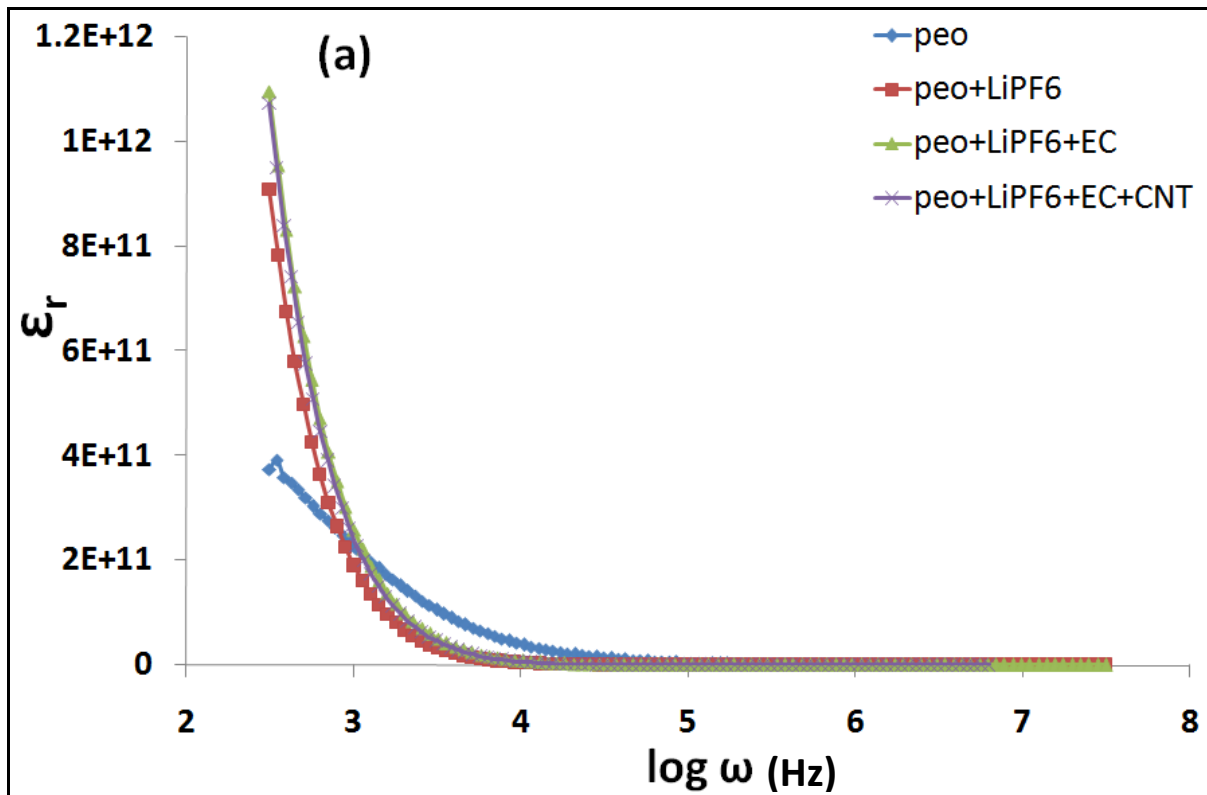
Figure 6.12. Variations of dielectric constant (ε_r) of nanocomposite polymer electrolytes with frequency for (a) 298K; (b) 373K.

(a)

peo
peo+LiPF6
peo+LiPF6+EC
peo+LiPF6+EC+CNT

(b)

peo
peo+LiPF6
peo+LiPF6+EC
peo+LiPF6+EC+CNT
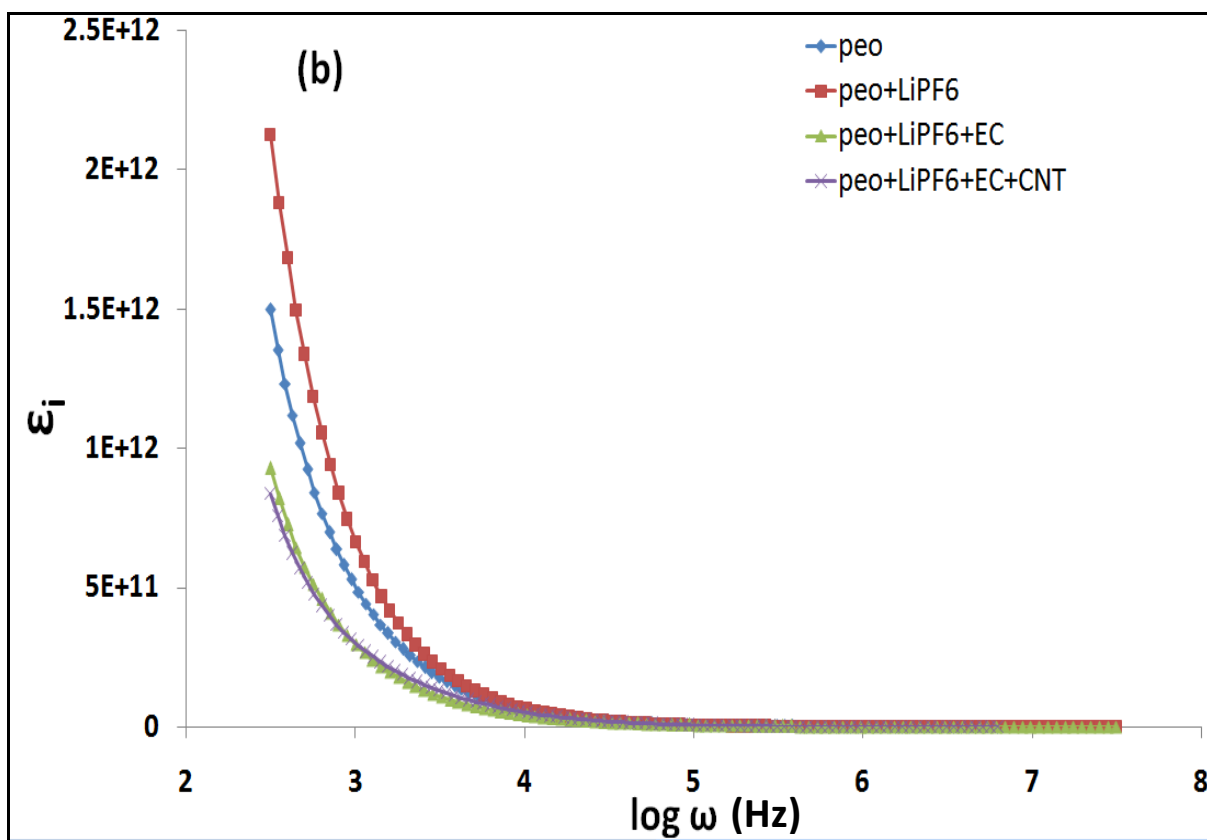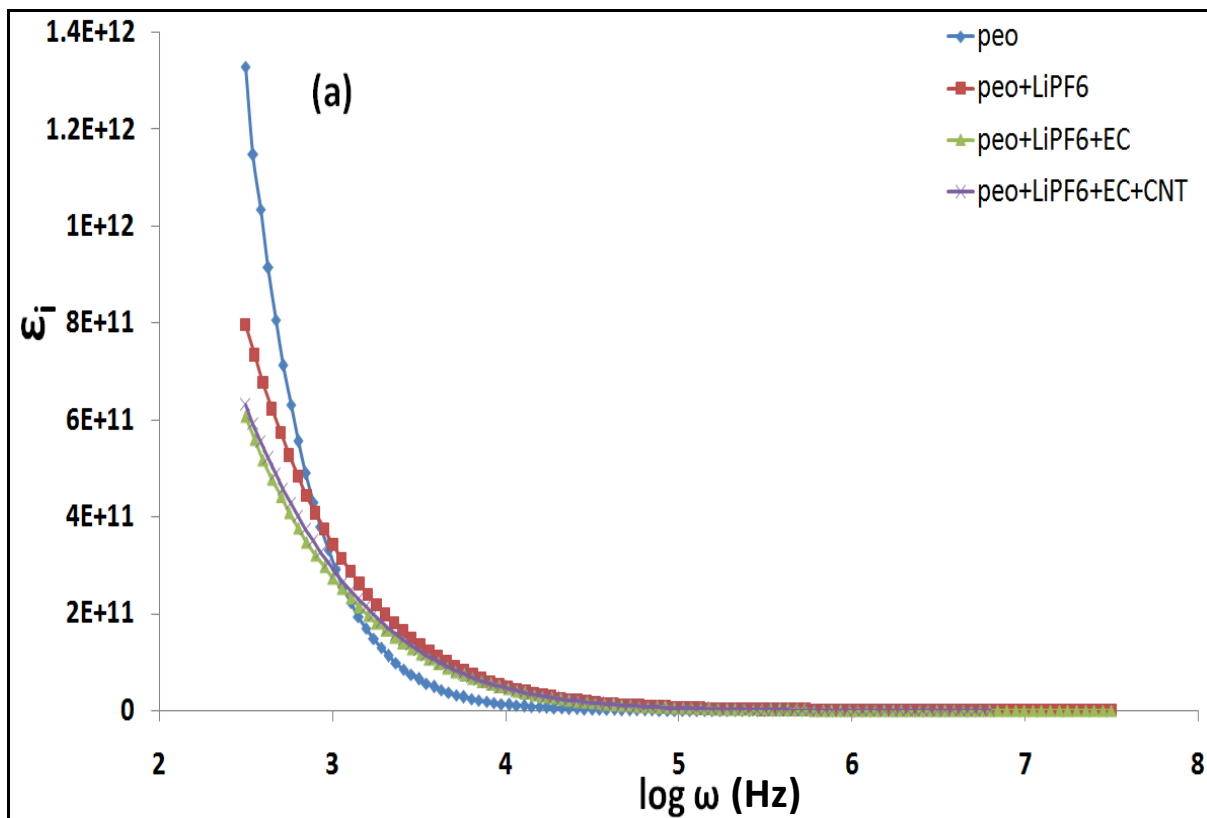
Figure 6.13 Variations of dielectric loss (ε_i) of nanocomposite polymer electrolytes with frequency for (a) 298K; (b) 373K

6.5.2 Electrical Modulus

Figures 6.14 and 6.15 depict the variations of real and imaginary electrical modulus (M_r & M_i) for PEO nanocomposite electrolytes. The long tail due to the large capacitance which is associated with the electrodes at low-frequency regions, confirms the non-Debye behaviour (Shafee, 1996; Muralidharan *et al.*, 2005; Baskaran *et al.*, 2006; Prabakar *et al.*, 2003). Since definitive peaks are not observed in the M_i plots for both cases, tan δ was plotted with respect to frequency for PEO nanocomposite. This is shown in Figure 6.16.
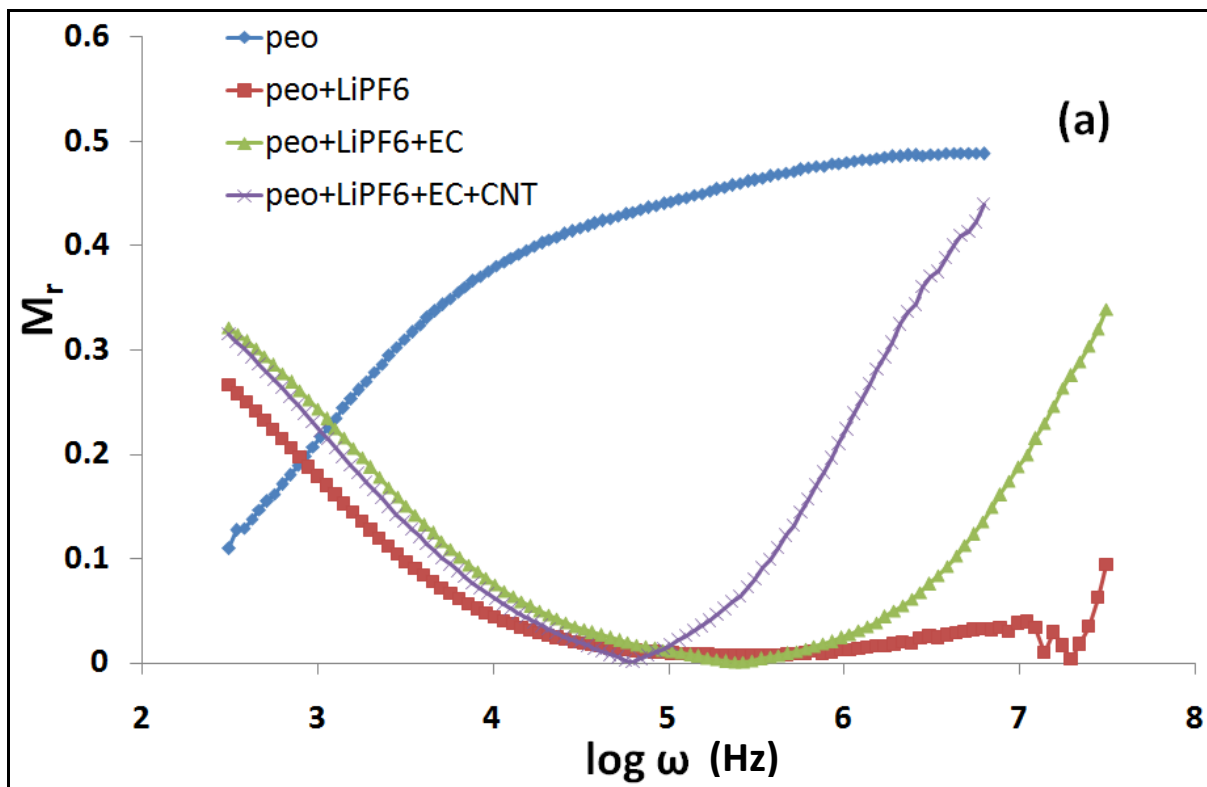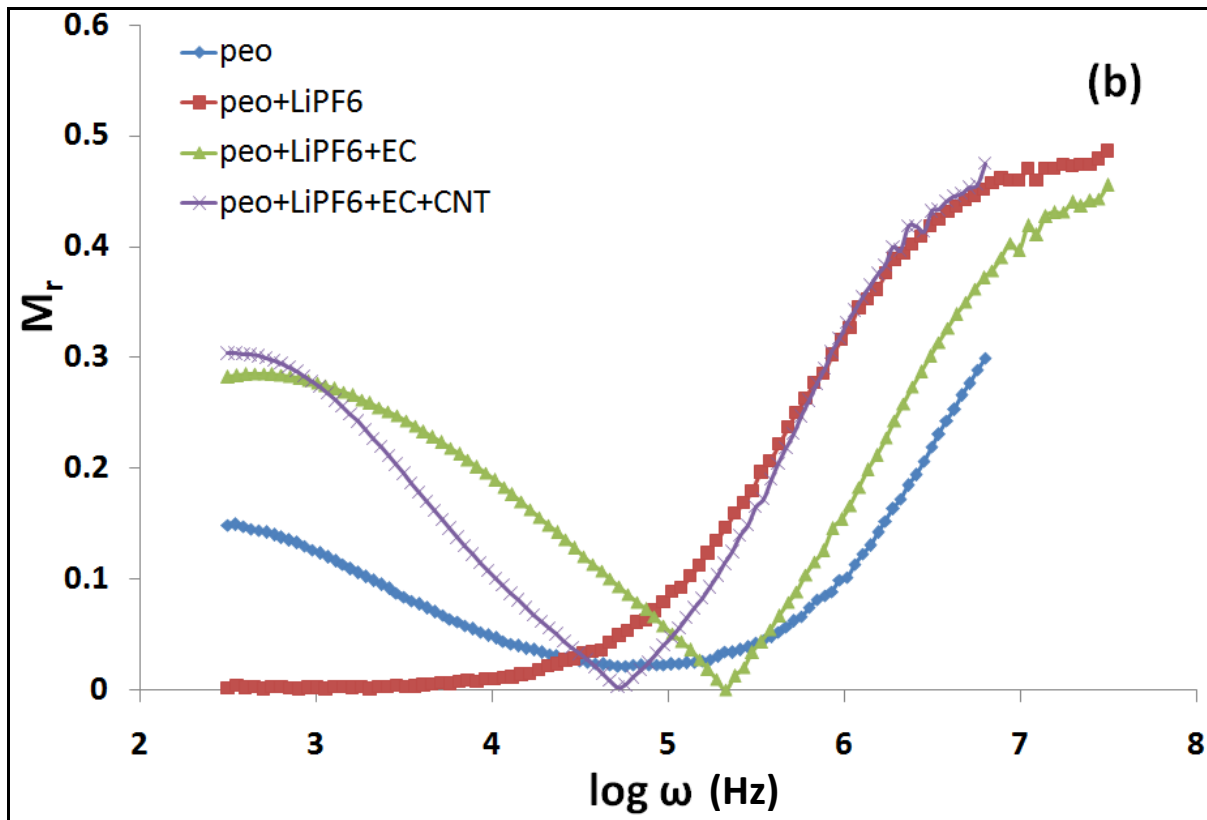
Figure 6.14 Variations of the real part of modulus M_r of nanocomposite polymer electrolytes with frequency for (a) 298K; (b) 373K.
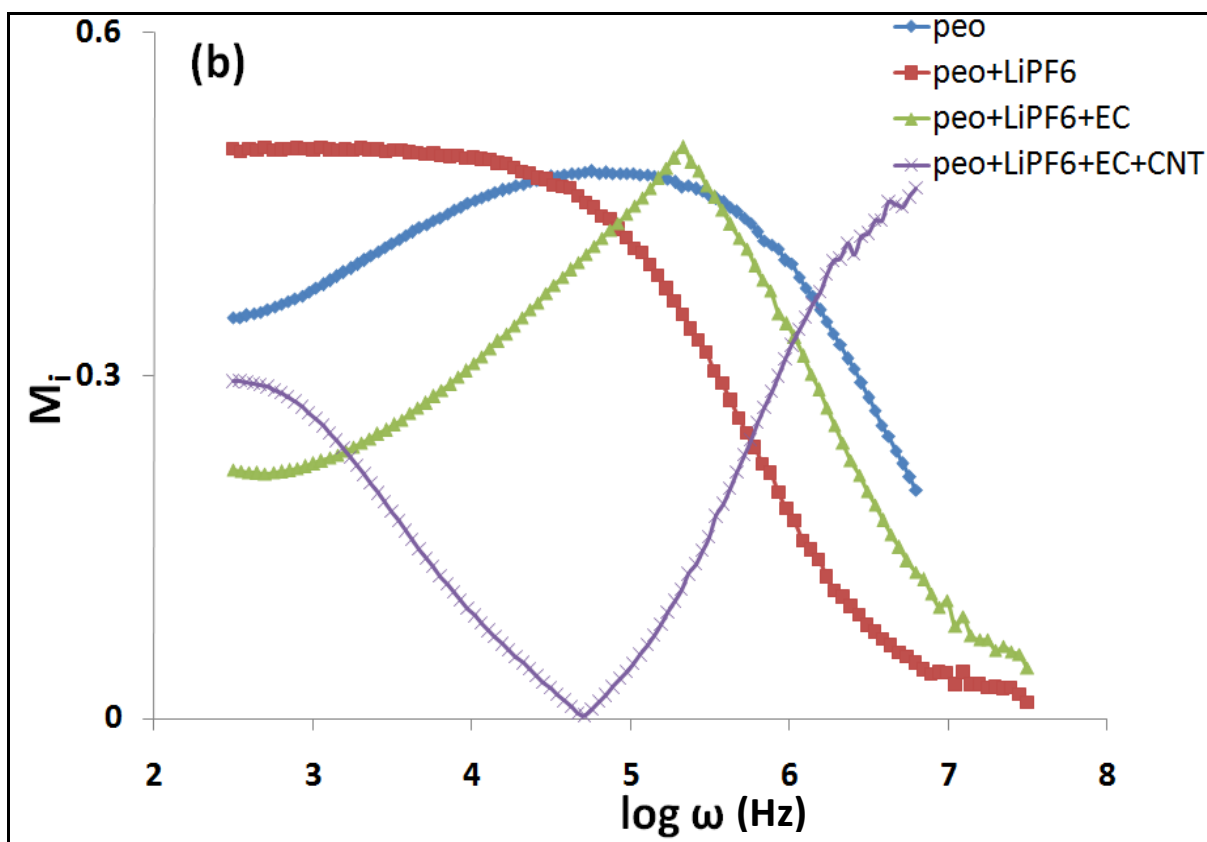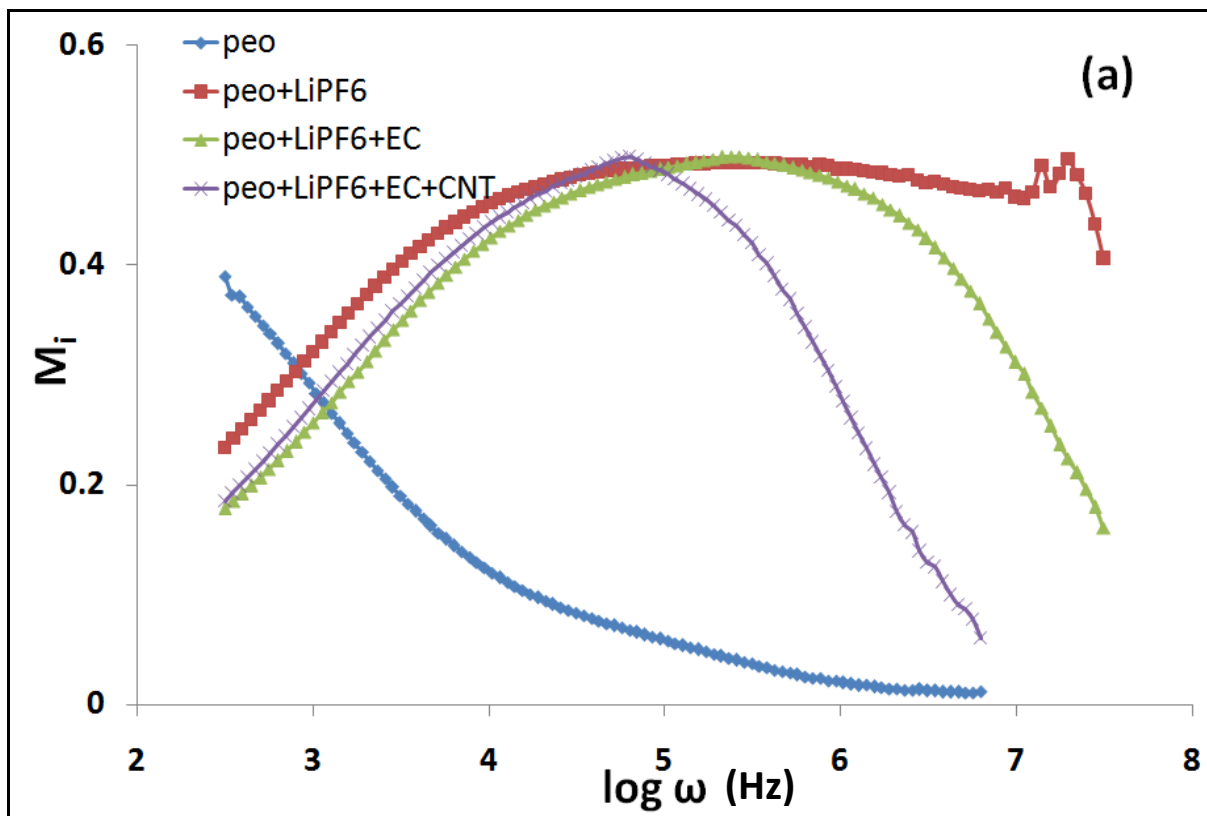
Figure 6.15 Variations of the imaginary part of modulus M_i of nanocomposites polymer electrolytes with frequency for (a) 298K; (b) 373K.

6.5.3 Loss tangent (tan δ)

From Figure 6.16, it can be seen that tan δ increases with increasing frequency, passes through a maximum value and thereafter decreases for pure PEO. The maxima of tan δ shifts towards higher frequencies and the height of the peak increases with increasing temperature. This is attributed to the increment in number of charge carriers for conduction which decreases the resistivity of the samples (Prabakar *et al*., 2003). When salt, EC and αCNTs were added into the polymer complex, a sharp peak is observed at low frequencies for PEO-LiPF$_6$ complex, and at high frequencies for PEO-LiPF$_6$-EC and PEO-LiPF$_6$-EC-αCNTs. For PEO-LiPF$_6$ complex, the relaxation peak shifts towards higher frequencies with increasing temperature, which indicates that the charge carrier is thermally activated. The dielectric response caused by ion relaxation was studied using the reciprocal quantity of electric permittivity (Gokulamurali *et al*, 1992). For PEO-LiPF$_6$-EC, the frequency values shift towards higher frequencies compared with the PEO-LiPF$_6$ complex
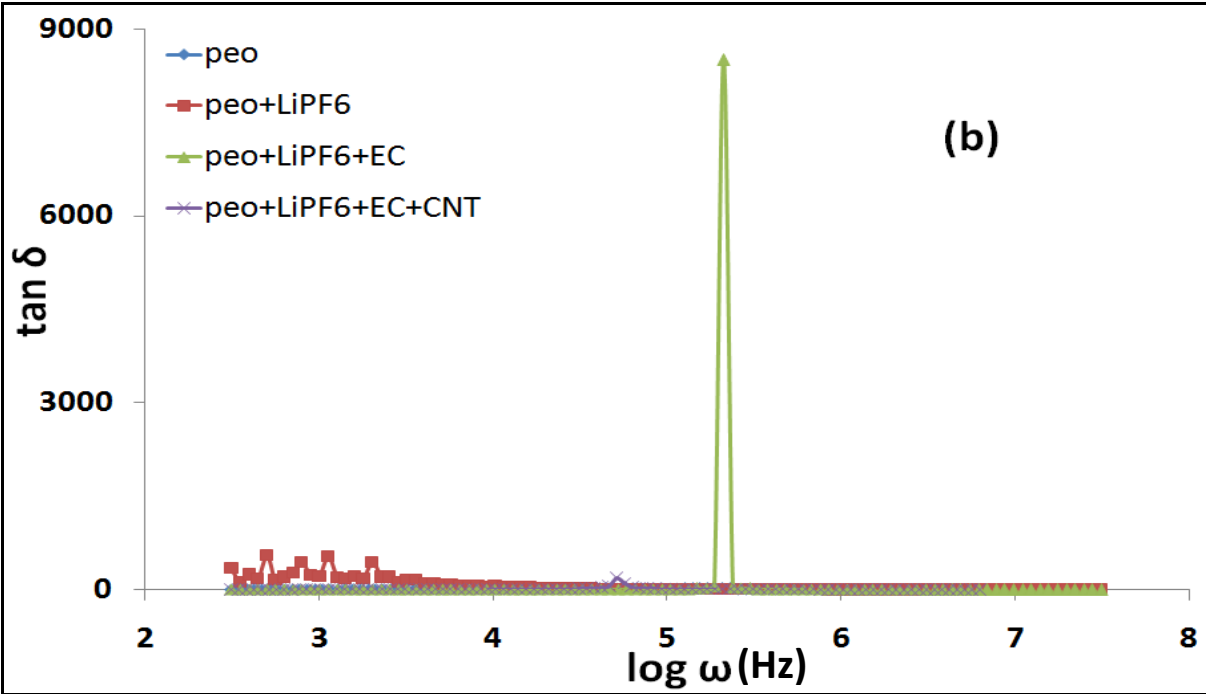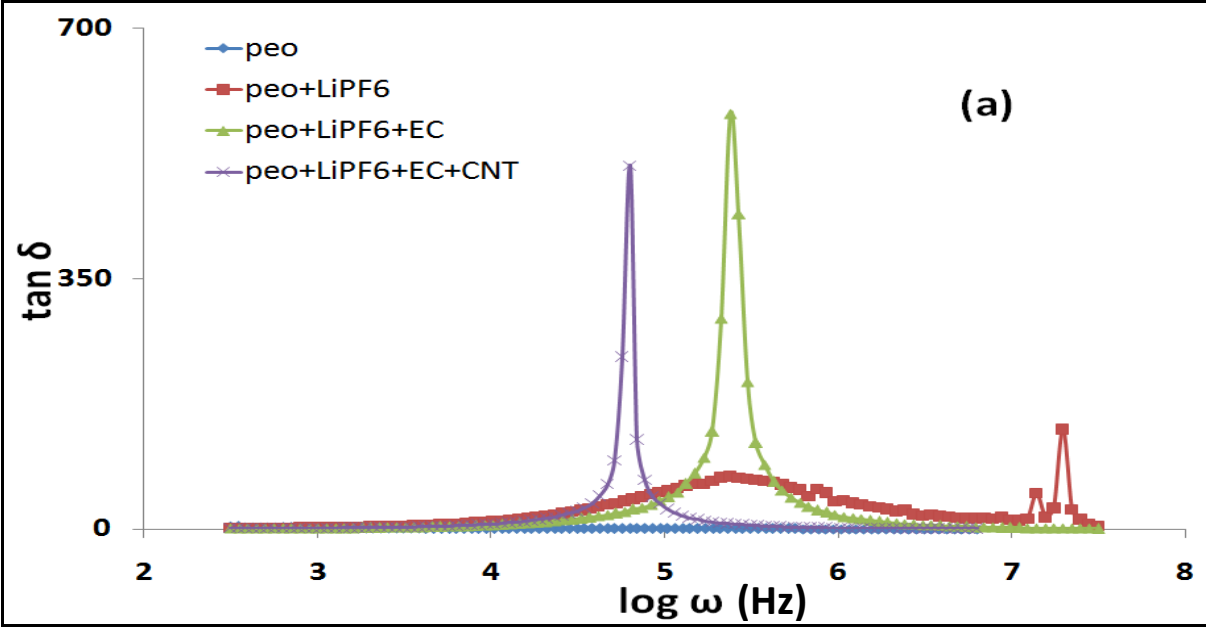
Figure 6.16 Variations of loss tangent (tan δ) of nanocomposite polymer electrolytes with frequency for (a) 297K; (b) 373K.

CHAPTER SEVEN

Optical Studies on Nanocomposite Solid Polymer Electrolytes

7.1   UV-Vis Analysis

Figure 7.1 shows the optical absorption spectra recorded for polymer electrolytes in the region of 200 – 300 nm. In the UV region, the band at 200 nm have been observed for pure PEO and PEO doped with various wt% of $LiPF_6$, EC and αCNT with different absorption intensities and wavelengths.
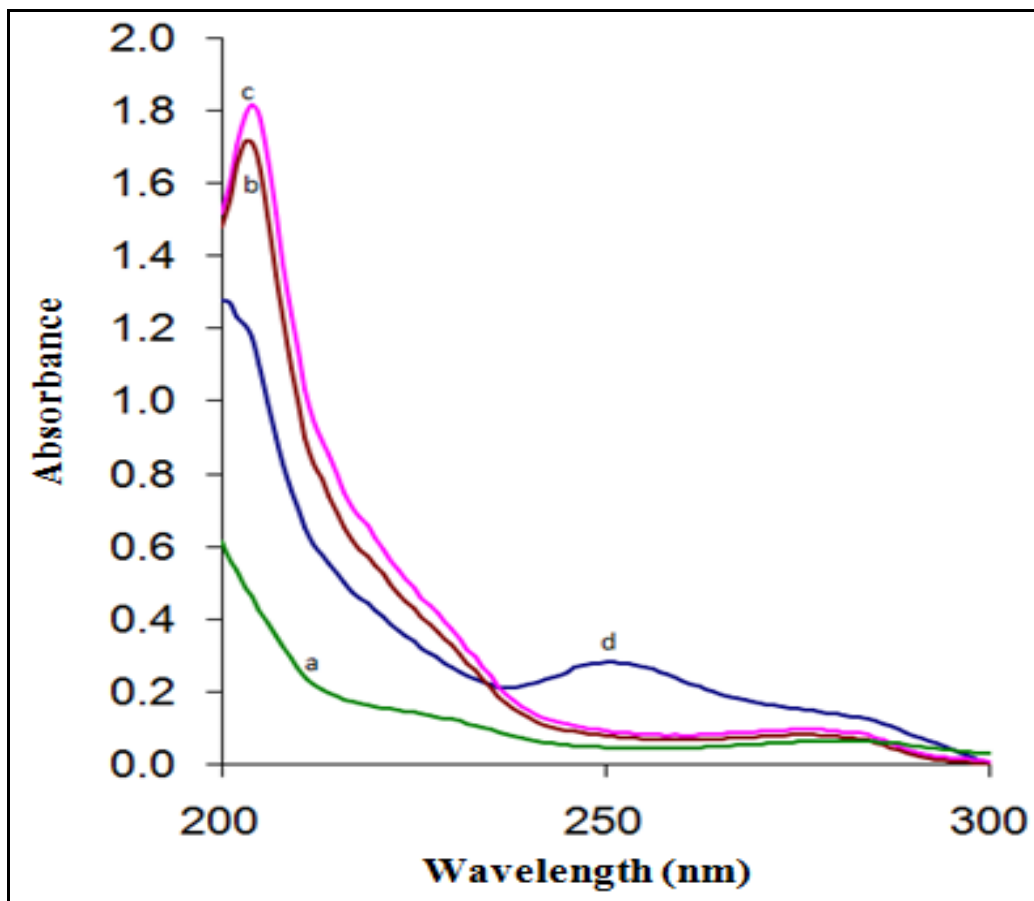
Figure 7.1 Absorption spectra for (a)PEO (b)PEO-LiPF$_6$ (c)PEO-LiPF$_6$-EC and (d) PEO-LiPF$_6$-EC-αCNT

This absorption peak may be attributed to the n→σ⁺ transition which is very sensitive to hydrogen bonding (Rao, 1967). The absorption band for PEO-LiPF$_6$-EC-αCNT at 250 nm may be assigned as π→π* which comes from unsaturated bonds mainly C=O and C=C, which are present in the anion (CH$_3$COO⁻) and tail head of the polymer, respectively (Rao, 1967). Figure 7.1 shows a shift in absorption edge (AE) towards the higher wavelengths. These shifts in the AE indicate the formation of inter/intra molecular hydrogen bonding mainly between lithium ions with that of these adjacent OH groups. These bonds reflect the variation of energy bandgap which arises due to the variation in crystallinity within the polymer matrix (Rao, 1967).

Figure 7.2 shows the transmittance spectra for polymer electrolytes in the region of 200 – 400 nm. As illustrated in Figure 7.2, the spectra show interference pattern with a sharp fall of transmittance at the band edge. One can observe for pure and doped polymer electrolytes, nearly zero transmission intensity in the wavelength range 200 - 220 nm. Then the transmission intensity starts increasing at 220 nm until it reaches 80% when LiPF$_6$ and EC were added. Then the intensity decrease below 60% when added with CNT. The transmission intensity gradually increases up to 330 nm and reaches a constant value.
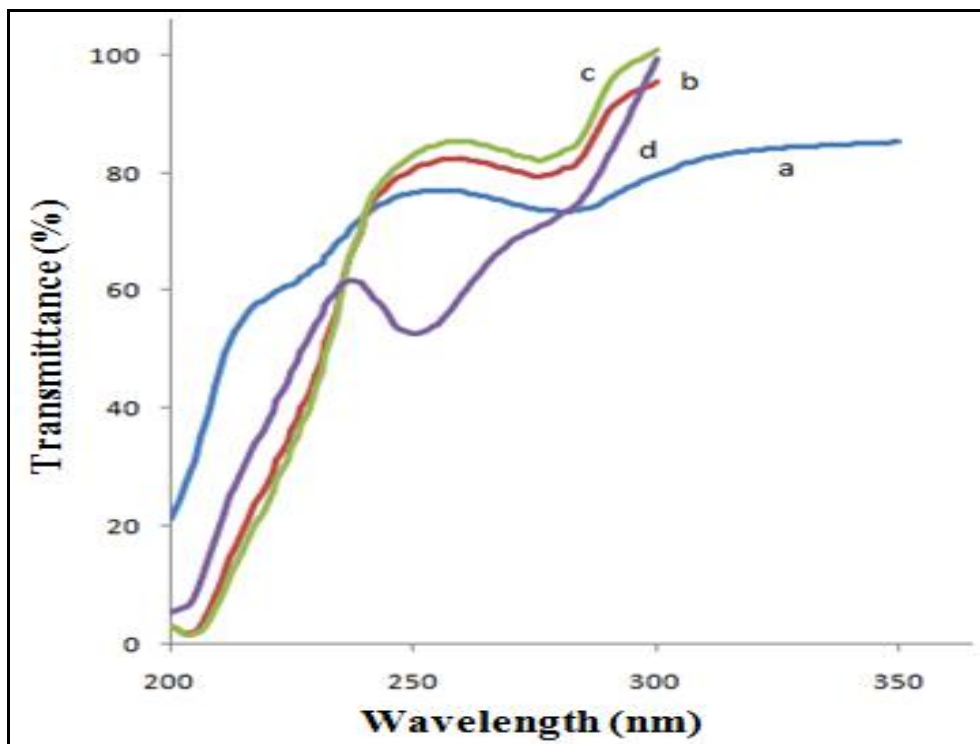
Figure 7.2 Transmittion spectra for (a) PEO (b) PEO-LiPF$_6$ (c) PEO-LiPF$_6$-EC and (d) PEO-LiPF$_6$-EC-αCNT

7.2   Photoluminescence (PL) Analysis

The photoluminescence spectra of all samples were recorded and shown in Figure 7.3. The wavelength of excitation chosen for all samples is 201-250 nm. It can be seen that the emission peaks are at various spectral positions (338, 340, 451 and 527 nm). These bands may be assigned to the recombination of free change carriers at the defects in PEO. It is found that the fluorescence intensity of the doped films is lower than that of pure PEO. The decrease in intensity of the emission peak may be due to the weak interactions between the dopant and the polymer and aggregation of dopant molecules (Mu *et al.*, 1998).
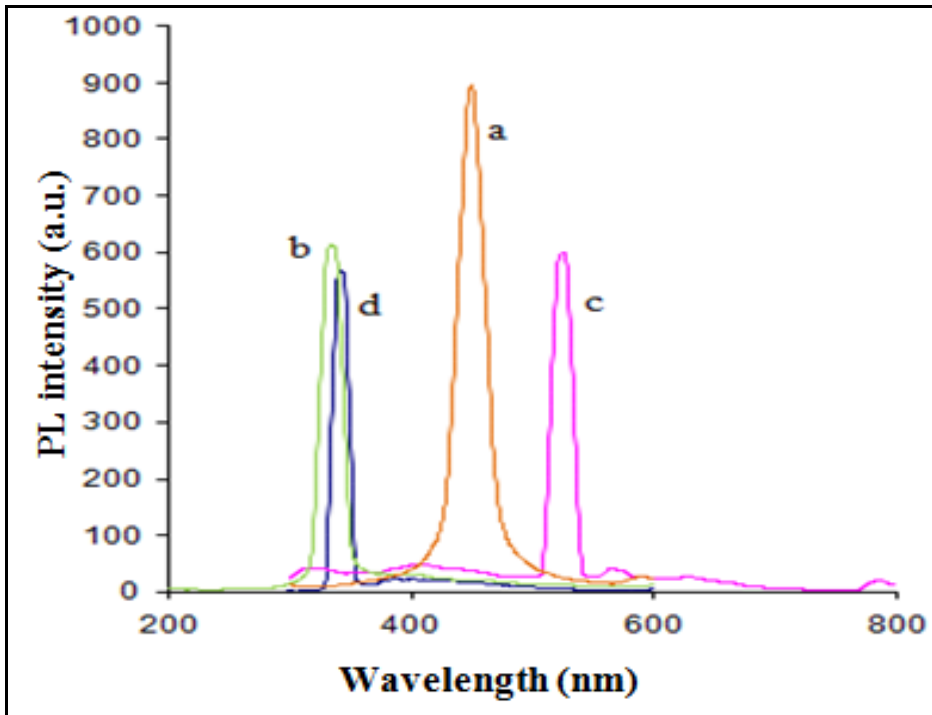
Figure 7.3 Photoluminescence spectra of (a) PEO (b)PEO-LiPF$_6$ (c)PEO-LiPF$_6$-EC (d)PEO-LiPF$_6$-EC-αCNT.

7.3 Determination of Optical Band Gap
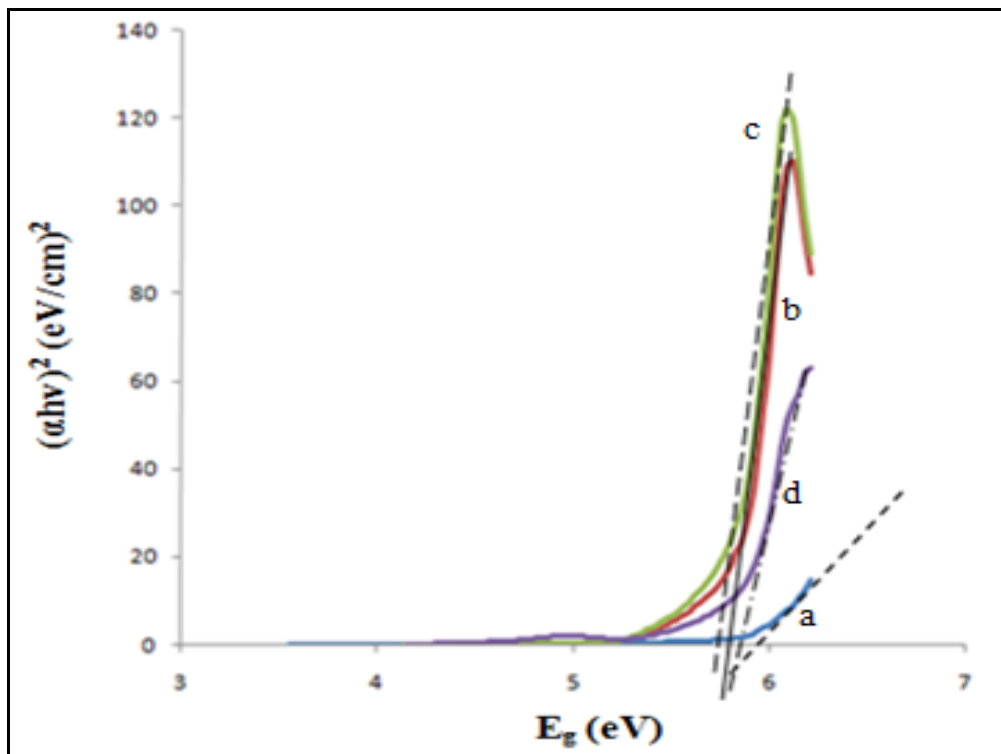
Figure 7.4 Plots for direct band gap in polymer electrolytes for (a) PEO (b)PEO-LiPF$_6$ (c)PEO-LiPF$_6$-EC (d)PEO-LiPF$_6$-EC-αCNT
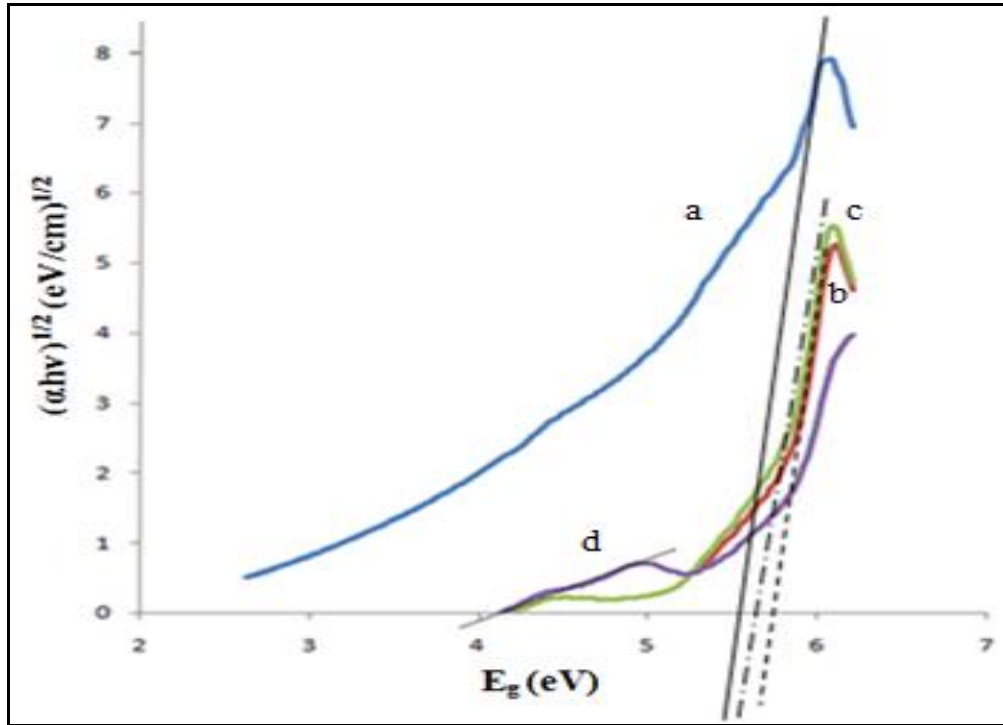
Figure 7.5 Plots for indirect band gap in polymer electrolytes for (a) PEO (b)PEO-LiPF$_6$ (c) PEO-LiPF$_6$-EC (d)PEO-LiPF$_6$-EC-αCNT

Table 7.1 Direct and indirect optical band gap

Sample	E$_g$ Direct	E$_g$ Indirect
PEO	5.92	5.70
PEO+20wt%LiPF$_6$	5.90	5.74
PEO+20wt%LiPF$_6$+15wt%EC	5.80	5.63
PEO+20wt%LiPF$_6$+15wt%EC +5wt%CNT	4.60	4.42

Figures 7.4 and 7.5 show the Tauc's plots with variation of $(\alpha h\upsilon)^{1/2}$ and $(\alpha h\upsilon)^2$ with hυ.

Optical band gap E_g can be determined by the extrapolation of best fit line between $(\alpha h\upsilon)^{1/2}$ and

$(\alpha h\upsilon)^2$ intercept the hυ axis. Variation of optical band gap with different concentrations of LiPF$_6$, EC and αCNT is summarized in Table 7.1. By adding different elements into PEO complexes, the optical band decrease from 5.92 to 4.60 eV for direct optical band gap and from 5.70 to 4.42 eV for indirect optical band gap. The decrease in band gap is caused by an alloying effect, namely a compositional change in the host material itself (Sharma *et al*., 2008; Kitao *et al*., 1981). This effect is due to the change in bond angles and/or bond lengths. This shows that αCNTs induce structural modifications in the parent matrix which are clearly reflected in the E_g values. LiPF$_6$, EC and αCNT are responsible for the formation of defects in the electrolytes. These defects produce the localized states in the optical band gap, or in other word, the increase in the degree of disorder in the films. Thus, this state is responsible for decreasing energy band gap.

Similar behaviour can also be seen in the activation energies obtained from the DC conductivity as shown in Table 6.1, in Chapter Six. The magnitudes of the activation energy obtained from conductivity values are small in comparison with optical band gap energy data. This is due to the fact that the nature between activation energy and optical band gap energy is different. The activation energy corresponds to the energy required for conduction from one site to another site, while the optical band gap corresponds to inter band transition (Umadevi *et al*., 2002). These results are in agreement with those obtained from XRD and thermal results in this work.

7.4   Refractive Index Analysis
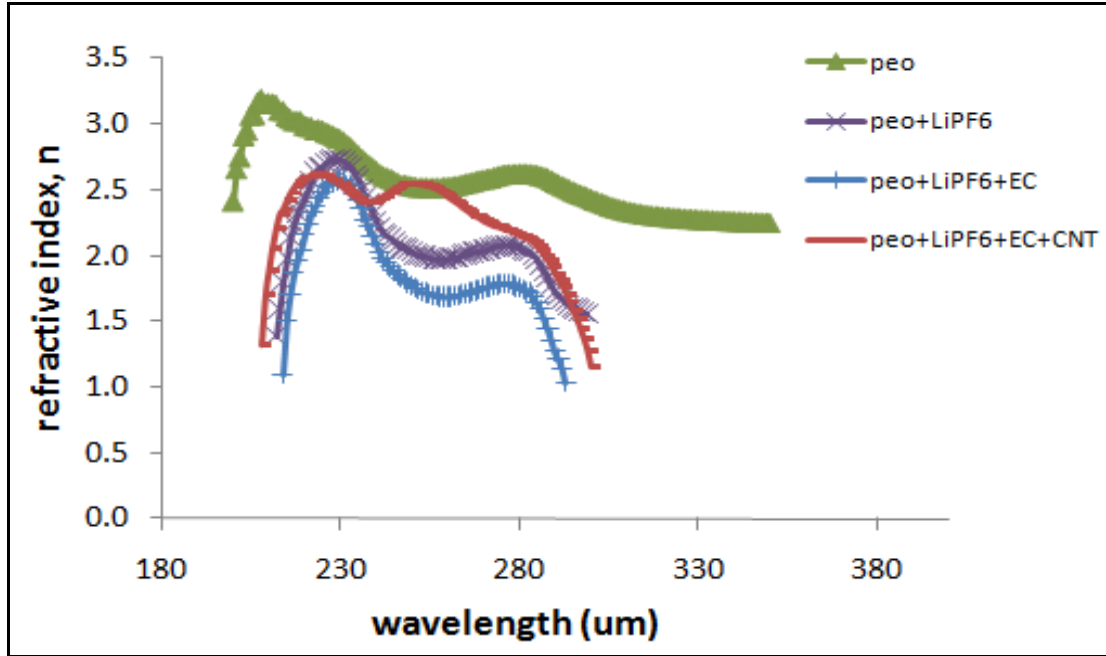
Figure 7.6 Refractive index of solid polymer electrolytes

Figure 7.6 shows refractive index changes for composite polymer electrolytes in the region of 200 – 350 nm. The refractive index was determined from the equations below:

$$n = \frac{(1 + \sqrt{R})}{(1 - \sqrt{R})} \tag{7.1}$$

$$R + T + (((= 1 \tag{7.2}$$

where R is reflectance and n is refractive index. The refractive index for pure PEO is maximum at 3.06 and starts to decrease at longer wavelengths. The refractive index is decreased when LiPF$_6$ and EC were added into polymer complex. The refractive index decreases to 2.69 and 2.04 in PEO-LiPF$_6$ and decrease to 2.57 and 1.73. When αCNTs was added into the polymer complex,

the refractive index increases to 2.61 and 2.53. In addition, the polymer films change colour from white transference to dark black-color. This is because different colours have different wavenumbers and refractive index of materials varies with the frequency of radiated light. Changes of colour from white to black also indicate a change in the refractive index, which can be related to changes in density or to increasing freedom of polymer chain movement (Marzantowicz *et al*., 2005).

CHAPTER EIGHT

Theoretical Studies on Nanocomposite Polymer Electrolytes using Neural Networks

8.1 Optimization of Neural Network for Ionic Conductivity of Nanocomposite Solid Polymer Electrolyte System (PEO–LiPF$_6$–EC–CNT)

The database compiled from experimental data consists of 5 inputs including the chemical compositions and temperature, as shown in Table A1 (See Appendix).

The network model for ionic conductivity consists of 5 input nodes, a number of hidden nodes and an output node representing the ionic conductivity. The complexity of the model is controlled by the number of hidden units Figure 3.18 and the values of the 7 regularisation constants σ_w, one associated with each of the 5 inputs, one for biases and one for all weights connected to the output. Figure 8.1 shows that the inferred noise level decreases as the number of hidden units increases. However, the complexity of the model also increases with the number of hidden units. A high degree of complexity may not be justifiable. To select the correct complexity, it is necessary to examine how the model generalises on previously unseen data in the test data set using the test error. The latter is defined as:

$$T_e = 0.5 \sum_n (y_n - t_n)^2 \tag{8.1}$$

where y_n is the predicted ionic conductivity and t_n is its measured value. Figure 8.2 shows that the test error first decreases, but begins to increase again as a function of the number of hidden units. Figures 8.3 – 8.4 show the behaviour of the training and test data which exhibit a similar degree of scatter in both graphs, indicating that the complexity of this particular model is optimum. The error bars in Figures 8.3 – 8.4 include the error bars of the underlying function and the inferred noise level in the dataset σ_v. The test error is a measure of the performance of a model. Another useful measure is the "log predictive error", for which the penalty for making a wild prediction is accompanied by an appropriately large error bar. Assuming that for each example n, the model gives a prediction with error (LPE) the log predictive error (LPE) as shown in Equation 8.2:

$$LPE = \sum_n \left[\frac{\frac{1}{2}(t_n - y_n)^2}{\sigma_n^2} + \log\left(\sqrt{2n}\sigma_n\right) \right] \qquad (8.2)$$

Figure 8.4 shows the log predictive error as a function of hidden units.
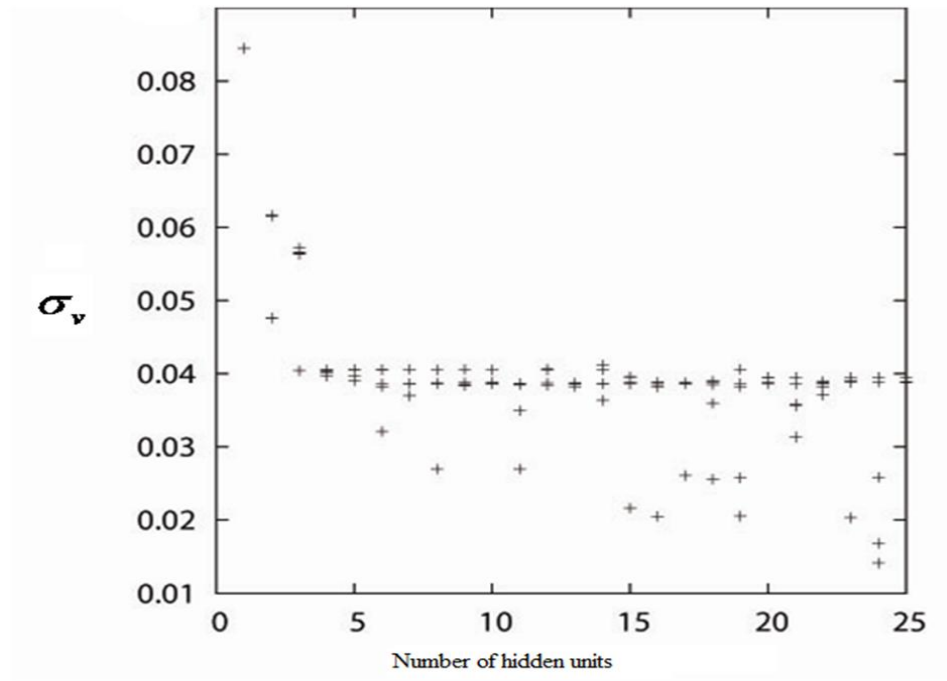
Figure 8.1: A variation in σ_v (the model perceived level of noise in the data) as function of number of hidden units
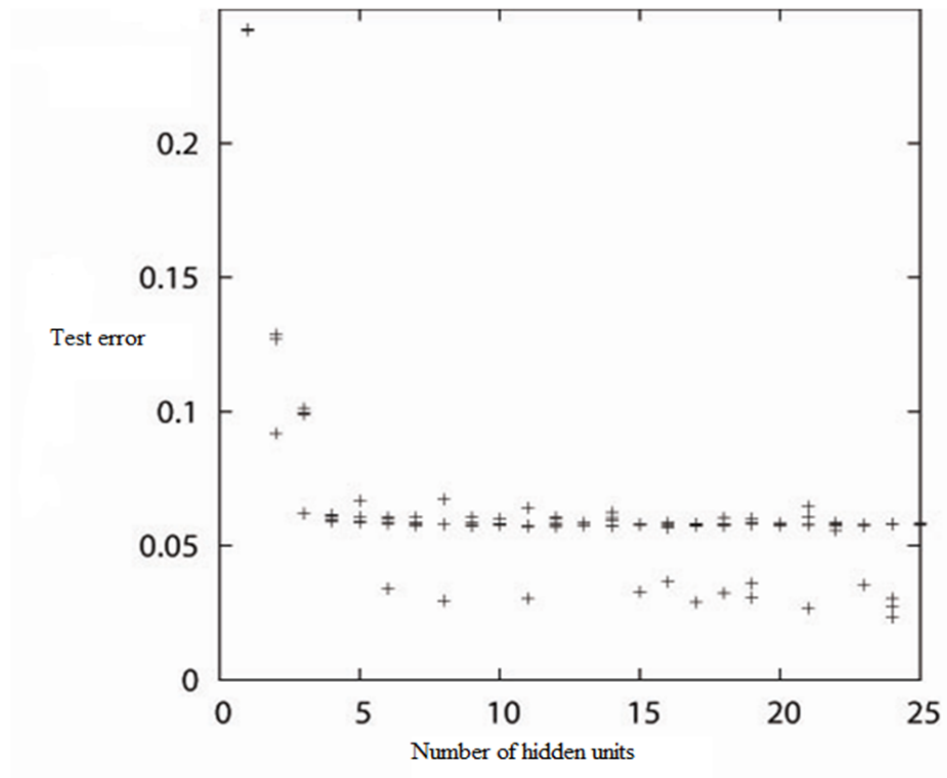
Figure 8.2: Test error as a function of the number of hidden units
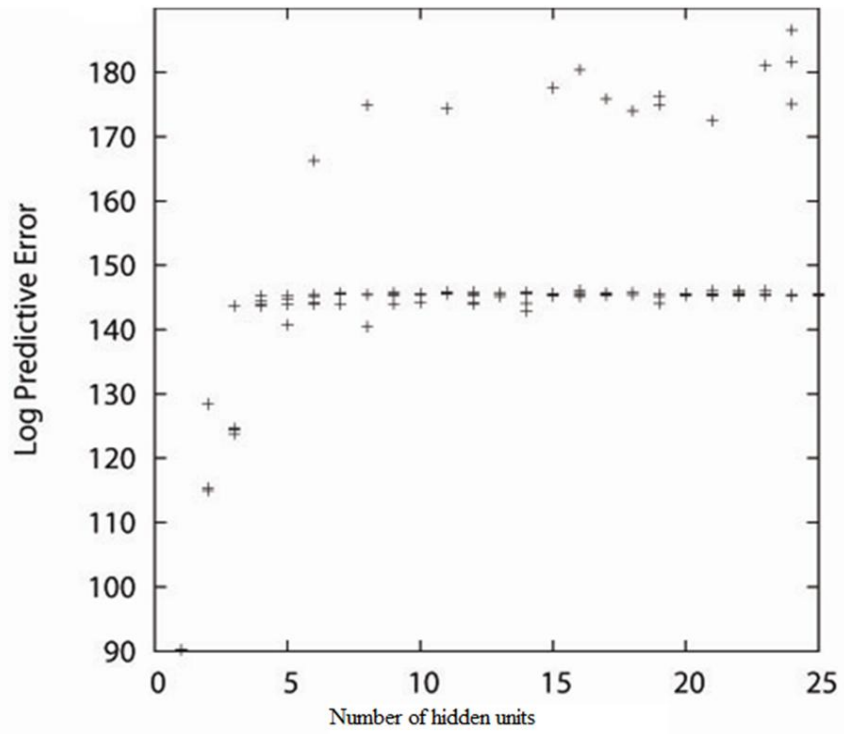
Figure 8.3: Log predictive error as a function of the number of hidden units
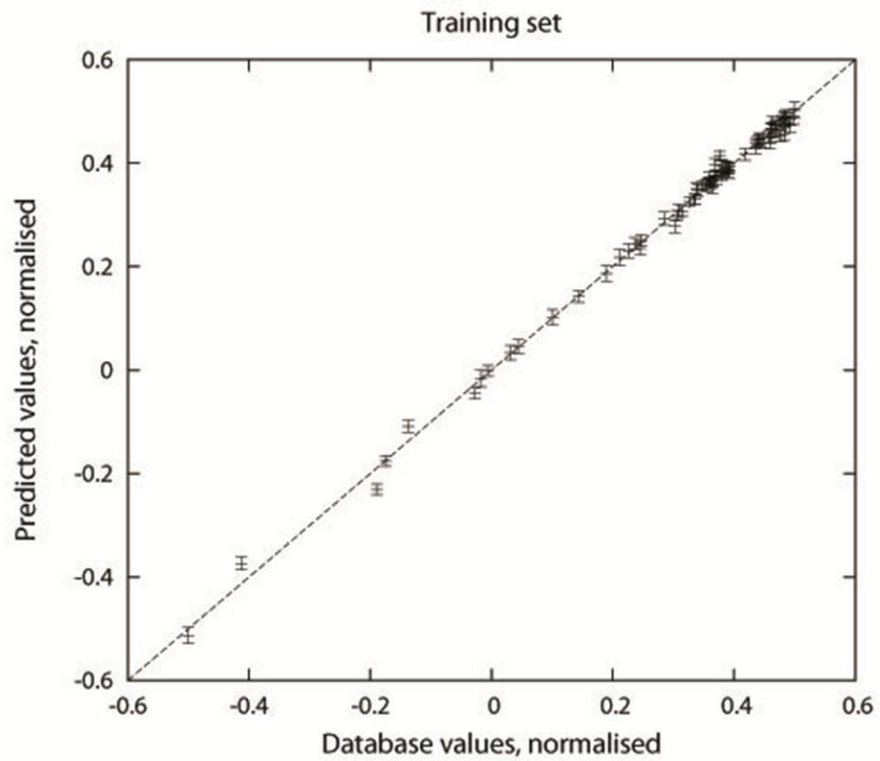
Figure 8.4: Typical performance of the trained model on training data
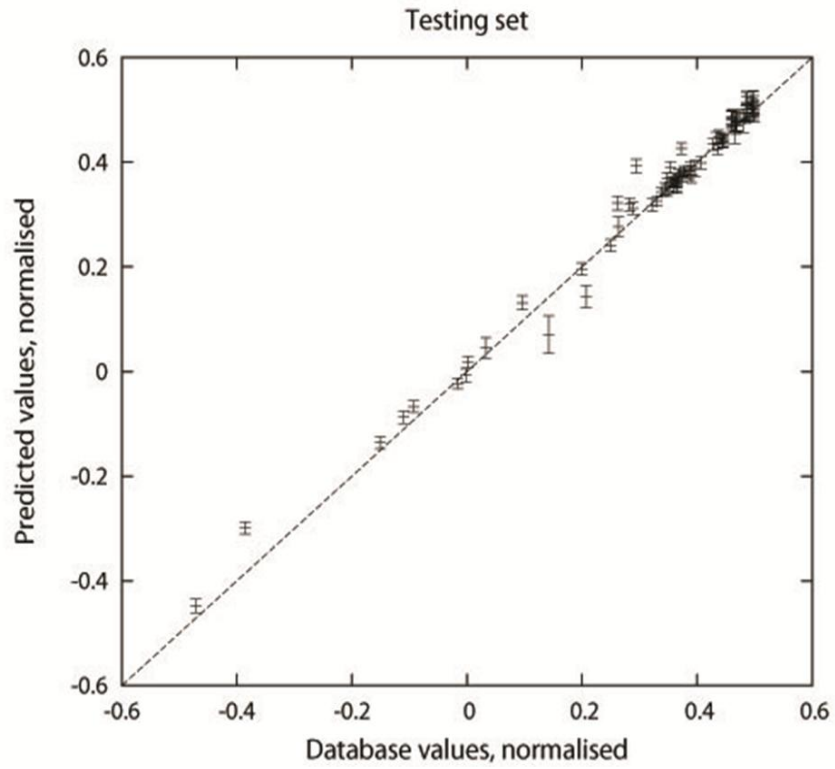
Figure 8.5: Typical performance of the trained model on test data
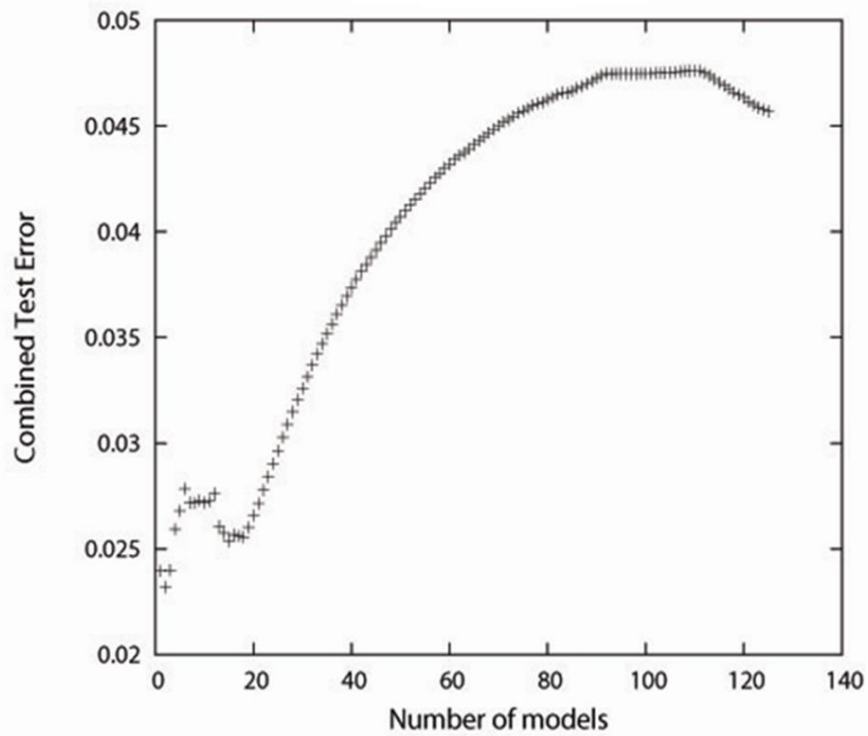
Figure 8.6: Test error as a function of the number of members in a committee

When making predictions, MacKay (Rupp et al., 2008; Ramesh et al., 2008; Appetecchi and Passerini, 2000) recommended the use of multiple good models instead of just one best model. This is called 'forming a committee'. The committee prediction $\bar{y}$ is obtained using the expression:

$$\bar{y} = \frac{1}{L} \sum_i y_i \qquad (8.3)$$

where L is the size of the committee and y_i is the estimate of a particular model i. The optimum size of the committee is determined from the validation error of the committee's predictions using the test dataset. In the present analysis, a committee of models is used to make more reliable predictions. The models are ranked according to their log predictive error. Committees are then formed by combining the predictions of best M models, where M gives the number of members in a given committee model. The test errors for the first 120 committees are shown in Figure 8.6. A committee of the best three models gives the minimum error. Each constituent model of the committee is therefore re-trained on the entire dataset, beginning with the weights previously determined. Figure 8.7 shows the results from the new training on the entire dataset. Consistent with the reduction in test error illustrated in Figure 8.6, it is evident that the committee model outperforms the single best model. The re-trained committee is then used for all further work.
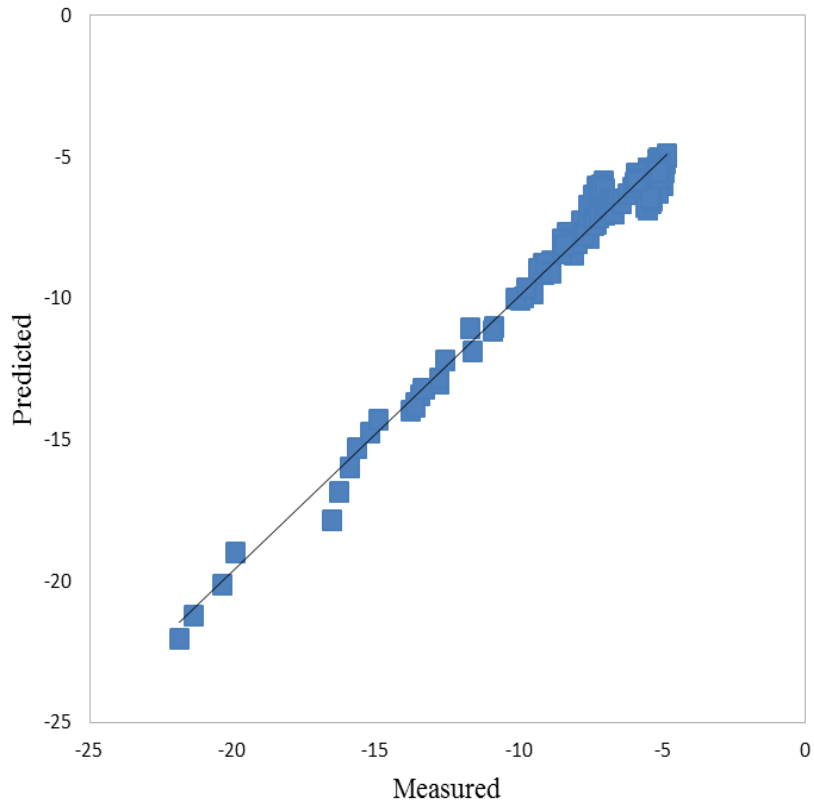
Figure 8.7: Training data for the best committee model (training is carried out on whole dataset)

A comparison of the measured and predicted conductivity is presented in Figures 8.8 – 8.13. In these cases, it can be seen that the measured values lie completely within the predicted values. The model is found to be capable of generalising sufficiently to reproduce the general trends in the data and is capable of making useful predictions of unseen composition and temperature.
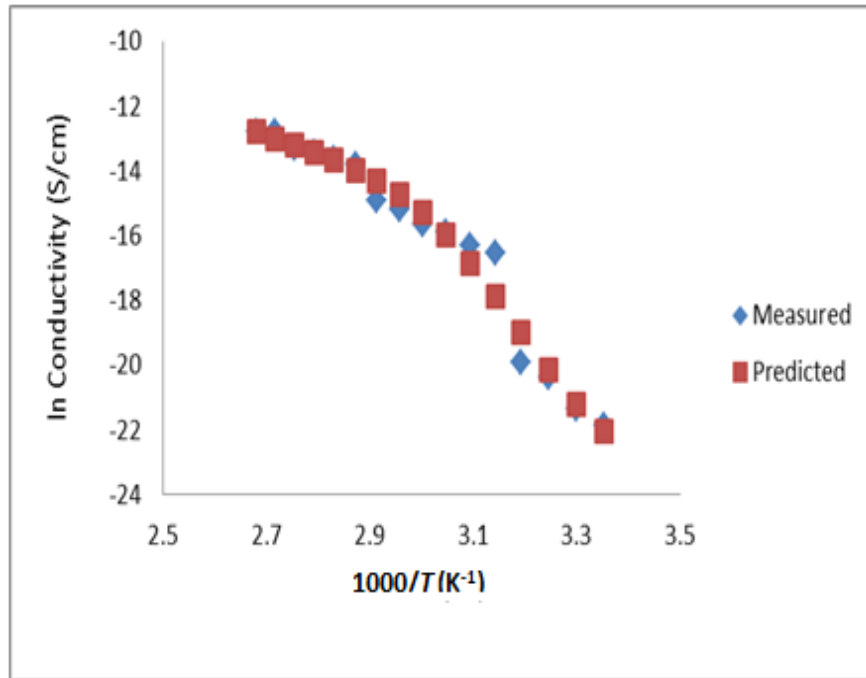
Figure 8.8: Experimental and neural network curves of pure PEO conductivity according to temperature

Figure 8.9: Experimental and neural network curves of pure PEO - Salt conductivity according to temperature
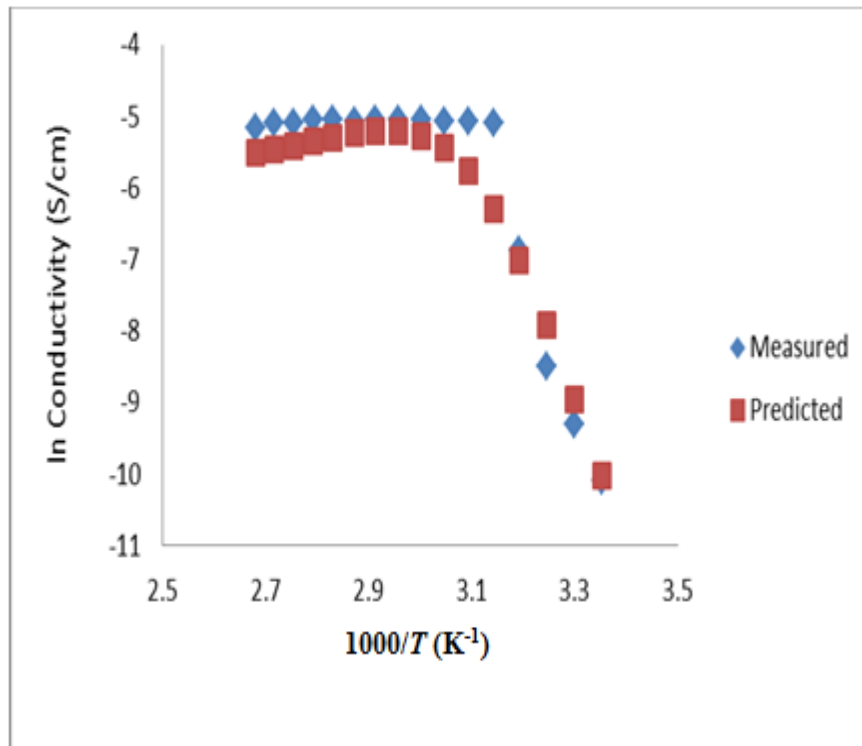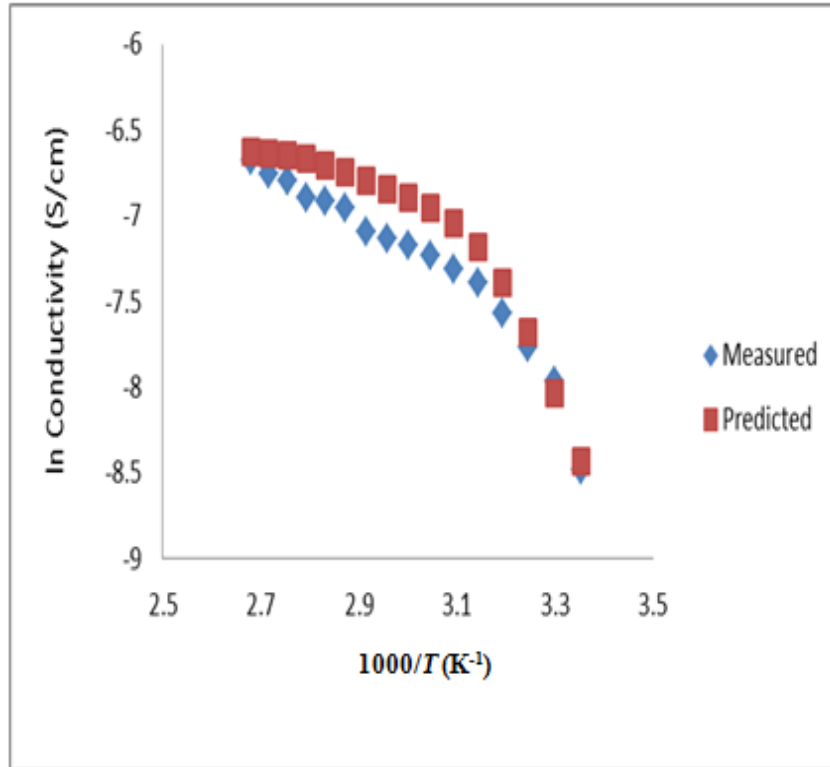
Figure 8.10: Experimental and neural network curves of PEO-Salt-EC conductivity according to temperature
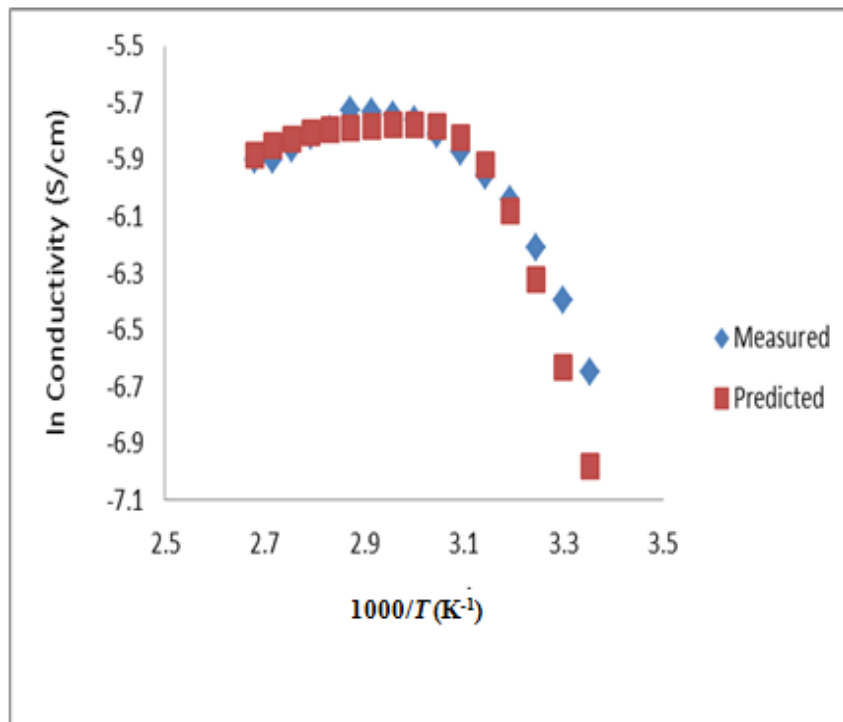
Figure 8.11: Experimental and neural network curves of PEO-Salt-EC-αCNT conductivity according to temperature
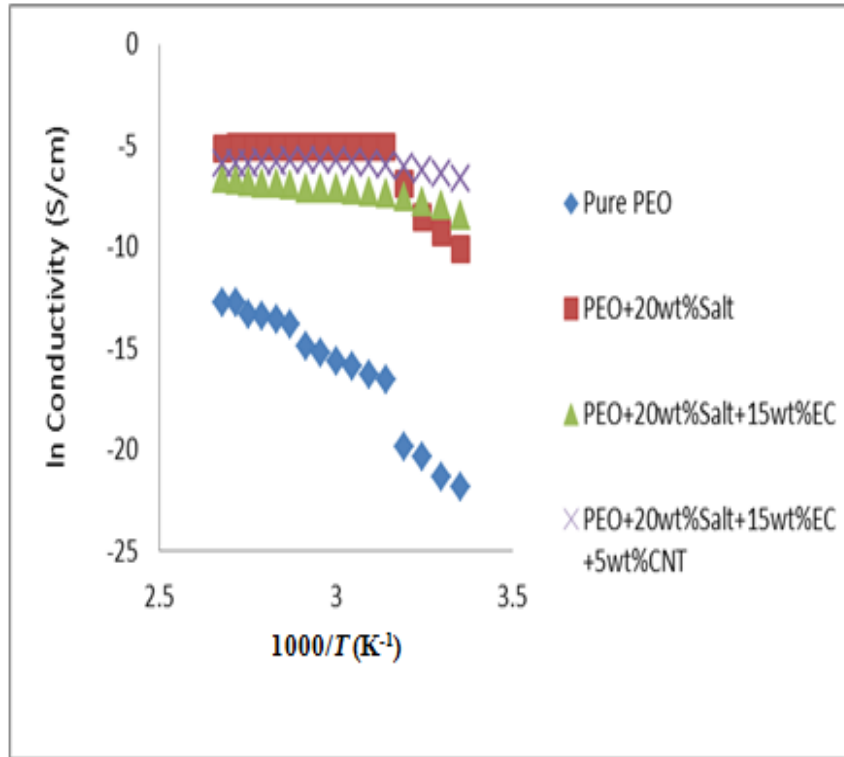
Figure 8.12: Temperature-dependent conductivity of polymer electrolyte system from experimental data
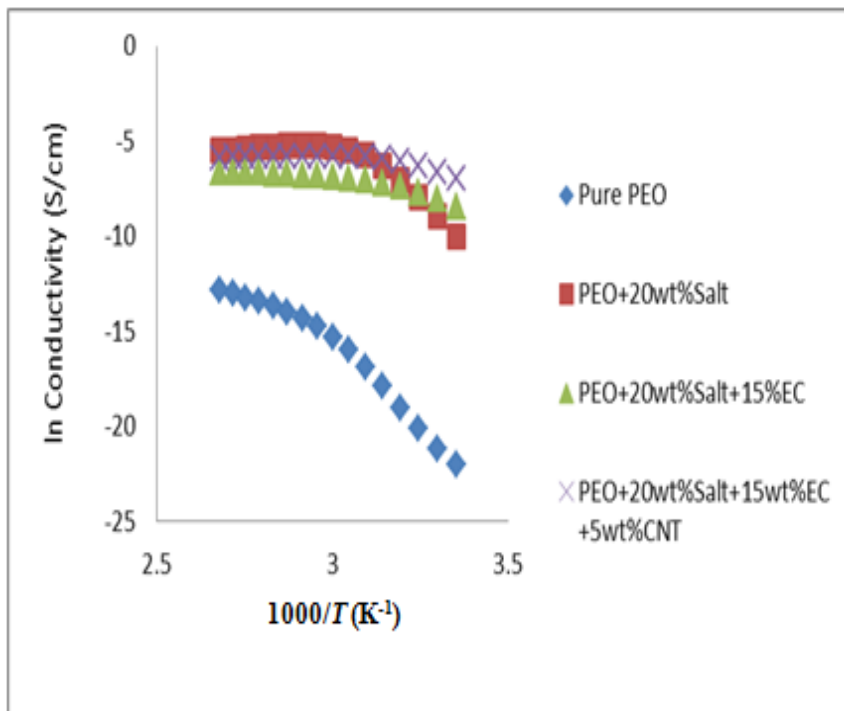
Figure 8.13: Temperature-dependent conductivity of polymer electrolyte system obtained from neural network's prediction

8.2 Neural networks for Nyquist Plots Prediction for Nanocomposite Polymer Electrolytes

The database compiled from the experimental data consisted of 5 inputs including the chemical compositions and real impedance. Table A2 (See Appendix) shows the experimental data number for the four type of SPE (total experimental data 396) which were adequate to develop the neural network model.

Figure 8.14 shows that the inferred noise level decreases as the number of hidden units increases. However, the complexity of the model also increases with the number of hidden units. A high degree of complexity may not be justified. Figure 8.14 shows that the test error at first decreases but then begins to increase again as a function of the number of hidden units. Figures 8.15 – 8.16 show the behaviour of the training and test data which exhibits a similar degree of scatter in both graphs, indicating that the complexity of this particular model is optimum. The error bars in Figures 8.15 – 8.16 include the error bars of the underlying function and the inferred noise level in the dataset σ_v. The test error is a measure of the performance of a model. Another useful measure is the "log predictive error" for which the penalty for making a wild prediction is accompanied by an appropriately large error bar.

Figure 8.17 shows the log predictive error as a function of hidden units. The calculated test error reaches a minimum of 3 hidden units and the log predictive error also exhibits a maximum at the same number of hidden units. This would have been the optimum model, had a single model been used for the analysis.
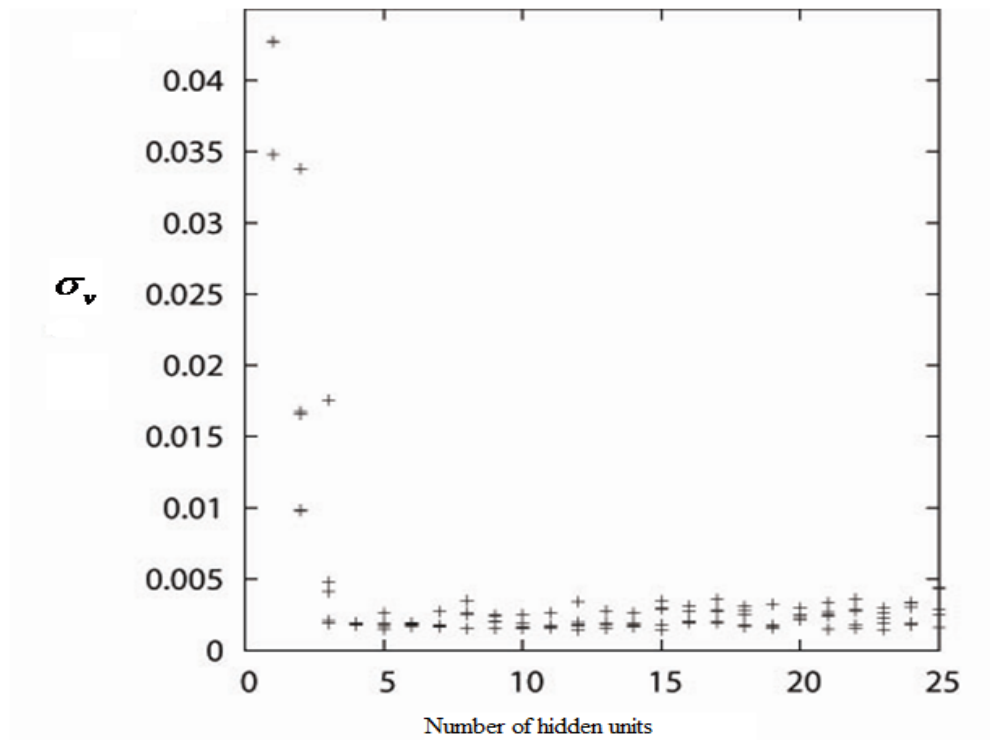
Figure 8.14: A variation in σ_v (the model perceived level of noise in the data) as function of number of hidden units
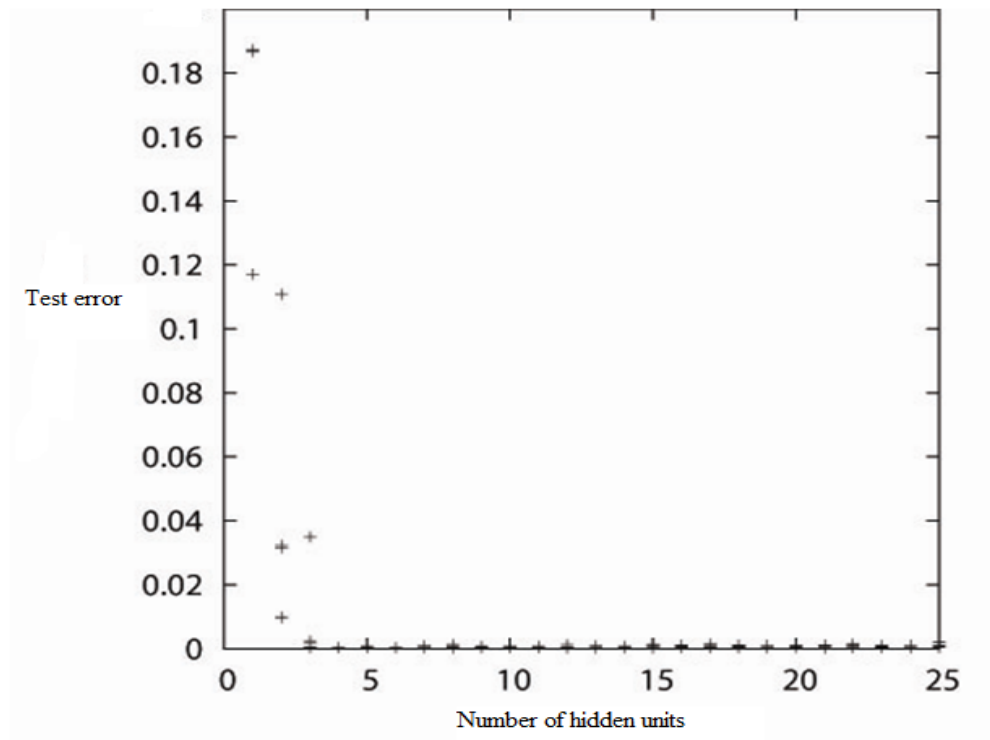
Figure 8.15: Test error as function of number of hidden units
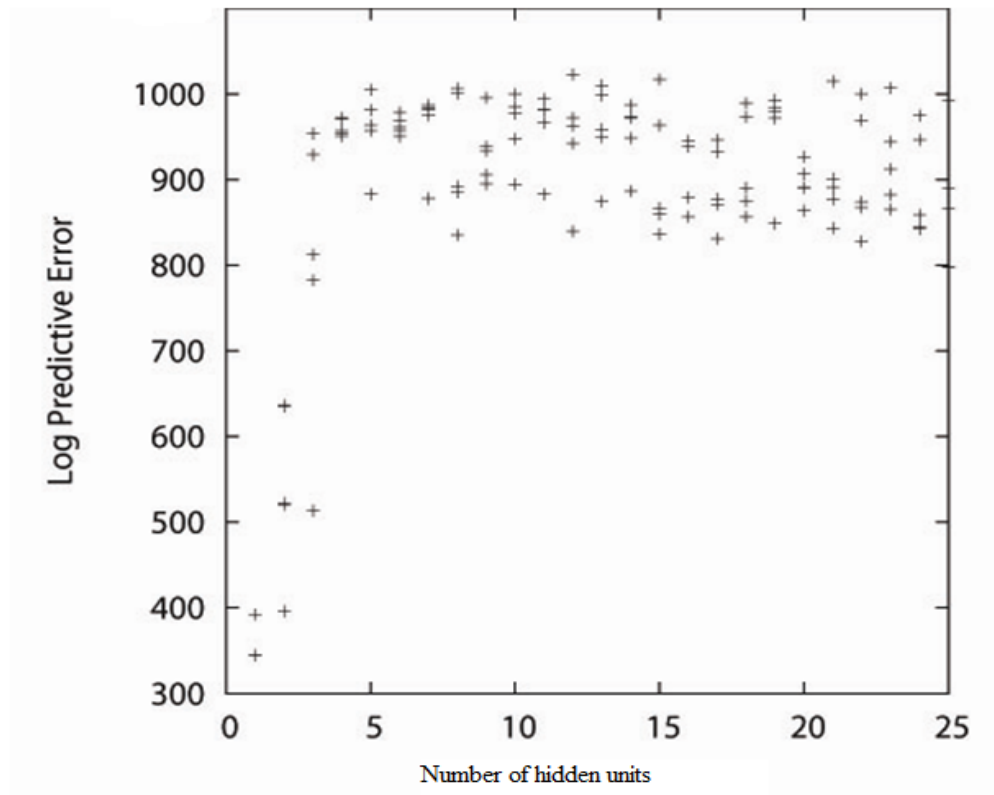
Figure 8.16: Log predictive error as function of number of hidden units
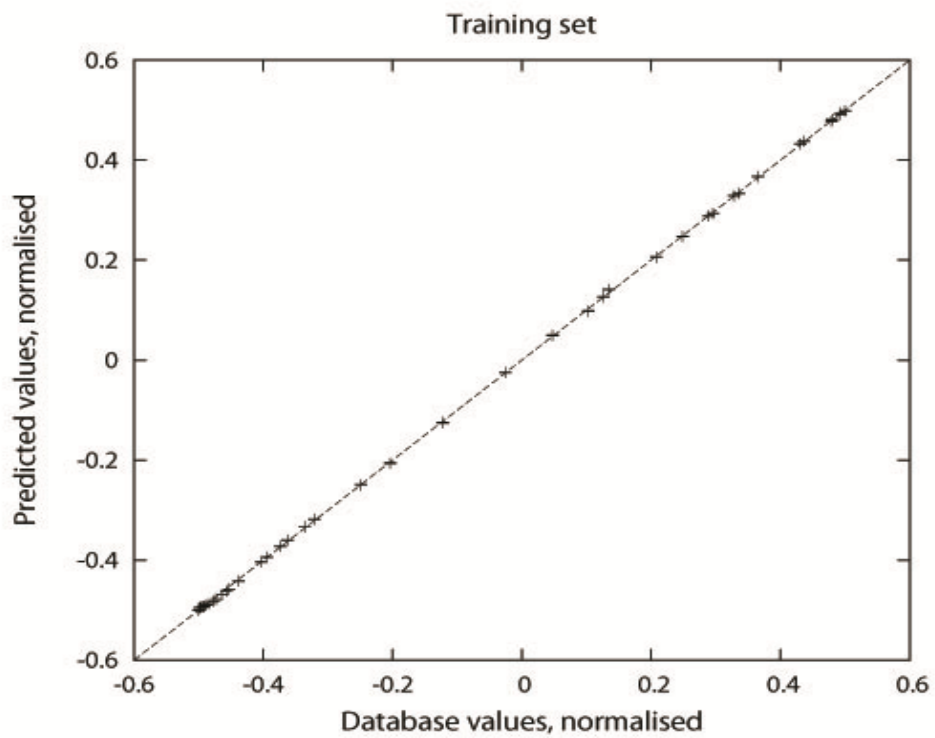
Figure 8.17: Typical performance of the trained model on training data
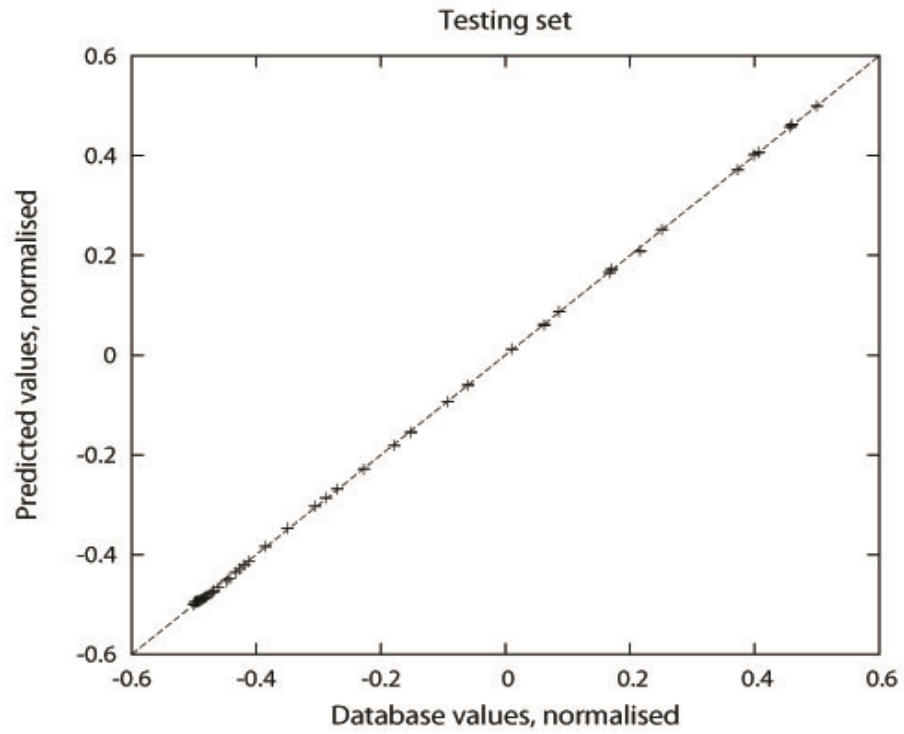
Figure 8.18: Typical performance of the trained model on test data
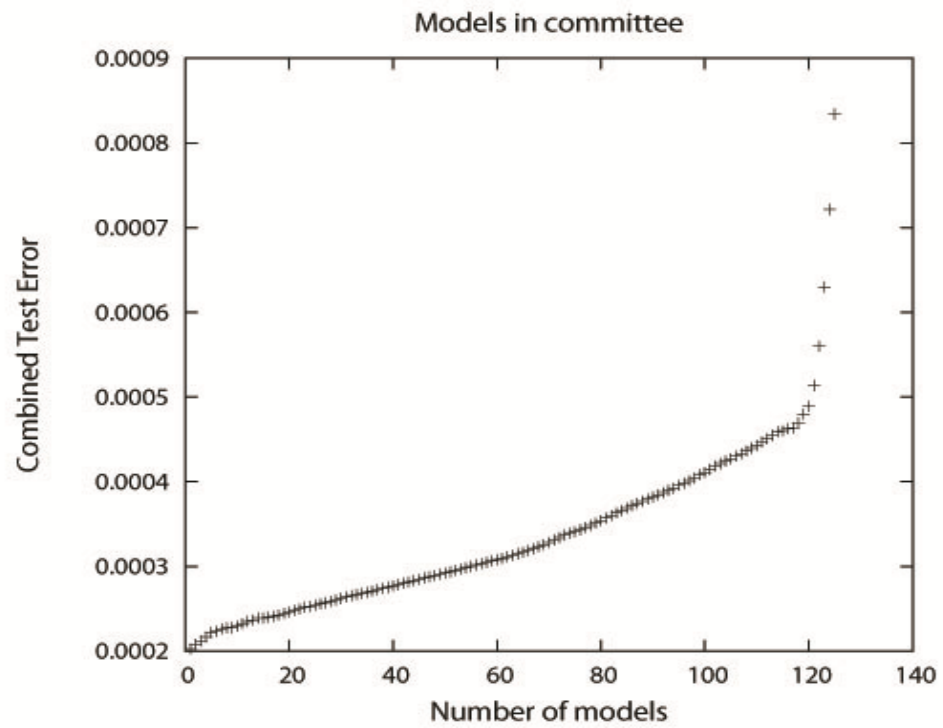
Figure 8.19: Test error as function of number of members in committee

When making predictions, MacKay (1992a,1992b,1995) recommended the use of multiple good models instead of just one best model. This is called 'forming a committee'.

In the present analysis, a committee of models was used to make more reliable predictions. The models were ranked according to their log predictive error. Committees were then formed by combining the predictions of best M models, where M gives the number of members in a given committee model. The test errors for the first 120 committees are shown in Figure 8.19. A committee of the best models gives the minimum error. Each constituent model of the committee was therefore re-trained on the entire dataset beginning with the weights previously determined. Figure 8.20 shows the results from the new training on the entire dataset. Consistent with the reduction in test error illustrated in Figure 8.19, it is evident that the committee model outperformed the single best model. The re-trained committee was used for all further work.
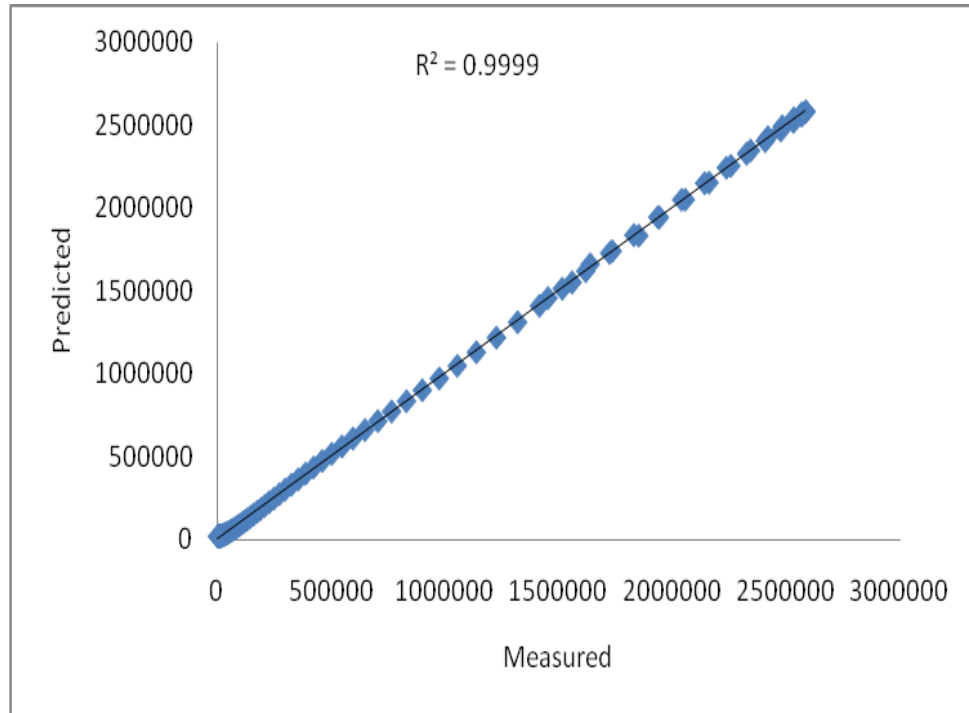
Figure 8.20: Training data for best committee model (training was done on the whole dataset)
Comparisons of the measured and predicted conductivities are presented in Figures 8.21 – 8.24.

In these cases, it can be seen that the measured values fall completely within the predicted

values. The model is found to be able to generalise sufficiently to reproduce the general trends in

the data and is capable of making useful predictions of unseen composition and temperature.
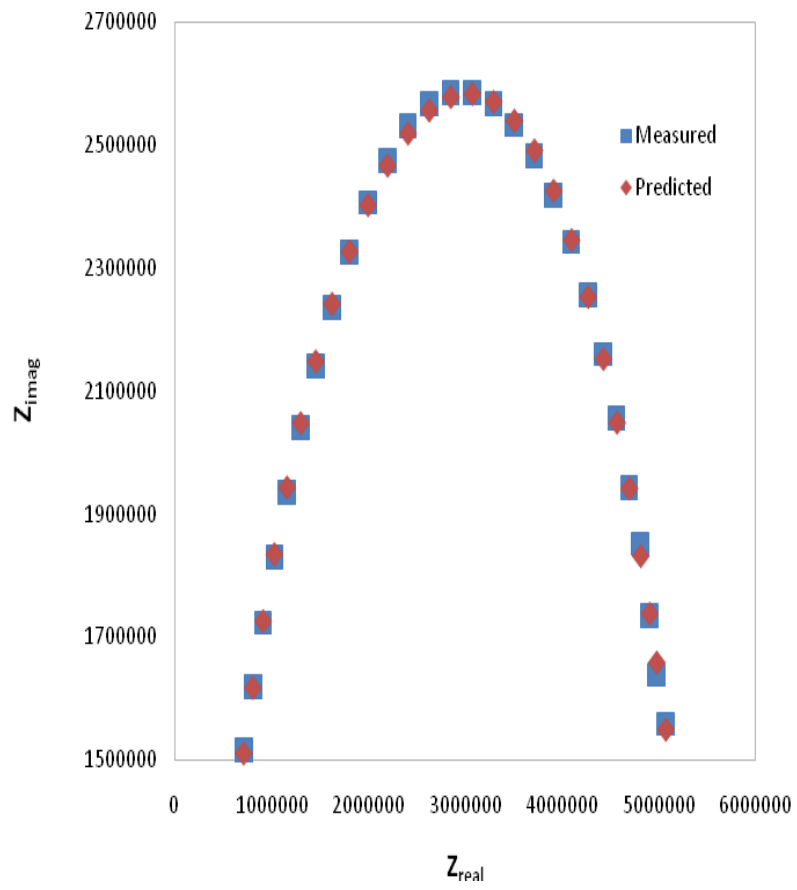
Figure 8.21: Nyquist plots of experimental and neural network results for pure PEO
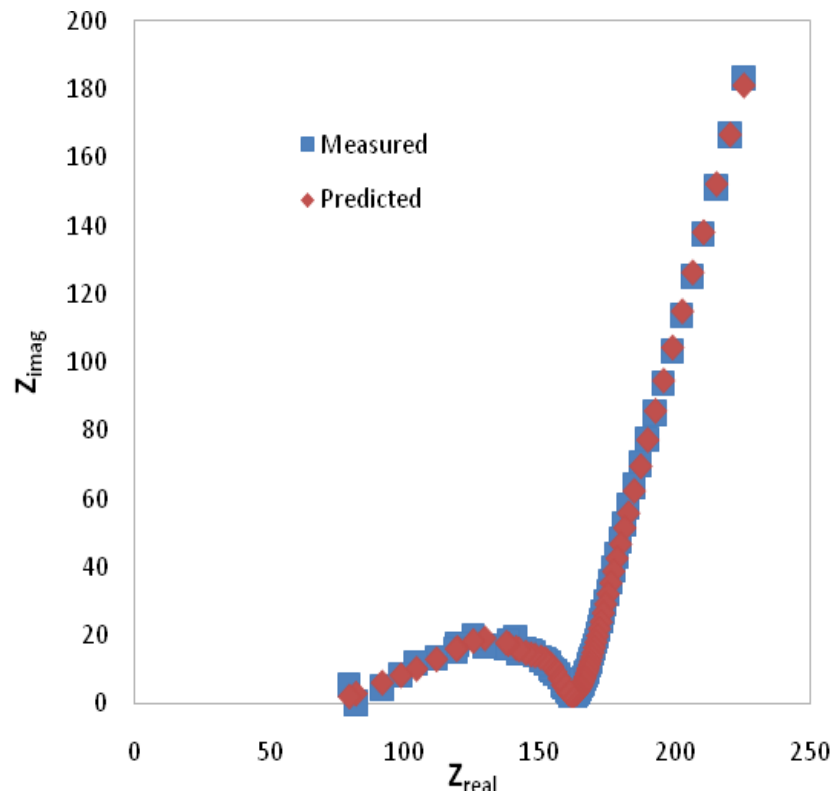
Figure 8.22: Nyquist plots of experimental and neural network results for PEO- salt system
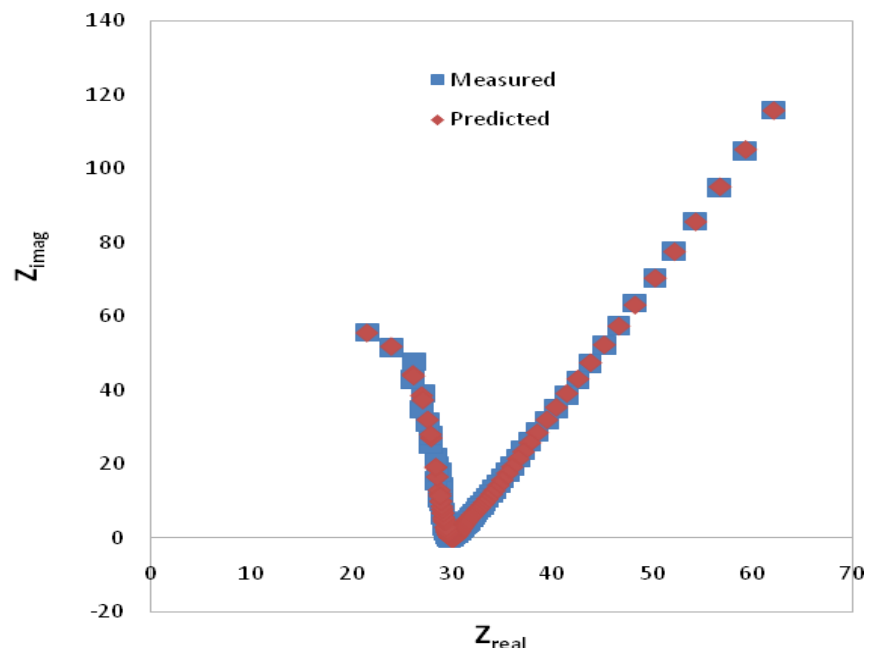
Figure 8.23: Nyquist plots of experimental and neural network results for PEO-salt-EC system
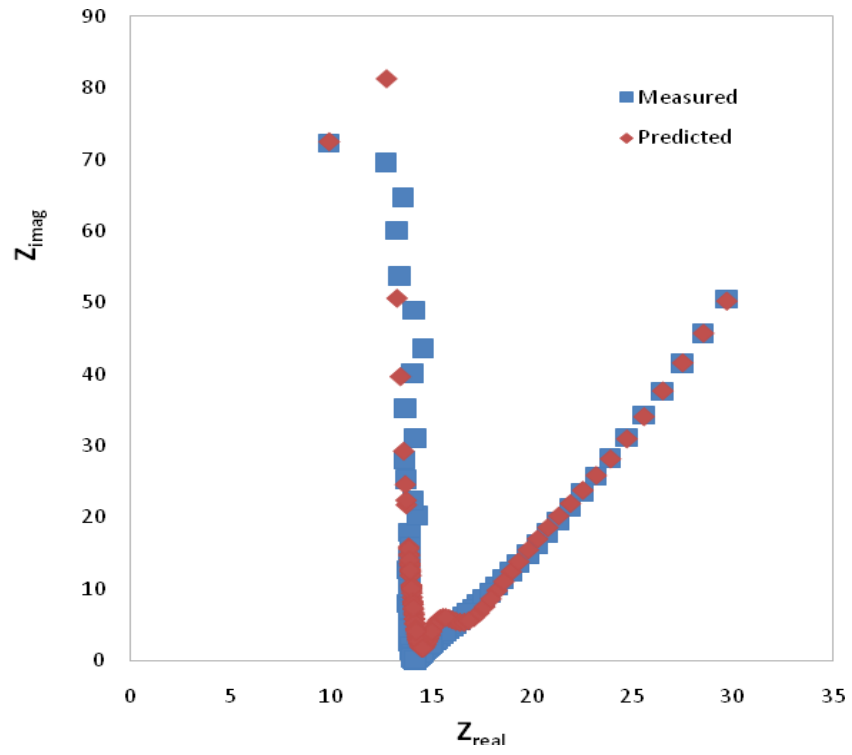
Figure 8.24: Nyquist plots of experimental and neural network results for PEO-salt-EC-CNT system

CHAPTER NINE

Conclusions and Future Studies

9.1   Conclusions

Solid polymer electrolyte (PEO-LiPF$_6$-EC-αCNTs) systems have been synthesized using solution-casting technique.

Studies on various concentrations of LiPF$_6$ salt have shown that conductivity at 25 - 100°C increases with increasing of LiPF$_6$ salt concentration, which is attributed to an increase in the number and kinetic energy of charge carriers within the matrix. The complex impedance plots show that R_b decreases with increasing salt concentration. This may be due to an increase in mobile charge carriers upon the addition of LiPF$_6$ salt. XRD studies reveal that the structure of salted polymer electrolytes changes from crystalline to semi–crystalline phase with increase LiPF$_6$ salt concentration. FTIR studies indicate a shift in wavelengths from 4000 – 500 cm^{-1} for salted polymer electrolytes due to interactions between polymer and salt. Morphology studies reveal that the surface appears rough when higher LiPF$_6$ salt concentration is added into the host polymer. However, thermal studies show a decrease in T$_g$ and T$_m$ for salted polymer electrolytes with increasing concentrations of LiPF$_6$ salt increase.

Studies on various of EC plasticizer exhibit that the conductivity at room temperature increases with increasing EC plasticizer concentration. EC effectively reduces inter-ion Coulomb interactions and therefore, more Li$^+$ ions contribute to the conductivity of the complexes. The

complex impedance plots show that R_b decreases with increased plasticizer at room temperature. XRD studies reveal that the structure of plasticized polymer electrolytes changes from crystalline to semi–crystalline phase with increased concentrations of EC plasticizer. FTIR studies show a shift in wavelengths from $4000 - 500$ cm^{-1} due to interactions between salted polymer electrolytes and EC. Morphology studies reveal that the surface becomes porous with higher EC plasticizer concentrations in salted polymer electrolytes. However, thermal studies show a decrease in T_g and T_m for plasticized polymer electrolytes with increased concentrations of EC plasticizer. The value of total weight loss increase with increased concentrations of EC plasticizer.

Studies on various amounts of αCNTs filler show that the conductivity at elevated tempearure increases with increasing αCNTs filler concentration. The nanosize αCNTs improve the conduction of mobile ions due to their extremely high surface energy. The complex impedance plots show that R_b decreases with increased filler concentration. This may be due to an increase in mobile charge carriers upon the addition of αCNTs filler. XRD studies reveal that the structure of nanocomposite polymer electrolytes change from crystalline to semi–crystalline phase with increased concentrations of αCNTs filler. FTIR studies exhibit a shift in wavelengths from $4000 - 500$ cm^{-1} due to interactions between the filler and plasticized polymer electrolytes. Morphology studies indicate that the surface of nanocomposite polymer electrolytes becomes smooth when αCNTs are added into the system. However, thermal studies show a decrease in T_g and T_m for nanocomposite polymer electrolytes. The value of total weight loss decreases with increased concentrations of αCNTs.

Studies on the optimum conductivity of nanocomposite polymer electrolytes show that the conductivity at elevated temperature increases. It has been demonstrated in this work that the

addition of various weight percent of salt, plasticizer and filler into the PEO matrix enhances conductivity and alters the structures of the host polymer. The complex impedance plots show that R_b decreases with addition of various weight percent of salt, plasticizer and filler into the PEO matrix. This may be due to an increase in mobile charge carriers upon the addition of various weight percent of salt, plasticizer and filler. XRD studies exhibit that the structure of nanocomposite polymer electrolytes changes from crystalline to mostly amorphous when various weight percent of salt, plasticizer and filler are added into the PEO matrix. FTIR studies reveal a shift in wavelengths from $4000 - 500$ cm^{-1} due to interactions between PEO, salt, plasticizer and filler in the system. Morphology studies show changes on the surface when various weight percent of salt, plasticizer and filler are added into the PEO matrix. However, thermal studies show a decrease in T_g and T_m for nanocomposite polymer electrolytes. The weight loss process of solid polymer electrolytes are gradual rather then abrupt as in the case for liquid electrolytes. For this reason, solid polymer electrolytes are more thermally stable than liquid electrolytes for application in lithium ion batteries.

The optical properties of polymer electrolytes appear to be strongly connected to the chemical and structural modifications induced in the polymer. The PL intensity decreases as elements are added into the polymer complexes. The optical band gap values show a decreasing trend with increasing dopant concentration. It is also observed that the absorption edge shifts towards longer wavelengths upon doping. Results of optical measurements indicate the presence of a well-defined $\pi \rightarrow \pi*$ transition associated with the formation of a conjugated (C=O and/or C=O electronic structure). The refractive index decreases when LiPF$_6$ and EC are added into the polymer complex, and increases when αCNTs are added into the PEO complex.

.   The dielectric behaviour of PEO and its complexes has been studied.   The dielectric constant, dielectric loss and loss tangent of PEO are found to increase upon the addition of $LiPF_6$ and these parameters are influenced significantly by the temperature and frequency. The dielectric constant and dielectric loss of PEO-$LiPF_6$ increase upon the addition of EC and αCNTs, and these parameters are also influenced significantly by the temperature and frequency. No significant effect is observed, however, for the loss tangent of this complex.

A model has been developed, which is capable of predicting the Nyquist plots of nanocomposite polymer electrolyte systems (PEO - $LiPF_6$ – EC - αCNTs). The generalization ability of the neural network is the basic consideration of this work. It is found that the Bayesian neural network is successful in predicting of the experimental results.

9.2   Recommendations for Future Work

In order to enable the results reported in this study to be implemented in real industrial applications, the results must be extended and improved in further research. In the case of nanocomposite polymer electrolytes, the key factors such as conductivity, moisture content, mechanical and electrochemical stability as well as optical properties may be further investigated via solution-casting technique. The optimization conditions may be considered to be achieved when the key factors, which control the reaction process, are highlighted.

A suitable heat treatment or other processing methods are needed to improve dispersion of carbon nanotubes in polymer electrolytes. αCNTs tend to aggregate into ropes or bundles due to the strong intrinsic Van der Waals forces between them, and thus cause poor dispersion in polymer matrix (Liao *et. al.* 2008) . The techniques that are specifically aimed at improving the

functionalities of αCNT surfaces include chemical treatments using high concentration acids, sheathing or wrapping the αCNTs with polymer chains (Manchado *et. al.* 2005; Rosa *et. al.* 2007), grafting of αCNTs with a thin layer of polymer chains based on plasma (Dweiri and Sahari, 2007), and a combination of these. Several literature have indicated that the physical method related to melt blending is one of the most promising routes (Seo and Park, 2004; Alig *et. al.*, 2007; Potschke *et. al.*, 2004). When composite materials are prepared by melt blending, the high shear force leads to better interactions between αCNTs and polymer matrix without damaging the structure of αCNTs, resulting in good processability and better performance of the composites (Zhang *et. al.*, 2006). Hence, melt blending method is considered as an effective method to enhance the dispersion of αCNTs in polymer.

Battery fabrication is the next step in order to study the effects of produced nanocomposite electrolytes in battery cells. By fabricating battery cells, the capacity of battery using the produced nanocomposite polymer electrolytes can be studied. Nevertheless, αCNT is a new type of filler for polymer electrolytes and intensive studies need to be carried out on the effects of anode and cathode materials as well as on the battery cell itself.

REFERENCES

Abraham K.M, *Electrochimicia Acta*, 38, 1233 (1993)

Abraham K.M., Alammmgir M. *Journal of Electrochemical Society*. 137, 1657 (1990)

Acosta J.L., Morales E., *Solid State Ionics* 85, 85 (1996).

Adachi K., Kotaka T., *Progress Polymer Science* 18, 585 (1993).

Adebahr J., Best A.S., Byrne N., Jacaosson P., MacFarlane D.R., Forsyth M., *Chemistry Physics.* 5, 720 (2003).

Agnihotry S.A., Pradeep S.S., Sekhon, *Electrochimica Acta* 44, 3121 (1999).

Ahmad Khiar A.S., Arof A.K., *Ionics* 16, 123 (2010)

Ajayan P, Zhou O. Applications of carbon nanotubes, carbon nanotubes. University of North Carolina; pg. 391–425 (2001).

Ajayan PM. *Chemistry Review* 99, 1787 (1999).

Ali A.M.M.A., Yahya M.Z.A., Bahron H., Subban R.H.Y., Harun M.K., Atan I., *Materials Letter.* 61, 2026 (2007)

Ali A.M.M.A., Subban R.H.Y., Bahron H., Winnie T., Latif F., Yahya M.Z.A., *Ionics*, 14, 491 (2008)

Anantha P.S., Hariharan K., *Solid State Ionics* 176, 155 (2005).

Anantram M.P., Leonard F. *Reports on Progress in Physics*. 69, 507 (2006).

Andreev Y.G., Bruce P.G., *Journal of Physics: Condensed Matter* 13, 8245 (2001)

Ansari S.M., Brodwin M., Stainer M., Druger S.D., Ratner M.A., Shriver D.F., *Solid State Ionics*. 17, 101 (1985).

Appetecchi G.B., Montanino M., Balducci A., Lux S.F., Winterb M., Passerini S., *Journal of Power Sources.* 192, 599 (2009)

Appetecchi G.B., Passerini S., *Electrochimica. Acta* 45, 2139 (2000)

Appeteechi G.B., Crose F., Persi L., Ronci F., Scrosati B., *Electrochimica Acta* 45, 1481 (2001)

Armand M., Solid State Ionics 9 & 10, 745 (1983)

Armand M.B., Chabagno J.M., Duclot M.J., Abstract 6.5 Extended Abstract, 2nd International Conference on Solid Electrolytes, St. Andrews, Scotland, Sept. 20-22 (1978)

Armand, M. B., Chabagni, J.M., Duclot, M.J. "Fast Ion Transport in Solids" Ed. By Vashista, P., Mundy, J.N., and Shenoy, G.K., North-Holland, NY, 131 (1979)

Armand, M.B., Duclot M.J., Rigaud P. *Solid State Ionics* 3, 429 (1981).

Armand, M.B., Polymer Electrolytes Reviews-1, Ed. MacCallum, J.R. and Vincent, C.A., Elsevier Applied Science, NY (1987) Shriver, D.F., Farringon, G.C., Chemical Engineering News, 63, May 20, 42 (1985)

Arof A.K., Ramesh S., Tan Winie. *European Polymer Journal* 43, 1963 (2007).

Azamian BR, Davis JJ, Coleman KS, Bagshaw CB, Green MLH., *Journal of the American Chemical Society*. 124, 12664 (2002).

Bachtold A, Hadley P, Nakanishi T, Dekker C. *Science* 294, 1317 (2001)

Bahri R., Singh H.P., *Thin Solid Films* 69, 281 (1980).

Balaya P., Goyal P.S., *Journal of Non-Crystalline Solids* 351, 1573 (2005).

D. J. Bannister, G. R. Davies, I. M. Ward, J. E. McIntyre. *Polymer* 25, 1600 (1984)

Baril D., Michot, Armand M., *Solid State Ionics*. 94, 35 (1997)

Baskaran R., Selvasekaranpandian S., Kuwata N., Kawamura J., Hattoriac T., *Materials Chemistry Physics.* 98, 55 (2006).

Baskaran R., Selvasekarapandian S., Kuwata N., Kawamura J., Hattori T., *Materials Chemistry Physics* 98, 55 (2004)

Baugham R, Zakhidov A, Heer W. *Science.* 297, 787 (2002).

Baughman R.H., Zakhidov A.A., de Heer W.A., *Science.* 297,787 (2002)

Belluci, S. *Physics State Solid.* **2**, 34 (2005).

Berber S., Kwon Y., Toma´nek D. *Physics Review Letter* 84, 4613 (2000).

Best A. S., Adebahr J., Jacobsson P., MacFarlane D.R., Forsyth M., *Macromolecules* 4, 4549 (2001).

Bethune DS, Kiang CH, DeVries M, Gorman G, Savoy R, Vazquez J. *Nature* 363, 605 (1993).

Bhadeshia H.K.D.H., *ISIJ International* 39, 966 (1999)

Bhadeshia H.K.D.H., Dimitriu R.C., Forsik S., Park J.H., Ryu J.H., *Materials Science Technology* 25, 504 (2009)

Biercuk M.J., Llaguno M.C. *Applied Physics Letters.* 80, 2767 (2002).

Biercuk MJ. *Applied Physics Letters.* 80, 2767 (2002).

Binks A.E., Sharples A., J. *Polymer Science: Part A-2,* 6, 407 (1968).

Biro LP, Horvath ZE, Szlamas L, Kertesz K, Weber F, Juhasz G. *Chemistry Physics Letters* 39, 402 (2003).

Blonsky, P.M.; Shriver, D.F.; Austin, P.E.; Allcock, H.R. *Journal of the American Chemical Society.* 106, 6854 (1984).

Bonnard JM, Salvetat JP, Stockli T, de Herr WA, Forro L, Chatelain A. *Applied Physics Letters.* 73, 396 (1998).

Borghini M.C., Mastrogostino M., Passerini S., Scrosati B., *Journal of Electrochemical Society.* 142, 2118 (1995)

Britto PJ, Santhanam KSV, Ajayan PM. *Journal of Bioelectrochemistry Bioenergtics* 41, 121 (1996).

Buriez O., Han Y.B., Hou J., Kerr J.B., Qiao J., Sloop S.E., Tian M.M., Wang S., *Journal of Power Sources,* 89, 149 (2000)

Callister W.D., Materials Science and Engineering, An Introduction. New York: Wiley; (2003).

Cameron G.G., Ingram M.D., Sarmouk K., *Polymer.* 26, 1097 (1990).

Campion, CL., Li, W., Euler, WB., Lucht, BL., Ravdel, B., DiCarlo, JF., Gitzendanner, R., Abraham, KM., *Electrochemical Solid-State Letters* 7, A194 (2004).

Campbell J.A., Goodwin A.A., Simon G.P., *Polymer.* 42, 4731 (2001).

Cao J., Wang Q., Rolandi M., Dai H. *Physical Review Letters*. 93, 1 (2004).

Capuano F., Croce F., Scrosati B., *Journal of Electrochemical Society*. 138, 1918 (1991)

Carothers W.H., *Chemistry Review*. 8, 353 (1931).

Chae, Han Gi; Kumar, Satish. *Journal of Applied Polymer Science.* 100, 791 (2006)

Chambers A, Park C, Baker RTK, Rodriguez NM. *Journal of Physics Chemistry B*. 102, 404 (1998).

Chang H, Lin C, Kuo C. *Thin Solid Films* 420, 219 (2002).

Change A., Carreb M., Willmann P., *Journal of Power Sources*. 109, 203 (2002).

Che G, Lakshmi BB, Fisher ER, Martin CR. *Nature* 384, 147 (1996).

Che G, Lakshmi BB, Fisher ER, Martin CR. *Nature* 393, 346 (1998).

Che G., Lakshmi B.B., Martin C.R., Fisher E.R., Ruoff R.S. *Chemistry Materials* 10, 260 (1998).

Chen C, Perry W, Xu H, Jiang Y, Phillips J. *Carbon* 60, 2555 (2003).

Chiang M, Liu K, Lai T, Tsai C, Cheng H, Lin I. *Journal of Vacuum Science Technology B.* 9,1034 (2001).

Coleman J.N., Cadek M., Blake R., Nicolosi V., Ryan K.P., Belton C. *Advanced Functional Materials* 14, 791 (2004).

Collins PG, Avouris P. *American Journal of Science.* 283, 62 (2000).

Collins PG, Zettle A, Bando H, Thess A, Smally RE. *Science.* 278,100 (1997).

Collins, Philip G. *Journal of Scientific American*. 67, 69 (2000).

Cooper C.A., Cohen S.R., Barber A.H., Wagner H.D., *Applied Physics Letters.* 81,3873 (2002)

Croce F., Brown S.D., Greenbaum S., Slane S.M., Salomon M., *Chemistry. Materials*. 5, 1268 (1993).

Croce F., Curini R., Martinelli A., Persi F., Scrosati B., Caminiti R., *Journal of Physics and Chemistry.* 103, 10632 (1999).

Croce F., Persi L., Scrosati B., Serriano F., Plichta E., Hendrickson M.A., *Electrochimica Acta*. 46, 2457 (2001).

D. Qian, E. C. Dickey, R. Andrews, T. Rantell, *Applied Physics Letters* 76, 2868 (2000).

Dai H. *Surface Science* 500, 218 (2002).

Dasgupta, S. British *Journal of Applied Physics* 267, 1792 (1966).

De Heer WA, Chatelain A, Ugarte D. *Science* 270, 1179 (1995).

Dekker, Cees. *Physics Today* 52, 22 (1999).

Delmotte JP, Rubio A. *Carbon* 40, 1729 (2002).

Demczyk, B.G.; Wang, Y.M.; Cumings, J.; Hetman, M.; Han, W.; Zettl, A.; Ritchie, R.O. *Materials Science Engineering A* 334, 173 (2002).

Dillon AC, Jones KM, Bekkedahl TA, Kiang CH, Bethune DS, Heben MJ. *Nature.* 386, 404 (1997).

Ding L., Shi J., Yang C., Dong S., *Polymer.* 29, 410 (1997).

Dissanayaka M.A.K.L., Jayathilakaa P.A.R.D., Bokalawala R.S.P., Albinsson I., Mellanander B.E., *Journal of Power Sources.* 119, 409 (2003).

Dresselhaus M, Dresselhaus G, Saito R. *Carbon.* 33, 883 (1995).

Dresselhaus MS, Dresselhaus G, Eklund PC. Science of fullerenes and carbon nanotubes. New York: Academic Press; 1996.

Druger S.D., Ratner M.A., Nitzan A., *Solid State Ionics* 9/10, 1115 (1983)

Ebbesen TW, Ajayan PM. *Nature.* 358,220 (1992).

Ehrlich, G. M. In Handbook of Batteries; Linden, D., Reddy, T. B., Eds.;McGraw-Hill: New York, pp 35.1-35.94 (2002).

El Shafee E., *Carbohydrate Polymer* 31, 93 (1996).

Faim T.D. The International Society for Optical Engineering 5250, 423 (2004)

Farajian A, Yakobson B, Mizeseki H, Kawazoe Y. *Physical Review* 67,1 (2003).

Fauteux D., Massucco A., McLin M., Buren M.V., Shi J., *Electrochimica Acta*, 40, 2185 (1995)

Fenton, D. E., Paker, J. M., Wright, P. V., *Polymer* 14, 589 (1973)

Flahaut, E.; Bacsa, R; Peigney, A; Laurent, C. *Chemistry Commmunications* 12, 1442 (2003).

Flory, P.J. Priciples of Polymer Chemistry; Cornell University Press: Itaca, NY (1953)

Forsyth M., MacFarlane D.R., Best A., Adebahr J., Jacobsson P., Hill A.J., *Solid State Ionics* 147, 203 (2002).

Frankland S.J.V., Caglar A., Brenner D.W., Griebel M., *Journal of Physics Chemistry B* 106, 3046 (2002).

Franklin NR, Li Y, Chen RJ, Javey A, Dai H. *Applied Physics Letters* 79, 4571 (2001).

Frech, R., Giffin, G. A., Yepez Castillo F., Glatzhofer D.T., Eisenblatter, *Journal of Electrochimica Acta* 50, 3963 (2005).

Fried, J.R. Polymer Science & Technology, 2nd ed., Prentice Hall: Upper SaddleRiver, NJ (2003)

Fu, L. J.; Liu, H.; Li, C.; Wu, Y. P.; Rahm, E.; Holze, R.; Wu, H. Q. *Progress Material Science*. 50, 881 (2005).

Fuhrer MS. *Science* 288, 494 (2000).

Furtado C.A., Silva G.G., Machado J.C., Pimenta M.A., Silva R.A., *Journal of Physics Chemistry B*. 103, 7102 (1999)

Gadjourova A., Andreev Y.G., Tunstall D.P., Bruce P.G., *Nature.* 421, 520 (2001)

Gao B. *Chemistry Physics Letters.* 307, 153 (1999).

Gao M, Dai LM, Wallace GG. *Electroanalysis.* 2003;15, 1089 (2003).

Garg A., Sinnott S.B., *Chemistry Physics Letters.* 295, 273 (1998).

Gauthier M., Armand M., Muller A. "Electroresponsive Molecular and Polymeric Systems", Skothiem, T.A., Ed., Vol. 1, Marcel Dekker, NY (1988)

Gokulamurali N., Suthanthiraj S.A., Maruthamuthu P., *Proceeding Solid State Ionics: Material Appllied* 373 (1992).

Gondivaraj G., Baskaran N., Shahi K., Monoravi P., *Solid State Ionics* 76, 47 (1995).

Gooding J. *Electrochimica* 50, 3049 (2004).

Gorecki M., Andreani R., Berthier C., Armand M.B., Mali M., Roos J., Brinkmann D., *Solid State Ionics* 18, 295 (1986).

Gray F.M., Polymer Electrolytes, RSC Materials Monographs, The Royal Society of Chemistry, Cambridge (1997).

Gray, F.M., Mixed Polymer Systems, in Polymer Electrolyte Reviews, C.A. Vincent, Editor. Elsevier Applied Science: London (1987)

Guan, Lunhui; Suenaga, Kazu; Iijima, Sumio. *Nano Letters* 8, 459 (2008)

H. D. Wagner. "Reinforcement". Encyclopedia of Polymer Science and Technology. John Wiley & Sons. (2002)

Hafner JH, Cheung CL, Leiber CM. *Nature* 398, 761 (1999).

Hamada N, Sawada S, Oshiyama A. *Physical Review Letters* 68, 1579 (1992).

Hayakawa T., Adachi K., *Polymer* 42, 1725 (2001).

Hayashi, Takuya; Kim, Yoong Ahm; Matoba, Toshiharu; Esaka, Masaya; Nishimura, Kunio; Tsukada, Takayuki; Endo, Morinobu; Dresselhaus, Mildred S. *Nano Letters*. 3, 887 (2003).

H.M.J.C. Pitawala, M.A.K.L. Dissanayake , V.A. Seneviratne. *Solid State Ionics.* 178, 885 (2007)

Hong, Seunghun; Myung, S. *Nature Nanotechnology.* 2, 207 (2007).

Hooper A., North J.M., *Solid State Ionics.* 9, 1161 (1983).

Hsiu G.H., Liu Y.L., Liao H.H., *Polymer Science Part A Polymer Chemistry* 39, 986 (2001)

Huggins, R. A. *Solid State Ionics*. 152, 61 (2002).

Huhtala, Maria. *Composites Physics Communications.* 146, 30 (2002).

Ibrahim S., Yassin ,M.M., Ahmad, R., Johan, M.R., *Ionics.* 17:399 (2011).

I. Palaci. *Physics Review Letters.* 94, 175502 (2005)

Iijima S, Barbec C, Maiti A, Bernholc J. *Journal of Chemistry Physics.* 104, 2089 (1996).

Iijima S, Ichihashi T. *Nature.* 636, 603 (1993).

Iijima S. *Nature.* 354, 391 (1991).

Ishu Sharma, Tripathi S.K., Barman P.B., *Applied Surface Science.* 255, 2791 (2008).

Jayathilaka P.A.R.D., Dissanayake M.A.K.L., Albinson I., Mellander B.E., *Electrochimica Acta.* 47, 3257 (2002)

J. Haruyama. *Physical Review Letters.* 96, 5 (2006).

Ji K.S., Moon H.S., Kim J.W., Park J.W., *Journal of Power Sources.* 117, 124 (2003)

Johan M.R., Leo B.F, *Ionics.* 16, 335 (2010)

Johan, M.R., Ibrahim, S. *Communications in Nonlinear Science and Numerical Simulation.* DOI. 10.1016/j.cnsns.2011.04.017

Johan, M.R., Ibrahim, S. *Ionics*. DOI.1007/s11981-011-0549-z.

Journet C, Bernier P. *Applied Physics A*. 1, 9 (1998).

Journet C, Maser WK, Bernier P, Loiseau A, Lamy de la M, Chapelle S,. *Nature.* 308,756 (1997).

Joykumar, Bhat S.V., *Materials Science Bulletin.* 26, 707 (2003)

K. Jensen, W. Mickelson, A. Kis, and A. Zettl. *Physics Review B*. 76, 195436 (2007)

Kelly I.E., Owen J.R., Steele B.C.H. *Journal of Power Sources.* 14,13 (1985)

Kelly I.E., Owen J.R., Steele B.C.H., *Journal of Electroanalytical Chemistry.* 168, 467 (1984).

Kerr J.B., Sloop S.E., Liu G., Han Y.B., Hou J., Wang S., *Journal Power Sources.* 110, 389 (2000)

Kilbride B.E., Coleman J.N., Fraysse J., Fournet P., Cadek M., Drury A. *Journal of Applied Physics*. 92:4024 (2002)

Killis A., Le Nest, J., Gadnini, A. and Cheradame, H., *Macromolecules*, 17, 63 (1984)

Kim J.Y., Kim S.H., *Solid State Ionics.* 124, 91 (2000).

Kim J.Y., Kim S.H., *Solid State Ionics.* 124, 91 (1999).

Kim P, Lieber CM. *Science.* 286, 2148 (1999).

Kim P, Lieber CM. *Science.* 286, 414 (1999).

Kim Y.W., Lee W., Choi B.K., *Electrochimica Acta.* 45, 1473 (2000)

Krause, LJ, Lamanna, W, Summerfield, J, Engle, M, Korba, G, Loch R, Atanasoski, R*, Journal of Power Sources.* 68, 320 (1997).

Kis A., Csanyi G., Salvetat J.P., Lee T.N., Couteau E., Kulik A.J. *Nature Materials.* 3, 153 (2004).

Kitao M., Akao H., Ishikawa T., Yamada S. *Physica Status Solidi (a).* 64, 493 (1981).

Kohjiya, S., Proceedings of the 2nd International Meeting on Polymer Electrolytes, ed. B. Socrati. New York: Elsevier (1990).

Kohjiya, S., In Solid State Ionics for Batteries; Minami, T., Tatsumisago, M., Wakihara, M., Iwakura, C., Kohjiya, S., Tanaka, I., Eds.; Springer - Verlag: Tokyo, pp 187-191 (2005).

Kong NR, Franklin C, Zhou MC, Chapline S, Peng K, Cho HD. *Science.* 287, 406 (2000).

Kong, Y, Hay JN, *Polymer.* 43, 3873 (2002).

Kudo T., Fueki K. *Solid State Ionics.* 40 567 (1990)

Kuila T., Acharya H., Srivastava S.K., Samantaray B.K., Kureti S., (2007) *Materials Science Engineering B.* 137, 217 (2007)

Kumar B., Scanlon L.G., *Solid State Ionics.* 124, 239 (1999).

Kumar B., Scanlon L.G., Spry R.J., *Journal of Power Sources.* 96, 337 (2001)

Kumar S., Dang T.D., Arnold F.E., Bhattacharyya A.R., Min B.G., Zhang X. *Macromolecules.* 35, 9039 (2002).

Kuzumaki T, Miyazawa K, Ichinose H, Ito K. *Journal of Materials Research.* 13, 244 (1998) .

Kwon YK, Toma'nek D. *Physical Review B.* 58, 16001 (1998).

Lahiff E., Leahy R., Coleman J.N., Blau W.J., *Carbon.* 44,1525 (2006)

Lahiff E., Ryu C.Y., Curran S., Minett A.I., Blau W.J., Ajayan P.M. *Nano Letters.* 3, 1333 (2003).

Lakshmi Narayana K., PhD Thesis. SV University; (1995).

Lammert PE, Zhang P, Crespi VH. *Physical Review Letters* 84, 2453 (2000).

Laplaze D, Alvarez L, Badie JM, Flamant G. *Carbon* 34, 1621 (2002).

Lee C, Liu X, Zhou C. *Applied Physics Letters* 79, 20 (2001).

Lee J.K., Lee Y.J., Chae W.S., Y. M. Sung Y.M., *Journal of Electroceramics* 17, 941 (1997).

Lee NS *Diamond and Related Materials.* 10, 265 (2001).

Lestel, L., Boileau S., C.H., Proceedings of the 2nd International Meeting on Polymer Electrolytes, ed. B. Socrati. New York: Elsevier (1990)

Lightfoot P., Mehta M.A., Bruce P.G., *Science.* 262, 883 (1993)

Liu Y, Gao L. *Carbon.* 47, 52 (2005).

Liu Ye, Wei W.L., Hsu K.Y., Ho W.H., *Thermochimica Acta.* 412, 139 (2004).

Liu, Lei; Guo, G. Y.; Jayanthi, C. S.; Wu, S. Y.. *Physical Review Letters*. 88, 217206 (2002).

Liu, Q; Ren, W; Chen, Z; Yin, L; Li, F; Cong, H; Cheng, H. *Carbon.* 47, 731 (2009).

Lu, X.; Chen, Z. *Chemical Reviews.*   105, 3643 (2005).

Lundberg, R. D., Bailey, F.E., and Callard, R.W., *Journal of Polymer Science Part A*. 4, 1563 (1996)

Biercuk ,M. J., *Applied Physics Letters.* 80, 2767 (2002).

Popov, M.. *Physics Review B.* 65, 033408 (2002).

Yu, M.-F. *Physical Review Letters.* 85, 1456 (2000)

Mac Callum J.R., Vincent C.A., Polymer Electrolytes Reviews 1 and 3, Elsevier, London, (1987/1989).

MacCallum, J.R. and Vincent, C.A., Ed., "Polymer Electrolytes Review I", Elsevier Applied Science, NY and London, 39 (1987)

Macdonald J.R., (Ed.), Impedance Spectroscopy, Wiley, New York, (1987)

Macfarlane D.R., Sun J., Meakin P., Fasoulopoulos P., Hey J., Forsyth M., *Electrochimica Acta.* 40, 2131 (1995).

MacGlashan G. S., Andreev Y.G., Bruce P.G., *Nature.* 398, 792 (1999)

MacKay D.J.C, *Neural Computation.* 4, 415 (1992)

MacKay D.J.C., *Network: Computational Neural System.* 6, 469 (1995)

MacKay D.J.C., *Neural Computation.* 4, 448 (1992)

Majid S.R., Arof A.K., *Physica B.* 390, 209 (2007).

Mamedov A.A., Kotov N.A., Prato M., Guldi D.M., Wicksted J.P., Hirsch A. *Nature Materials.* 1,190 (2002).

Manoratne C.H., Rajapakse R.M.G., Dissanayake M.A.K.L., *International Journal of Electrochemical Science.* 1, 32 (2006)

Manuel Stephan A., Prem Kumar T., Renganathan N.G., Pitchumani S., Thirunakaran R., Muniyandi N. *Journal of Power Sources.* 89, 80 (2000)

Margolis, J.M., "Conductive Polymers and Plastics", Chapman and Hall, NY and London (1989)

Mark, H., Whitby, G.S. Collected Papers of Wallace Hume Carothers in High Polymer Substances; Interscience Publishers: New York, (1940).

Martel, R., Derycke, V., Lavoie, C., Appenzeller, J., Chan, K. K., Tersoff, J., Avouris, Ph. *Physical Review Letters.* 87, 256805 (2001).

Martins M.A.G., Sequeira C.A.C., *Journal of Power Sources*. 32, 107 (1990)

Marzantowicz M. *Electrochimica Acta*. 50, 3969 (2005).

McCreery RL. Bard AJ, editor. Electroanalytical Chemistry, vol. 17. New York: Marcel Dekker; p. 401 (1991).

Meo, Michele; Rossi, Marco. *Composites Science and Technology*. 66**,** 1597 (2006).

Mingo, N.; Stewart, D. A.; Broido, D. A.; Srivastava, D. *Physical Review B*. **77**, 033418 (2008).

Mintmire, J.W.; Dunlap, BI; White, CT. *Physics Review Letters*. 68, 631 (1992).

Mishra R., Baskaran N., Ramakrishna P.A., Rao K.J. *Solid State Ionics*. 112, 261 (1998).

Missan H.P.S., Chua P.P., Sekhon S.S. *Journal of Power Sources.* 158, 1472 (2006)

Molak A., Ksepko E., Gruszka I., Ratuszna A., Paluch M., Ujma Z. *Solid State Ionics.* 176, 1439 (2005).

Morishita K, Takarada T. *Journal of Materials Science*. 34,1169 (1999).

Mu W.B., Wang M.L., Sun Y.M., Hang W., Cni P., Xu C.X., *Journal of Physics Chemistry Solids*. 69, 76 (1998).

Muralidharan P., Venkateswarlu M., Satyanarayana N., *Journal of Non-Crystalline Solids*. 351, 583 (2005).

Nan C.W., Fan L., Lin Y., Cai Q. *Physical Review Letters.* 91, 266104 (2003).

Nanno, T.; Yoshizawa, H.; Ikoma, M. In Solid State Ionics for Batteries; Minami, T., Tatsumisago, M., Wakihara, M., Iwakura, C., Kohjiya, S.,Tanaka, I., Eds.; Springer-Verlag: Tokyo, p 12-18 (2005).

Nagayama, K., Kamioka, K., Iwata, E., Oka, H., Tokunaga, Y, Okada, T., *Electrochemistry.* 69 , 6 (2001).

Naveed A. Siddiqui, Erin L. Li, Man-Lung Sham, Ben Zhong Tang, Shang Lin Gao, Edith Mader, Jang-Kyo Kim. *Composites: Part A*. 41, 539 (2010)

Ng, M.N., Johan, M.R., INEC 2010 - 2010 3rd International Nanoelectronics Conference, Proceedings , art. no. 5424772, pp. 392-393.

Olek M., Ostrander J., Jurga S., Mohwald H., Kotov N., Kempa K. *Nano Letters*. 4, 1889 (2004).

Ong JK, Franklin NR, Zhou C, Chapline MG, Peng S, Cho K. *Science*. 287, 622 (2000).

Onoda M., Manada Y., Moritn S., Yoshino K., *Journal of Physical Society of Japan.* 58, 1985 (1989)

Organic Solvents-Physical Properties and Methods of Purification: Techniques of Chemistry, eds. J.A. Riddick, W.B. Bunger and T.K. Sakano, (John Wiley, New York, Vol II (1986).

Osman M.A., Srivastava D. *Nanotechnology*. 12, 21 (2001).

Osman Z., Arof A.K., *Electrochimica Acta.* 48, 993 (2003)

Pankove J.I., Optical Processes in Semiconductors. Prentice-Hall, Englewood cliffs, NJ, (1971).

Papke B. L., Ratner M. A., Shriver D.F., *Journal Electrochemical Society*. 129,1434 (1982).

Papke B.L., Dupon R., Ratner M.A., Shriver D.F., *Solid State Ionics*. 5, 685, (1981)

Papke B.L., Ratner M.A., Shriver D.F., *Journal of Physics and Chemistry of Solids.* 42, 493 (1981).

Park Y., Nagai M., Kim J.D., Kobayashi K., *Journal of Power Sources*. 137, 175 (2004).

Paruthimal K.G., Kang M-S., Kang Y.S., *Solid State Ionics*. 177, 1091 (2006)

Patel M., Kadihalli G., Chandrappa, Aninda J., Bhattacharyya, *Electrochimica Acta*. 54, 209 (2008).

Patrick A., Glasse A., Lathan R., Linford R., *Solid State Ionics*. 18&19, 1063 (1986)

Paula Obreja, Mihai Kusko, Dana Cristea, Munizer Purica, Florin Comanescu, Proceesing of the Symposium on Photonics Technologies for Framework Program Wroclaw 12 – 14 October (2006).

Pearson R.G., *Journal of American Chemical Society*, 85, 3533 (1963)

Pederson, Broughton M. *Physical Review Letters*. 69, 405 (1992).

Peigney A, Laurent C, Rousset A. *Key Engineering Materials*. 132, 743 (1997).

Petersen, G. Jacobsson, P. Torell, L. M., *Electrochimica Acta*. 37, 1495 (1992).

Planeix JM, Coustel N, Coq B, Brotons V, Kumbhar PS, Dutartre R,. *Journal of American Chemical Society*. 116,7935 (1994).

Plocharski, J., Wieczorek W. *Solid State Ionics*. 28, 979 (1988)

Poncharal P., Wang Z.L., Ugarte D., de Heer W.A., *Science*. 283, 1513 (1999)

Pop, Eric et al.; Mann, David; Wang, Qian; Goodson, Kenneth; Dai, Hongjie. *Nano Letters*. 6, 96 (2005).

Popov V. *Materials Science and Engineering: R: Reports*. 43, 61 (2004).

Prabakar K., Narayandass K., Mangalaraj D., *Materials Science and Engineering B*. 98, 225 (2003).

Pradhan D.K., Samantaray B.K., Choudhary R.N.P., Thakur A.K. *Ionics*. 11, 95 (2005)

P. Raghavana, X. Zhaoa, J-K. Kima, J. Manuela, S. Ghanshyam. Chauhana, J-H. Ahna, C. Nahb, *Electrochimica Acta*. 54, 228 (2008).

Preechatiwong W., Schulta, J.M., *Polymer.* 37, 23, 5109, (1996)

Proneanu S., Toren R., Brie M., Mihilesan G., *Materials Science Forum.* 191, 241 (1995)

Przluski J., Siekierski M., Wieczorek W., *Electrochimica Acta.* 40, 2101 (1995)

Puatrakul T., Doctoral Dissertation, University of Akron (2000)

Qin S., Qin D., Ford W.T., Zhang Y., Kotov N.A. *Chemistry of Materials.* 17, 2131 (2005).

Quartarone E., Musrarelli P., Magistris A., *Solid State Ionics.* 110, 1 (1998)

Qwens B.B., Argue G.R., *Science.* 157, 308 (1967).

Ruoff, R.S. *Nature.* 364, 514 (1993)

Raja V., Mohar V.M., Sharma A.K., Narasimha Rao V.V.R. *Ionics.* 15, 519 (2009)

Rajendran S., Mahendran O., Kannan R., *Journal of Physics and Chemistry of Solids.* 63, 303 (2002)

Rajendran S., Sivakumar P., Shanker Babu R., *Journal of Power Sources.* 164, 815 (2007)

Ramesh S., Arof A.K., *Materials Science Engineering B.* 85, 11 (2001)

Ramesh S., Fung Yuen T., Jun Shen C., *Spectrochimica Acta A.* 69, 670 (2008)

Ramesh S., Tai F.Y., Chia J.S., *Spectrochimica Acta A.* 69, 670 (2008)

Rao N.R., ultraviolet and visible Spectroscopy, Chemical applications, Butterworth, London (1967)

Ratner M.A., Nitzan A., *Faraday Discuss Chemical Society.* 88, 19 (1989).

Ratner M.A., Shriver D.F., *Chemical Reviews.* 88, 109 (1998).

Ravdel, B., Abraham, KM., Gitzendanner, R., DiCarlo, J., Lucht, BL., Campion, C., *Journal of Power Sources.* 119, 805 (2003).

Reddeppa N., Reddy C.V.S., Achari V.B.S., Rao V.V.R.N., Sharma A.K. *Ionics.* 15, 255 (2009)

Reddy C.V.S., Sharma A.K., Narasimha Rao V.V.R. *Materials Science Letters.* 21, 105 (2002).

Reddy C.V.S., Sharma A.K., Narasimha Rao V.V.R. *Journal of Power Sources.* 111, 357 (2002).

Reddy C.V.S., Sharma A.K., Narasimha Rao V.V.R. *Polymer.* 47, 1318 (2006)

Reddy M.J, Chu P.P., *Electrochimica Acta.* 47, 1189 (2002).

Reddy, T. B.; Hossain, S. In Handbook of batteries; Linden, D., Reddy, T.B., Eds.; McGraw-Hill: New York, pp 34.1-34.62 (2002).

Reicha F.M., El-Hiti M., El-Sonabati A.Z., Diab M.A. *Journal of Physics D Applied Physics.* 24, 369 (1991).

Resasco DE, Alvarez WE, Pompeo F, Balzano L, Herrera JE, Kitiyanan B. Journal *of Nanoparticle Research.* 4,131 (2002).

Rinzler AG. *Science*. 269, 1550 (1995).

Rinzler AG, Hafner JH, Nikolaev P, Lou L, Kim SG, Tomanek D. *Science*. 269, 1550 (1995).

Robertson, A. D.; West, A. R.; Ritchie, A. G. *Solid State Ionics*. 104, 1 (1997)

Rosen R. *Applied Physics Letters.* 76, 1668 (2000).

Ruan S.L., Gao P., Yang X.G., Yu T.X., *Polymer*. 44, 5643 (2003)

Rueckes T, *Science*. 289, 94 (2000).

Ruoff R, Lorents D. *Carbon*. 33,925 (1995).

Rupp B., Schmuck M., Balducci A., Winter M., Kern W. *European Polymer Journal*. 44, 2986 (2008)

Saika D., Chen-Yang Y.M., Chen Y.T., Li Y.K., Lin S.I. *Desalination.* 234, 24 (2008)

Saito S. *Science*. 278, 77 (1997).

Saito Y, Uemura S. *Carbon.* 38, 169 (1999).

Saito Y, Uemura S. *Carbon.* 38, 169 (2000).

Schadler LS, Giannaris SC, Ajayan PM. *Applied Physics Letters*. 73,3842 (1998).

Scharff P. *Carbon.* 36, 481 (1998).

Scrosati B., Croce F., Persi L., *Journal of the Electrochemical Society*. 147, 1718 (2000).

Seki, M and Sato, K., Yosomiya, R, *Macromolecular Chemistry*. 193, 2971 (1992)

Shanmukaraj D., Murugan R., *Journal of Power Sources.* 149, 90 (2005)

Shu-Hang Liao, Chuan-Yu Yena, Cheng –Chih Wenga, Yu-Feng Lina, Chen-Chi M.Maa, Ching-Hung Yang, Ming-Chi Tsai, Ming-Yu Yena, Min Chien Hsiao, Shuo Jen Leed, Xiao-Feng Xiee, Yi-Hsiu Hsiao, *Journal of Power Sources.* 185, 1225 (2008).

Smagin, AA., Matyuka VA., V.P. Korobtsev, VP. *Journal of Power Sources.* 68 ,(1997), 326.

Singh K.P., Gupta P.N., *European Polymer Journal.* 34, 1023 (1997).

Sinha, Saion, Barjami, Saimir; Iannacchione, Germano; Schwab, Alexander; Muench, George. *Journal of Nanoparticle Research*. **7**, 651 (2005).

Sinnott, Susan B, Andrews, Rodney. *Critical Reviews in Solid State and Materials Sciences*. 26, 145 (2001).

Siva Kumar J., Subrahmanyam A.R., Jaipal Reddy M., Subba Rao U.V. *Materials Letters.* 60, 3346 (2006)

Sloop, SE, Pugh, JK, Wang, S, Kerr, JB, Kinoshita, K. *Electrochemica Solid-State Letters.*

4 , A42 (2001).

Sloop, SE., Kerr, JB., Kinoshita, K., *Journal of Power Sources.* 119, 330 (2003).

Song J.M., Kang H.R., Kim S.W., Lee W.M., Kim H.T. *Electrochmica Acta*. 48, 1339 (2003)

Soundarrajan P, Patil A, Liming D. *American Vacuum Society*. 8 1198–201 (2002).

Staryga E., Swiatek J. *Thin Solid Films.* 56, 311 (1979).

Stephan A.H., Nahm K.S. *Polymer* 47, 5952 (2006)

Stevens J.R., Wieczorek W., Raducha D., Jeffrey K.K., *Solid State Ionics*. 97, 347 (1997).

Stoeva Z., Martin-Litas I., Staunton E., Andreev Y.G., Bruce P.G., *Journal of the American Chemical Society.* 125, 4619 (2003)

Stygar J., Zukowska G., Wieczorek W., *Solid State Ionics*. 174, 2645 (2005)

Subban R.H.Y., Arof A.K., *European Polymer Journal.* 40, 1841 (2004).

Sugie H. *Applied Physics Letters.* 78, 2578 (2001).

Sundar M., Selladurri S., *Ionics.* 12, 281 (2006).

Tabatn M., Satoh M., Kanoto K., Yoshiro K., *Journal of the Physical Society of Japan.* 55, 1305 (1986).

Taner Ozel, Anshu Gaur, John A. Rogers, Moonsub Shim, *Nano Letters.* 5, 905 (2005)

Tang ZK. *Science.* 292, 2462 (2001).

Tans SJ, Verschueren RM, Dekker C. *Nature.* 393 (1998).

Tarascon J.M., Armand M., *Nature.* 414, 359 (2001)

Tasaki, K., Kanda, K., Nakamura, S., Ue, M., *Electrochemical Society.* 150, A1628 (2003).

Tekleab D, Carroll DL, Samsonidze GG, Yakobson BI. *Physical Review B*. 64, 035419 (2001).

Teng X-G., Li F-Q., Ma P-H., Ren Q-D., Li S-Y., *Thermochimica Acta*. 436, 30 (2005)

Thostenson, Erik; Li, C; Chou, T. *Composites Science and Technology*. 65, 491 (2005).

Thoteson E, Ren Z, Chou T. *Composites Science and Technology*. 61,1899 (2001).

Tibbetts G.G., Beetz C.P. *Journal of Physics D: Applied Physics*. 20, 292 (1987).

Tobishima S., Yamaji A., *Electrochimica Acta*. 29, 267 (1984).

Tominaga Y., Takizawa N., Ohno H., *Electrochimica Acta*. 45, 1285 (2000).

Turky G., Dawy M., *Materials Chemistry Physics*. 77, 48 (2002)

Ulanski J., Polanowski P., Traiez A., Hofmann M., Dormann E., Laukhina E., *Synthetic Metals*. 94, 23, (1998)

Uma Devi C., Sharma A.K., Rao V.V.R.N., *Materials Letters*. 56, 167 (2002).

Vogel H., *Physics and Astronomy*. 22, 645 (1921)

Volel, M., Armand M., Gorecki W., *Macromolecules*. 37, 8373 (2004).

Wall A., Coleman J.N., Ferreira M.S., *Physical Review B*. 71, 125421 (2005).

Walls H.J., Zhou J., Yerian J.A., *Journal of Power Sources*. 89, 156 (2000)

Wang B, Liu X, Wu D, Wang H, Jiang J, Wang X. *Journal of Materials Chemistry*. 6, 1124 (2003).

Wang QH, Setlur AA, Lauerhaas JM, Dai JY, Seelig EW, Chang RH. *Applied Physics Letters*. 72, 399 (1998).

Wang WK, Cao LM. *Russian Physics Journal*. 44, 178 (2001).

Wang Z., Liang Z., Wang B., Zhang C., Kramer L. *Composites Part A: Applied Science and Manufacturing.* 35, 1225 (2004).

Wang, X.; Li, Q.; Xie, J.; Jin, Z.; Wang, J.; Li, Y.; Jiang, K.; Fan, S. *Nano Letters.* 9, 3137 (2009).

Watanabe, M., Sanui, K. and Ogata N., *Journal of Applied Physics.* 57, 123 (1985)

Wen S.J., Richardson T.J., Ghantous D.I., Striebel K.A., Ross P.N., Cairns E.J., *Journal of Electroanalytical Chemistry.* 408, 113 (1996)

Wen Z.Y., Itoh T., Hirata N., Ikeda M., Kubo M., Yamamoto O., *Journal of Power Sources.* 90, 20 (2000).

Wendsjo A., Lindgren J., Thomas J.O., Farrington G.C., *Solid State Ionics.* 53, 1077 (1992)

Weston, J.E., Steele B.C.H., *Solid State Ionics.* 7, 75 (1982).

Wetton R.E., James D.B., Whiting W.J., *Polymer Science.:Polymer Letters.* 14, 577 (1976)

Whang W.T., Lu C.L., *Applied Polymer Science.* 56, 1635 (1995).

Whittaker, Brink J, Husseni M, Linford G, Davis M. *Appled Science Letters.* 83, 25 (2003).

Wieczoreck W., Zaleswka A., Raducha D., Florjanczyk Z., JStevens J.R., Ferry A., Jacobsson P., *Macromolecules.* 29, 143 (1996).

Wieczorek W., Lipka P., Zukowska G., Wycislik J. *Physical Chemistry B.* 102, 6968 (1998).

Wieczorek W., Stevens J.R., Florjanczyk Z. *Solid State Ionics.* 85,76 (1996).

Wieczorek W., Such K., Wycislik H., Plosharski J. *Solid State Ionics.* 36, 255 (1989).

Wieczorek, W. *Synthetic Metals.* 45, 373 (1991)

Wiliams M.L., Landel R.F., Ferry J.D., *Journal of.American Chemial Society.* 77, 3701 (1955)

Winter, M.; Brodd, R. *Chemical Reviews*. 104, 4245, (2004).

Wintersgill M.C., Fontanella J.J., in Polymer Electrolyte Reviews 2, ed. MacCullum J.R., Vincent C.A., Elsevier, London, p. 45 (1989).

Wright P. V., Br. *Polymer.* 7, 319 (1975).

Xia, D.W., Soltz D., Smid J., *Solid State Ionics.* 14, 221 (1984).

Xu W, Deng Z.H., Zhang X.Z., Wan G.X., *Journal of Solid State Electrochemistry*. 2, 257 (1998)

Y.H.Yang. *Applied Physics Letters.* 98, 041901 (2011).

Yahya M.Z.A., Arof A.K., *European. Polymer Journal.* 38, 1191 (2002)

Yamabe T. *Synthetic Metals.* 8, 1511 (1995).

Yang L.L., Huq R., Farrington G.C., Chiadelli G., *Solid State Ionics*. 18/19, 315 (1986)

Yu, Min-Feng; Lourie, Oleg; Dyer, Mark J.; Moloni, Katerina; Kelly, Thomas F.; Ruoff, Rodney S. *Science*. 287, 637 (2000).

Zain N.M., Arof A.K., *Materials Science Engineering B*. 52, 40 (1998)

Zhang H., Maitra P., Wunder S.L., *Solid State Ionics.* 178, 1975 (2008)

Zhang, X, Ross, PN., Kostecki, R., Kong, F., Sloop, S., Kerr, JB., Streibel, K., Cairns EJ., F. McLarnon, F., *Journal of Electrochemical Society*. 148, A463 (2001).

Zhao Q, Gan Z, Zhuang Q. *Electroanalysis.* 23, 1609 (2002).

Zhao, X.; Liu, Y.; Inoue, S.; Suzuki, T.; Jones, R. O.; Andol, Y. *Physical Review Letters.* 92, 125502 (2004).

Zhou W., Ooi Y.H., Russo R., Papanek P., Luzzi D.E., Fischer J.E. *Chemical Physics Letters.* 350,6 (2001).

Zhu J, Peng H, Rodriguez F, Margrave J, Khabashesku V, Imam A. *Advanced Functional Materials* 8, 643 (2004).

Internet Sources

"A Better Way to Make Nanotubes". Berkeley Lab.. January 5, 2009.

http://newscenter.lbl.gov/feature-stories/2009/01/05/better-way-to-make-nanotubes/.

CarboLex". http://carbolex.com.

Carbon Nanohoops: Shortest Segment of a Carbon Nanotube Synthesized". Berkeley Lab..

http://www.lbl.gov/msd/assets/docs/highlights/09-Bertozzi.pdf.

Carbon Solutions, Inc.". http://www.carbonsolution.com.

internet sources; http://www.wikipedia.org/

The Web site of Hyperion Catalysis International, Inc., is available at www.fibrils.com

Bernard A. Applied sciences aims its nanotubes at the near-term market for polymers,
SMALLTIMES, 2002. Available from: http:// www.smalltimes.com.

Smith J. Slicing it extra thin, Tireview, 2005. Available from: http://www.tireview.com.

APPENDICES

Table A1: Conductivity values of different composition polymer electrolyte samples at elevated temperature

PEO (wt%)	LiPF$_6$ (wt%)	EC (wt%)	CNT (wt%)	Temp (K^{-1})	Conductivity (Scm^{-1})
100	0	0	0	3.35402	-21.8472
100	0	0	0	3.29870	-21.3619
100	0	0	0	3.24517	-20.3656
100	0	0	0	3.19336	-19.9035
100	0	0	0	3.14317	-16.5504
100	0	0	0	3.09454	-16.2984
100	0	0	0	3.04739	-15.8950
100	0	0	0	3.00165	-15.6734
100	0	0	0	2.95727	-15.2018
100	0	0	0	2.91418	-14.9211
100	0	0	0	2.87233	-13.7957
100	0	0	0	2.83166	-13.6085
100	0	0	0	2.79213	-13.4302
100	0	0	0	2.75368	-13.3027
100	0	0	0	2.71628	-12.7967
100	0	0	0	2.67989	-12.7717
100	5	0	0	3.35402	-13.6310
100	5	0	0	3.29870	-13.3716
100	5	0	0	3.24517	-12.5725
100	5	0	0	3.19336	-11.6943
100	5	0	0	3.14317	-9.47620
100	5	0	0	3.09454	-8.87486
100	5	0	0	3.04739	-8.32398
100	5	0	0	3.00165	-5.51057
100	5	0	0	2.95727	-5.44313
100	5	0	0	2.91418	-5.43535
100	5	0	0	2.87233	-5.49597
100	5	0	0	2.83166	-5.48116
100	5	0	0	2.79213	-5.48859
100	5	0	0	2.75368	-5.49597
100	5	0	0	2.71628	-5.48859
100	5	0	0	2.67989	-5.48116
100	10	0	0	3.35402	-11.6154
100	10	0	0	3.29870	-10.8729
100	10	0	0	3.24517	-9.93411
100	10	0	0	3.19336	-9.12474
100	10	0	0	3.14317	-8.11720
100	10	0	0	3.09454	-7.62530
100	10	0	0	3.04739	-7.47011

100	10	0	0	3.00165	-7.21983
100	10	0	0	2.95727	-7.07010
100	10	0	0	2.91418	-7.04993
100	10	0	0	2.87233	-5.91742
100	10	0	0	2.83166	-5.20805
100	10	0	0	2.79213	-5.16630
100	10	0	0	2.75368	-5.13286
100	10	0	0	2.71628	-5.10347
100	10	0	0	2.67989	-5.15405
100	15	0	0	3.35402	-10.9114
100	15	0	0	3.29870	-9.81122
100	15	0	0	3.24517	-9.15581
100	15	0	0	3.19336	-7.60044
100	15	0	0	3.14317	-6.92684
100	15	0	0	3.09454	-4.93584
100	15	0	0	3.04739	-4.90384
100	15	0	0	3.00165	-4.86741
100	15	0	0	2.95727	-4.86234
100	15	0	0	2.91418	-4.84352
100	15	0	0	2.87233	-4.84352
100	15	0	0	2.83166	-4.84179
100	15	0	0	2.79213	-4.83658
100	15	0	0	2.75368	-4.82257
100	15	0	0	2.71628	-4.84179
100	15	0	0	2.67989	-4.81727
100	20	0	0	3.35402	-10.1023
100	20	0	0	3.29870	-9.30859
100	20	0	0	3.24517	-8.50518
100	20	0	0	3.19336	-6.87561
100	20	0	0	3.14317	-5.10705
100	20	0	0	3.09454	-5.06966
100	20	0	0	3.04739	-5.06966
100	20	0	0	3.00165	-5.05043
100	20	0	0	2.95727	-5.05043
100	20	0	0	2.91418	-5.05043
100	20	0	0	2.87233	-5.06966
100	20	0	0	2.83166	-5.06009
100	20	0	0	2.79213	-5.06009
100	20	0	0	2.75368	-5.09783
100	20	0	0	2.71628	-5.09783
100	20	0	0	2.67989	-5.16929
100	20	5	0	3.35402	-9.73212
100	20	5	0	3.29870	-9.07921
100	20	5	0	3.24517	-8.18058
100	20	5	0	3.19336	-7.84160
100	20	5	0	3.14317	-7.57361

100	20	5	0	3.09454	-7.40133
100	20	5	0	3.04739	-7.22931
100	20	5	0	3.00165	-7.16757
100	20	5	0	2.95727	-7.11998
100	20	5	0	2.91418	-7.11998
100	20	5	0	2.87233	-7.11817
100	20	5	0	2.83166	-7.21463
100	20	5	0	2.79213	-7.28898
100	20	5	0	2.75368	-7.20970
100	20	5	0	2.71628	-7.10544
100	20	5	0	2.67989	-7.00130
100	20	10	0	3.35402	-8.85455
100	20	10	0	3.29870	-8.08584
100	20	10	0	3.24517	-7.53347
100	20	10	0	3.19336	-7.30017
100	20	10	0	3.14317	-6.97964
100	20	10	0	3.09454	-5.56302
100	20	10	0	3.04739	-5.36315
100	20	10	0	3.00165	-5.33624
100	20	10	0	2.95727	-5.37196
100	20	10	0	2.91418	-5.36315
100	20	10	0	2.87233	-5.35426
100	20	10	0	2.83166	-5.36315
100	20	10	0	2.79213	-5.35426
100	20	10	0	2.75368	-5.37196
100	20	10	0	2.71628	-5.36315
100	20	10	0	2.67989	-5.40645
100	20	15	0	3.35402	-8.48561
100	20	15	0	3.29870	-7.96573
100	20	15	0	3.24517	-7.76506
100	20	15	0	3.19336	-7.57437
100	20	15	0	3.14317	-7.39641
100	20	15	0	3.09454	-7.30940
100	20	15	0	3.04739	-7.23554
100	20	15	0	3.00165	-7.17852
100	20	15	0	2.95727	-7.13254
100	20	15	0	2.91418	-7.09931
100	20	15	0	2.87233	-6.95413
100	20	15	0	2.83166	-6.91266
100	20	15	0	2.79213	-6.89292
100	20	15	0	2.75368	-6.79894
100	20	15	0	2.71628	-6.75986
100	20	15	0	2.67989	-6.67681
100	20	15	1	3.35402	-8.42083
100	20	15	1	3.29870	-7.69855
100	20	15	1	3.24517	-7.38929

100	20	15	1	3.19336	-7.19753
100	20	15	1	3.14317	-7.04879
100	20	15	1	3.09454	-7.00047
100	20	15	1	3.04739	-6.93712
100	20	15	1	3.00165	-6.85699
100	20	15	1	2.95727	-6.72915
100	20	15	1	2.91418	-6.69749
100	20	15	1	2.87233	-6.65784
100	20	15	1	2.83166	-6.72264
100	20	15	1	2.79213	-6.77112
100	20	15	1	2.75368	-6.69480
100	20	15	1	2.71628	-6.65364
100	20	15	1	2.67989	-6.59004
100	20	15	5	3.35402	-6.64774
100	20	15	5	3.29870	-6.39311
100	20	15	5	3.24517	-6.21264
100	20	15	5	3.19336	-6.04334
100	20	15	5	3.14317	-5.95460
100	20	15	5	3.09454	-5.87469
100	20	15	5	3.04739	-5.81026
100	20	15	5	3.00165	-5.76295
100	20	15	5	2.95727	-5.74536
100	20	15	5	2.91418	-5.73145
100	20	15	5	2.87233	-5.72543
100	20	15	5	2.83166	-5.79537
100	20	15	5	2.79213	-5.81946
100	20	15	5	2.75368	-5.86073
100	20	15	5	2.71628	-5.90204
100	20	15	5	2.67989	-5.89866

Table A2: Comparison between simulated and experimental data

PEO	Salt	EC	CNT	Z_{real}	Z_{imag} (measured)	Z_{imag} (Predicted)
100	0	0	0	5146800	1452700	1455449.125
100	0	0	0	5070800	1558600	1549859
100	0	0	0	4976900	1638100	1659234.875
100	0	0	0	4904000	1734700	1738784.625
100	0	0	0	4812400	1851700	1832318.25
100	0	0	0	4694800	1942400	1942340.25
100	0	0	0	4567400	2055900	2049387.125
100	0	0	0	4427800	2160000	2153022
100	0	0	0	4270200	2256100	2253987
100	0	0	0	4097700	2342500	2346466
100	0	0	0	3912300	2418800	2426605
100	0	0	0	3714700	2482100	2492036.75
100	0	0	0	3507900	2532400	2540522.5
100	0	0	0	3294100	2567500	2571191
100	0	0	0	3074100	2584800	2583947
100	0	0	0	2851900	2584700	2578968.75
100	0	0	0	2629500	2567700	2557023.75
100	0	0	0	2411800	2530800	2519541.5
100	0	0	0	2199400	2475300	2467556
100	0	0	0	1997400	2406500	2403298
100	0	0	0	1805600	2325100	2327775.25
100	0	0	0	1625500	2236300	2242549.25
100	0	0	0	1457900	2140600	2149173.25
100	0	0	0	1302400	2039700	2048740.875
100	0	0	0	1160700	1935300	1944064.25
100	0	0	0	1030800	1829700	1835616.375
100	0	0	0	914020	1723500	1726664.5
100	0	0	0	808600	1618500	1617942.625
100	0	0	0	714130	1515400	1511291.25
100	0	0	0	630180	1415200	1408511.75
100	0	0	0	555220	1319100	1309793.125
100	0	0	0	488680	1226300	1216163.875
100	0	0	0	429820	1137900	1128125.625
100	0	0	0	378140	1054200	1046249.5
100	0	0	0	332460	975010	969705.8125
100	0	0	0	292250	900600	898404.125
100	0	0	0	257140	831070	832401.25
100	0	0	0	226010	765690	770174.75
100	0	0	0	198900	705030	712370.875
100	0	0	0	175110	648460	658134.0625

100	0	0	0	154260	596060	607221.1875
100	0	0	0	135900	547640	559169.75
100	0	0	0	119810	502720	514065
100	0	0	0	105630	461190	471558
100	0	0	0	93191	422940	431790.8438
100	0	0	0	82268	387690	394680.875
100	0	0	0	72666	355230	360142.8125
100	0	0	0	64169	325310	327918.0313
100	0	0	0	56650	297820	297967.9688
100	0	0	0	50049	272560	270465.7188
100	0	0	0	44196	249360	245057.1406
100	0	0	0	39039	228070	221822.3594
100	0	0	0	34479	208520	200575.3281
100	0	0	0	30380	190610	180881.7656
100	0	0	0	26833	174280	163364.5156
100	0	0	0	23646	159170	147235.4219
100	0	0	0	20824	145390	132631.2656
100	0	0	0	18342	132790	119526.3281
100	0	0	0	16101	121190	107483.75
100	0	0	0	14126	110600	96697.35156
100	0	0	0	12381	100900	87032.78906
100	0	0	0	10842	91991	78397
100	0	0	0	9464.2	83854	70577.99219
100	0	0	0	8246.2	76387	63596.41016
100	0	0	0	7184.8	69564	57457.49219
100	0	0	0	6249.8	63336	52006.17188
100	0	0	0	5411.3	57650	47084.76172
100	0	0	0	4693.9	52454	42845.63281
100	0	0	0	4061.9	47723	39092.50781
100	0	0	0	3501.4	43393	35747.80859
100	0	0	0	3023.6	39440	32886.41797
100	0	0	0	2609.2	35830	30392.08789
100	0	0	0	2249.7	32544	28225.99609
100	0	0	0	1931.1	29539	26297.78125
100	0	0	0	1655.8	26805	24628.01367
100	0	0	0	1413.6	24321	23157.2207
100	0	0	0	1221.2	22086	21986.31836
100	0	0	0	971.86	20122	20466.45703
100	0	0	0	925.55	18207	20184.74805
100	0	0	0	813.83	16574	19502.3125
100	0	0	0	717.21	14907	18910.39063
100	0	0	0	623.2	13599	18336.57031
100	0	0	0	497.77	12305	17566.31836
100	0	0	0	438.36	11186	17204.41602
100	0	0	0	320.95	10139	16483.31055

100	0	0	0	262.74	9133	16126.57031
100	0	0	0	274.93	8287.8	16201.52344
100	0	0	0	206.55	7504.6	15780.22949
100	0	0	0	196.51	6805.6	15720.75977
100	0	0	0	182.51	6157.2	15632.86523
100	0	0	0	141.03	5563.8	15379.58008
100	0	0	0	133.36	5037.9	15330.43359
100	0	0	0	111.57	4543.7	15198.62988
100	0	0	0	101.13	4106.5	15133.99902
100	0	0	0	87.162	3710	15048.72363
100	0	0	0	67.315	3356.2	14927.24219
100	0	0	0	66.831	3024.7	14922.08106
100	0	0	0	60.185	2722.9	14880.71484
100	0	0	0	52.506	2448.3	14834.18652
100	0	0	0	49.925	2205	14818.70313
100	20	0	0	225.17	183.24	181.11011
100	20	0	0	220.08	166.61	166.72405
100	20	0	0	215.06	151.35	152.25565
100	20	0	0	210.23	137.6	138.16116
100	20	0	0	206.22	125.17	126.385
100	20	0	0	202.36	113.82	115.01898
100	20	0	0	198.76	103.34	104.40847
100	20	0	0	195.47	93.922	94.704399
100	20	0	0	192.47	85.294	85.840721
100	20	0	0	189.6	77.44	77.328461
100	20	0	0	187.03	70.34	69.655495
100	20	0	0	184.63	63.8	62.421936
100	20	0	0	182.49	57.978	55.895237
100	20	0	0	181.09	52.59	51.578552
100	20	0	0	179.57	47.825	46.845699
100	20	0	0	178.25	43.386	42.697685
100	20	0	0	177.04	39.404	38.867966
100	20	0	0	175.96	35.745	35.434307
100	20	0	0	174.96	32.461	32.250713
100	20	0	0	174.02	29.472	29.264141
100	20	0	0	173.19	26.754	26.642338
100	20	0	0	172.37	24.315	24.077246
100	20	0	0	171.72	22.085	22.070465
100	20	0	0	171.03	20.1	19.975513
100	20	0	0	170.42	18.226	18.162273
100	20	0	0	169.87	16.544	16.565811
100	20	0	0	169.36	15.071	15.124664
100	20	0	0	168.88	13.77	13.807723
100	20	0	0	168.41	12.486	12.561213
100	20	0	0	168.03	11.365	11.587825

100	20	0	0	167.63	10.376	10.599983
100	20	0	0	167.31	9.4441	9.839533
100	20	0	0	166.97	8.6418	9.062793
100	20	0	0	166.48	7.967	8.004339
100	20	0	0	166.25	7.2911	7.534205
100	20	0	0	165.92	6.5849	6.891373
100	20	0	0	165.63	5.9704	6.358853
100	20	0	0	165.29	5.4866	5.775299
100	20	0	0	164.97	5.1009	5.268021
100	20	0	0	164.79	4.7645	5.001486
100	20	0	0	164.62	4.3751	4.762395
100	20	0	0	164.29	3.9245	4.334513
100	20	0	0	164.02	3.6801	4.021146
100	20	0	0	163.72	3.4544	3.712904
100	20	0	0	163.5	3.3504	3.514054
100	20	0	0	163.38	3.1639	3.415823
100	20	0	0	163.26	2.9445	3.324352
100	20	0	0	163.08	2.7284	3.200693
100	20	0	0	162.88	2.6062	3.082519
100	20	0	0	162.6	2.5422	2.950802
100	20	0	0	162.39	2.5623	2.878363
100	20	0	0	162.26	2.6014	2.844884
100	20	0	0	162.16	2.5664	2.825126
100	20	0	0	162	2.4239	2.803908
100	20	0	0	161.84	2.4905	2.796041
100	20	0	0	161.62	2.5244	2.806285
100	20	0	0	161.5	2.5741	2.822204
100	20	0	0	161.26	2.7253	2.875801
100	20	0	0	161.15	2.8823	2.910011
100	20	0	0	160.84	2.9983	3.037699
100	20	0	0	160.78	3.2109	3.067701
100	20	0	0	160.53	3.4828	3.210937
100	20	0	0	160.32	3.7825	3.353257
100	20	0	0	160.16	4.1717	3.474544
100	20	0	0	160.5	3.4122	3.229958
100	20	0	0	160.24	4.2127	3.412709
100	20	0	0	158.55	5.1327	5.221555
100	20	0	0	158.37	5.4193	5.463213
100	20	0	0	159.5	5.5484	4.084807
100	20	0	0	158.14	6.0152	5.780969
100	20	0	0	158.42	6.8968	5.395343
100	20	0	0	157.03	7.8929	7.400476
100	20	0	0	156.94	8.0541	7.534205
100	20	0	0	155.63	9.0658	9.414213
100	20	0	0	154.54	9.9221	10.776514

100	20	0	0	153.93	10.392	11.425932
100	20	0	0	153.59	11.637	11.749903
100	20	0	0	152.26	12.145	12.765734
100	20	0	0	151.5	12.941	13.185749
100	20	0	0	150.16	13.191	13.712964
100	20	0	0	147.92	14.548	14.265792
100	20	0	0	146.46	15.133	14.582811
100	20	0	0	144.53	15.866	15.094112
100	20	0	0	140.91	19.248	16.437578
100	20	0	0	142.04	14.809	15.974574
100	20	0	0	138.12	18.042	17.611464
100	20	0	0	137.31	16.339	17.928852
100	20	0	0	129.37	16.923	19.256584
100	20	0	0	125.1	19.554	18.468138
100	20	0	0	119.29	17.337	16.385441
100	20	0	0	118.81	15.691	16.187508
100	20	0	0	111.48	13.275	13.117148
100	20	0	0	104.09	11.801	10.332903
100	20	0	0	98.347	8.2903	8.431856
100	20	0	0	91.404	4.5357	6.259886
100	20	0	0	81.706	0.30649	3.076843
100	20	0	0	79.278	5.4967	2.217426
100	20	15	0	62.066	115.87	115.66007
100	20	15	0	59.266	104.81	105.11639
100	20	15	0	56.709	94.836	95.057816
100	20	15	0	54.3	85.799	85.595917
100	20	15	0	52.192	77.694	77.522591
100	20	15	0	50.259	70.353	70.346718
100	20	15	0	48.249	63.547	63.098663
100	20	15	0	46.632	57.53	57.382969
100	20	15	0	45.186	52.114	52.317707
100	20	15	0	43.81	47.197	47.504208
100	20	15	0	42.557	42.755	43.101082
100	20	15	0	41.452	38.741	39.186306
100	20	15	0	40.402	35.105	35.42852
100	20	15	0	39.472	31.821	32.064537
100	20	15	0	38.516	28.802	28.570908
100	20	15	0	37.781	26.16	25.862926
100	20	15	0	37.122	23.738	23.423504
100	20	15	0	36.603	21.564	21.499771
100	20	15	0	36.013	19.56	19.318024
100	20	15	0	35.541	17.836	17.585228
100	20	15	0	35.04	16.117	15.769941
100	20	15	0	34.632	14.614	14.32077
100	20	15	0	34.217	13.225	12.885504

100	20	15	0	33.916	12.031	11.876713
100	20	15	0	33.555	10.947	10.710239
100	20	15	0	33.26	9.9311	9.797035
100	20	15	0	33.003	8.9721	9.0319
100	20	15	0	32.717	8.1704	8.211268
100	20	15	0	32.501	7.4063	7.607756
100	20	15	0	32.304	6.6986	7.063216
100	20	15	0	32.095	6.0831	6.482065
100	20	15	0	31.921	5.51	5.986649
100	20	15	0	31.76	4.9891	5.510465
100	20	15	0	31.629	4.5477	5.10519
100	20	15	0	31.475	4.1056	4.602474
100	20	15	0	31.356	3.7236	4.191754
100	20	15	0	31.239	3.3749	3.767478
100	20	15	0	31.134	3.0567	3.370079
100	20	15	0	31.016	2.7692	2.90664
100	20	15	0	30.917	2.508	2.507735
100	20	15	0	30.816	2.2673	2.096552
100	20	15	0	30.718	2.03	1.70031
100	20	15	0	30.646	1.8284	1.415992
100	20	15	0	30.552	1.6496	1.060998
100	20	15	0	30.477	1.4852	0.797881
100	20	15	0	30.42	1.3255	0.613781
100	20	15	0	30.332	1.189	0.364451
100	20	15	0	30.279	1.0557	0.239091
100	20	15	0	30.236	0.92274	0.153239
100	20	15	0	30.162	0.80874	0.04352
100	20	15	0	30.107	0.69908	-0.003173
100	20	15	0	30.061	0.58873	-0.016612
100	20	15	0	30.007	0.48858	-0.00039
100	20	15	0	29.959	0.39139	0.045374
100	20	15	0	29.92	0.2991	0.105506
100	20	15	0	29.877	0.20308	0.196918
100	20	15	0	29.828	0.09001	0.33456
100	20	15	0	29.776	0.010463	0.521323
100	20	15	0	29.775	0.080788	0.525263
100	20	15	0	29.758	0.20272	0.596054
100	20	15	0	29.703	0.32193	0.857085
100	20	15	0	29.672	0.44482	1.026473
100	20	15	0	29.637	0.54559	1.237219
100	20	15	0	29.581	0.80697	1.618052
100	20	15	0	29.57	0.9816	1.699153
100	20	15	0	29.633	1.0708	1.262594
100	20	15	0	29.477	1.2342	2.468344
100	20	15	0	29.583	1.4477	1.603453

100	20	15	0	29.522	1.6823	2.077551
100	20	15	0	29.423	2.037	2.982993
100	20	15	0	29.51	2.227	2.178347
100	20	15	0	29.409	2.6128	3.124454
100	20	15	0	29.432	2.9184	2.893781
100	20	15	0	29.275	3.292	4.640477
100	20	15	0	29.286	3.7509	4.505269
100	20	15	0	29.247	4.2335	4.992923
100	20	15	0	29.23	4.7627	5.212709
100	20	15	0	29.196	5.3516	5.664792
100	20	15	0	29.112	6.0467	6.850149
100	20	15	0	29.113	6.8179	6.835436
100	20	15	0	29.046	7.7085	7.844572
100	20	15	0	28.995	8.6473	8.647015
100	20	15	0	28.909	9.7397	10.058764
100	20	15	0	28.791	10.955	12.09314
100	20	15	0	28.739	12.344	13.016655
100	20	15	0	28.915	13.773	9.958199
100	20	15	0	28.403	15.565	19.140293
100	20	15	0	28.827	17.762	11.462516
100	20	15	0	28.54	19.437	16.634716
100	20	15	0	28.395	21.957	19.285698
100	20	15	0	27.934	25.348	27.177933
100	20	15	0	27.875	27.797	28.09137
100	20	15	0	27.594	31.418	32.069519
100	20	15	0	26.984	34.856	38.624386
100	20	15	0	27.121	39.098	37.379707
100	20	15	0	26.114	43.021	44.34634
100	20	15	0	26.202	47.708	43.896225
100	20	15	0	23.961	51.509	51.894123
100	20	15	0	21.551	55.633	55.566986
100	20	15	5	18.224	10.407	9.75597
100	20	15	5	18.917	12.386	12.3838
100	20	15	5	18.554	11.351	11.0157
100	20	15	5	14.105	0.31629	5.77679
100	20	15	5	13.697	25.359	21.7198
100	20	15	5	13.955	1.6202	10.1849
100	20	15	5	15.828	4.3218	5.84935
100	20	15	5	13.815	7.9545	15.8634
100	20	15	5	14.616	1.3864	1.97844
100	20	15	5	13.996	1.0692	8.80526
100	20	15	5	14.675	1.5416	2.25113
100	20	15	5	14.434	0.86812	1.77534
100	20	15	5	14.17	31.114	4.40587
100	20	15	5	15.997	4.7142	5.64488

100	20	15	5	13.899	17.902	12.2799
100	20	15	5	14.239	0.30822	3.28871
100	20	15	5	15.164	2.7322	5.16787
100	20	15	5	14.324	0.58345	2.35456
100	20	15	5	13.95	2.0408	10.3622
100	20	15	5	13.838	6.3254	14.8311
100	20	15	5	15.383	3.3057	5.84256
100	20	15	5	13.91	15.959	11.8494
100	20	15	5	13.945	3.4259	10.5414
100	20	15	5	14.081	48.917	6.36417
100	20	15	5	9.8535	72.303	72.452
100	20	15	5	13.909	5.6205	11.8882
100	20	15	5	15.279	3.0206	5.59306
100	20	15	5	14.368	0.66719	2.04457
100	20	15	5	14.272	20.231	2.87075
100	20	15	5	14.07	22.387	6.64835
100	20	15	5	14.261	0.40138	3.002
100	20	15	5	13.887	3.0803	12.7599
100	20	15	5	14.551	43.65	1.77585
100	20	15	5	13.399	53.745	39.6348
100	20	15	5	23.163	25.772	25.8348
100	20	15	5	14.558	1.2369	1.79175
100	20	15	5	13.842	4.9332	14.6555
100	20	15	5	20.755	17.781	18.5538
100	20	15	5	14.014	0.76465	8.24108
100	20	15	5	13.947	1.8616	10.4695
100	20	15	5	14.103	0.20741	5.82406
100	20	15	5	22.492	23.472	23.7602
100	20	15	5	13.565	64.759	29.2221
100	20	15	5	29.673	50.484	50.1893
100	20	15	5	27.471	41.542	41.562
100	20	15	5	16.173	5.1537	5.44736
100	20	15	5	13.821	12.662	15.5905
100	20	15	5	12.713	69.599	81.249
100	20	15	5	13.894	3.9176	12.4786
100	20	15	5	13.232	60.105	50.5858
100	20	15	5	25.543	34.27	34.0424
100	20	15	5	14.138	0.027827	5.0411
100	20	15	5	16.371	5.6408	5.31408
100	20	15	5	13.685	35.275	22.3639
100	20	15	5	14.464	1.0006	1.72244
100	20	15	5	13.869	8.9637	13.5002
100	20	15	5	14.212	0.22657	3.68579
100	20	15	5	15.521	3.6159	5.99658
100	20	15	5	14.052	0.51234	7.13354

100	20	15	5	26.484	37.627	37.6501
100	20	15	5	13.966	1.4109	9.80194
100	20	15	5	14.808	1.8799	3.05252
100	20	15	5	17.318	7.9922	6.61092
100	20	15	5	28.509	45.721	45.6979
100	20	15	5	13.876	2.6507	13.2094
100	20	15	5	21.875	21.391	21.9085
100	20	15	5	13.867	7.1536	13.584
100	20	15	5	14.129	0.11311	5.23357
100	20	15	5	13.87	11.284	13.4585
100	20	15	5	13.977	1.2354	9.42827
100	20	15	5	21.292	19.499	20.1738
100	20	15	5	16.581	6.1715	5.32268
100	20	15	5	17.067	7.3196	5.97858
100	20	15	5	19.301	13.548	13.7824
100	20	15	5	14.386	0.76304	1.94895
100	20	15	5	14.745	1.7028	2.65052
100	20	15	5	15.061	2.5017	4.65602
100	20	15	5	17.602	8.6914	7.49318
100	20	15	5	20.246	16.232	16.9656
100	20	15	5	14.881	2.077	3.53748
100	20	15	5	14.027	40.164	7.84942
100	20	15	5	15.659	3.9436	5.99173
100	20	15	5	14.29	0.49152	2.67286
100	20	15	5	13.89	14.228	12.6389
100	20	15	5	23.875	28.334	28.1405
100	20	15	5	13.959	2.3783	10.0446
100	20	15	5	14.017	0.91693	8.14958
100	20	15	5	24.693	31.158	30.9466
100	20	15	5	19.776	14.838	15.427
100	20	15	5	14.028	0.63054	7.81986
100	20	15	5	14.045	0.39804	7.32904
100	20	15	5	13.857	10.061	14.0071
100	20	15	5	14.514	1.1115	1.71868
100	20	15	5	14.959	2.2779	4.0471
100	20	15	5	13.893	4.4873	12.5185
100	20	15	5	13.645	28.052	24.5694
100	20	15	5	14.171	0.058809	4.3873
100	20	15	5	14.188	0.14862	4.08172
100	20	15	5	16.811	6.6781	5.52708
100	20	15	5	17.912	9.5101	8.58584